

**ARMY RESEARCH OFFICE
AND
AIR FORCE OFFICE OF SCIENTIFIC RESEARCH**



**2001
CONTRACTORS' MEETING
IN
CHEMICAL PROPULSION**

**University of Southern California
June 18-19, 2001**

20020508 113

REPORT DOCUMENTATION PAGE

AFRL-SR-BL-TR-02-

Public reporting burden for this collection of information is estimated to average 1 hour per response, including the time for reviewing data needed, and completing and reviewing this collection of information. Send comments regarding this burden estimate or any of this burden to Department of Defense, Washington Headquarters Services, Directorate for Information Operations and Reports (07 4302). Respondents should be aware that notwithstanding any other provision of law, no person shall be subject to any penalty for valid OMB control number. PLEASE DO NOT RETURN YOUR FORM TO THE ABOVE ADDRESS.

ing the
ducing
'202-
currently

039

1. REPORT DATE (DD-MM-YYYY) 09-01-2002		2. REPORT TYPE Technical		3. DATES COVERED (From - To) 1 June 2000 - 31 May 2001	
4. TITLE AND SUBTITLE (U) ARO and AFOSR Contractors Meeting in Chemical Propulsion				5a. CONTRACT NUMBER	
				5b. GRANT NUMBER	
				5c. PROGRAM ELEMENT NUMBER 61102A, 61102F	
				5d. PROJECT NUMBER	
				5e. TASK NUMBER	
6. AUTHOR(S) David M. Mann and Julian M. Tishkoff				5f. WORK UNIT NUMBER	
7. PERFORMING ORGANIZATION NAME(S) AND ADDRESS(ES) Army Research Office Research Triangle Park NC 27709-2211 Air Force Office of Scientific Research Arlington VA 22203-1977				8. PERFORMING ORGANIZATION REPORT NUMBER	
9. SPONSORING / MONITORING AGENCY NAME(S) AND ADDRESS(ES) AFOSR/NA 801 North Randolph Street Room 732 Arlington VA 22203-1977				10. SPONSOR/MONITOR'S ACRONYM(S)	
				11. SPONSOR/MONITOR'S REPORT NUMBER(S)	
12. DISTRIBUTION / AVAILABILITY STATEMENT Approved for public release; distribution is unlimited				AIR FORCE OFFICE OF SCIENTIFIC RESEARCH (AFOSR) NOTICE OF TRANSMITTAL DTIC. THIS TECHNICAL REPORT HAS BEEN REVIEWED AND IS APPROVED FOR PUBLIC RELEASE LAW AFR 190-12. DISTRIBUTION IS UNLIMITED.	
13. SUPPLEMENTARY NOTES					
14. ABSTRACT Abstracts are given for 6.1 basic research in chemical propulsion sponsored by the Army Research Office and the Air Force Office of Scientific Research.					
15. SUBJECT TERMS Flames, Propulsion, Gas Turbines, Diesel Engines, Scramjets, Pulse Detonation Engines, Hydrocarbon Fuels, Chemistry, Sprays, Droplets, Supercritical Fluids, Diagnostics, Combustion					
16. SECURITY CLASSIFICATION OF:			17. LIMITATION OF ABSTRACT UL	18. NUMBER OF PAGES 185	19a. NAME OF RESPONSIBLE PERSON Julian M. Tishkoff
a. REPORT Unclassified	b. ABSTRACT Unclassified	c. THIS PAGE Unclassified			19b. TELEPHONE NUMBER (include area code) (703) 696-8478

ARO/AFOSR Contractors' Meeting in Chemical Propulsion
TABLE OF CONTENTS

Agenda	iv
AFOSR Sponsored Research in Combustion and Diagnostics J.M. Tishkoff, AFOSR/NA	1
The US Army Research Program in Propulsion and Energetics D.M. Mann, Engineering Sciences Directorate, US Army Research Office	3
Ramjet Research T.A. Jackson and M.R. Gruber, AFRL/PRA	5
Mixing, Chemical Reactions, and Combustion in High-Speed Turbulent Flows P.E. Dimotakis and F.N. Egolfopoulos, California Institute of Technology	9
Diesel Engine Injection Rate-Shape Optimization Using Genetic Algorithms and Multidimensional Modeling P.V. Farrell, D.E. Foster, J.B. Ghandhi, J.M. Moskwa, R.D. Reitz, C.J. Rutland and M.L. Corradini, University of Wisconsin-Madison	13
Effects of Advanced Fuel Injection Strategies on DI Diesel Emissions M. Mellor, S.L. Plee, R.J. Tabaczynski, Vanderbilt University	17
Pulse Detonation Physiochemical and Exhaust Relaxation Processes Fred Schauer, Air Force Research Laboratory	21
Intelligent Turbine Engines S. Menon, M. Allen, M. Brooke, A. Glezer, W. Haddad, J. Jagoda, Y. Neumeier, J. Prasad, L. Sankar, J. Seitzman and B. Zinn, Georgia Institute of Technology	24
Filtered Mass Density Function for Subgrid Scale Modeling of Turbulent Diffusion Flames P. Givi and F.A. Jaber, State University of New York at Buffalo	28
PDF Modeling of Turbulent Combustion S.B. Pope, Cornell University	32
Lattice Boltzman Method for Turbulent Combustion S.S. Girimaji, Texas A & M University and L. Luo, NASA Langley Research Center	36
Chemical Kinetics and Aerodynamics of Ignition C.K. Law, Princeton University	40
Physical and Chemical Processes in Flames C.K. Law, Princeton University	.44
Stabilization and Blowout of Gaseous- and Spray-Jet Flames K.M. Lyons, North Carolina State University	48

Investigation of the Structure of a Reacting Hydrocarbon-Air Planar Mixing Layer Corradini, Farrell, Foster, Ghandhi, Reitz and Rutland, University of Wisconsin-Madison	52
Statistical Interpretation of Power Spectral Densities Measured by Picosecond Time-Resolved Laser-Induced Fluorescence in Turbulent Nonpremixed Flames N.M. Laurendeau, G.B. King and J.P. Gore, Purdue University	56
Experimental and Computational Characterization of Combustion Phenomena J. R. Gord and W. M. Roquemore, AFRL/PRTS	60
Concurrent Research on High Gravity (g) Combustion and Enabling Materials W.M. Roquemore (PR) and R.J. Kerans (MLLN), Air Force Research Laboratory	64
Abstracts of Work Units Not Presented at the Meeting	65
Improved Modeling of Drop Vaporization and Combustion in Diesel Sprays John Abraham, Purdue University	66
Large Eddy Simulations of Supercritical Multicomponent Mixing Layers Josette Bellan, Jet Propulsion Laboratory	70
The Chemistry Controlling Ignition of Hydrocarbons and Their Mixtures at High Pressures David L. Miller and Nicholas P. Cernansky, Drexel University	74
Advanced Supercritical Fuels Tim Edwards, Jim Gord, and Chris Bunker, AFRL/PRSF	78
Drop/Gas Interactions in Dense Sprays G. M. Faeth, University of Michigan	82
Advanced Stimulated Scattering Measurements in Supercritical Fluids Gregory W. Faris, SRI International	86
Sub- and Super-Critical Evaporation and Combustion of a Moving Droplet George Gogos, University of Nebraska	90
Crossed-Plane Laser Imaging of Premixed Turbulent Combustion Processes F. C. Gouldin, Cornell University	94
Simultaneous Measurement of Relative OH Concentration, Temperature, and Flow Velocity in H ₂ /O ₂ Flame by Saturated Photothermal Spectroscopy R. Gupta, University of Arkansas	98
Shock Tube Measurements of Ignition Processes in Diesel-Related Fuels Ronald K. Hanson, Stanford University	102
Advanced Diagnostics for Reacting Flows Ronald K. Hanson, Stanford University	104

Modeling Diesel Engine Injector Flows Stephen Heister and Gregory A. Blaisdell, Purdue University	108
Autoignition, Combustion Instability and White Smoke under Transient Conditions with JP-8 Fuel Naeim Henein, Wayne State University	112
Planar Image Particle Analyzer for Whole Field Spray Applications Cecil Hess, MetroLaser, Inc.	116
Flame Spreading and Combustion Behavior of Gun Propellants under High Loading Density Conditions Kenneth K. Kuo, Pennsylvania State University	120
Planar Thermometry in Sooting Transient Diffusion Flames William Roberts, North Carolina State University	122
Soot Morphology in Unsteady Counterflow Diffusion Flames William Roberts, North Carolina State University	126
Chemical-Kinetic Characterization of Autoignition and Combustion of Diesel and JP-8 Kalyanasundaram Seshadri, University of California, San Diego	130
Catalytic Ignition as a Tool for Converting Small Engines to Efficient JP-8 Operation J. Steciak, S. Beyerlein, D. McIlroy, and D. Blackketter, University of Idaho	134
Experimental Study of Plasma-Propellant Interactions Stefan T. Thynell and Thomas A. Litzinger, Pennsylvania State University	137
Experimental Investigation of the Interaction of Electrothermal Plasmas With Solid Propellants Philip L. Varghese and Noel T. Clemens, University of Texas at Austin	141
Development and Optimization of a Comprehensive Kinetic Model of Hydrocarbon Fuel Combustion Hai Wang, University of Delaware	145
Fuels Combustion Research: Supercritical Fuel Pyrolysis Mary Julia Wornat, Princeton University	149
Invitees	153

ARO/AFOSR CONTRACTORS MEETING

IN

CHEMICAL PROPULSION

University of Southern California

Los Angeles CA

18-19 June 2001

MONDAY, 18 JUNE

8:00 - 8:15 AFOSR Sponsored Research in Combustion and Diagnostics
Julian Tishkoff, AFOSR

8:15 - 9:00 The US Army Research Program in Propulsion and Energetics
David Mann, ARO

Topic: Supersonic Combustion

9:00 - 9:30 Ramjet Research
Thomas Jackson and Mark Gruber, AFRL/PRA

9:30 - 10:15 Mixing, Chemical reactions, and Combustion in High-Speed
Turbulent Flows
Paul Dimotakis, California Institute of Technology and Fokion
Egolfopoulos, University of Southern California

10:15 - 10:45 BREAK

Topic: Propulsion Devices

10:45 - 11:15 Diesel Engine Injection Rate-Shape Optimization Using Genetic
Algorithms and Multi-Dimensional Modeling
P. V. Farrell, D. E. Foster, J. B. Ghandi, J. M. Moskwa, R. D. Reitz,
C. J. Rutland, and M. L. Corradini, University of Wisconsin

11:15 - 11:45 Effects of Advanced Fuel Injection and Strategies on DI Diesel
Emissions
A. M. Mellor, Vanderbilt University and Steven Plee, Motorola, and
R. J. Tabaczynski, Ford Motor Company

11:45 - 12:15 Pulsed Detonation Physiochemical and Exhaust Relaxation
Processes
Fred Schauer, AFRL/PRTS

12:15 - 1:30 LUNCH

Topic: Turbulent Combustion

- 1:30 - 2:00 Intelligent Turbine Engines
S. Menon, M. Allen, M. Brooke, A. Glezer, W. Haddad, J. Jagoda,
Y. Neumeier, J. Prasad, L. Sankar, J. Seitzman, and B. Zinn,
Georgia
Institute of Technology
- 2:00 - 2:30 Filtered Mass Density Function for Subgrid Scale Modeling of
Turbulent Diffusion Flames
Peyman Givi and Farhad Jaber, State University of New York at
Buffalo
- 2:30 - 3:00 PDF Modeling of Turbulent Combustion
Stephen Pope, Cornell University
- 3:00 - 3:30 Lattice Boltzman Method for Turbulent Combustion
Sharath Girimaji, Texas A&M University
- 3:30 - 4:00 BREAK
- 4:00 - 4:30 Chemical Kinetics and Aerodynamics of Ignition
C. K. Law, Princeton University
- 4:30 - 5:00 Physical and Chemical Processes in Flames
C. K. Law, Princeton University
- 5:00 - 5:30 Stabilization and Blowout of Gaseous- and Spray-Jet Flames
Kevin Lyons, North Carolina State University

TUESDAY, 19 JUNE

- 8:15 - 8:30 Announcements

TOPIC: Turbulent Combustion

- 8:30 - 9:00 Investigation of the Structure of a Reacting Hydrocarbon-Air Planar
Mixing Layer
M. Corradini, P. Farrell, D. Foster, J. Ghandi, R. Reitz, and C.
Rutland, University of Wisconsin-Madison
- 9:00 - 9:30 Statistical Interpretation of Power Spectral Densities Measured by
Picosecond Time-Resolved Laser-Induced Fluorescence in
Turbulent Nonpremixed Flames
Normand Laurendeau, Purdue University
- 9:30 - 10:00 Experimental and Computational Characterization of Combustion
Phenomena
J. R. Gord and W. M. Roquemore, AFRL/PRTS

10:00 – 10:30	BREAK
10:30 – 11:00	ARO Business Session
11:00 – 12:00	AFOSR Business Session
12:00 - 1:30	LUNCH
1:30 - 4:00	Concurrent Research on High Gravity (g) Combustion and Enabling Materials W. M. Roquemore, AFRL/PRTS Ronald Kerans, AFRL/ML Brian Cox, Rockwell Science Center Garry Brown, Princeton University
4:00	ADJOURN

AFOSR SPONSORED RESEARCH IN COMBUSTION AND DIAGNOSTICS

PROGRAM MANAGER: JULIAN M. TISHKOFF

**AFOSR/NA
801 North Randolph Street, Room 732
Arlington VA 22203-1977**

SUMMARY/OVERVIEW: The Air Force Office of Scientific Research (AFOSR) program in combustion and diagnostics currently is focused on five areas of study: high-speed propulsion, turbulent combustion, atomization and sprays, diagnostics, and supercritical fuel behavior. An assessment of major research needs in each of these areas is presented.

TECHNICAL DISCUSSION

AFOSR is the single manager for Air Force basic research, including efforts based on external proposals and in-house work at the Air Force Research Laboratory (AFRL). Combustion and Diagnostics is assigned to the AFOSR Directorate of Aerospace and Materials Sciences along with programs in rocket and space propulsion, fluid and solid mechanics, and structural materials.

Interests of the AFOSR Combustion and Diagnostics subarea are given in the SUMMARY section above. Many achievements can be cited for these interests, yet imposing fundamental research challenges remain. The objective of the program is publications in the refereed scientific literature describing significant new understanding of multiphase turbulent reacting flow. Incremental improvements to existing scientific approaches, hardware development, and computer codes fall outside the scope of this objective.

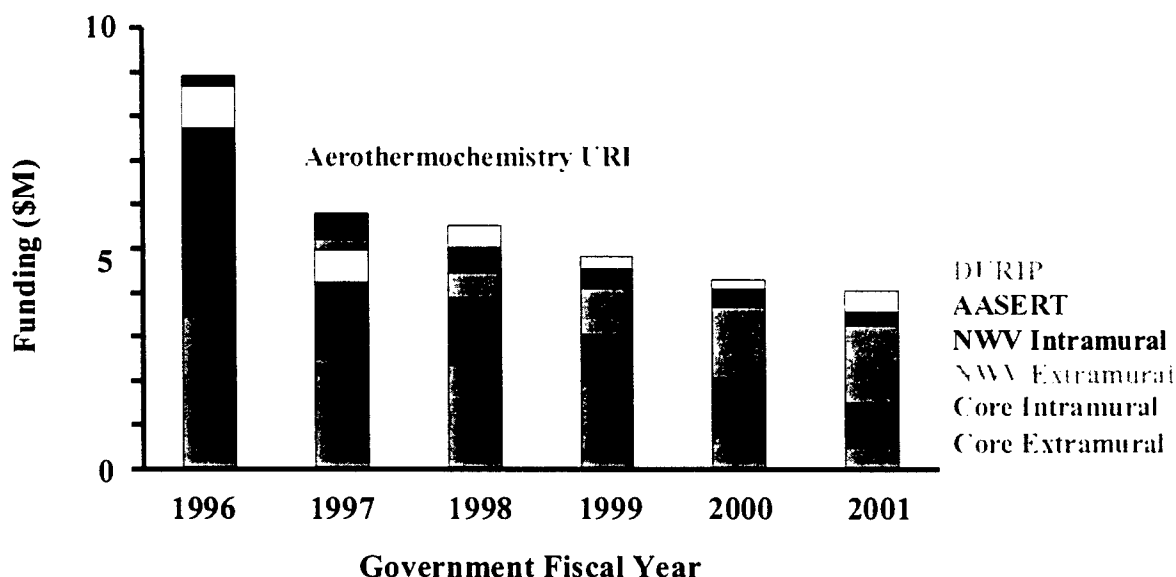
The Combustion and Diagnostics subarea reflects a new Air Force commitment to support space science and technology. Accordingly, the research in this subarea will address research issues related to chemical propulsion for all Air Force aerospace missions, including combined cycle propulsion for access to space. This program will complement related research activities in space propulsion and energetic materials.

Future airbreathing propulsion systems will require fuels to absorb substantial thermal energy, raising fuel temperatures to supercritical thermodynamic conditions. Understanding and controlling fuel properties at these conditions will be crucial for avoiding thermal degradation and for optimizing subsequent processes within the combustor. Environmental concerns and the availability of petroleum supplies also will contribute to future propulsion system design and operational needs.

In the current fiscal year new research opportunities emerged in two areas: plasma-based ignition and combustion enhancement; and combustion-based approaches for the destruction of chemical and biological agents. Plasma research was supported through one of three AFOSR Theme topics, as announced through Broad Agency Announcement 2001-2. The destruction of chemical and biological agents is being pursued through the STTR program. The research community is encouraged to suggest other new directions for combustion research.

Decisions on support for research proposals are based on scientific opportunities and technology needs. Researchers interested in submitting proposals should contact Dr. Tishkoff for information on time constraints associated with proposal evaluations. Further information on research interests and proposal preparation can be found on the AFOSR web site, <http://www.afosr.af.mil>. The availability of funds places a major constraint on program redirection and growth. Figure 1 shows the recent trend of funding for basic research in combustion and diagnostics from Air Force and DOD sources. Funding in the next fiscal year (FY 2001) is expected to be roughly the same as that for FY 2000. Informal inquiries for new research are encouraged throughout the year. Formal proposals should be submitted by 1 April for peer review by the National Research Council.

The purpose of this abstract has been to communicate AFOSR perceptions of research trends to the university and industrial research communities. However, communication from those communities back to AFOSR also is desirable and essential for creating new research opportunities. Therefore, all proposals and inquiries for fundamental research are encouraged even if the content does not fall within the areas of emphasis described herein. Comments and criticisms of current AFOSR programs also are welcome.



The US Army Research Program in Propulsion and Energetics

David M. Mann
Acting Director, Engineering Sciences Directorate
Manager, Propulsion and Energetics
US Army Research Office

Currently, the Army's mechanics research program is executed by the Army Research Office, the Army Research Laboratory, four Research, Development and Engineering Centers, and the Corps of Engineers. In order to jointly develop the Army's mechanics basic research agenda for the future, a Mechanics Research Strategy Planning Workshop was convened on 17-18 January 2001 with participants from all the pertinent Army agencies. The report from that meeting is still in the draft form. However, in the interest of providing the attendees at this ARO-AFOSR Contractors Meeting in Chemical Propulsion with the vision of the participants at the planning meeting, I have copied below the introduction from the propulsion and energetics section of that report. In my presentation, I will highlight some of the aspects of the report.

**U.S. ARMY
MECHANICS RESEARCH STRATEGY
PLANNING WORKSHOP
17-18 JANUARY 2001
DUCK, NORTH CAROLINA**

PROPULSION AND ENERGETICS

Introduction

Propulsion and energetics research supports the Army's need for higher performance propulsion systems. These systems must also provide reduced logistics burden (lower fuel/propellant usage) and longer life than today's systems. Fundamental to this area are the extraction of stored, chemical energy and the conversion of that energy into useful work, for vehicle and projectile propulsion. In view of the high temperature and pressure environments encountered in these combustion systems, it is important to advance current understanding of fundamental processes as well as to advance the ability to make accurate, detailed measurements for the understanding of the dominant physical processes and the validation of predictive models. Thus, research in this area is characterized by a focus on high pressure, high temperature combustion processes and on the peculiarities of combustion behavior in systems of Army interest.

Current ground and air vehicle propulsion relies on reciprocating (Diesel) and gas turbine engines. These engines must be capable of delivering high power with high fuel efficiency. These thrusts, power density and efficiency, are the heart of the Army's initiative for the Future Combat System. The development of reliable, predictive models for vehicle engines will require advances in understanding fundamental processes, such as turbulent flame structure, heat transfer, and chemical kinetics, as well as understanding and control of the complex chain of fuel injection-atomization-ignition-combustion processes. An additional complication is presented by the high

pressure/temperature environment, encountered in Diesel engines, which influences liquid behavior and combustion processes at near-critical and super-critical conditions. It should be noted that over 95% of Army vehicles are diesel-powered and that the Army desires the capability to use a single, logistics fuel in all engines, both diesel and turbine.

Gun and missile propulsion relies on the rapid, controlled release of energy from high energy density propellants, which exhibit unique combustion characteristics. Modern composite, solid propellants are characterized by a complex, multi dimensional flame structure, with solid, liquid, liquid-gas, and gas phase reaction zones. The small scales of the combustion zones, typically on the order of microns, and the high pressures, up to 100,000 psi, present formidable challenges for combustion diagnostics. There are systems whose future development requires new directions in combustion research. Among these is the electrothermal-chemical (ETC) gun, in which the ignition, and potentially combustion control, of solid propellant is achieved by high temperature plasmas. Concepts for advanced, variable thrust missile propulsion also pose difficult challenges, e.g. the interaction/combustion of hypergolic propellants, the development of novel combustion chambers (c.f. vortex combustors), the dynamics of pintle nozzles, etc. An underlying concern with all high energy density systems is the hazard and system vulnerability posed by the propellant. Thus, research is also needed to determine the response of these materials to inadvertent ignition stimuli and factors controlling undesired combustion behavior, such as pressure oscillations. A key goal is the coupled analysis of propellant composition, material characterization, combustion dynamics, and sensitivity.

TITLE: RAMJET RESEARCH

AFOSR TASK 2308BW

Principal Investigators: Thomas A. Jackson
Mark R. Gruber

Propulsion Sciences and Advanced Concepts Division
Propulsion Directorate
Air Force Research Laboratory
Wright-Patterson AFB OH 45433

SUMMARY/OVERVIEW

This research task includes work in three primary focus areas: (1) multiphase flows relevant to fuel injection into very high-speed, oxidizing streams, (2) shock - boundary interactions within reactive media, and (3) multidisciplinary laser measurements for benchmarking modeling and simulation of high-speed, reacting flows. Within each of these areas there is a strong relevance to the scramjet propulsion system, and that relationship helps frame the context of our research. The focus of this abstract will be on the shock – boundary layer interactions in and around a recess in the walls that confine the supersonic core flow. A flow recess, or cavity, is an essential element of a scramjet flameholder. Its interaction with the core flow and the method of introducing fuel and in sustaining a stable, combustible mixture within the cavity are the subject of our research in this area. A joint computational-experimental study has revealed the cavity to be difficult to fuel uniformly in space and that the interchange with the core flow varies substantially in time.

TECHNICAL DISCUSSION

A cavity is a pervasive feature of scramjet combustion piloting devices. Its function is to decelerate a small portion of the high-speed core flow, establish a stable combustible mixture and hold flame. Ideally, it would perform this function insulated from the flow fluctuations of the core, interacting with the shock system like a locally thick boundary layer. It does not. Expansion fans and shocks dominate the mass exchange between cavity and core flow. Local stoichiometry varies widely in all three spatial dimensions and in time.

We have begun examining the flow around a model cavity-based flameholder in non-reacting and reacting, supersonic flows. Our initial work included a parametric assessment of the effects of cavity geometry (including length-to-depth ratio and aft wall angle) on global features such as drag, acoustic stability, and entrainment rate. More recently two-species Raman scattering has been used to map the fuel-air distribution around a wall cavity immersed in a Mach 2 flow with and without an imposed shock train. Wide spatial variations in local stoichiometry are observed. These experimental studies are complemented by computations based on a hybrid flow solver. The hybrid solver combines the strengths of a Reynolds-Averaged Navier Stokes (RANS) code with those of a Large Eddy Simulation (LES). These computations reveal significant temporal fluctuations within the recessed cavity exposed to a supersonic flow. The mass exchange with the core is highly oscillatory. One result is that fueling the cavity indirectly, through entrainment

of both fuel and air from the core flow, may be more stable than direct fueling where the cavity stoichiometry varies temporally with variations in air entrainment.

The configuration of interest is a confined flow over a cavity located in one wall of a rectangular cross section. A facility nozzle accelerates the core flow to Mach 1.9. The flow enters a rectangular duct with a nominal aspect ratio of 3:1. Several duct heights downstream of the inlet the flow passes over a cavity. Cavities of various length-to-depth ratios have been evaluated. Cavity close-out surfaces angled 90 to 16 degrees to the core flow have been studied. Figure 1 illustrates the flow in cross-section of one such cavity. Depicted are the results of a RANS-based computation for flow over a cavity with no back-pressure and no fuel or fuel-simulant injected. The streamlines within the cavity are shown as well as the computed pressure field, represented by the gray-scale shading. Pressure measurements along the cavity walls match the computed field for all designs evaluated. This particular cavity establishes primary and corner recirculation zones. The shear layer separating core and cavity flow fields is steady in the computation.



Figure 1. Mach 1.9 flow over a cavity – shadowgraph and RANS computation (1)

For fuel-air mixing studies gaseous fuel is injected into either the core flow and entrained into the cavity, or directly into the cavity. For injection into the core flow, only a single ethylene injector, angled at 15° to the primary flow direction, is used.

This facility cannot sustain enough heat release to establish the desired pre-combustion shock system through combustion. Instead a back-pressure valve is used to create combustion-like pressure conditions over the cavity. Unobstructed, the flow over the cavity remains supersonic, representing the pre-ignition flow environment. Appropriately back-pressured to simulate different levels of combustion, the flow is subsonic in the mean at this condition. This flow represents the steady-state combustor environment within the scramjet operating at a flight Mach number of approximately 4. Figure 2 compares the static pressure along the wall of this facility at different levels of back-pressure with similar measurements taken on this geometry during full combustion testing in another facility. At increasing levels of heat release the pre-combustion shock system is pushed forward and peak pressures approach normal shock pressure rise. The cold-flow, back-pressured experiment replicates the wall pressure distribution of the combustion case.

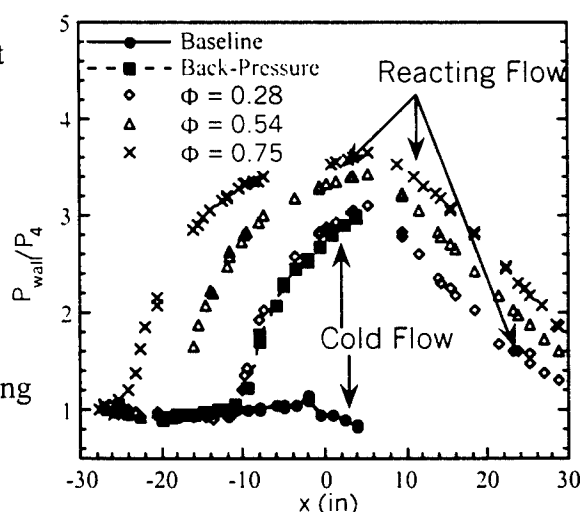


Figure 2. Static pressure distribution in cold and reacting flow

A Raman scattering system was configured to simultaneously measure ethylene and nitrogen concentrations. Ethylene was injected through the single injector upstream of the cavity at two injection pressures. The main air stream is the only source of nitrogen in the experiment.

Ratioing the two Raman measurements throughout the cavity established the spatial variation of the cavity stoichiometry. This was done with and without back-pressure applied to the core flow. Figure 3 is a sample of the results at a single axial position within the cavity (2). These results offer no insight into the temporal variations of the cavity stoichiometry – only the spatial distribution. At low fuel injection pressure, into either the supersonic (no back-pressure) or subsonic (back-pressured) core flows, the ethylene does not significantly penetrate the boundary layer and is entrained into the cavity. It is, however, slow to disperse in the transverse direction. At higher injection pressure the fuel penetrates the boundary layer of both core flows and fails to provide much fuel to the cavity. High pressure ethylene injected into the supersonic core flow sustains a very tightly bound fuel plume and begins to form vortical, kidney-shaped structures as it is transported downstream. While the trend of entrainment and injection pressure is predictable, it is noteworthy that the fuel dispersion differs substantially within the supersonic and subsonic core flows. Dispersion of fuel transverse to the main flow direction is slow in both situations.

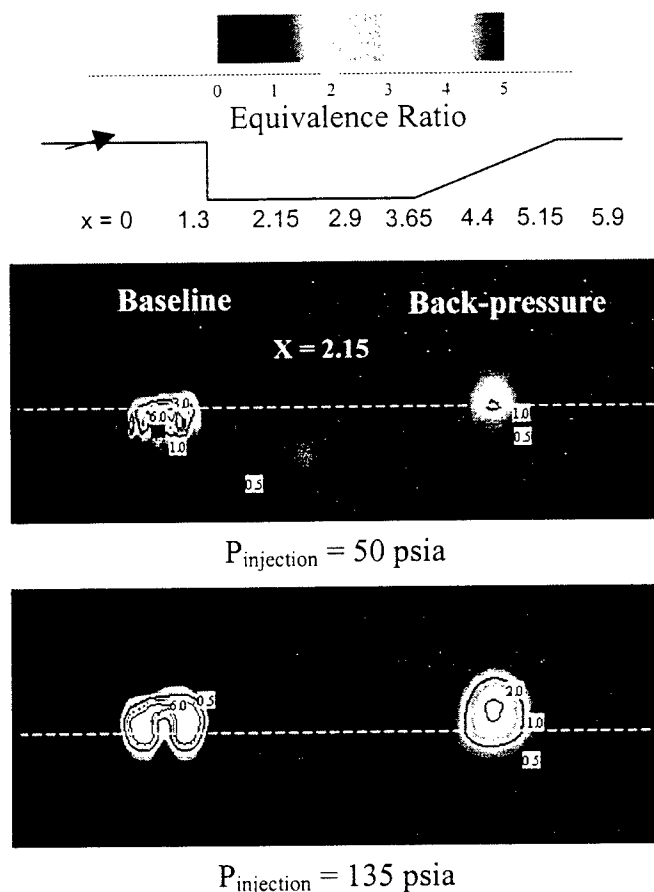


Figure 3. Local stoichiometry variations in cavity in a high-speed cross-flow using Raman scattering.

Temporal uniformity of cavity fueling has been investigated numerically. A Large Eddy Simulation (LES) flow solver has been patched into a hybrid solver with a RANS code and utilized to examine mass exchange between cavity and core flow. Coding details have been reported (3). Applied to the problem of continuously supplying a combustible mixture to the scramjet cavity through core flow entrainment and/or direct injection, this computational method is well suited. The supersonic flow in the constant-area duct up-stream of the cavity is well modeled with the RANS solver. In the cavity region the code reverts to the LES solver that can resolve details of the free-shear layer emanating from the forward step of the cavity. Figure 4 illustrates one frame of the periodic flow captured by the computation. The flow field is displayed as a numerical Schlieren image. When viewed as a series of images the flow is clearly not steady. Vortices are formed and shed from the forward lip of the cavity suggesting mass exchange between cavity and core flows is highly periodic. This image is sharp contrast to that depicted in Figure 1 where the RANS solver fails to capture any instability in the shear layer over the cavity.

Two-species Raman scattering and the hybrid RANS-LES solver are powerful tools in studying the mass exchange between core and cavity-entrained flows in the confined supersonic flow characteristic of the scramjet propulsion system. Mixing entrained or direct-injected fuel in the



Figure 4. Numerical simulation of a supersonic core flow over a cavity. Result based on a hybrid LES-RANS computation.

transverse direction is slow. And, the unsteady nature of the exchange between core and cavity makes stabilization of the combustion process challenging with the cavity-based flame-holder. Our studies suggest better ways to fuel the cavity flame-holder and are leading us toward alternative ways to define a stable scramjet pilot.

Acknowledgements:

Dr. Mark Hsu of Innovative Scientific Solutions, Inc. and Dr. Rob Baurle of Taitech, Inc. are leading the Raman measurements of fuel entrainment by a cavity and the development of the hybrid RANS-LES solver, respectively. They are part of the research team at Wright-Patterson Air Force Base.

References:

1. Gruber, M., Baurle, R., Mathur, T., and Hsu, K., "Fundamental Studies of Cavity-Based Flameholder Concepts for Supersonic Combustors," *J. of Propulsion and Power*, Vol. 17, No. 1, pp 146-153, 2001
2. Hsu, K.-Y., Carter, C., Mathur, T., and Gruber, M., "Fuel Distribution about a Cavity Flameholder in Supersonic Flow," AIAA Paper 2000-3585, July 2000.
3. Baurle, R. A., Tam, C. J., and Dasgupta, S., "Analysis of Unsteady Cavity Flows for Scramjet Applications," AIAA Paper 2000-3617, July 2000.

MIXING, CHEMICAL REACTIONS, AND COMBUSTION IN HIGH-SPEED TURBULENT FLOWS

AFOSR Grant F49620-01-1-0006

P. E. Dimotakis and F. N. Egolfopoulos¹

Graduate Aeronautical Laboratories

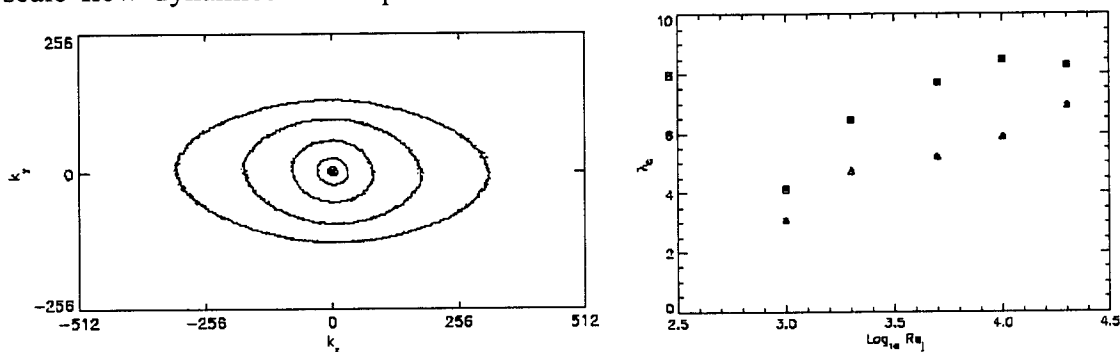
California Institute of Technology, Pasadena, CA 91125

Summary/Overview

This research focuses on fundamental investigations of mixing, chemical-reaction, and combustion, in turbulent, subsonic, and supersonic flows. It is comprised of an experimental effort; an analytical, modeling, and computational effort; and a diagnostics- and instrumentation-development effort. Computational studies are focusing on fundamental issues pertaining to hydrocarbon ignition and combustion as well as investigations of the Rayleigh-Taylor instability.

Technical discussion

Transport and mixing in turbulent jets in a crossflow is important for fuel injection in SCRAMJETS (Mathur *et al.* 1999), blade and endwall cooling in gas-turbine engines, and other applications. Experiments measured the jet-fluid-concentration fields in turbulent transverse jets, using laser-induced fluorescence and digital-imaging techniques. One finding is that the resulting scalar field can be anisotropic, even at small length scales. Ensemble-averaged, two-dimensional, scalar power spectra are computed for liquid-phase transverse jets at $x/d_j = 50$, where x is the downstream distance and d_j is the jet diameter, in a plane transverse to the flow direction (Fig. 1, left). Contours indicate increasing anisotropy at higher wavenumbers, *i.e.*, at smaller scales. Anisotropy also registers in the microscales of scalar fluctuations. Analogously to the Taylor microscale, a scalar microscale, $\lambda_{C,i}$, for a given direction, is introduced as, $\lambda_{C,i} = \langle C'^2 \rangle / \langle (\partial C' / \partial x_i)^2 \rangle$. Scalar microscales for $1.0 \times 10^3 \leq Re_j \leq 20 \times 10^3$ are shown in Fig. 1, right. The scalar microscale in the vertical, y , direction is consistently larger than the horizontal, z , microscale. The observed scalar-field anisotropy is a consequence of extensional strain along the vertical direction, caused by the dominant, kidney-shaped vortex pair in the transverse jet. Anisotropic, large-scale flow dynamics can impose themselves on even the smallest features of the scalar



field.

Fig. 1 Transverse-jet scalar field measures at $x/d_j = 50$. Left: Ensemble-averaged, 2-D power spectrum for $Re_j = 1.0 \times 10^3$. Right: Scalar microscale as a function of jet Reynolds number (squares: vertical, y , microscales; triangles: horizontal, z , microscales).

¹ Dept. of Mechanical Engineering, U. Southern California, Los Angeles, CA 90089.

Figure 2 depicts a space-time image of an isosurface of the jet-fluid concentration, illustrating the “kidney” vortex pair as well as a strong, secondary vortex, which was not evident in 2-D slices. The data are for a jet Reynolds number of 1000 and a jet-to-freestream velocity ratio of 10.1. A first documentation of this work will be available as a Ph.D. thesis (Shan 2001). Work in this area presently in progress is focused on quantifying the anisotropy as well as aspects of the three-dimensional behavior of the mixing and scalar field.

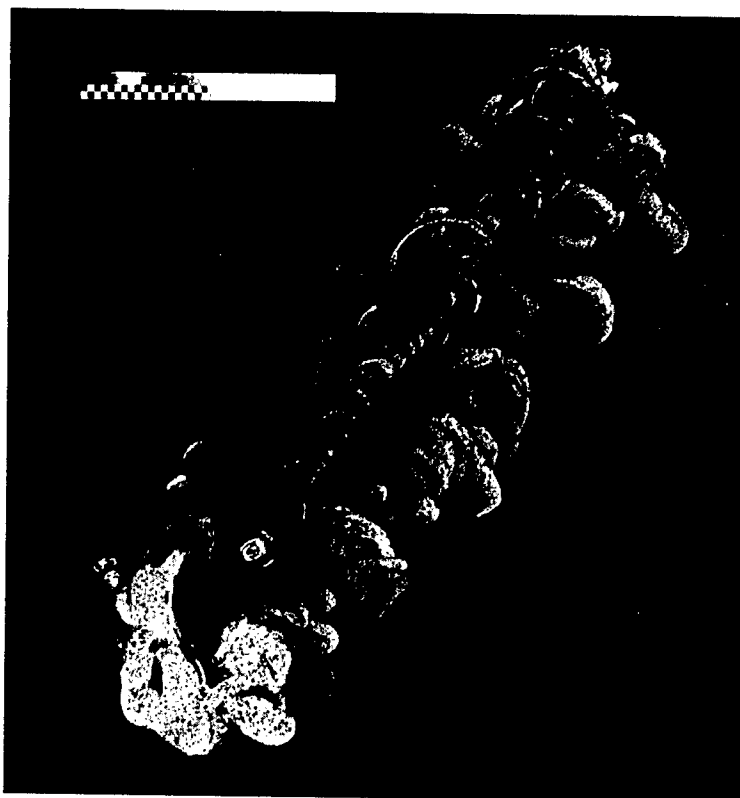


Fig. 2 Three-dimensional visualization of an isosurface in a transverse jet (Shan 2001, $Re_j = 10^3$, $U_j/U_\infty = 10.1$). Visualization by S. Lombeyda (Caltech, CACR).

Experiments were performed to explore the aerodynamic control of internal flows, as occur, for example, in subsonic diffusers and scramjet combustors. To date, the work has focused on subsonic diffusers, as a first step, and on the behavior of flow over a backward-facing perforated ramp, with variable mass injection, velocity ratio, and Reynolds number. Diagnostics included upper-guidewall pressure measurements, total-pressure measurements at the test-section exit, and schlieren images recorded on a 1024²-pixel, 30fps CCD camera. A performance parameter in such flows is the pressure coefficient, $C_p = 2(p_2 - p_1)/\rho U^2$. Figure 3 plots C_p versus the freestream-to-injection velocity ratio, for the two freestream velocities indicated. Point 1 is on the top guidewall, above the ramp start. Point 2, also on the top guidewall, is at the downstream location of the total-pressure-probe array. The pressure coefficient is higher at smaller velocity ratios and at higher freestream velocities, indicating Reynolds number effects. As the velocity ratio is increased, the pressure coefficients converge and decrease, as flow in both cases approaches a conventional shear layer with a small streamwise pressure gradient. Work in progress is focusing on measurements of mixing between the freestream and injected fluid, using the $(H_2 + NO)/F_2$ chemical reaction, to assess the behavior of turbulent shear layers in the vicinity of solid boundaries as well as explore the additional benefits of dilatation in diffuser operation. This work is part of the graduate research of W.-J. Su and M. Johnson.

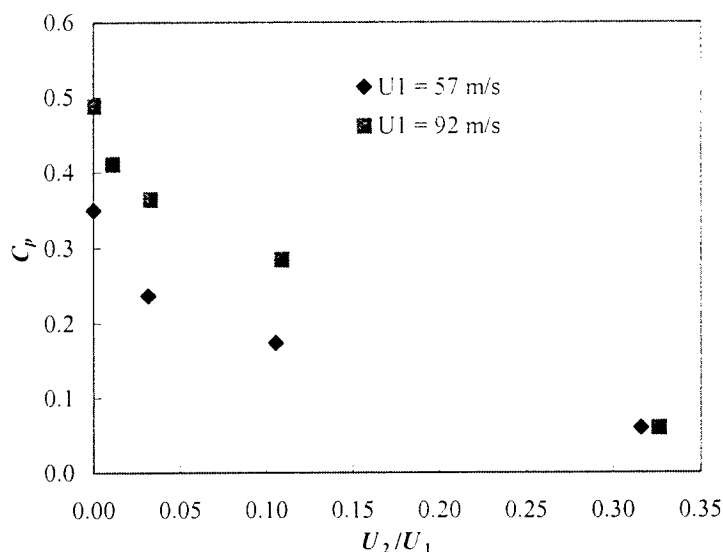


Fig. 3 Internal-flow pressure coefficient (see text) as a function of mass-injection (U_2) to freestream (U_1) speed ratio.

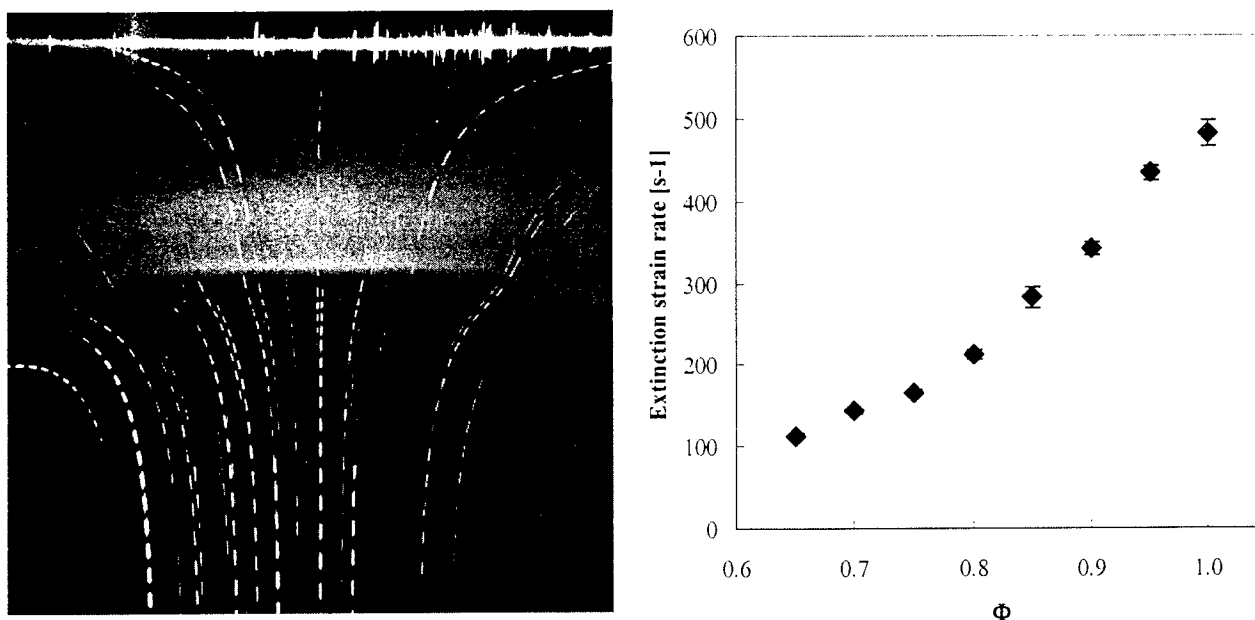


Fig. 4 Left: CH₄-air flame ($\Phi = 0.8$, $Re_d = 500$, chemiluminescence and PSV). $\sigma_{\max} = 112 \text{ s}^{-1}$. Right: Extinction strain rates, σ_{ext} , against a room-temperature plate, vs. equivalence ratio, Φ .

A new experimental method was developed for the study of premixed hydrocarbon-air flames in a stagnation-flow configuration. Experiments were conducted at $p = 1 \text{ atm}$ focusing on methane-air and ethylene-air flames and investigated a range of fuel concentrations (equivalence ratio, Φ) and ratios of stagnation-plate separation distance to nozzle diameter (L/d_j). Methane-air flame properties measured include laminar flame speeds, flame speeds for strained flames vs. imposed strain rate, and extinction strain rates. The experiments relied on digital imaging of flame chemiluminescence, particle-streak velocimetry (PSV), laser-Doppler velocimetry (LDV), and jet-exit velocity measurements using a Bernoulli pressure-drop method. Figure 4 (left) displays the flow-field for a methane-air flame ($\Phi = 0.8$, $Re_d \cong 500$). The results are in good agreement

with previous experimental data. New extinction strain-rate data for CH₄-air flames against a room-temperature stagnation plate were acquired and compared against numerical simulations for four different chemical-kinetic schemes. Figure 4 (right) displays a preliminary set of measured extinction strain rates for lean methane-flames. In attempting to simulate the extinction strain-rate values, we noted that the conventional one-dimensional formulation for the streamfunction used in the flame codes does not capture cold-flow velocity profiles along the stagnation streamline and, as a consequence, the measured strain-rate field at the L/d_j values was relied upon. A careful reexamination of the boundary conditions at the cold plate, vis-à-vis reacting species, is also underway. A first report of this work was recently presented (Vagelopoulos and Dimotakis 2001).

Direct Numerical Simulation (DNS) studies of the Rayleigh-Taylor instability have continued, with a first documentation of this work accepted for publication (Cook & Dimotakis 2001). Work in progress is focusing on post-processing existing three-dimensional data. A new set of DNS runs will study density-ratio effects and mixing in accelerating flows, and increase Reynolds numbers to values closer to the mixing transition (Dimotakis 2000). This is a collaborative effort with A. Cook (LLNL), and T. Mattner and D. Meiron of Caltech, and is cosponsored by the Caltech ASCI/ASAP program.

Preparatory work for experimental investigations of the behavior of spheres and drops in the transitional Reynolds number regimes pertaining to droplet combustion is continuing. In this regime, disturbances grow, spatial and temporal symmetries can be broken, and topological structure varies. Our objective, in part, is to document and understand these phenomena. To this end, a new, dedicated, liquid-phase drop tank facility was designed that will permit multi-dimensional, fully resolved (spatially and temporally) data to be recorded. The new facility is under construction. To allow the flow to be imaged in the frame of the sphere/drop, a drive mechanism, consisting of a computer-controlled platform will move the digital-imaging system along with the transmitting/receiving optics in the frame of the moving sphere or droplet. In the case of sphere flows, the sphere-controlling mechanism is coupled to the transmitting/receiving optics mechanism. This work is part of the graduate research of S. Malhotra.

References

- Cook, A. W., and Dimotakis, P. E. 2001 "Transition stages of Rayleigh-Taylor instability between miscible fluids," *J. Fluid Mech.* (to appear).
- Dimotakis, P. E. 2000 "The mixing transition in turbulence," *J. Fluid Mech.* **409**, 69-98.
- Mathur, T., Billig, F., Streby, G., Gruber, M., Jackson, K., Donbar, J., Donaldson, W., Jackson, T., and Smith, C. 1999 "Supersonic combustion experiments with a cavity-based fuel injector," 35th *AIAA/ASME/SAE/ASEE Joint Propulsion Conference and Exhibit* (20-24 June 1999, Los Angeles, CA).
- Shan, J. W. 2001 *Mixing and Isosurface Geometry in Turbulent Transverse Jets*, Ph.D. thesis, California Institute of Technology.
- Vagelopoulos, C. M., and Dimotakis, P. E. 2001 "Rapid recording of flame propagation and extinction behavior in methane-air mixtures," 2nd U.S. Joint Meeting (Combustion Institute, 25-28 March 2001, Oakland, CA), Paper 136.

DIESEL ENGINE INJECTION RATE-SHAPE OPTIMIZATION USING GENETIC ALGORITHMS AND MULTIDIMENSIONAL MODELING

(Grant/Contract Number DAAD19-00-1-0487)

Principal Investigator(s): P. V. Farrell, D. E. Foster, J. B. Ghandhi, J. M. Moskwa,
R. D. Reitz, C. J. Rutland, and M. L. Corradini
Engine Research Center
University of Wisconsin-Madison

This work was performed by Prof. R. D. Reitz, D. Montgomery, and P. K. Senecal.

SUMMARY/OVERVIEW:

A computational optimization study was performed for a heavy-duty direct-injection diesel engine using the recently developed KIVA-GA computer code. The effects of 11 engine input parameters on emissions and performance were studied. Start of injection (SOI), amount of EGR, boost pressure and eight parameters defining the fuel injection rate-shape were included in the search. The optimized configuration results in very low soot and NOx emissions together with relatively low fuel consumption.

TECHNICAL DISCUSSION

It is well known that diesel combustion and emissions formation strongly depend on the rate of fuel injection. Diesel fuel injection systems typically employ either a square, rising or falling rate of injection. Rising rate-shapes are commonly believed to be "optimal," however this view was established when injection durations were typically long in length and injection timings were relatively advanced. It is clear that alternative rate-shapes should be investigated with the use of modern high-pressure, short duration injections. Recently, a number of experimental and computational investigations have demonstrated the capability of multiple injections to reduce both NOx and soot emissions simultaneously. For example, Montgomery and Reitz [1] showed experimentally that particulate and NOx emissions, as well as fuel consumption, can be reduced over the entire engine operating map with the use of multiple injections and EGR.

Senecal and Reitz [2] performed a computational optimization study including two split injection parameters, as well as boost pressure, EGR, injection duration and start of injection timing. In that study, a realistic split injection rate-shape was used, with the amount of mass in the first injection pulse and the dwell between injections changing in the optimization. The KIVA-GA code was introduced was used to find an optimal set of parameters that resulted in significantly lower emissions, as well as improved fuel consumption, compared to the baseline case. The present study is similar to the study of Senecal and Reitz [2], however a much more general rate-shape parameterization is included, as described below. The parameterization allows for single or double injections, different peak injection velocities for each of the two injections, and a range of opening and closing durations.

Baseline Design

A single cylinder version of the Caterpillar 3400 Series diesel engine was chosen for the present study due to the large amount of available experimental data for this engine [1]. The baseline engine specifications and operating conditions are presented in Table 1. For this study, a 57% load, 1737 rev/min operating point was investigated. It has been shown that the present multi-dimensional model predictions agree well with measured data at this operating point for a variety of boost pressures, EGR levels and injection strategies [2].

Bore \times Stroke	137.2 \times 165.1 mm
Compression Ratio	16.1
Displacement	2.44 L
Combustion Chamber	Quiescent
Engine Speed	1737 rev/min
% of Maximum Load	57

Table 1. Engine specifications and operating conditions for the baseline engine case.

The design factors and ranges considered in the present study are given in Table 2. The parameter ranges for boost pressure, EGR and SOI are identical to those used in the previous study of Senecal and Reitz [2], however, a much more general injection rate-shape parameterization is used in this study. As shown in Fig. 1, eight parameters are used to define the injection velocity profile. The present parameterization allows for single or double injections.

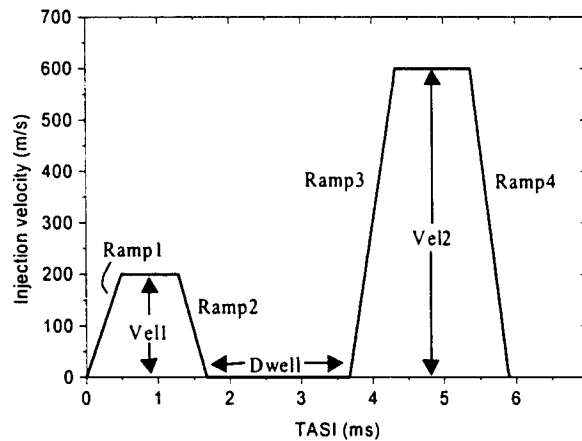


Figure 1. Example injection rate-shapes in the present parameterization. Injection velocities are presented as a function of Time After the Start of Injection (TASI) in ms.

Objective Function and its Evaluation

The objective (merit) function used previously by Montgomery and Reitz [3] and Senecal and Reitz [2] is also used in the present study. The merit function includes fuel consumption and engine-out NO_x, Hydrocarbon (HC) and soot emissions levels, and is given by

$$f(\mathbf{X}) = \frac{1000}{R_1^2 + R_2^2 + R_3}$$

where

$$R_1 = \frac{\text{NOx} + \text{HC}}{W_1(\text{NOx} + \text{HC})_m} \quad R_2 = \frac{\text{PM}}{W_2 \text{PM}_m} \quad R_3 = \frac{\text{BSFC}}{\text{BSFC}_0}$$

and the parameter vector \mathbf{X} is defined in Table 2. In addition $(\text{NOx} + \text{HC})_m$ and PM_m are EPA mandated emissions levels (3.35 and 0.13 g/kW-hr, respectively) and BSFC_0 is a baseline fuel consumption (215 g/kW-hr in the present work). Furthermore, W_1 and W_2 are weighting constants (safety factors) set to 0.8 for this study.

Parameter	Range	Resolution
Boost Pressure (kPa)	165 → 284	64
EGR (%)	0 → 50	32
SOI (deg. atdc)	-10 → 10	32
Vel1 (m/s)	100 → 700	32
Vel2 (m/s)	100 → 700	32
P1 (%)	10 → 90	32
Ramp1 (%)	0 → 100	16
Ramp2 (%)	0 → 100	16
Ramp3 (%)	0 → 100	16
Ramp4 (%)	0 → 100	16
Dwell (deg.)	0.0 → 15.0	32

Table 2. Design parameters, ranges and resolutions.

Results

900 function evaluations (i.e., 75×12 KIVA runs) were performed, requiring approximately three weeks of CPU time for convergence. The parameters for this optimal case are summarized in Table 3. In addition, the optimum's injection profile is presented in Fig. 2. This rate-shape features two injection pulses, with a 4.4 deg. dwell between them. The first pulse has a relatively long opening ramp, followed by a near-maximum injection velocity of 660 m/s and a minimum closing ramp parameter of zero. The second pulse is similar to the first, but with a smaller duration and a higher peak injection velocity of 700 m/s.

Figure 3 presents soot vs. NOx points for a majority of the cases considered in the KIVA-GA optimization simulation. It is clear that the optimum design results in emissions levels well within the 2002/2004 mandates, and a relatively low BSFC value of 197 g/kW-hr was also achieved at the optimum point.

The 2002/2004 emissions mandates were also met with the less flexible injection profile considered by Senecal and Reitz [3]. However, the present optimum case reached lower NOx levels (i.e., 0.7 vs. about 1.0 g/kW-hr), similar soot levels (0.04 g/kW-hr) and lower BSFC (i.e., 197 vs. about 212 g/kW-hr) than that of the the previous study. This points out the advantage of using a more flexible injection system.

Parameter	Optimized value
Boost Pressure (kPa)	216
EGR (%)	44
SOI (deg. atdc)	-6.5
Vel1 (m/s)	660
Vel2 (m/s)	700
P1 (%)	64
Ramp1 (%)	27
Ramp2 (%)	0.0
Ramp3 (%)	27
Ramp4 (%)	6.7
Dwell (deg.)	4.4

Table 3. Optimized values of the eleven design variables.

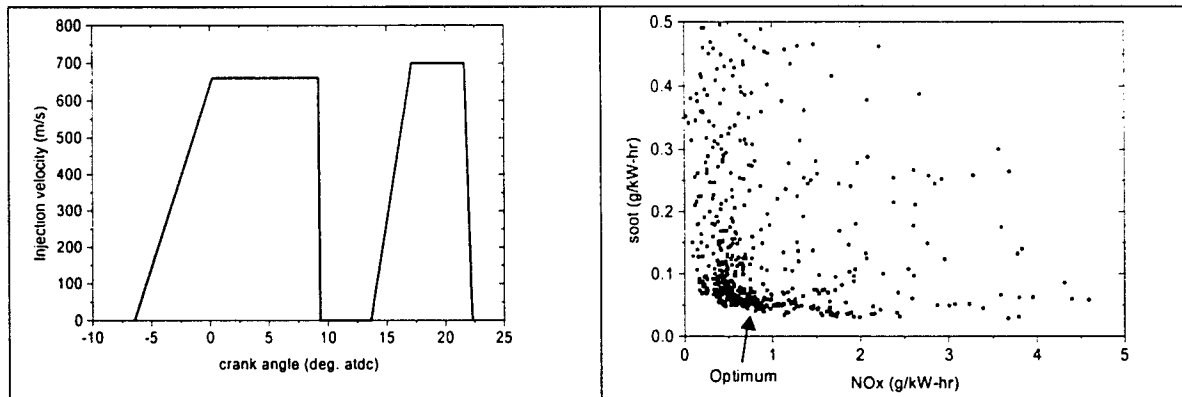


Fig. 2. Predicted optimum injection rate-shape. **Fig. 3.** Predicted Soot-NOx tradeoff

Conclusions

The KIVA-GA computational design methodology was applied to study the effects of injection rate-shape on emissions and performance in a heavy-duty diesel engine. The μ GA efficiently determined a set of engine input parameters resulting in soot and NOx emissions well within the 2002/2004 mandates at the considered operating condition. The optimum case also had a relatively low fuel consumption value. The present methodology provides a useful tool for engine designers investigating the effects of a large number of input parameters on emissions and performance.

Acknowledgements

The authors thank the following organizations for their generous support during the course of this work: the Army Research Office, Caterpillar, Inc., TACOM and DOE/Sandia National Laboratories.

References

1. Montgomery, D.T., Reitz, R.D., *SAE 960316* (1996).
2. Senecal, P.K., Reitz, R.D., *SAE 2000-01-1890* (2000).
3. Montgomery, D.T., Reitz, R.D., *SAE 2000-01-1962* (2000).

EFFECTS OF ADVANCED FUEL INJECTION STRATEGIES ON DI DIESEL EMISSIONS

ARO Grant DAAG55-98-I-0433

A. M. Mellor*, S. L. Plee, R. J. Tabaczynski

*Vanderbilt University, VU Station B 351592
2301 Vanderbilt Place, Nashville, TN 37235-1592

SUMMARY/OVERVIEW:

The focus of the program is developing engineering models for Diesel emissions and performance that (1) stand alone as preliminary design tools, (2) provide submodels for CFD, spray-marching, and cycle simulations, and (3) offer real-time algorithms for control of smart engines. These models, because of their simplicity, also provide the design engineer with valuable insight into the predominate processes governing engine emissions and performance. The model equations are derived from first principles and are based on Damköhler numbers describing the pollutant chemistry and fluid flow processes. To date emissions of oxides of nitrogen (NO_x) have received primary emphasis. Both quasi-steady and dynamic models have been developed and examined with data from various engines. Development of similar models for particulate emissions and power density continues. One of the topics examined in the past year is the effect of multiple fuel injections on emissions of nitric oxide.

TECHNICAL DISCUSSION:

Due to recent advances in injector technology, many modern injectors now have the ability to inject multiple pulses of fuel into the cylinder during a given cycle. Experimental engine results using injectors capable of multiple injections are plentiful in the literature and indicate that NO_x , particulates, and/or fuel consumption may be reduced by using optimized fuel injection schemes. However, methods of determining optimized fuel injection strategies have not been presented. To date, modeling of multiple injections has been accomplished through the use of computational fluid dynamics codes and cycle simulation type codes. These codes, while providing an estimation of the expected engine performance and emissions for a given injection scheme, provide little insight as to what the best injection scheme is. Typically various injection schemes are modeled in hopes of finding one which approaches the optimum.

The objectives of the present work are to develop semi-empirical models for engines using multiple injections that can be used to estimate engine performance and emissions a priori and also provide the design engineer with insight into the optimization process. Efforts to date have been focused on the development of a quasi-steady NO_x model. This model is a modification to that originally developed at Vanderbilt under a previous ARO grant for use with single injections [1], which was successful in correlating NO_x emissions from a 2.2L high speed direct injection (HSDI) Diesel engine [2].

Model Formulation for Single Injections: The model is based on the assumption that NO forms in the stoichiometric contour surrounding the fuel plume (see Fig. 1; referred to as zone 1 below). The characteristic temperature and pressure for this zone are the start of combustion, stoichiometric flame temperature ($T_{\phi=1}$) and pressure. The NO chemistry is based on a skeletal mechanism for NO_x emissions [1] which includes reactions from the extended Zeldovich

mechanism [3] and select reactions from the nitrous oxide mechanism [4]. Assuming O-atom in equilibrium, N-atom in steady-state, and NO decomposition negligible, the chemical kinetic time for NO formation can be defined as

$$\tau_{no} = \frac{[NO]_{eq1'}}{2[O]_{eq1}[N_2]_{eq1}(k_{lf} + k_{sf})} \quad (1)$$

where k_{lf} and k_{sf} are the rate coefficients for the leading reaction in the extended Zeldovich mechanism and the termolecular reaction of the nitrous oxide mechanism, respectively. $[NO]_{eq1'}$ is a normalizing concentration that will be shown to cancel in the final form of the model equation.

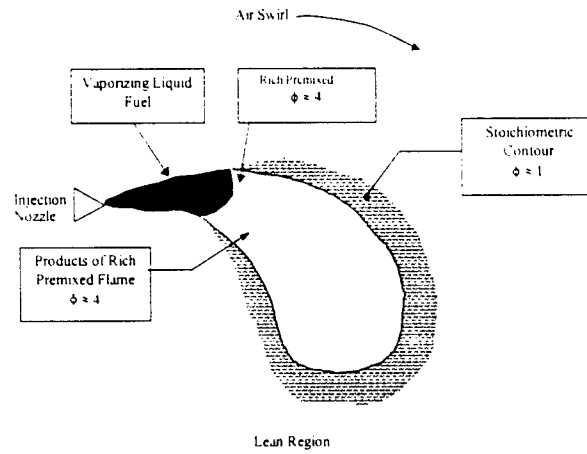


Figure 1: Quasi-steady schematic of DI Diesel fuel plume based on laser diagnostic results of Flynn et al. [5]. NO chemistry occurs in the stoichiometric contour of the spray plume.

The residence time for a NO forming eddy in the NO formation zone (mixing time for NO formation) was found in previous work to be given by [2],

$$\tau_{fi, no} = \left(\frac{We}{Re} \right)^{1.5} \frac{l_{bowl}}{V_{fuel}} \quad (2)$$

where l_{bowl} is the radius of the bowl and the subscript fi stands for fuel injection because the fuel injection event dominates the mixing process. Here the Weber and Reynolds numbers have been defined as

$$We = \frac{\rho_{fuel} d_{noz} V_{fuel}^2}{\sigma_{fuel}} \quad Re = \frac{\bar{S}_p B}{V_{air}} = \frac{2LNB}{V_{air}} \quad (3)$$

where V_{fuel} is the peak injection velocity. The mass of NO_x emitted from the combustion chamber per firing stroke is now given by

$$m_{NO_2} (gNO_2/st) = m' V_1 \frac{\tau_{fi, no}}{\tau_{no}} [NO]_{eq1'} \quad (4)$$

where V_1 is the volume of the NO formation zone (calculated using the ideal gas law) and m' is a model constant that accounts for the characteristic mixing time being proportional to the actual mixing time instead of equal.

Model Formulation for Multiple Injections: For the work presented here, the reduction in NO_x due to the use of multiple injections is of concern. Therefore, the mass of NO_x emitted by the engine when using multiple injections is normalized by the NO_x emissions from the engine at the same speed and load condition when using single injection, thereby allowing the model constant, as well as many other terms, to be cancelled. The above model is modified for use with multiple injections by considering each injection separately. The model equation can now be stated as,

$$m^* = \frac{m_{\text{no,multiple}}}{m_{\text{no,single}}} = \sum_{i=1}^{\text{\#inj}} \left(y_i \times \frac{T_{\varphi=1,i}}{T_{\varphi=1,\text{single}}} \times \frac{P_{\text{soc,single}}}{P_{\text{soc},i}} \times \frac{\tau_{\text{no,single}}}{\tau_{\text{no},i}} \times \frac{V_{\text{inj},i}^2}{V_{\text{inj,single}}^2} \right) \quad (5)$$

where y_i is the mass fraction of fuel in injection pulse i , and the injection velocities are evaluated at their peaks for each injection pulse. Note that in Eq. (5) the definition of the mixing time for NO formation given in Eq. (2) has been used as well as substituting the ideal gas law for the volume of the NO formation zone, with many of the terms canceling due to the normalization. In the above derivation of the model, the characteristic temperature of the NO formation zone was calculated at the SOC conditions, which were taken to be the bulk temperature and pressure in the cylinder. For application to the multiple injection case the conditions at the start of combustion for each injection pulse are taken to be the motored pressure and temperature in the cylinder.

Evaluation of Experimental Data: Engine tests were conducted on a 1.2L HSDI Diesel engine (0.3 L/Cyl.) equipped with a common rail fuel injection system capable of multiple injections [6]. For the present analysis the effect of multiple injections on emissions and performance was evaluated by holding the engine speed, brake mean effective pressure (BMEP), and exhaust gas recirculation (EGR) rate constant while changing the injection strategy between single, double and triple injections. Presently three such conditions are available for analysis. The injection rate and normalized cumulative heat release profiles for one condition are presented in Fig. 2.

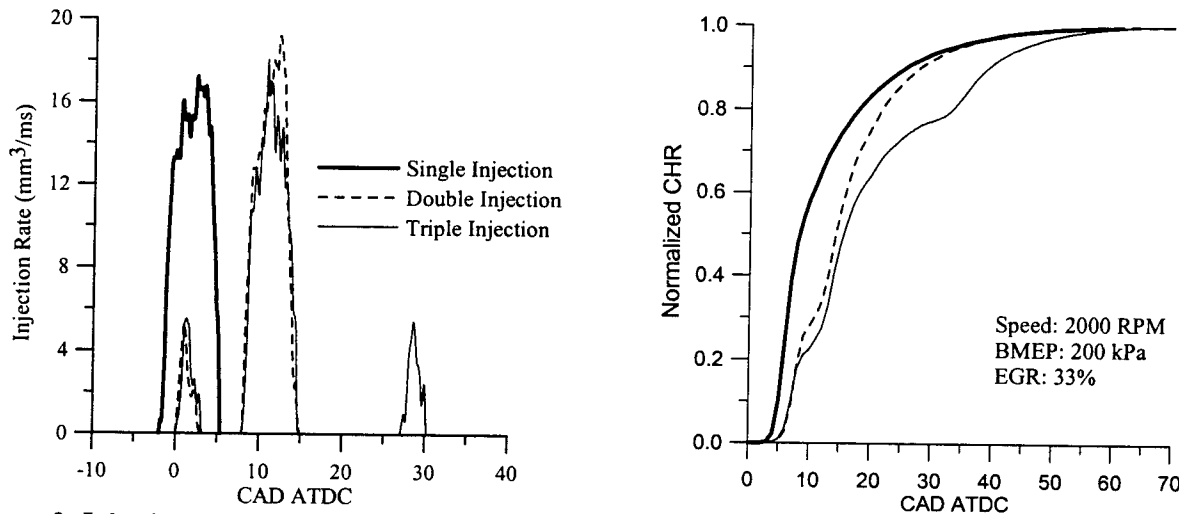


Figure 2: Injection rate and normalized cumulative heat release (CHR) profiles for the 2000 RPM, 200 kPa BMEP, 33% EGR operating condition. For the engine tests the engine speed, BMEP, and EGR rate were held constant while the injection profiles were varied from single to double to triple injections.

The predicted normalized emissions of NO_x from the engine using Eq. (5) are compared with the measured normalized emissions of NO_x from the engine in Fig. 3. If the model were

perfect the data would lie on the 45° line that has been included on the graph. The results are very promising, as all the data are near the line.

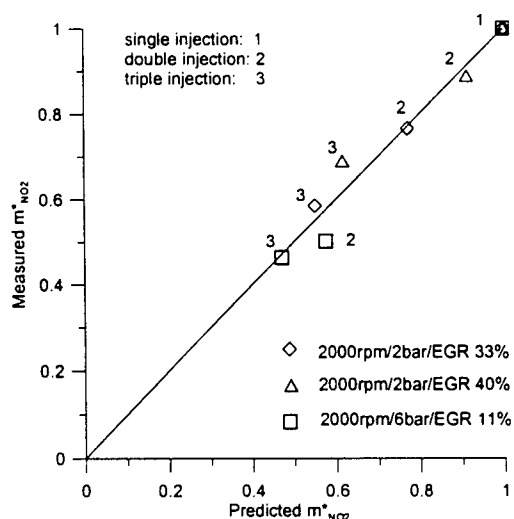


Figure 3: Normalized measured NO_x emissions versus predicted normalized NO_x emissions using Eq. (5).

Future efforts are focused on the continued development and validation of the model presented here and a cycle simulation type model targeted for use in DI Diesel engine optimization. The cycle simulation code will incorporate a dynamic NO_x model previously developed at Vanderbilt, as well as soot, combustion, and heat loss models. Also, tests have begun on a light-duty DI Diesel engine, which examine the effects of injector type, injection strategy (including multiple injections), bowl geometry, boosting, aftercooling, and EGR on engine operation and emissions. The results from these engine tests will be used for further model development and validation.

REFERENCES:

- 1) Mellor, A. M., Mello, J. P., Duffy, K. P., Easley, W. L., and Faulkner, J. C. (1998), "Skeletal mechanism for NO chemistry in Diesel engines," SAE Paper 981450.
- 2) Duffy, K. P. and Mellor, A. M. (1998), "jadf;lkajdf," SAE Paper .
- 3) Lavoie, G. A., Heywood, J. B., and Keck, J. C. (1970), "Experimental and theoretical study of nitric oxide formation in internal combustion engines," Combustion Science and Technology, Vol. 1, pp. 313-326.
- 4) Malte, P.C. and Pratt, D. T. (1974), "The role of energy-releasing kinetics in NO_x formation: fuel lean, jet-stirred CO -air combustion," Combust. Sci. Tech. 9, 221-231.
- 5) Flynn, P. F., Durrett, R. P., Hunter, G.L., zur Loye, A. O., Akinyemi, O. C., Dec, J. E., and Westbrook, C. K. (1999), "Diesel combustion: an integrated view combining laser diagnostics, chemical kinetics, and empirical validation," SAE Paper 1999-01-0509.
- 6) Chen, S. K. (2000), "Simultaneous reduction of NO_x and particulate emissions by using multiple injections in a small Diesel engine," SAE Paper 2000-01-3084.

PULSE DETONATION PHYSIOCHEMICAL AND EXHAUST RELAXATION PROCESSES

Principal Investigator: Dr. Fred Schauer (AFRL/PRTS)

AFRL/PRTS, Bldg 490
1790 Loop Road North
WPAFB OH 45433-7103

SUMMARY/OVERVIEW:

The objective of this program is to establish the scientific knowledge of detonation initiation, propagation, and blow-down needed to develop a pulse detonation engine (PDE) that will operate on hydrocarbon fuels. Detonation tube exhaust blow-down conditions, which are predicted to have a significant impact upon performance, will be explored in order to achieve basic understanding of the relationships between detonations, nozzles, and multiple detonation tube interactions.

TECHNICAL DISCUSSION

The technological motivation for this program is the need to develop low-cost high-performance PDE's that can operate on hydrocarbon fuels. PDE's rely upon detonation combustion to produce a pressure rise in the combustion chamber instead of the expensive rotating machinery used in gas turbine engines. Consequently, the most expensive and maintenance-intensive components of a conventional turbine engine, namely the compressor and turbine stages, will not be necessary in PDE's. PDE's operates on a near-constant-volume heat addition cycle as opposed to the constant-pressure cycle employed in nearly all conventional aero-propulsion systems. The constant volume cycle offers improvements to specific thrust, specific fuel consumption, and specific impulse at a greatly reduced cost. In theory, the PDE can efficiently operate at Mach numbers from zero to above four without using a combined cycle/rocket approach. However, there are some major technical problems that must be resolved before the full potential of PDE's can be realized.

Foremost among the hurdles for a practical PDE system are the requirements for initiation and successful propagation of a detonation with hydrocarbon fuels in air. Although this has not been achieved in 60 years of PDE research, modern computational fluid mechanics (CFD), laser diagnostics, and high-speed instrumentation have not been applied to this challenge until recently. CFD and experimental studies of deflagration-to-detonation transition (DDT) and propagation are being carried out in order to explore the

parameters controlling detonation initiation including: geometry effects, plasma ignition, hybrid fueled pre-detonators, and endothermic fuels. In addition to existing high-frequency instrumentation, an optically accessible test section will be coupled with our high-framing rate cameras to observe the deflagration to detonation transition processes and compare with models. The imaging and laser diagnostics experience obtained from our AFOSR Combustion Research program will also be used to study the detonator tube blow down. High-frequency Schlieren, PLIF, and/or planar Raman imaging will be used to investigate the exit boundary conditions influence on thrust. Two-dimensional nozzles are used in these investigations, and an optical test section will be employed to study both the nozzle flow conditions and multi-tube interactions. CFD calculations are used to gain an understanding of the mechanisms whereby the thrust is influenced by the conditions established when the detonation wave reaches the exit plane. For example, our Chin detonation spiral was developed recently because modeling of the detonation initiation processes indicated a new mechanism for starting detonations. The insight gained from discovering these phenomena resulted in propane/air detonations with no oxygen enrichment.

This research couples the Combustion Science Branch's extensive basic combustion research experience with the pulse detonation engine in-house research program and high-fidelity detonation modeling capabilities in order to gain the understanding required to overcome the fundamental technological hurdles bracketing the PDE tube: detonation initiation and blow down conditions. Prior 6.2 studies conducted by AFRL/PRTS have made tremendous progress, but we lack understanding of the mechanisms enabling this progress. The techniques developed under this research effort are producing this understanding and then applied to the challenges of detonation initiation and tube blow down.

Computational modeling and experiments have been conducted in order to understand the mechanisms required for deflagration-to-detonation-transition (DDT). The complex interaction of chemistry, gas dynamics, and geometry was found to play a key role in the generation of coalescing compression waves that were ultimately responsible for the creation of 'hot

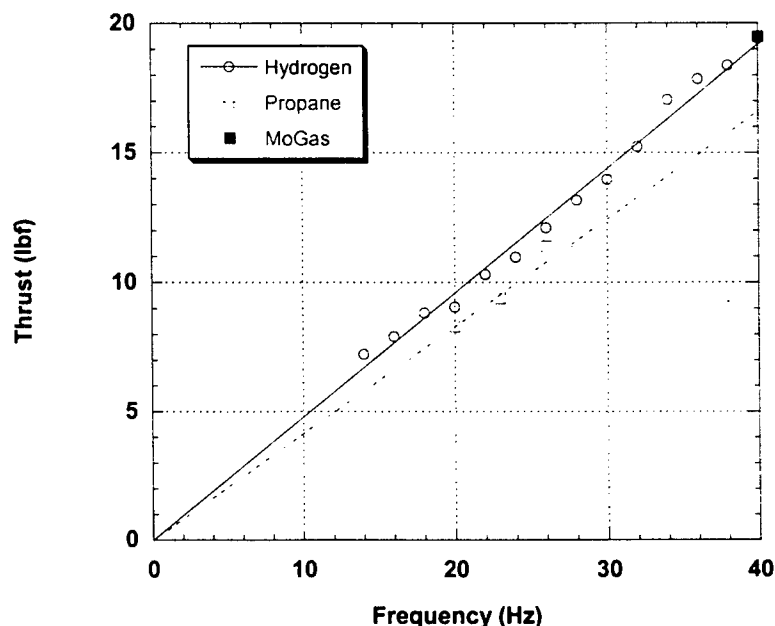


Figure 1. Variation of thrust versus frequency for various fuel-air mixtures.

spots' required for successful DDT. Mechanisms studied by this research for DDT include: obstructions such as classical Shelkin spirals which create compression wave reflections while increasing flame speed through turbulence and flame mixing enhancement; 'Smirnov' type cavities which generate compression waves that subsequently interact with the flame front; and flame propagation in small detonator tube to cell width ratios which result in increased transverse wave reflection events.

The understanding gained of these complex mechanisms through CFD, DDT is experimentally achieved in complex hydrocarbon-air mixtures that did not previously achieve DDT in a practical configuration. Furthermore this work has been extended from detonation of vapor fuel/air mixtures, to the detonation of liquid fuel/air mixtures. Sample results of thrust versus detonation frequency are shown in figure 1 with hydrogen, propane, and liquid gasoline fuels. The mechanisms described above have subsequently been applied towards successful detonation initiation in motor gasoline, av-gas, JP4, JP8, and ethanol with stoichiometries ranging from 0.7 to over 4.

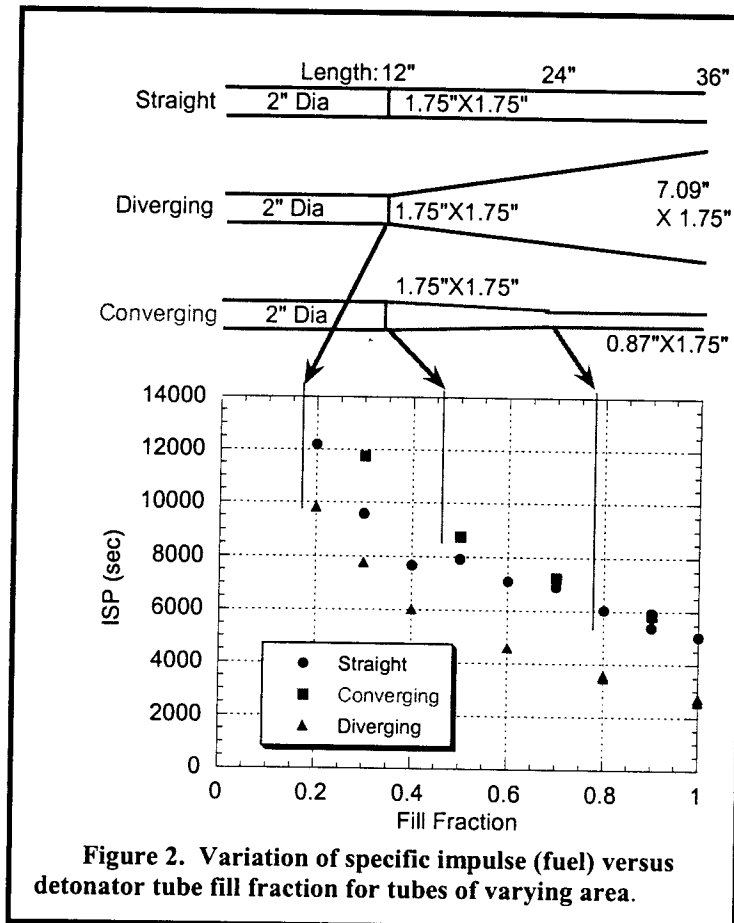


Figure 2. Variation of specific impulse (fuel) versus detonator tube fill fraction for tubes of varying area.

Exhaust relaxation processes have also been studied both numerically and experimentally. The detonator tube blow down process had previously been found to have a significant impact on the resulting PDE performance and is also the source of much controversy as small changes in the exit conditions may impact the pressure relaxation portion of each detonation cycle. The effects of nozzles, bleeding off detonation pressure, ejectors, and other detonator geometry's which impact the sensitive tube exit boundary conditions are being examined. Some sample results depicting the impact of changing detonator tube shape are contained in figure 2. Axial variations in tube area were found to produce variations in efficiency as high as 50%. Details and similar effects will be reported for other changes in exit boundary conditions.

Background information and further details on this program and will be presented at the Contractor's Review meeting.

Intelligent Turbine Engines

Grant Number DAAH04-96-1-0008

Principal Investigators: S. Menon, M. Allen, M. Brooke, A. Glezer, W. Haddad, J. Jagoda, Y. Neumeier, J. Prasad, L. Sankar, J. Seitzman, B. Zinn

Georgia Institute of Technology
Schools of Aerospace, Electrical and Computer, and Mechanical Engineering
Atlanta, GA 30332-0150

SUMMARY/OVERVIEW:

This program focuses on the fundamental and practical issues that hinder development of intelligent control systems for improving the performance of turbine engines, such as rotorcraft turboshaft engines. Our approach to the development of an intelligent control system has focused on advances in the basic understanding of engine processes through experiments and advanced computational models, refinement of appropriate sensor and actuator technologies, and development of practical control strategies for control of steady-state and transient performance. Substantial advances have been made on: unsteady modeling of compressor and combustor flows, control strategies for compressor surge and stall; combustor control using synthetic jets and smart fuel injectors; model-based, fuzzy logic and neural network control approaches; and MEMS and optical sensors able to operate in high temperature environments. In this report, we highlight advances in simulations, control theory, and compressor control (since last year's report focused on sensor and actuator technologies).

TECHNICAL DISCUSSION:

COMBUSTOR CONTROL

The work described below involves efforts toward improved understanding and design of controllable combustor modeling and simulation, and investigation of new control hardware and architectures for combustor control.

TWO-PHASE LES

A generalized Large-Eddy Simulation (LES) methodology has been developed to simulate premixed and non-premixed gas-phase and two-phase combustion in complex flows such as those typically encountered in gas-turbine combustors. The LES methodology uses a new subgrid-based scalar mixing and combustion model. The unique feature of the model is that scalar mixing and the reaction-diffusion processes in the subgrid domain are simulated inside every LES cell. This more fundamental treatment allows the study and analysis of the physics involved in the interaction between the flame, gas-phase, and liquid flow dynamics. Earlier studies under this MURI validated and demonstrated the method's ability to accurately capture Le, Sc, Re, Ka and Da number effects without requiring any explicit or *ad hoc* adjustments to the model.

Results have been obtained for a number of configuration, including a lean premixed combustor with swirl stabilization (Fig. 1). The results showed that the swirl stabilization reduced the magnitude of the amplitude of the pressure oscillation and that the dominant mode

shape was the three-quarter acoustic mode of the combustor. It was also found that heat release plays a similar role in determining the stability of the combustion. The effects of swirl and heat release on the 'Vortex-Breakdown' phenomenon are currently under study. In two-phase systems, significant modification to the high shear regions due to vaporization of droplets is observed. Droplets with stokes number of the order of one, are seen to concentrate preferentially in regions of low vorticity and when they vaporize, the gaseous fuel gets entrained into regions of high vorticity. This process plays a major role in fuel-air mixing and combustion processes in two-phase systems. On the other hand,

it was also observed that the heavier particles, with a higher inertia do not show a tendency to collect in low-vorticity regions. This emphasizes the existence of an optimum ratio of particle time constant to fluid time scale such that particles show preferential accumulation. The effect of the mass loading ratio, droplet vaporization rate, and Stokes number on mixing and combustion are currently being studied.

HARDWARE NEURAL NETWORKS

We have demonstrated a single chip learning neural network that can learn (from a zero weight state) to control an simulated combustion instability. Two features differentiate this work from similar work.

First, the chip operates in real-time on an analog system. The chips inputs and outputs are analog, and are not clocked or gated in any way. Thus once the chip has learnt to control the combustor, changes in the analog inputs result in controls in less than a microsecond. Second, the learning algorithm used requires no knowledge of the system to be controlled. It need only be fed an error signal (in this case differential pressure) to begin seeking weights that minimize the error.

HYBRID RESETTING CONTROLLERS

A new class of controllers, called hybrid resetting controllers, has been developed for control of combustion instabilities. The key idea of hybrid resetting control is to achieve enhanced energy dissipation between interconnected systems. Specifically, if a dissipative or lossless plant is at a high energy level, and a dissipative feedback controller at a low energy level is attached to it, then energy will generally tend to flow from the plant into the controller, decreasing the plant energy and increasing the controller energy. Of course, emulated energy, and not physical energy, is accumulated by the controller. Conversely, if the attached controller is at a high energy level and the plant is at a low energy level, then energy can flow from the controller to the plant, since a controller can generate real, physical energy to effect the required energy flow. Hence, if and when the controller states coincide with a high emulated energy level, then we can *reset* these states to remove the emulated energy so that the emulated energy is not returned to the plant. Since active energy flow resetting control for interconnected systems gives rise to discontinuous closed-loop motions, impulsive differential equations provide the mathematical foundation for analyzing hybrid resetting controllers.

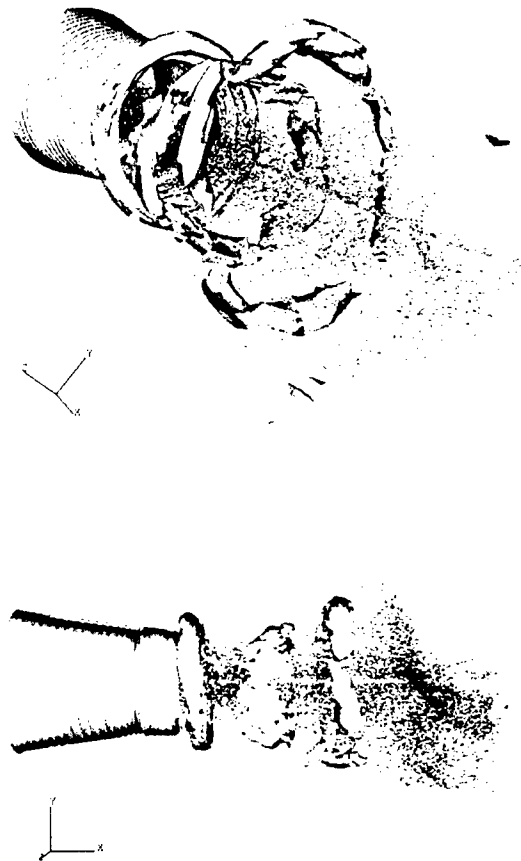


Figure 1. Perspective (top) and side (bottom) views of instantaneous isovorticity and droplet distributions in LM6000 combustor, nonreacting.

To date, we have developed a general framework for feedback systems possessing discontinuous motions by addressing stability, dissipativity, feedback interconnections, and optimality of nonlinear impulsive dynamical systems. The results provide a general analysis and synthesis framework for hybrid feedback control systems in that they apply to nonlinear dynamical systems with abstract energy notions for which a physical system energy interpretation is not necessary.

We have applied this approach to a combustion model (time-averaged) that captures thermoacoustic instabilities. Utilizing this model, we developed active energy flow resetting controllers to mitigate combustion induced pressure instabilities in combustion systems. The hybrid resetting controller can be viewed as a specialized technique for severing the coupling between the acoustics and unsteady combustion to effectively enhance the removal of energy in the combustor. In particular, significant modal energy dissipation is achieved via the hybrid resetting controller to suppress thermoacoustic oscillations.

COMPRESSOR CONTROL

The current work aims to produce active/passive control strategies that will result in reduced stall margin requirements. This involves efforts toward improved understanding of compressor stall and surge phenomena through modeling, simulation and experimentation; investigation of control mechanisms for reducing compressor stall and surge; and development of hybrid control methods by combining control-theoretic and decision-theoretic techniques.

MODELING AND SIMULATION

We have developed a general analytic model for compressor dynamics that includes finite duct effects and compressibility in the inlet and exit flows. The model indicates stall inception variations about the pressure peak as a function of inlet geometry, Mach number, and gas properties. In addition if the flow at the inlet is slightly yawed in the direction of blade rotation, then the stall inception is delayed beyond the peak performance point.

The Navier-Stokes solver for simulating unsteady viscous fluid flow in turbomachinery components, developed during the previous years, was used to study fluid dynamic phenomena that lead to instabilities in centrifugal compressors. These studies indicated that large flow incidence angles, at reduced flow rates, can cause boundary layer separation near the blade leading edge. High-pressure jets upstream of the compressor face were studied as a means of controlling compressor instabilities. Steady jets were found to alter the leading edge flow pattern and effectively suppress compressor instabilities. It was also observed that yawed jets are more effective than parallel jets and an optimum yaw angle exists for each compression system. Pulsed jets were found to yield additional performance enhancements and lead to a reduction in external air requirements for operating the jets. Jets pulsed at higher frequencies were found to perform better than low-frequency

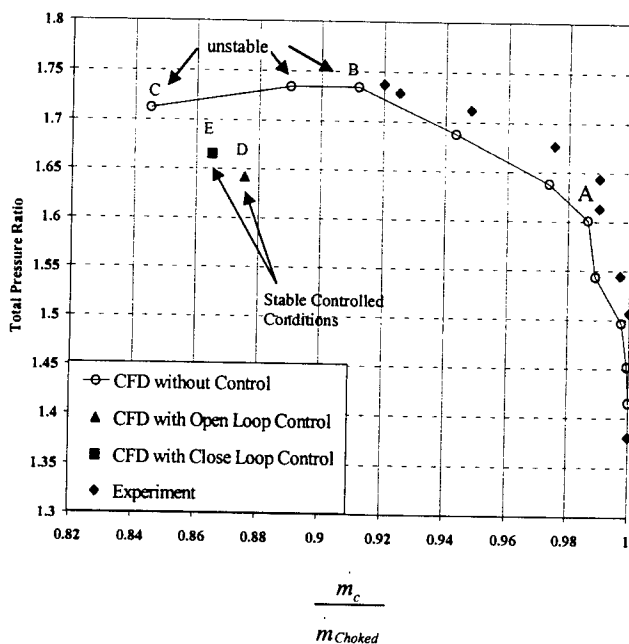


Figure 2. Stabilization of a NASA Lewis 4:1 axial compressor using open- and closed-loop control.

jets.

Work was also performed on the stabilization of axial compressors through bleeding; both open- and closed-loop control were examined. In the open-loop case mass is removed at a fixed, preset rate from the diffuser. For closed-loop control, the rate of bleed is linked to pressure fluctuations upstream of the compressor face. The bleed valve is activated when the amplitude of pressure fluctuations sensed by the probes exceeds a certain range. Calculations show that both types of bleeding eliminate rotating stall and modified surge, and suppress the precursor disturbances upstream of the compressor face. It is observed that smaller amounts of compressed air need to be removed with the closed-loop control, as compared to open-loop control. These concepts were demonstrated by extending the useful operating range of a 4:1 transonic compressor (Fig. 2).

EXPERIMENTS AND CONTROLS

We have also developed and experimentally implemented (Fig. 3) an active control scheme based on a real-time observer that identifies the frequency and amplitude of the dominant modes of the pressure variations. Combined with a fuzzy logic control scheme that evaluates how close the identified frequencies and amplitudes are to a set of values that depend on compressor RPM, the active control system sends feedback signals to either bleed valves or to the combustor fuel flow rate in order to *prevent* (rather than suppress) surge. The compressor then operates at the maximum attainable pressure while avoiding surge. This system has been experimentally implemented. In addition, the control approach does not require high bandwidth actuators and requires little information on the specific compressor characteristics.

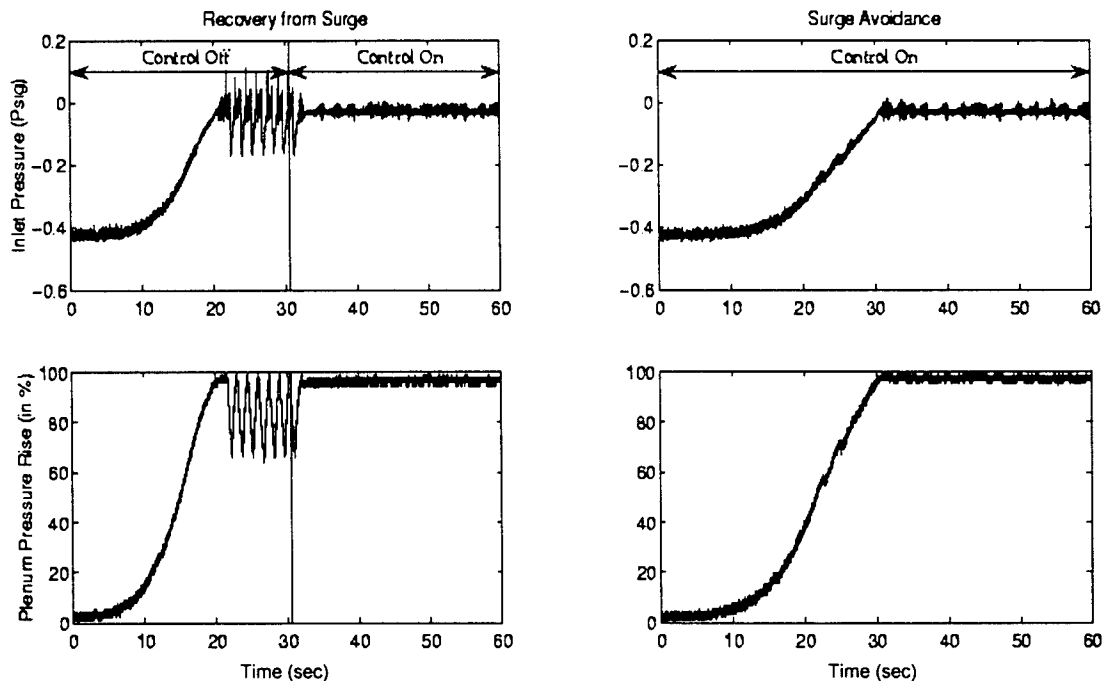


Figure 3. Suppression and **avoidance** of surge in GT compressor facility using active control system and real-time observer.

FILTERED MASS DENSITY FUNCTION FOR SUBGRID SCALE MODELING OF TURBULENT DIFFUSION FLAMES

Grant Number F49620-00-1-0035

Principal Investigators: Peyman Givi and Farhad A. Jaber^{*}

Department of Mechanical and Aerospace Engineering
State University of New York at Buffalo
Buffalo, NY 14260-4400

SUMMARY/OVERVIEW:

The objectives of this work are: (i) to further develop and improve the "filtered density function" (FDF) methodology for modeling of the subgrid scales (SGS) in turbulent reacting flows, and (ii) to implement the resulting SGS closure for reliable large eddy simulation (LES) of turbulent diffusion flames.

TECHNICAL DISCUSSION

The filtered density function (FDF) methodology¹ has proven very effective for large eddy simulation (LES) of turbulent reacting flows.²⁻⁶ In all contributions to-date, the FDF of the "scalar" quantities is considered: Colucci *et al.*² developed a transport equation for the FDF in constant density turbulent reacting flows. Jaber^{et al.³ extended the methodology for LES of variable density flows by consideration of the "filtered mass density function" (FMDF), which is essentially the mass weighted FDF. The fundamental property of the PDF methods is exhibited by the closed form nature of the chemical source term appearing in the transport equation governing the FDF (FMDF). This property is very important as evidenced in several applications of FDF for LES of a variety of turbulent reacting flows.²⁻⁵ However, since the FDF of only the scalar quantities are considered, all of the "hydrodynamic" effects are modeled. In all of previous simulations, these effects have been modeled via "non-FDF" methods.}

Within the past year, our efforts have been concentrated on three issues: (1) development of the FDF for SGS modeling of the velocity field, (2) development of the joint velocity-scalar FDF methodology, (3) implementation of the currently available FMDF for LES of a turbulent jet flame.

In efforts pertaining to (1), a methodology termed the velocity filtered density function (VFDF) is developed. The VFDF is basically the PDF of the SGS velocity vector. The exact transport equation governing the evolution of the VFDF is derived. It is shown that the effects of SGS convection in this equation appear in a closed form. The unclosed terms are modeled similar to that in PDF methods in Reynolds averaged simulation (RAS) procedures.⁷ In this way, the

^{*} Current Address: Department of Mechanical Engineering, Michigan State University, East Lansing, MI.

VFDF is at least equivalent to a second-order moment SGS closure. The modeled VFDF transport equation is solved numerically via a Lagrangian Monte Carlo scheme in which the solutions of the equivalent stochastic differential equations (SDEs) are obtained. The numerical scheme preserve the Itô-Gikhman nature of the SDEs and provide a reliable solution for the VFDF. The consistency of the VFDF formulation and the convergence of its Monte Carlo solutions are assessed. This is done via comparisons between the results obtained by the Monte Carlo procedure and the finite difference solution of the transport equations of the first two filtered moments of VFDF into the LES-FD. With inclusion of the third moments from the VFDF into the LES-FD, the consistency and convergence of the Monte Carlo solution is demonstrated by good agreements of the first two SGS moments of VFDF with those obtained by LES-FD.

The VFDF predictions are compared with those with LES results with no SGS model, with the Smagorinsky⁸ SGS closure, and with the dynamic Smagorinsky^{9, 10} model. All of these results are also compared with direct numerical simulation (DNS) results of a three-dimensional, temporally developing mixing layer in a context similar to that conducted by Vreman *et al.*¹¹ This comparison provides a means of examining some of the trends and overall characteristics as predicted by LES. It is shown that the VFDF performs well in predicting some of the phenomena pertaining to the SGS transport. The magnitude of the SGS Reynolds stresses as predicted by VFDF is significantly larger than those predicted by the other SGS models and much closer to the filtered DNS results. The temporal evolution of the production rate of the SGS kinetic energy is predicted well by VFDF as compared with those via the other closures. The VFDF is also capable of accounting for the SGS backscatter without any numerical instability problems, although the level predicted is substantially less than that observed in DNS.

The results of *a priori* assessments against DNS data indicates that the values of the model coefficients as employed in VFDF are of the range suggested in the equivalent models previously used in RAS. The results of *a posteriori* assessments do not give any compelling reasons to use values other than those suggested in RAS. Most of the overall flow features, including the mean velocity field and the resolved and total Reynolds stresses as predicted by VFDF are similar to those obtained via the dynamic model. This is interesting in view of the fact that the model coefficients in VFDF are kept fixed. It may be possible to improve the predictive capabilities of the VFDF by development of a dynamic procedure to determine the model coefficients, and/or implementation of higher order closures for the generalized Langevin model parameters.¹²

In efforts pertaining to (2), a methodology termed the "velocity-scalar filtered density function" (VSFDF) is developed. Compared to standard LES, this approach has the advantage of treating chemical reaction in a closed form; and, compared to scalar FDF has the advantage of treating convective transport (of momentum and species) in closed form. These modeling advantages have an associated computational penalty. An exact transport equation is derived for the VSFDF in which the effects of the SGS convection and chemical reaction appear in closed form. The unclosed terms in this transport equation are modeled. Again, a system of stochastic differential equations which yields statistically equivalent results to the modeled VSFDF transport equation is constructed. These SDEs are solved numerically by a Lagrangian Monte Carlo procedure in which the Itô character of the SDEs is preserved. The consistency of the proposed SDEs and the convergence of the Monte Carlo solution are currently being assessed. The VSFDF results are also being compared with those obtained via existing SGS

closures. It is expected that VSFDF will not be much more expensive than the scalar FDF, at least for multi-species turbulent flame simulations.

In efforts pertaining to (3), the FMDF methodology is being utilized for LES of a hydrocarbon jet flame. The flow field under investigation is that of a round jet in which the fuel is issued from a high-speed jet into a low speed or stagnant coflowing stream of oxidizer. This flow is inherently time-dependent and 3D. Nevertheless, some 2D (planar) simulations are also conducted (via both LES and DNS) for validation of the numerical methods and for determining the range of parameters. We have primarily considered methane/air combustion because of the rich extent of literature on methane oxidation mechanism, and availability of significant data in such flames. Up to now, we have conducted several DNS and LES of 2D and 3D jet flames. Most of the LES are conducted via the scalar FMDF methodology; the use of the joint velocity-scalar FMDF is the subject of our ongoing investigation. The SGS mixing term in this equation is modeled via the IEM closure as discussed in Ref.³ The finite-rate chemistry effects are explicitly included in this way since the chemistry is closed in the formulation. Numerical solution of the scalar FMDF is obtained with a hybrid Eulerian/Lagrangian scheme. The hydrodynamic field is obtained by solving the filtered continuity and momentum equations with a compact parameter finite-difference scheme. The scalar quantities include mass fraction of chemical species and enthalpy. The FMDF is represented by an ensemble of Lagrangian Monte Carlo particles, which are transported in the physical space by the combined actions of large scale convection and diffusion (molecular and subgrid). Transport in the composition space occurs due to chemical reaction and SGS mixing. Thus, the grid-free Lagrangian procedure considers notional particles whose evolution can be computed stochastically to simulate motion in physical space by convection and diffusion. The compositional values of particles are changed due to mixing and reaction. The oxidation of methane is simulated via a one-step global mechanism.¹³ The simulated results are used to analyze the "spatial" and the "compositional" structure of the flame. It is shown that the LES/FMDF predictions compare favorably with DNS data provided that the mixing frequency coefficient in the IEM closure is assigned properly. This coefficient is somewhat dependent on the flow conditions. The reason for this dependency is that the flow is not fully turbulent, specially near the inlet. Nevertheless, the values of the SGS scalar dissipation predicted by the model correlates very well with those obtained via DNS. In addition to DNS and LES/FMDF, we also simulated the jet flames via a conventional LES in which the SGS scalar correlations are ignored (this is labeled as LES-FD). A comparison between DNS and LES-FD indicates that the SGS scalar correlations have a strong influence on the large scale flow quantities; so if they are neglected the results would be erroneous.

WORK IN PROGRESS

Work is in progress on the following issues:

- (I) We are considering the reduced kinetics mechanism of methane-air oxidation¹³ in conjunction with the ISAT routine¹⁵ in our scalar LES/FMDF. If this scheme proves to be computationally feasible, we will utilize it in our future simulations.
- (II) We are conducting a feasibility assessment of a new computational methodology, termed the "Spectral/hp Element" method.¹⁶ The advantage of this methodology is that it contains spectral accuracy and it also allows for utilization of "unstructured" grids. This assessment is being done for possible replacement of our current mean

flow solver with this methodology, so that we can consider a larger computational domain for our LES and DNS of jet flames.

ACKNOWLEDGMENT

We are indebted to Professor Stephen B. Pope (Cornell University) for his collaboration on various aspects of this work.

References

- [1] Pope, S. B., in *Proceedings of 23rd Symp. (Int.) on Combustion*, pp. 591-612, The Combustion Institute, Pittsburgh, PA, 1990.
- [2] Colucci, P. J., Jaber, F. A., Givi, P., and Pope, S. B., *Phys. Fluids*, **10** (2): 499-515 (1998).
- [3] Jaber, F. A., Colucci, P. J., James, S., Givi, P., and Pope, S. B., *J. Fluid Mech.*, **401**:85-121 (1999).
- [4] Garrick, S. C., Jaber, F. A., and Givi, P., in Knight, D. and Sakell, L., editors, *Recent Advances in DNS and LES, Fluid Mechanics and its Applications*, Vol. 54, pp. 155-166, Kluwer Academic Publishers, The Netherlands, 1999.
- [5] James, S. and Jaber, F. A., *Combust. Flame*, **123**:465--487 (2000).
- [6] Pope, S. B., *Turbulent Flows*, Cambridge University Press, Cambridge, UK, 2000.
- [7] Pope, S. B., *Phys. Fluids*, **6**(2): 973--985 (1994).
- [8] Smagorinsky, J., *Monthly Weather Review*, **91**(3): 99--164 (1963).
- [9] Germano, M., *J. Fluid Mech.*, **238**:325--336 (1992).
- [10] Lilly, D. K., *Phys. Fluids A*, **4**(3): 633-634 (1992).
- [11] Vreman, B., Guerts, B., and Kuerten, H., *J. Fluid Mech.*, **339**:357--390 (1997).
- [12] Pope, S. B., *Ann. Rev. Fluid Mech.*, **26**:23--63 (1994).
- [13] Bhui-Pham, M. N., Ph.D. Thesis, University of California, San Diego, San Diego, CA, 1992.
- [14] Sung, C. J., Law, C. K., and Chen, J. -Y., *Proceedings of 27th Symp. (Int.) on Combustion*, pp. 295-303, The Combustion Institute, Pittsburgh, PA, 1998.
- [15] Pope, S. B., *Combust. Theo. Modelling*, **1**:41 (1997).
- [16] Karniadakis, G. E. and Sherwin, S. J., *Spectral/hp Element Methods for CFD*, Oxford University Press, New York, NY, 1999.

PDF MODELLING OF TURBULENT COMBUSTION

AFOSR Grant F-49620-00-1-0171
Principal Investigator: Stephen B. Pope

Mechanical & Aerospace Engineering
Cornell University
Ithaca, NY 14853

SUMMARY

Important advances are being made in our understanding of turbulent combustion through the comparison between PDF model calculations and detailed experimental data. Previous calculations for the Sandia piloted jet flames have been extended in order to study the sensitivity to the pilot flame temperature and to radiative heat loss. Research is in progress on a new methodology ISAT-DR (*in situ* adaptive tabulation with dimension reduction) to incorporate detailed chemistry in turbulent combustion computations in an efficient manner. Both aspects of the work performed are advancing and demonstrating the capabilities of turbulent combustion modeling that can be applied to practical combustion devices.

PILOTED NONPREMIXED FLAMES

The piloted nonpremixed flames studied experimentally at Sandia (Barlow & Frank 1998) provide an excellent test of turbulent combustion models. These flames show distinct levels of interaction between turbulence and chemistry because of the increasing jet bulk velocities from flame *D* to *F*: flame *D* is close to equilibrium with a small amount of local extinction, whereas flame *F* is on the verge of global extinction. In each of these flames, the amount of local extinction reaches a peak at an axial distance of about 30 jet radii, with re-ignition occurring downstream. Several advanced approaches based on LES, CMC and PDF methods have been applied to compute these phenomena and have made significant progress. Notably, the joint PDF calculations of these flames by Xu and Pope (2000) and Lindstedt et al. (2000) show the best detailed agreement obtained between computations and the experimental data.

The PDF calculations of Xu & Pope (2000) and Tang et al. (2000) are capable of calculating, quantitatively, the observed phenomena of local extinction and reignition. These calculations are based on the modelled transport equation for the joint PDF of velocity, turbulence frequency, and composition. The sub-models of this method include the simplified Langevin model (SLM) for velocity and the Jayesh-Pope model (JPM) for turbulent frequency (see Pope 2000). The molecular mixing is modeled by the Euclidean minimal spanning tree (EMST) model of Subramaniam & Pope (1998), which features mixing locally in the composition space through interacting particles with neighboring particles. The reaction mechanism used is the 19 species, 15-step augmented reduced mechanism of Sung et al. (1998) which includes *NO* chemistry, and is denoted by ARM2. The chemical reaction calculations are performed using the *in situ* adaptive tabulation (ISAT) algorithm (Pope 1997). It should be pointed out that for each full-

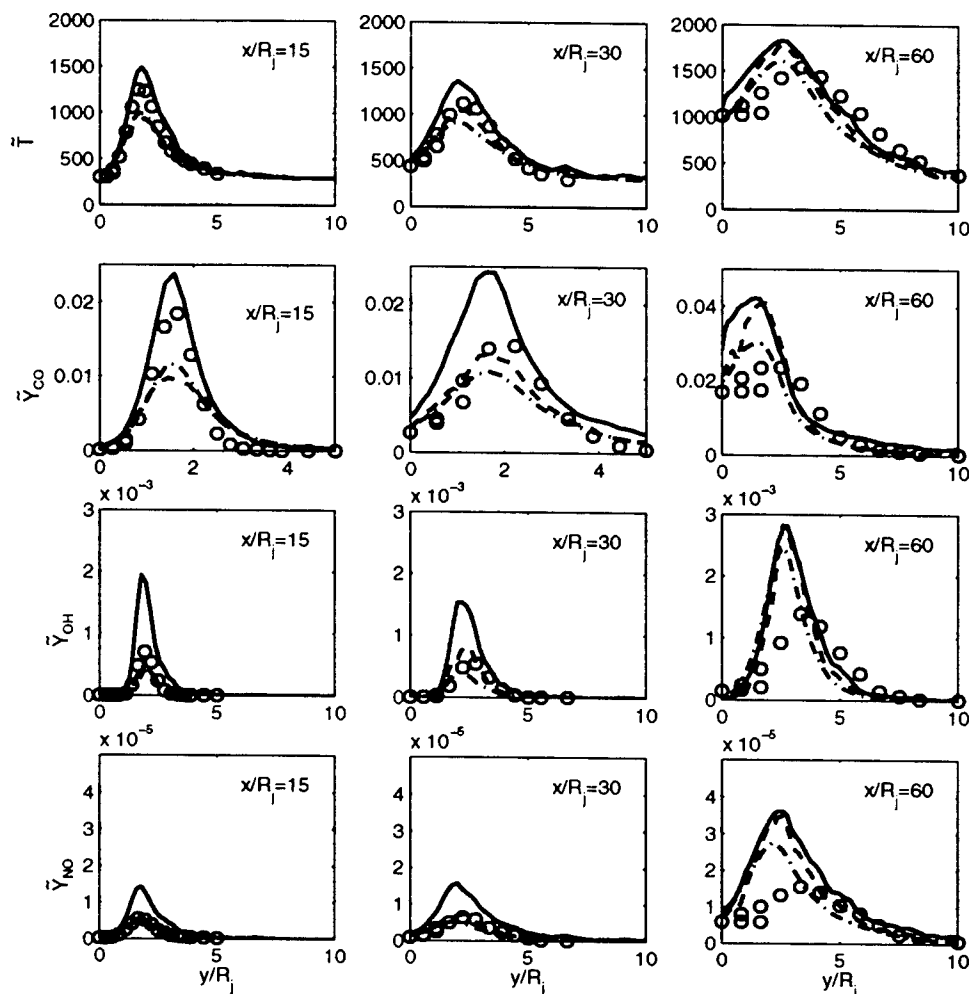


Fig. 1. Radial profiles of mean temperature and mass fractions in flame *F*: sensitivity to pilot temperature, T_p . Symbols, experimental data; solid line $T_p = 1880\text{K}$; dashed line $T_p = 1870\text{K}$; dot-dashed line $T_p = 1860\text{K}$.

scale PDF method calculation, the solution to the reaction equation system (20 dimensional) is required (of order) 10^9 times. ISAT can handle these computations economically and accurately. Recent work on PDF methods for these flames---now described---concerns sensitivity to the pilot flame temperature and to radiative heat loss.

It was observed by Xu & Pope (2000) that calculations of flame *F* exhibit some sensitivity to the pilot temperature T_p which is specified as a boundary condition. The experimental data show T_p in the range 1860K – 1880K, but the experimental accuracy may be no greater than 10-20K. This influence was studied systematically by performing calculations of flames *D* and *F* with pilot temperatures of $T_p = 1860, 1870$ and 1880K . For flame *D* it is found that the calculations are insensitive to T_p . But, as shown on Fig. 1, flame *F* exhibits extreme sensitivity. For example, at $x/R_j = 15$ and 30 the peak temperature decreases by about 500K and the mass fractions of *OH* decrease by a factor of more than two with a 10K decrease in pilot temperature. Similar trends exist for other variables. Particularly for *NO*, the results calculated using lower pilot temperatures give a perfect match with the experimental data at the first two locations shown in the figure. However, further downstream, all the modeled *NO* profiles overshoot the peak value by a factor of more than two and do not predict correctly on the fuel rich side, although the temperature profiles seem to be satisfactory.

Figure 2 shows another manifestation of the sensitivity to the pilot temperature. The burning index (BI) is defined to be unity for complete combustion and zero for complete extinction. The figure shows substantially different results for $T_p = 1860\text{K}$ and $T_p = 1880\text{K}$, with the experimental data generally falling between these two calculated values.

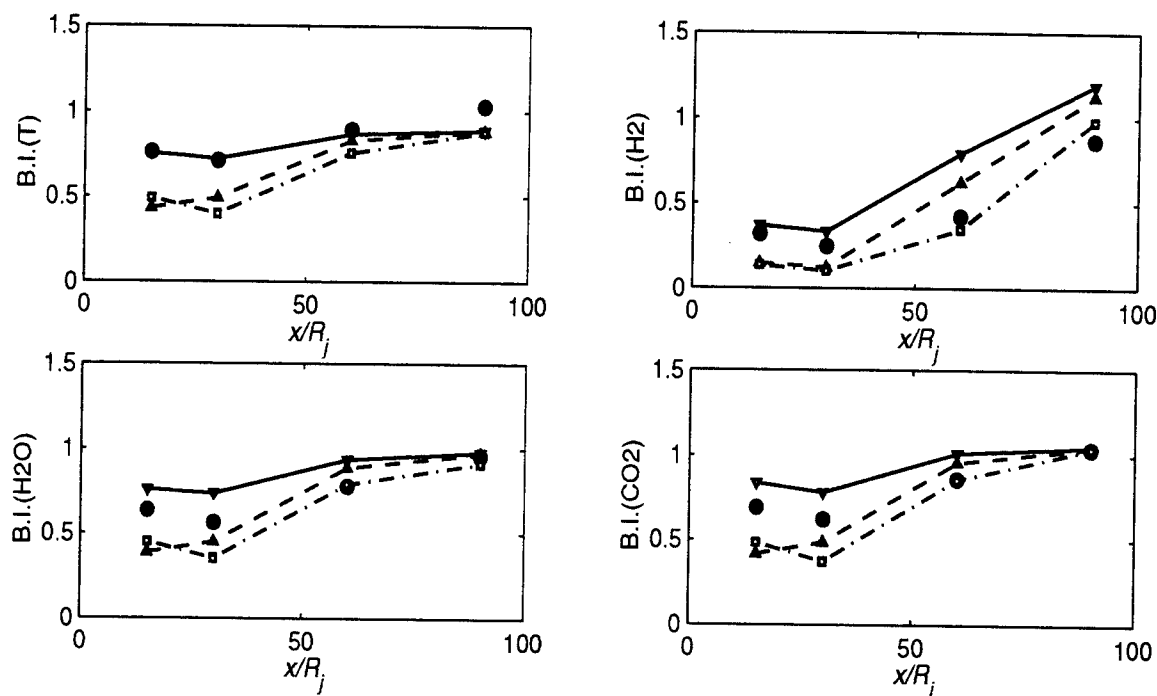


Fig. 2. Burning index (based on T and species) vs. axial distance in flame F . Symbols and lines as in Fig. 1.

The effects of radiative heat loss were investigated by performing “adiabatic” and “radiant” calculations. In the former all heat loss is neglected: in the latter, radiative heat loss is accounted for from the primary radiating species, CO_2 , H_2O , CO and CH_4 . We adopt an optically-thin limit radiation model, although the validity of this model for the 4.3-micron band of CO_2 is still in debate. Implemented in the framework of ISAT, the model includes the above four gas-phase emitting species with their Plank mean absorption coefficients calculated by RADCAL.

For flame D (not shown) the effect of radiation is to reduce the peak temperature by about 30K and to decrease the peak NO by 15%. Figure 3 presents the conditional mean profiles of four scalars, and shows completely different picture from the flame D results. For $T_p = 1880\text{K}$, the inclusion of radiation induces significant decreases in temperature and species mass fractions at the first three axial locations. The largest differences appear at $x/R_j = 30$ where the peak temperature decreases more than 500K and the species mass fractions decrease by a factor of two or three. This fact indicates that thermal radiation can significantly alter the local extinction status in this flame: not only is the NO chemistry strongly influenced by radiation, but also the reactions of other species such as OH and CO . The last column of Fig. 3 tells us that further downstream, the flame becomes closer to the equilibrium state as re-ignition takes place and the radiation tends to be less important.

Evidently, flame F is extremely sensitive to a decrease in temperature, whether it arises from T_p or from radiation.

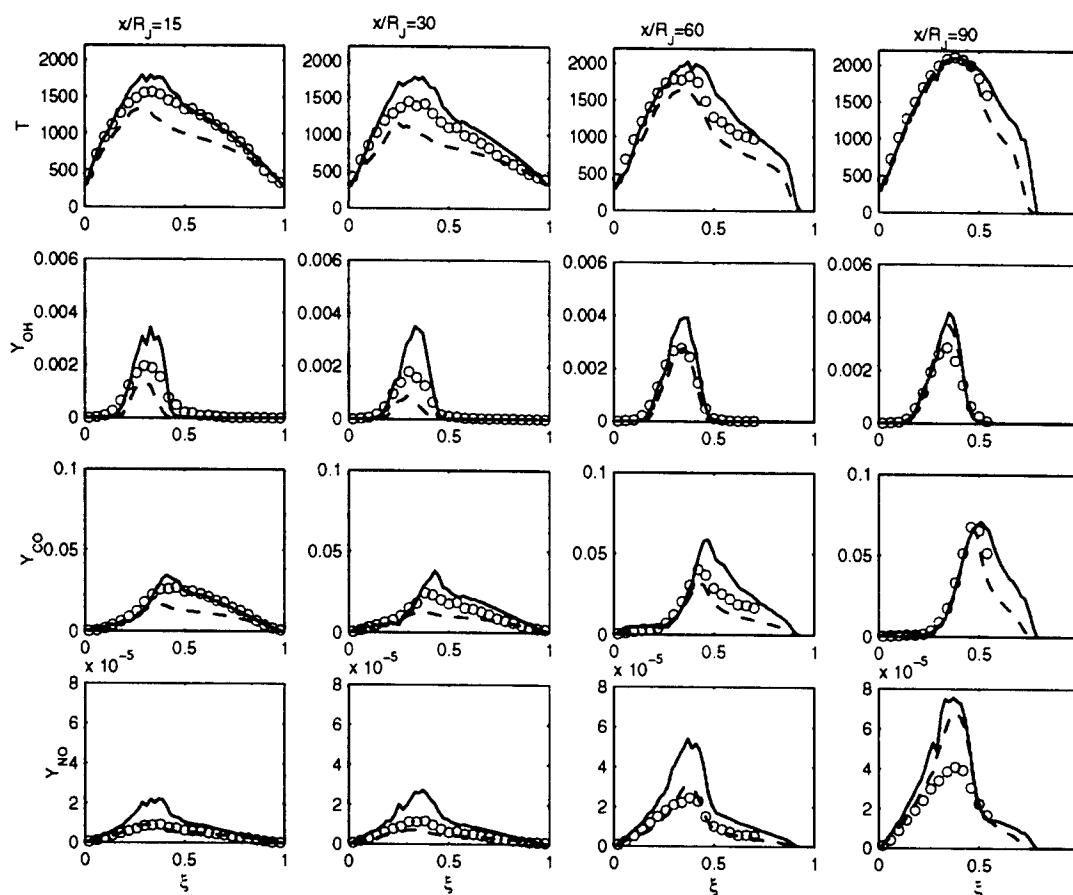


Fig. 3. Effect of radiative heat loss on means conditional on mixture fraction in flame *F*. Symbols, experimental data; solid line, adiabatic calculation; dashed line, radiant calculation.

REFERENCES

- R.S. Barlow, and J.H. Frank (1998). *Proc. Combust. Inst.* Vol. 27, pp. 1087-1095.
- R.P. Lindstedt, S.A. Louloudi, and E.M. Váos (2000). *Proc. Combust. Inst.*, (to be published) Vol. 28.
- S.B. Pope (2000). *Turbulent Flows*, Cambridge University Press.
- S.B. Pope (1997). *Combust. Theo. Modelling*, 1:41-63.
- S. Subramaniam and S.B. Pope (1998). *Combust. Flame*, 115:487-514.
- C.J. Sung, C.K. Law and J.-Y. Chen (1998). *Proc. Combust. Inst.*, Vol. 27, pp. 295-304.
- Q. Tang, J. Xu and S.B. Pope (2000). *Proc. Combust. Inst.*, (to be published) Vol. 28.
- J. Xu and S.B. Pope (2000). *Combust. Flame*, 123:281-307.

Lattice Boltzman Method for turbulent combustion

Sharath S. Girimaji, Texas A & M University
Li-Shi Luo, ICASE, NASA Langley Research Center

1 Introduction

Over the last few years, the Lattice Boltzman methods – Lattice Boltzman Equation (LBE) and Lattice Gas Automata (LGA) – have made significant strides in both theory and application. On the theoretical front, rigorous mathematical proof now exists demonstrating that the LBE method is a special finite difference scheme of the *Boltzmann equation that governs all fluid flow* [1]. (Recall that the Navier-Stokes equation also has its basis in the Boltzmann equation.) It has also been shown that the LBE method can be related to some conventional CFD methods and the proof brings to light the advantages of the LBE method. Detailed numerical studies with the LBE method have demonstrated the physical accuracy and computational tractability for solving complex fluid flow problems. In its current state, the LBE method is fully developed and well-tested for moderate-Reynolds number, isothermal flows. Many complex flow phenomena have already been studied with this approach (see recent reviews [2, 3] and references therein). The LBE method is now an accurate engineering tool for simulating inert turbulence and is at an ideal stage for extension to chemically reacting turbulent flows.

We propose the development of a new methodology for calculating turbulent combustion based on the Boltzman equation rather than Navier-Stokes equation. Our ultimate objective is to perform large eddy simulations of the Lattice Boltzman equation (LBE-LES) for chemically reacting turbulent flows. The Boltzman equation is potentially a better hydrodynamic platform for LES calculations of turbulent combustion than is the Navier-Stokes equation. The advantages lay both in improved physical accuracy and better computational characteristics.

Computational advantages.

1. The LBE method solves a simplified version of the Boltzmann equation with a linear advection term and a local collision term. In NS methods, the advection term is non-linear and both the advection and viscous terms are non-local.
2. In the LBE method, the pressure is obtained *via* the simple ideal-gas equation of state, again a local calculation. In the continuum model, the pressure is typically obtained from a computationally intensive global solution of the Poisson equation.
3. Due to the locality of the numerical scheme, LBE is ideally suited for large-scale, especially, parallel computing. The scheme incurs very little communication penalty and in some special cases is known to scale superlinearly with increase in the number of processes. In principal, the LBE can also be solved with Boolean algorithms resulting in even faster computations [4].
4. Due to the kinetic nature of the LB method, it is particularly easy to handle complicated boundary geometries (including phase interfaces, flame fronts) without sacrificing computational speed. The treatment of complex boundaries in the NS-methods can get very tedious.

5. Multi-phase flow and flows with phase transitions can be easily handled in the LB method since all the hydrodynamic and thermodynamic properties are available locally. In the NS methods, calculating these features can be prohibitively expensive.
6. Multi-component diffusion can present a daunting computational challenge in NS methods. That can be handled with relative ease in the LB methods.

Physical advantages.

1. *LBE is more easily amenable to subgrid-scale modeling than is the Navier-Stokes equation.* This is due to the fact that the advection operator is linear.
2. The molecular-diffusion process which is a major source of modeling error in the PDF method appears in closed form in the LBE approach. In the PDF-method, a stochastic model is typically used for modeling this process.
3. With the LB-based methods, one has the choice of using a deterministic or a stochastic calculation for chemical kinetics. The stochastic method has several advantages over the deterministic scheme.
4. The LB-based models are better capable of accurately accounting for turbulence-chemistry interactions.
5. Advection (large-scale stirring) appears in closed form in both the methods.

2 LES of Boltzman equation for turbulent combustion.

Filtered Boltzman equation for turbulent reacting flows. We start with the one-particle velocity distribution function $f(\mathbf{v}; \mathbf{x}, t)$. According to the Boltzman equation, the distribution function of a species β evolves as:

$$\frac{\partial f_\beta}{\partial t} + v_j \frac{\partial f_\beta}{\partial x_j} = J_\beta = C_\beta + R_\beta. \quad (1)$$

The left hand side represents the advection of the distribution function in velocity phase space and J_β represents the collision operator for species β . If the flow is reacting, then the collision term can be split into two parts: one part due to non-reacting (inert) elastic collisions (C_β) and the second part due to reactive collisions (R_β). The distribution function f_β is normalized such that the species continuum density (ρ_β) and temperature (T_β) are obtained from the following integrations:

$$\rho_\beta(t) = \int m f_\beta(\mathbf{v}, t) d\mathbf{v}; \quad \frac{3}{2} \rho_\beta T_\beta(t) = \int (\frac{1}{2} m v^2) f_\beta(\mathbf{v}, t) d\mathbf{v}. \quad (2)$$

In the above m is the particle mass and κ is the Boltzman constant.

In the LES of the Navier-Stokes equations, the velocity and the scalar fields are decomposed into two parts: one part representing the resolved scales of motion and the second from the unresolved scales. Here, we perform a similar decomposition of the velocity distribution function.

$$f(\mathbf{v}; \mathbf{x}, t) = f^<(\mathbf{v}; \mathbf{x}, t) + f^>(\mathbf{v}; \mathbf{x}, t), \quad (3)$$

where, as per standard convention, the superscripts $<$ and $>$ represent, respectively, the resolved and unresolved parts of the distribution function. We reiterate here that \mathbf{v} is a phase-space variable and is absolutely unaffected by the filtering in physical space. From equation (1), we can write the evolution equations of the resolved and unresolved distribution functions:

$$\frac{\partial f_\beta^<}{\partial t} + v_j \frac{\partial f_\beta^<}{\partial x_j} = C_\beta^< + R_\beta^<; \quad \frac{\partial f_\beta^>}{\partial t} + v_j \frac{\partial f_\beta^>}{\partial x_j} = [C_\beta - C_\beta^<] + [R_\beta - R_\beta^<]. \quad (4)$$

The resolved distribution function deserves some discussion. Since advection process linear in the velocity distribution function, the left hand side of the above equation needs no closure modeling. Whereas, with the Navier-Stokes equation, filtering of the non-linear advection operator leads to unclosed terms which are the main sources of modeling error. In the filtered Boltzman equation, the non-linearity appears in a more benign algebraic form in the collision operator. The terms $C_\beta^<$ and $R_\beta^<$ certainly need closure modeling. It is expected that the modeling of these terms would be less challenging than their NS counterparts. One of the reasons is that the resolved continuum variables (which is what we are after) are likely to be insensitive to the models of $C^<$ and $R^<$ at the mesoscopic scales. The closure modeling of these terms is the principle objective of the present research.

A second feature that make the LES of Boltzman equation very attractive for turbulent combustion is that fact that once the resolved distribution function is known, all the relevant resolved variables can be derived from it with no further approximation. Further, the relationship between the velocity distribution function and the continuum variables is linear in physical space:

$$\rho_\beta^< = \int m f_\beta^< d\mathbf{v}; \quad \rho_\beta^> = \int m f_\beta^> d\mathbf{v}; \quad (\rho_\beta \mathbf{u}_\beta)^< = \int m \mathbf{v} f_\beta^< d\mathbf{v}; \quad (\rho_\beta \mathbf{u}_\beta)^> = \int m \mathbf{v} f_\beta^> d\mathbf{v} \quad (5)$$

In the LES of the Navier-Stokes equations, subgrid-scale models are required for stresses, thermal flux and scalar flux. Further, models are also required for timescales of unresolved velocity, scalar and temperature fields. Models for these are typically derived independently based on different sets of assumptions. Even if each model is independently adequate, there is a real danger of incompatibility among them models resulting not only in large errors, but also in stifling numerical stiffness. In the LES of the Boltzman equation, all the models for all processes emerge from a single and, hence, internally-consistent methodology.

3 LBE-LES: Model development

Modeling of filtered non-reacting collision operator Non-reacting collisions in inert flows are typically modeled with the BGK approximation. The Boltzman equation with the BGK approximation is, in fact, the super-set of the Navier-Stokes equation. For a species β we have

$$C_\beta = -\omega_\beta(f_\beta - g_\beta); \quad C_\beta^< = -\omega_\beta(f_\beta^< - g_\beta^<), \quad (6)$$

where, ω_β is the inverse of the relaxation timescale and g_β is the Boltzman-Maxwell equilibrium distribution. *In the absence of reaction, the only term that is non-linear and, hence, needs closure modeling is the resolved-scale equilibrium distribution function.* The equilibrium distribution is of the form

$$g_\beta = \frac{\rho_\beta}{2\pi T_\beta} \exp[-(\mathbf{v} - \mathbf{u})^2/2T_\beta]. \quad (7)$$

One of the main thrusts of the present research is to develop a closure model for $g^<$.

Modeling of reacting collision operator The reaction operator can be represented in several different ways depending on the degree of accuracy required. At the most fundamental level we can consider the reactions at the molecular collision level following the methodology of Kugerl (Solution of the Boltzman Equation for a reacting gas mixture, *Phil. Trans. R. Soc. Lond. A*, 1993, pp 414 - 437). However, for most practical combustion applications the deterministic reaction-rate approach will be quite adequate. For the Lattice-Boltzman equation method we will use the standard deterministic law of mass-action, Arrhenius-type reaction model. The modeling and numerical issues will then be similar to those encountered on Navier-Stokes hydrodynamic platforms and similar strategies can be used. If, however, one were to use the Lattice Gas Automata scheme, stochastic approaches are possible for computing reactions. This stochastic chemistry method is definitely superior to the deterministic method both in terms of theoretical validity and computability. These issues will be addressed in detail in the present research.

Reduced-chemistry models. If the deterministic chemistry approach is used, ways must be found to obtain reduced representations for the full chemical kinetics. Some of the simpler methods (quasi-steady state approximation and partial equilibrium approximation) tend to be too inaccurate and the more sophisticated ones (ILDM, CSP) continue to be too computation intensive. Two procedures that are adequately accurate and computationally viable are the minimization of the evolution rate method [5] and a high-order quasi-steady state approximation currently under development [6].

Conclusion We propose the development of an innovative computational tool for turbulent combustion that is based on the Boltzman equation rather than on the navier-Stokes equation. The proposed LBE-LES method for turbulent combustion is still very much in its infancy, offering a tremendous opportunity for ground-breaking advancement.

References

- [1] X. He and L.-S. Luo, *A priori derivation of the lattice Boltzmann equation*, Phys. Rev. E, **55**:R6333 (1997); *Theory of the lattice Boltzmann method: From the Boltzmann equation to the lattice Boltzmann equation*, *ibid*, **56**:5311 (1997).
- [2] S. Chen and G. Doolen, *Lattice Boltzmann method for fluid flows*, Ann. Rev. Fluid Mech., **30**:329 (1998).
- [3] L.-S. Luo, *The future of lattice-gas and lattice Boltzmann methods*, to appear in the proceedings of the workshop on "Computational Aerosciences in the 21st Century," April 22 - 24, 1998, Hampton, Virginia.
- [4] B. Boghosian, J. Yepes, F. J. Alexander, and N. Margolus, *Integer lattice gases*, Phys. Rev. E, **55**:4137-4147 (1997).
- [5] S. S. Girimaji, *Reduction of large dynamical systems by minimization of evolution rate*, Phys. Rev. Lett., **82**:2282-2285 (1999).
- [6] S. S. Girimaji, *Higher-order steady state approximations for reducing large systems*. To be submitted (2001).

CHEMICAL KINETICS AND AERODYNAMICS OF IGNITION

(ARO Grant No. DAAG19-01-0004)

Principal Investigator: Chung K. Law

Princeton University
Princeton, NJ 08544

SUMMARY/OVERVIEW

This program investigates ignition of nonhomogenous systems, such as those found in practical combustion devices, by looking at ignition in a counterflow. During the reporting period, major effort was expanded on ignition in a nonpremixed turbulent counterflow where a hot air jet ignites an ambient temperature fuel jet. Specifically, the non-reacting turbulent flow was first investigated experimentally to provide data in support of other ignition and turbulence modeling studies. Subsequently, experiments were conducted to determine the ignition temperatures over a range of fuel concentrations, pressures, and strain rates. Preliminary modeling of turbulent ignition was also accomplished by first solving for the flow field using a Reynolds stress model and then solving for the chemistry by using a joint scalar PDF equation and Monte Carlo techniques. This two step approach is possible because of the small amount of heat release prior to ignition.

TECHNICAL DISCUSSION

1. Characterization of non-reacting turbulent flow fields

High fidelity experimental data for turbulent non-reacting counterflows are necessary to interpret turbulent non-premixed ignition experiments and to develop and evaluate numerical models for turbulent ignition. It is particularly important to have measurements of counterflows where one jet has a significantly different density than the other, as such data is not available in the literature. Counterflowing jets of heated air and cold nitrogen were investigated using a two-component laser Doppler anemometry system to measure velocity moments, spectra, and autocorrelations throughout the flow field. Operating conditions spanned a range of pressures, bulk strain rates, perforated plate configurations, and air temperatures. In addition to measuring velocity moments along the counterflow axis, mean and fluctuating velocity profiles were made in the radial direction at each nozzle exit. These profiles are important for establishing boundary conditions in turbulent flow models. The radial velocity gradients are needed in quasi-one dimensional turbulence models and the profiles themselves are needed for higher dimensional Reynolds stress models and Large Eddy Simulations.

Autocorrelation measurements at the burner exits were used with Taylor's hypothesis to estimate the flow's integral length scale. The length scales were about 70% of the perforated plate hole diameters, in agreement with theory and other experiments. The length scale is important for modeling efforts since it can be used to estimate the turbulent dissipation rate.

Turbulent power spectra were determined at the burner exits to further characterize the turbulence for a given perforated plate configuration. For example, due to the difficulties associated with generating turbulence in a strongly heated flow, some experiments have been conducted with only one perforated plate, located in the cold flow. The use of this configuration

was justified by the observation that the turbulent fluctuations look like those in a turbulent counterflow that has perforated plates in both nozzles as shown in Fig. 1. However, a comparison of the power spectra measured at the hot side of the burner, Fig. 2, shows that there is a significant difference between the two cases. The spectrum of the case without a second perforated plate is suggestive of very young, undeveloped turbulence, indicating that it is important to have a perforated plate in both sides of the burner when studying turbulence.

2. Turbulent non-premixed ignition experiments

Earlier experiments on ignition in non-homogenous systems have either looked at laminar ignition or ignition in an atmospheric turbulent counterflow with only one perforated plate. Since most practical combustion systems are turbulent and, as noted above, two perforated plates are necessary to produce well-characterized turbulence, the earlier work has been extended. The non-premixed ignition temperature was measured in a turbulent counterflow generated by two perforated plates for a range of hydrogen concentrations, bulk strain rates, and pressures. The effect of fuel concentration is shown in Fig. 3. The increasing sensitivity as the fuel concentration decreases and the nearly constant ignition temperature at higher fuel concentrations are qualitatively similar to what was observed in previous non-premixed ignition studies for both hydrogen and other fuels. For all the cases shown, ignition was repeatable and once ignited the turbulent flame persisted, even when the air temperature was subsequently reduced. For lower concentrations, intermittent ignition was observed where above a certain temperature a flame would be repeatedly ignited and extinguished. No hysteresis was observed.

The effect of pressure on ignition is shown in Fig. 4. In light of the laminar hydrogen ignition results, the turbulent data are indicative of a transition between the dominance of second limit chemistry at lower pressures to third limit behavior at the highest pressures. This data will be crucial to evaluating turbulent ignition models because hydrogen displays a significantly higher sensitivity to changes in pressure than changes in other parameters.

3. Modeling of turbulent non-premixed ignition

The complex non-linear interactions between reaction, convection, diffusion, and turbulence make general modeling of turbulent reacting flows very difficult. Modeling turbulent ignition, however, is somewhat simplified by the fact that prior to ignition there is very little heat release and consequently, the chemistry does not significantly alter the velocity field. To take advantage of this situation, turbulent ignition modeling is being addressed in two steps. In the first step, the non-reacting flow field is solved using a Reynolds stress turbulence model and assuming pure mixing. These calculations have been found to be in reasonable agreement with experimental measurements. Chemistry is treated in the second step by using Monte Carlo methods to solve a joint scalar PDF transport equation for the previously calculated flow conditions. With this approach, a detailed hydrogen-oxygen mechanism can be used. Preliminary calculations show that an ignition kernel can be identified through the mean radical concentrations. It is also found that the peak concentrations increase gradually as the air temperature increases until there is a sudden acceleration as ignition occurs.

4. Augmented Reduced Mechanism for Methane Oxidation with NO_x Chemistry

We have previously proposed the concept of developing Augmented Reduced Mechanisms (ARM) for the description of chemical kinetics in complex situations. The primary premise is that while simplifications of detailed reaction mechanisms must be made for the description of chemistry in complex flows, they have to remain sufficiently comprehensive in terms of the system dependence on temperature, pressure and concentration in order to retain the essential

chemical information. As such, existing reduced mechanisms that typically consist of four to five steps have been shown that, while simple and physically illuminating, they have restricted ranges of comprehensiveness. Consequently, a 12-step, sixteen species augmented reduced mechanism has been developed for methane oxidation that has shown a high degree of comprehensiveness in its ability to simulate the global responses of various combustion phenomena over extensive ranges of system parametric variations. The validation has now been extended to the temporal and spatial profiles of the temperature and species (both major and minor) concentrations.

The 12-step mechanism for methane oxidation has been extended to account for NO formation, with a 14-step mechanism to describe the thermal, prompt, and nitrous oxide mechanism, and a 15-step mechanism to include the NH₃-related reactions. These ARMs demonstrate good performance in simulating results from the detailed mechanism.

MAJOR PUBLICATIONS

- [1] "Ignition of CO/H₂/N₂ versus Heated Air in Counterflow: Experimental and Modeling Results," by C.G. Fotache, Y. Tan, C.J. Sung and C.K. Law, *Combustion and Flame*, Vol. 120, pp. 417-426 (2000).
- [2] "Non-Premixed Ignition of n-Heptane and iso-Octane in a Laminar Counterflow," by J.D. Blouch and C.K. Law, *Proceedings of the Combustion Institute*, Vol. 28, pp. 1679-1686 (2000).
- [3] "Further Validation of an Augmented Reduced Mechanism for Methane Oxidation: Comparison of Global Parameters and Detailed Structure," by C.J. Sung, C.K. Law, and J.Y. Chen, *Combustion Science and Technology*, Vol. 150, pp. 201-220 (2000).
- [4] "Augmented Reduced Mechanisms for NO Emission in Methane Oxidation," by C. J. Sung, C.K. Law, and J.Y. Chen, *Combustion and Flame*, in press.

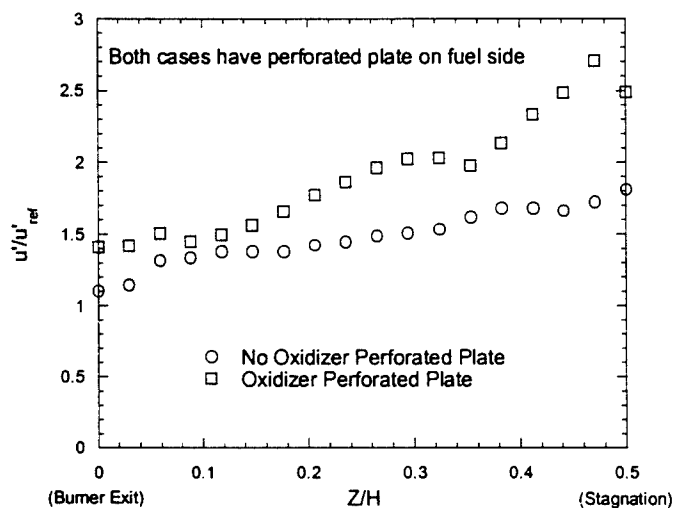


Figure 1: Velocity fluctuations on oxidizer side of stagnation plane.

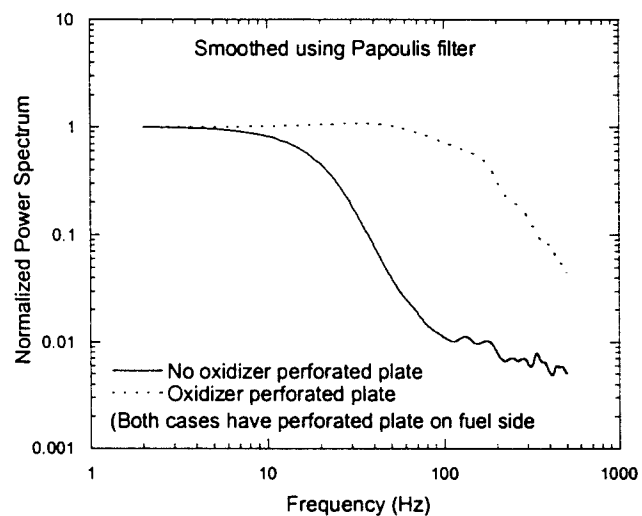


Figure 2: Power spectrum at oxidizer exit ($Z=0$) normalized by value at 2Hz.

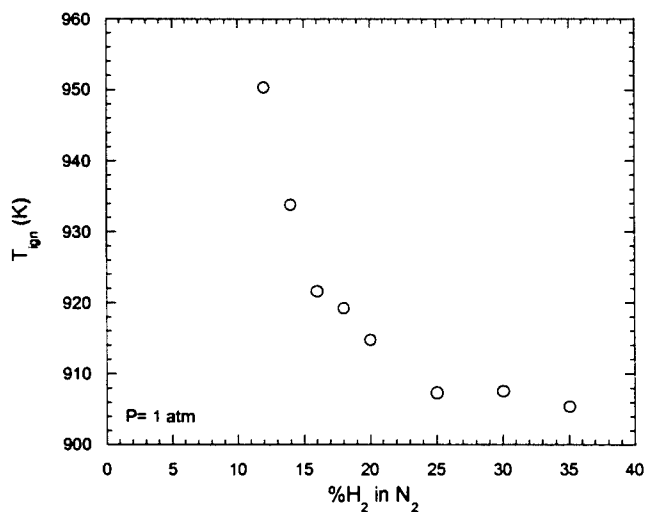


Figure 3: Effect of fuel concentration on ignition temperature.

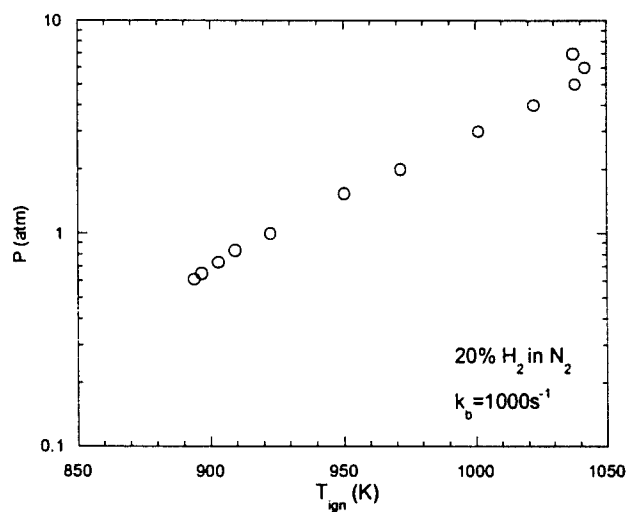


Figure 4: Effect of pressure on ignition temperature.

PHYSICAL AND CHEMICAL PROCESSES IN FLAMES

(AFOSR Grant No. F49620-01-1-0029)

Principal Investigator: Chung K. Law

Department of Mechanical and Aerospace Engineering
Princeton University
Princeton, NJ 08544

SUMMARY/OVERVIEW

The objectives of the present program are to develop detailed and simplified chemical kinetics model for hydrocarbon combustion, and to understand and quantify the dynamics of flames. During the reporting period progress were made in the following projects: (1) Laminar flame speeds of mixtures of ethylene and *n*-butane were studied. Results suggest the dominant influence of the adiabatic flame temperature in assessing the mixture flame speed. (2) A theory of complex CSP (computational singular perturbation) for chemistry reduction and analysis was developed. An algorithm was derived through which detailed mechanisms can be systematically reduced to simpler ones without compromising the comprehensiveness of the original mechanism. (3) Stretch effects on premixed flame pulsation were computationally and analytically studied. Results show that positive (negative) stretch promotes (retards) the development of pulsating instability, which is completely opposite to the influence of stretch on cellular instability. (4) Pulsating instability of near-limit diffusion flames were computationally studied. Results show that the instability and the subsequent extinction of methane and hydrogen flames assume the characteristics of diffusion and premixed flames respectively.

TECHNICAL DISCUSSION

1. Laminar Flame Speeds of Ethylene/*n*-Butane/Air Mixtures

The laminar flame speed is a useful parameter towards development and validation of detailed kinetic mechanisms of hydrocarbon fuels. The objectives of the present study are: (a) to extend our previous study involving single fuels to fuel blends, and (b) to experimentally determine the flame speeds by using Digital Particle Image Velocimetry (DPIV).

Regarding the first objective, we note that since nearly all practical fuels are multi-component, it is important to develop theoretical and semi-empirical capabilities to predict the flame speeds of fuel mixtures. Furthermore, existing reaction models of hydrocarbon combustion were mostly developed based on results from single fuels and as such have not been adequately verified for fuel mixtures. Finally, it is also of interest to develop semi-empirical mixing rules.

Mixtures of ethylene and *n*-butane were selected for study because ethylene is an important intermediate in hydrocarbon oxidation while *n*-butane is a representative *n*-alkane. Figure 1.1 shows experimental data of the laminar flame speeds of ethylene/air and *n*-butane/air mixtures. These experimental data compare well with the calculated values obtained by using the kinetics model developed under the present program.

Using this kinetics model, further calculations were performed for mixtures of ethylene and *n*-butane in the ratios of 2:1, 1:1, and 1:2, as shown in Fig. 1.2. As is reasonable to expect, the flame speeds of the fuel mixtures are bounded by those of ethylene/air and *n*-butane/air. However, results for the mixtures seem to be weighted towards the *n*-butane values. The same

biasing is also exhibited for the calculated adiabatic flame temperatures (Fig. 1.2), indicating that the flame temperature instead of kinetic coupling could have the dominant influence on the flame speed.

The biasing could simply be a consequence of how the composition of mixture is defined. The present mixing ratio is the conventional one, based on the molar ratios. There are, however, other definitions that could be more relevant physically. This aspect is being studied.

Preliminary experimental data were also taken for the laminar flame speeds of the fuel blends, showing the same trend of biasing. In order to prepare ourselves for massive amount of data taking, we have been developing a DPIV system which, compared to LDV, is capable of significantly reducing the test time and positioning error.

Results of the above activities are reported in Publication No. 1.

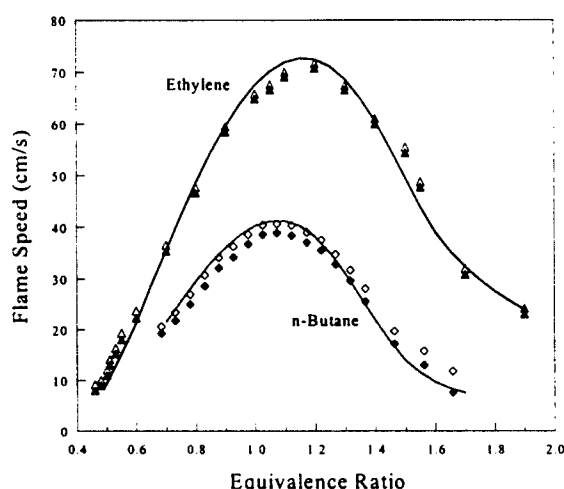


Figure 1.1. Experimental and computed laminar flame speeds of ethylene/air and *n*-butane/air mixtures.

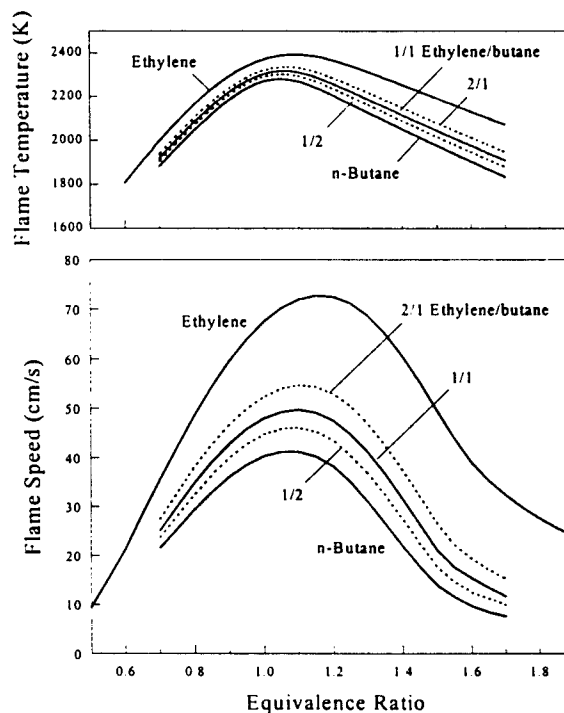


Figure 1.2. Computed adiabatic flame temperatures and laminar flame speeds of mixtures of ethylene and *n*-butane fuels.

2. Theory of Complex Computational Singular Perturbation

The method of Computational Singular Perturbation (CSP) for the analysis and reduction of detailed chemical mechanisms has been extended [3] to the complex eigensystem. Results show that the time scales of chemical species change dramatically and non-monotonically, and that oscillatory modes appear frequently in large chemical reaction mechanisms. The present method is then employed to generate reduced mechanisms for hydrogen/air and methane/air oxidation. Using the hydrogen/air system as an example, Fig. 2.1 shows that the number of complex modes increases with decreasing residence time and hence increasing chemical sensitivity. Figure 2.2 shows the relation between the size of the reduced mechanism with a measure of the residence time – the longer the residence time (smaller α) the more the number of steady-state species and hence the smaller the mechanism. The validity of these reduced mechanisms is evaluated based on the responses of the perfectly stirred reactors and the one-dimensional planar propagating premixed flames. Comparison between the reduced and detailed chemistries over a wide range of pressures and equivalence ratios show good agreement on the flame speed, temperature and structure.

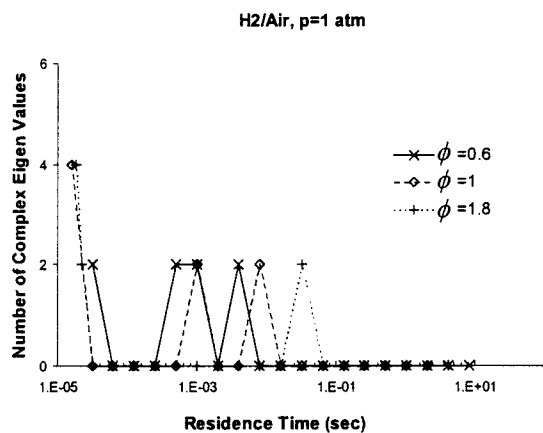


Figure 2.1 Number of complex modes for hydrogen/air mixtures for different residence times in the PSR.

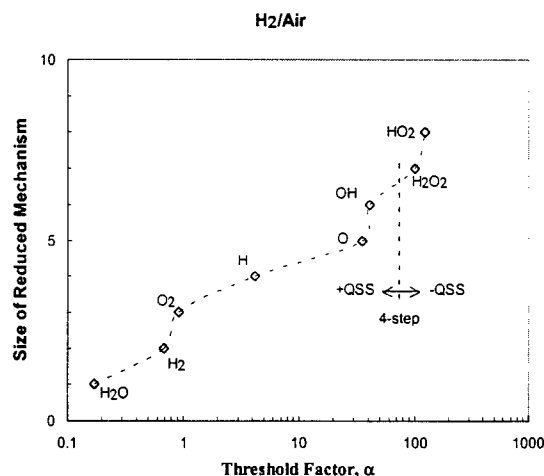


Figure 2.2 Diagram indicating the variation of the size of the reduced mechanism with different residence times; smaller α implies longer residence time, more steady-state species, and smaller reduced mechanism.

3. Effects of Stretch on Flame Pulsation

Effects of stretch on the pulsating instability of premixed flames have been investigated [10] via the negatively-stretched inwardly propagating spherical flame (IPF) and the positively-stretched counterflow flame (CFF). Computational and asymptotic analysis results show that pulsating instability is suppressed by the former and promoted by the latter.

In particular, it is shown that for a given rich hydrogen/air mixture whose one-dimensional, freely propagating flame is pulsatingly unstable, the IPF initially propagates at the laminar flame speed when the flame radius is large. Oscillation subsequently develops, and is then amplified, damped, and eventually suppressed as the flame propagates inward and the magnitude of stretch increases.

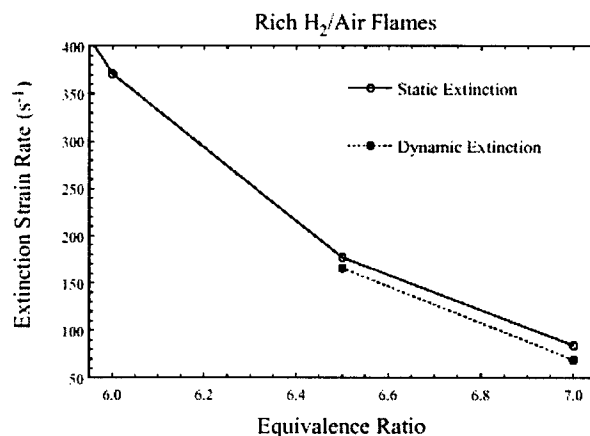


Figure 3.1 Extinction strain rates for the steady and oscillating counterflow flames

For the positively stretched rich hydrogen/air CFF, oscillation is initiated at an equivalence ratio much smaller than the one-dimensional rich threshold. Furthermore, the critical strain rate leading to pulsation is smaller than the corresponding static extinction limit, implying that the flame extinguishes in the pulsating instead of the steadily propagating mode such that the flammable range is accordingly narrowed (Fig. 3.1). In addition, it is seen that the pulsating flames are quasi-steady in nature in that the period of oscillation is larger than the characteristic

flame time. As such, the unsteady flame cannot recover once the instantaneous flame temperature is reduced below the corresponding steady-state extinction temperature.

The computationally determined pulsation limits using realistic chemistry and transport were also found to agree well with the asymptotic results based on simplified chemistry and transport, provided that the global activation energies and Lewis numbers are appropriately extracted from laminar flame responses.

4. Oscillatory Extinction of Diffusion Flames

The transient behavior of spherical diffusion flames was computationally studied [11] in both the high-velocity and radiation-induced limit of the isola response of flame extinction. Oscillatory instability was observed near both steady-state extinction limits, with the oscillation amplitude growing until it becomes large enough to extinguish the flame. For the hydrogen and methane flames studied, oscillation always leads to extinction, although the characteristics of oscillation are qualitatively different. Specifically, the methane flame exhibits large amplitude temperature fluctuations at a frequency of about 0.35 Hz, while the hydrogen flame has small amplitude fluctuation with a frequency of about 60 Hz. The oscillations in the methane flame appear to be characteristic of those studied based on the diffusion flame structure, while those of hydrogen flames are reminiscent of those observed in rich hydrogen/air premixed flames.

MAJOR/RELEVANT PUBLICATIONS (May 2000 – April 2001)

1. "Determination of laminar flame speeds of ethylene/n-butane/air flames using digital particle image velocimetry," Paper No. 138, Second Joint Meeting of the US Section of the Combustion Institute, Oakland, CA, March 25-28, 2001.
2. "Detailed kinetic modeling of 1,3-butadiene oxidation at high temperatures," by A. Laskin, H. Wang, and C. K. Law, *International Journal of Chemical Kinetics*, Vol. 32, pp. 589-614 (2000).
3. "Theory of complex CSP for chemistry reduction and analysis," by T. Lu, Y. Ju, and C. K. Law, *Combustion and Flame*, in press.
4. "Structure, aerodynamics, and geometry of premixed flamelets," by C.K. Law and C.J. Sung, *Progress in Energy and Combustion Science*, Vol. 26, pp. 459-505 (2000).
5. "Structural sensitivity, response, and extinction of diffusion and premixed flames in oscillating counterflow," by C. J. Sung and C. K. Law, *Combustion and Flame*, Vol.123, pp. 375-388 (2000).
6. "On curvature-affected pulsating instability in inwardly-propagating spherical flames," by C. J. Sung, C. J. Sun, and C. K. Law, *Combustion Science and Technology Communications*, Vol.1, pp.7-10 (2000).
7. "Radiation induced instability of stretched premixed flames," by Y. Ju, C. K. Law, K. Maruta, and T. Niioka, *Proceedings of the Combustion Institute*, Vol. 28, pp. 1891-1900 (2000).
8. "The role of pulsating instability and global Lewis number on the flammability limit of lean heptane/air flames," by E. W. Christiansen, C. K. Law, and C. J. Sung, *Proceedings of the Combustion Institute*, Vol. 28, pp. 807-814 (2000).
9. "Steady and pulsating propagation and extinction of rich hydrogen/air flames at elevated pressures," by E. W. Christiansen, C. J. Sung, and C. K. Law, *Combustion and Flame*, Vol. 124, pp. 35-49 (2001).
10. "On stretch-affected pulsating instability in rich hydrogen/air flames: asymptotic analysis and computation," by C.J. Sung, A. Makino, and C.K. Law, Paper No. 262, Second Joint Meeting of the US Section of the Combustion Institute, Oakland, CA, March 25-28, 2001.
11. "A computational study on oscillatory extinction of spherical diffusion flames," by E.W. Christiansen, S.D. Tse, and C.K. Law, AIAA-2001-1084, 39th Aerospace Sciences Meeting, January 8-11, 2001, Reno, NV.

STABILIZATION AND BLOWOUT OF GASEOUS- AND SPRAY-JET FLAMES

ARO Grant/Contract Number: AMSRL-RO-RI 40131-EG

Principal Investigator: Kevin M. Lyons

North Carolina State University
Department of Mechanical and Aerospace Engineering
Raleigh, NC 27695-7910

SUMMARY/OVERVIEW:

A research program to focus on experimental work in lifted flames (gaseous and spray) has been initiated. In particular, the group is interested in the similarities of spray and gaseous lifted-flame structures, similarities and differences in apparent stabilization phenomena, the role of mixing in each and blowout phenomena. Discussed in this report are the details of experimental findings in gaseous combustion and proposed experiments primarily in spray combustion and how the information and data to be obtained aids in understanding the physics of flame stabilization in general.

TECHNICAL DISCUSSION:

GASEOUS COMBUSTION. A sufficient understanding of the concepts governing the stability of turbulent diffusion flames is essential because of their widespread appearance in combustion applications (Schefer and Goix 1998). Examining the lifted diffusion flame, from both spray and gaseous sources, provides a meaningful system in which to develop this understanding. Simultaneous velocity and concentration field measurements in reacting flows are desirable because they provide a deeper understanding of the flow behavior, including stabilization and local extinction. Experiments have been performed by our group to measure the instantaneous velocity and CH radical concentration fields in a lifted methane jet diffusion flame.

CH is an excellent radical for marking the reaction zone of hydrocarbon flames. The short-lived transient nature of CH at an intermediate stage of combustion makes it an accurate Planar Laser-Induced Fluorescence (PLIF) imaging tool for indicating flame front location and thus the region of stabilization. Additionally, the well-defined reaction surface indicated by the fluorescence signals of CH provide an excellent means for evaluating the role of local extinction in lifted flames. Instantaneous velocity field measurements, indicated by Particle Image Velocimetry (PIV), in conjunction with CH images present an improved indicator of the flowfield behavior near these regions.

The simultaneous PIV/CH-PLIF measurements provide an accurate method for determining the location of the stabilization point and the flow velocity at this critical location. While previous studies have estimated the stabilization point velocity by assuming the flame stabilizes in the region of low seed particle density indicated by the PIV images, the CH profiles of this study provide a more accurate indication of the flame front location. An important conclusion that supports previous findings is that the flame is stabilized against the incoming unburned gas in a region of relatively low velocity (1.18 m/s) that is comparable to the premixed laminar burning velocity ($\sim 3S_L$).

The extent of premixing at the flame front and its role as a stabilization mechanism is a common source of disagreement among current theories. Recently, triple, or tribrachial, flames have received substantial consideration as the anchoring mechanism for lifted flames (Kioni et al 1999). Triple flames consist of an ordinary diffusion flame surrounded by two premixed flames, one fuel-rich and one fuel-lean, which join at the triple point. The two premixed zones allow for flame propagation against the incoming unburned flow while the trailing diffusion flame extends downstream from the premixed regions.

Our group at N.C. State, in collaboration with the Air Force Research Laboratory, recently reported some of the first experimental evidence for the "leading edge" flame as a primary stabilization mechanism in lifted diffusion flames. CH is an excellent radical for marking the reaction zone of hydrocarbon flames. The "leading edge" flame phenomenon refers to the outward-extending branch of CH fluorescence at the base of the streamwise CH zones. The "leading edge" flame is regarded as a source of thermal energy which anchors the trailing diffusion flame. Whether the "leading edge" flame is a special case of the more general triple flame is a question which remains unanswered. It is evident from previous computational studies that the triple flame, when interacting with a vortex or pair of vortices, can take on characteristics of the "leading edge" flames introduced in the present study. Several diagnostic studies involving lifted flames present the lifted flame structure as a continuous flame surface, similar to a distorted cylindrical object, emanating from a ring-shaped structure where the flame is stabilized. Most previous work, however, does not give experimental evidence of the *mechanism* of lifted flame stabilization. Shown in Fig 1 (see Watson et al 1999) are several CH-PLIF images from our work which provide such evidence. Each image was collected from the same spatial location and represents an instantaneous realization of the flame zone. The images clearly show a continuous vertical distribution of CH which represents the primary diffusion flame reported in many previous studies.. In addition to the vertical trailing diffusion flame, a structure is witnessed near the flame base which curls toward the outside, or fuel-lean, portion of the reaction zone. In comparison to ideal, laminar tribrachial structures, evidence of both rich and lean branches of premixed flame are not present, only the one branch extending outward near the jet edge. However, the rich branch on the fuel side of the diffusion flame may be overlapped into the diffusion flame by the flowfield. It is believed that the branch in the CH zone is a "leading edge" flame, stabilized by opposing the flow in the relatively low speed region (approx. 1.0 m/s) near the outside edge of the jet.

The extent of mixing and the entrainment of ambient air into the fuel is of central importance to this problem. Based on comparisons with mixture fraction images, which illustrate that the portion at the base of a lifted methane flame has a flammable composition, the PI is confident that the leading edge flame lies in a flammable mixture fraction region (Kelman et al 1998). Furthermore, fluctuations in the axial location of the leading edge, along with its orientation relative to the trailing diffusion flame, imply propagation into the unburned gas region. Together, these facts support the notion of premixing as a primary mechanism of lifted flame stabilization even for flames in the near-field.

SPRAY COMBUSTION. The current work in spray flame stabilization is motivated by the results discussed earlier on observation of leading edge phenomena in gaseous jet flames. There have been many studies published on bluff-body stabilization of flames that attempt to account for flame stabilization. In the context of spray flames (Stepowski et al 1994, Cessou et al 1999), these studies have been largely geared toward understanding phenomena in gas turbine combustion and other systems where fuel is injected as a spray. If one views the combustion zone down from a flame holder (bluff body) as a homogeneous chemical reactor (homogeneous composition and temperature), then flame extinction is thought to occur when the amount of heat needed to ignite the fresh reactants exceeds that amount received by local combustion. Central to this picture is the recirculation zone and the need for entrainment into the wake region, whether spray or gaseous combustion is considered. As is true of earlier work in gaseous lifted-flame combustion, the lack of appendages in the flow to create recirculation zones in our geometries makes it difficult to apply results from previous flameholding studies. Thus our main reason for continued interest in the lifted spray flame is to acquire experimental data indicative of the nature of the flamefront in lifted spray flames and contrast the structures with our gaseous flame results. For example, it is not clear if the leading edge phenomena witnessed in our gaseous studies correspond with the dual fronts witnessed in the vaporization regime of spray combustion or if the phenomena are fundamentally different. The nature of the flamefront in the stabilization region of a corresponding *spray-jet flame* is currently unknown. Whether spray flames exhibit "leading edge" flame structures as shown by our group for the gaseous case is a major question to be addressed by this research. Detailed study of spray jet flames (see typical experimental setup in Figure 2) is being currently initiated in order to illuminate the features common to both systems and show differences in the flame structure and dynamics of the spray and gaseous systems.

References

- Cessou, A., Goix, P. and Stepowski, D., "Simple Description of the Combustion Structures in the Stabilization Stage of a Spray Jet Flame" *Atomization and Spray*, Vol. 9, 1999, pp. 1 – 27.
- Kelman, J. B., Eltobaji, A. J., and Masri, A. R., "Laser Imaging in the Stabilisation Region of Turbulent Lifted Flames," *Combustion Science and Technology*, Vol. 135, 1998, pp. 117-134.
- Kioni, P. N., Bray, K. N. C., Greenhalgh, D. A., and Rogg, B., "Experimental and Numerical Studies of a Triple Flame," *Combustion and Flame*, Vol. 116, 1999, pp. 192-206.
- Schefer, R. W., and Goix, P. J., "Mechanism of Flame Stabilization in Turbulent, Lifted-Jet Flames," *Combustion and Flame*, Vol. 112, 1998, pp. 559-574.
- Stepowski, D., Cessou, A. and Goix, P., "Flame Stabilization and OH Fluorescence Mapping of the Combustion Structures in the Near Field of a Spray Jet" *Combustion and Flame* 99: 516-522 (1994)

Watson, K. A., Lyons, K. M., Donbar, J. M., and Carter, C. D., "Observations on the Leading Edge in Lifted Flame Stabilization," *Combustion and Flame*, 119: 199-202 (1999).

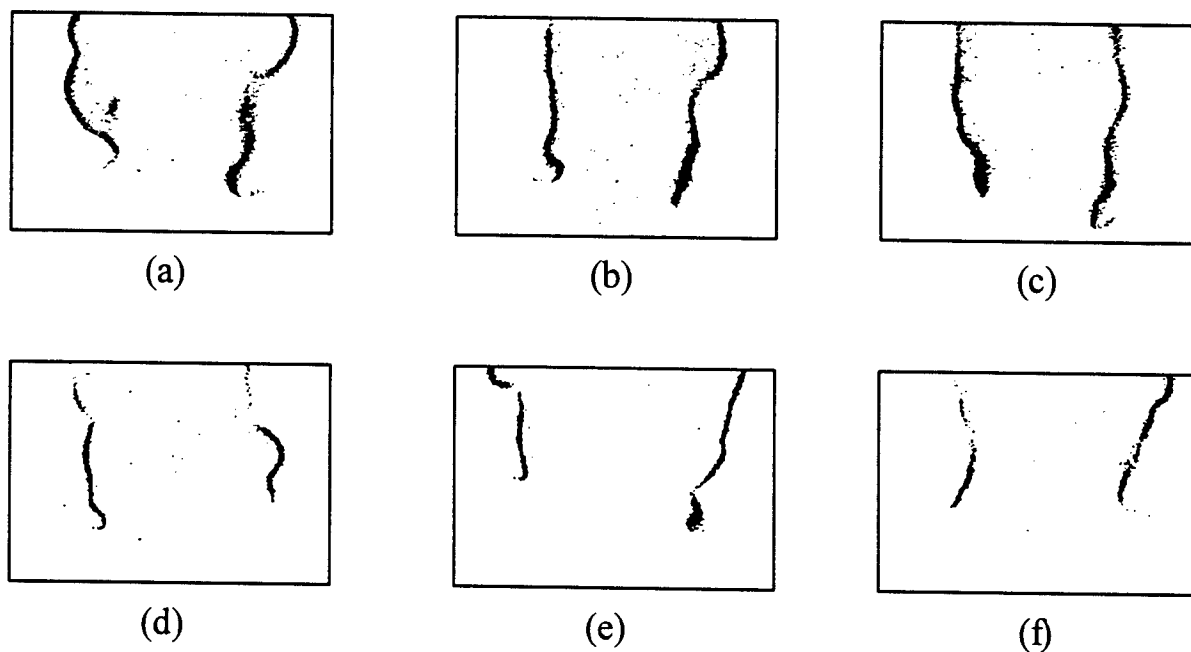


Figure 1 – Shown are the leading edge flame structures (CH) near the stabilization zone in a lifted gaseous methane flame. These observations help drive our interest in examining spray flames for the presence of similar structures.

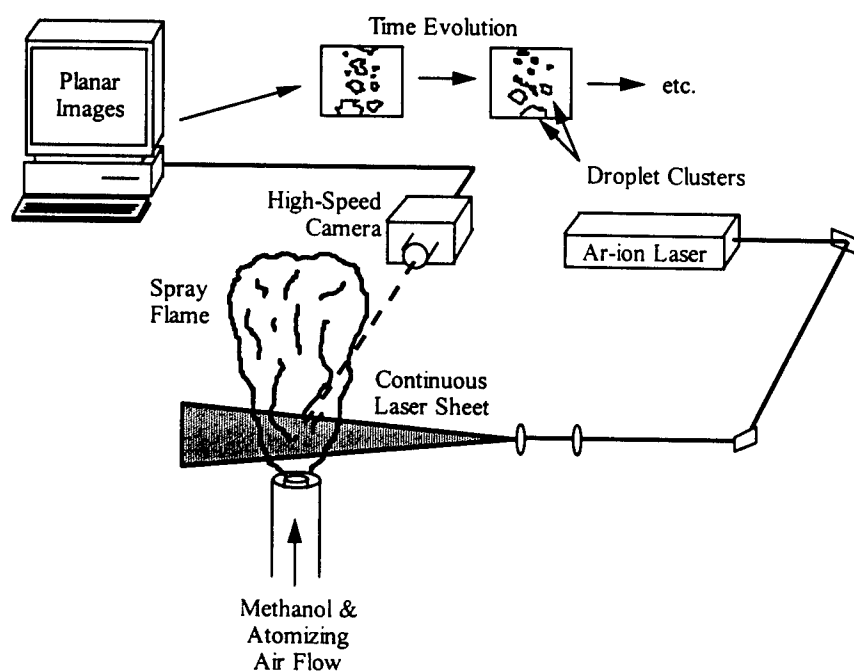


Figure 2 – Schematic of typical experimental setup for examining spray flames

INVESTIGATION OF THE STRUCTURE OF A REACTING HYDROCARBON-AIR PLANAR MIXING LAYER

Grant/Contract Number: DAAH04-94-G-0328.

Principal Investigator(s): Corradini, Farrell, Foster, Ghandhi, Reitz, Rutland

Engine Research Center
University of Wisconsin-Madison
1500 W. Engineering Dr.
Madison, WI 53706

SUMMARY

Mixing-controlled combustion of a hydrocarbon-air system was investigated experimentally in a planar two-stream mixing layer using planar laser-induced fluorescence of OH for visualization of the reaction zone, and planar LII of soot, which was found to effectively mark the edge of the parent fuel entrainment. The high-temperature combustion was found to locate on the lean reactant (air) side of the mixing layer, and was minimally perturbed by the fluid motion, resulting in the formation of an 'internal' mixing layer, reminiscent of a non-reacting mixing layer, between the combustion products and the neat fuel stream. For the same inlet hydrodynamic conditions, the large-scale structure spacing was found to decrease when the high-speed stream contained the fuel, whereas air as the high-speed fluid resulted in a lengthening of the structure spacing compared to non-reacting conditions. The effective density ratio established by the high temperature reaction zone located on the air side of the mixing layer is believed to be the cause for this behavior. A tripped high-speed boundary layer was found to have a large effect on non-reacting passive scalar measurements, but was not found to affect the mixing layer structure under reacting conditions, suggesting that the heat release serves to make the Kelvin-Helmholtz instability dominant.

TECHNICAL DISCUSSION

The latter stages of Diesel combustion are limited by the mixing of the partially oxidized products with the available air in the time available. High power density operation requires the mixing times to be quite short to enable the energy release due to combustion to be realized by the piston expansion, however for low particulate operation the time scale of importance is the time for the exhaust valve to open, significantly longer. The investigation of these processes in realistic engines is complicated by the high pressures, temperatures and the strong luminosity of the combusted gases. Additionally, modeling of the late-stage combustion is limited by the relative simplicity of the chemistry included in multi-dimensional models, which is required to facilitate the computation of this difficult flow. Thus, in order to develop a better fundamental understanding of mixing-controlled combustion under controlled conditions, a planar shear layer has been constructed.

A schematic of the shear layer apparatus is shown in Figure 1. Air (possibly heated), at the left, and a mixture of fuel and argon, at the right, pass through a series of flow conditioning

elements, consisting of perforated plates, tube bundles, and mesh screens, which reduce the turbulence level and isolate upstream acoustical modes from the shear layer. The streams meet at the tip of a splitter plate where they mix and react in an optically accessible test section. A symmetrical nozzle producing a 1.75:1 contraction ratio and a 3.8° tapered splitter plate (nominal tip thickness is 0.1 mm) were used to create the shear flow. The velocity profile at the splitter plate tip was measured to be uniform within 1.3%, with turbulence intensities $< 0.5\%$. The test section downstream of the splitter plate was 5 cm in the cross-stream direction and 20 cm in the spanwise direction. The test section had two hinged walls that could be adjusted to eliminate the streamwise pressure gradient in the flow. For reacting experiments, the walls were extended 2° from the vertical position. The entire flow conditioning run and test section were enclosed in a pressurized containment vessel designed for operation at pressures up to 6 atm. Optical access was provided with fused silica windows at each quadrant of the test section and containment vessel. At the top of the containment vessel, the exhaust and slave gases were throttled to atmospheric pressure and then cooled and further diluted in a water quench tower before entering the laboratory exhaust system. The mixing layer was ignited with a swirl-stabilized ignitor mounted flush with the side wall. With reaction engaged in the mixing layer and the proper system pressure and flow rates established, the ignitor was shut off, leaving the mixing layer to sustain combustion on its own accord, undisturbed by the perturbation of the ignitor.

Planar LIF of OH was accomplished with a Nd:YAG pumped dye laser whose output was frequency doubled to 283.92 nm to pump the overlapping $Q_1(8)$ and $Q_2(9)$ lines of the $A^2\Sigma^+ \leftarrow X^2\Pi(1,0)$ band of OH. Figure 2 shows sample images acquired position B (see Fig. 1). Fig 2.a was obtained with the laser tuned on the OH transition while Fig. 2.b was obtained with the laser tuned off the OH line (283.75 nm). The filtering scheme allowed significant transmission from 310 - 358 nm. Comparison of the online and offline images clearly indicates that the strong signal at the left is OH, while the fainter signal to the right originates from a different, laser-excited source. To investigate whether this signal arose from particulate matter or polycyclic aromatic hydrocarbons (PAHs) which have broadband absorption and emission characteristics, elastic scatter images were collected, see Fig. 2.c. The strong similarity between the elastic scattering and offline images suggests that the source of the offline signal is scattering from particulate matter and not fluorescence. The spectral shift of the offline interference signal and its coincidence with the elastic scattering suggests that the source of the offline signal is laser-induced incandescence (LII) from soot particles. However, it is not possible to exclude the possibility of PAH fluorescence from the spatial locations where the soot exists.

To further investigate the nature of the signal originating from the soot particles, the fuel/argon stream was visualized by seeding the stream with ($\sim 2\%$ by volume) acetone and performing PLIF under

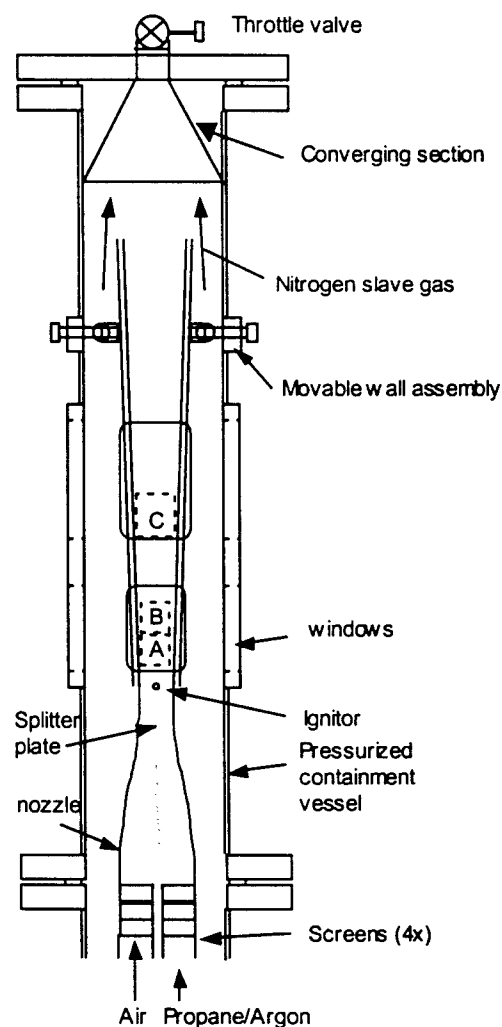


Figure 1 Shear layer apparatus

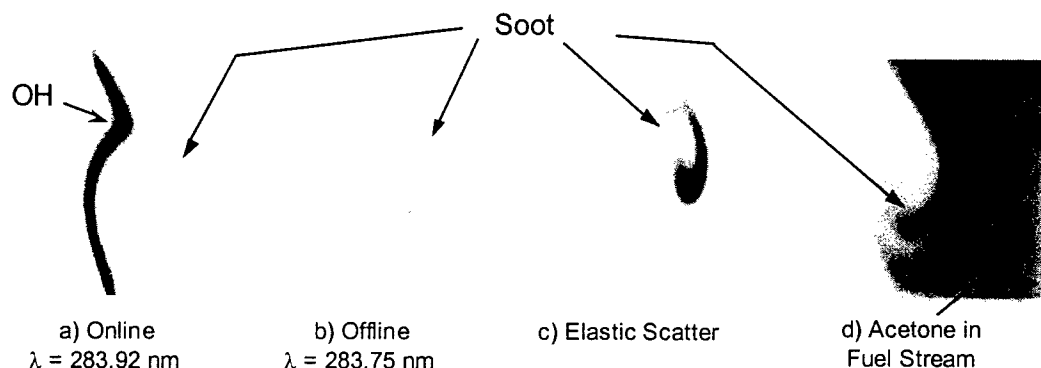


Figure 2 Signals obtained under reacting conditions with the high speed stream containing air ($U_1=2$ m/s, $T_1=400$ K) at the left and the low-speed stream containing 40% DME and 60% argon ($U_2=0.8$ m/s, $T_2=300$ K) at the right. Dark regions indicate stronger signals.

reacting conditions with the laser tuned off the OH transition, see Fig. 2.d. The acetone PLIF filtering scheme does not discriminate broadband fluorescence from LII. In Fig. 2.d the flat field of uniform intensity at the right is the acetone fluorescence. Near the core of the vortex there is a high intensity signal that is spatially separated from the acetone fluorescence. Based on the previous findings, it is believed that this is the LII signal. The low intensity region seen between the LII and the acetone fluorescence corresponds to the location where the parent fuel has come in contact with the hot products and undergone pyrolysis. Upon closer inspection it can be seen that the soot signal forms a connected region that borders the acetone signal.

Upon examination of the entire set of images for both propane and DME flames it was discovered that the LII signal was always present, and spatially separated from the OH region such that it could be clearly distinguished. The LII signal was also found to be an excellent marker of the parent fuel entrainment and of the internal structures of the mixing layer. As a result, the collection filter combination for a particular case was chosen to provide the best visualization of both the OH and LII.

Shown in Fig. 3 is a schematic illustrating the dominant features for both the air high-speed (AHS) and fuel high-speed (FHS) cases. These cases have identical inlet conditions, except that the high- and low-speed compositions are switched. In both FHS and AHS cases the mixing layer appeared to consist of two regions: a high temperature reaction zone with a fairly laminar appearance found on the oxidizer side of the mixing layer and an 'internal' mixing layer

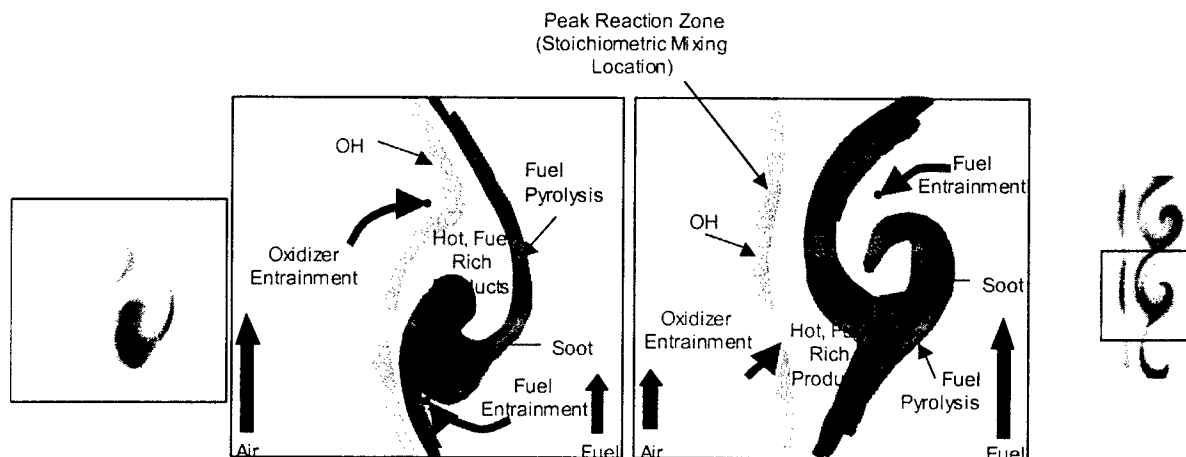


Figure 3 Schematic of the mixing layer structure for air on the high speed (left) and fuel on the high speed (right). Conditions are the same as Figure 2 except the fuel was propane.

in which products mix with pyrolyzed fuel in a manner reminiscent of a non-reacting two-stream mixing layer. The reaction zone seems only mildly influenced by the dynamics of the mixing layer. However, the processes affecting soot formation appear closely tied to the behavior of the mixing layer with a strong dependence upon the motion of the structures.

Figure 4 shows a direct comparison of the AHS and FHS operation with the non-reacting case shown as a reference. As in previous images, the OH signal is found to the left and the LII signal is found to the right. It is evident that the AHS cases have a much larger structure spacing than the FHS cases, and that the non-reacting case is intermediate to the two limits. This was a consistent result for all of the data sets acquired. Changes in the state of the high-speed boundary layer were unable to explain the magnitude of the effect that was observed.

The cause for the observed change in the observed instability wavelength is believed to be the result of the effective density profile that results from the combustion heat release. Since the stoichiometric mixture fraction is low, the flame will always be located on the air side of the mixing layer. In the AHS case this causes the high-speed stream to have a lower density, and in the FHS case the low-speed stream density will be lower. A linear stability analysis performed by Trounev *et al.*¹, in which a hyperbolic tangent profile was assumed for both the inlet velocity and density profiles, showed that the low-density high-speed configuration produces an increase in instability wavelength, while the low-density low-speed configuration produces a decrease in the instability wavelength. This is consistent with the results shown in Figure 4.

The effects of heat release are expected to change the vorticity dynamics of the structures as well as modifying the gas properties of the mixing layer. However, to a first order, the dilation effect in vorticity reduction and the increase in viscosity associated with the heat release from the combustion are the same for the FHS and AHS cases (the adiabatic flame temperature is identical in both cases). While these effects, long considered to be important in jet flames, are believed to be important in both FHS and AHS cases, they do not account for the large differences in the instability wavelength.

The effect of tripping the high-speed boundary layer was found to have little discernible effect on the reacting structure (space constraints limit this discussion), but strongly affected the passive scalar results. Thus, the initial Kelvin-Helmholtz instability appears to be enhanced by the heat release.

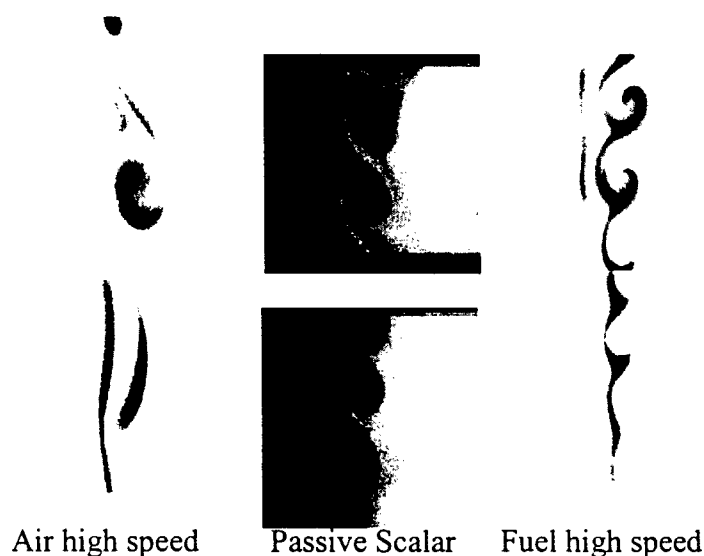


Figure 4 Comparison of reacting cases with non-reacting passive scalar images at the same inlet conditions. The air is on the left side in all images. The images are from positions A (lower) and B (upper) and the conditions are the same as Figure 3.

¹ Trounev, A., Candel, S.M. and Daily, J.W. AIAA Paper 88-0149, (1988).

STATISTICAL INTERPRETATION OF POWER SPECTRAL DENSITIES MEASURED BY PICOSECOND TIME-RESOLVED LASER-INDUCED FLUORESCENCE IN TURBULENT NONPREMIXED FLAMES

AFOSR Grant Number F49620-00-1-0017

Principal Investigators: Normand M. Laurendeau, Galen B. King and Jay P. Gore

School of Mechanical Engineering, Purdue University, West Lafayette, IN 47907-1288

SUMMARY/OVERVIEW

This research is concerned with the application of time-series measurements for minor-species concentrations to turbulent nonpremixed flames, so as to better understand scalar fluctuation rates. In the previous report, measurements of OH and CH concentrations were presented for jet diffusion flames composed of H₂, CH₄, and N₂. The fluctuations in the time series were generally well characterized by only the integral time scale. In this report, a stochastic model based on the laminar flamelet concept is presented which can predict these integral time scales. Improvements over a prior version of this model and a more systematic application to the previous H₂/CH₄/N₂ flames permit a reasonable prediction of the experimental trends. An application of this model to extrapolating mixture fraction statistics is discussed.

TECHNICAL DISCUSSION

Measurements of minor-species concentrations in turbulent flames are of interest owing to their importance in pollutant chemistry and to their use as markers of instantaneous flame structure. Time-scale information can be provided by scalar time series when measurement repetition rates are sufficiently fast to resolve turbulent fluctuations. This approach has been demonstrated for many scalars, including the concentrations of CH¹ and OH². These time series of minor-species concentrations are recovered by use of picosecond time-resolved laser-induced fluorescence (PITLIF), which directly accounts for potential variations in both the electronic quenching rate coefficient and the background flame emission.

In the previous report, concentration measurements were reported for OH and CH in seven jet diffusion flames with a fuel composition of 33.2% H₂, 22.1% CH₄, and 44.7% N₂ (by volume), burner diameters of 3.4 and 7.8 mm, and Reynolds numbers ranging from 2800 to 15,200. In the present report, a stochastic simulation is presented to predict some of the measured statistics, including the scalar integral time scale. The approach of these simulations is to assume values for certain critical mixture fraction statistics and to construct a realistic time series meeting these statistics. The probability density function (PDF) and power spectral density (PSD) were chosen as the base Z statistics since considerable information is available about their shapes. With this approach, a synthetic Z time series has the correct frequency content and the correct range of instantaneous values. A simulated mixture fraction time series was constructed using

$$Z(t_i) = \bar{Z} + \mathfrak{I}^{-1} \left\{ \sqrt{\bar{Z}^2 \tau_{i,Z} \text{PSD}_Z(f_i \tau_{i,Z})} \times e^{i\Phi(f_i)} \right\}, \quad (1)$$

¹ Renfro, M. W., King, G. B. and Laurendeau, N. M., *Combust. Flame* 122:139-150 (2000).

² Renfro, M. W., Gutfenfelder, W. A., King, G. B. and Laurendeau, N. M., *Combust. Flame* 123:389-401 (2000).

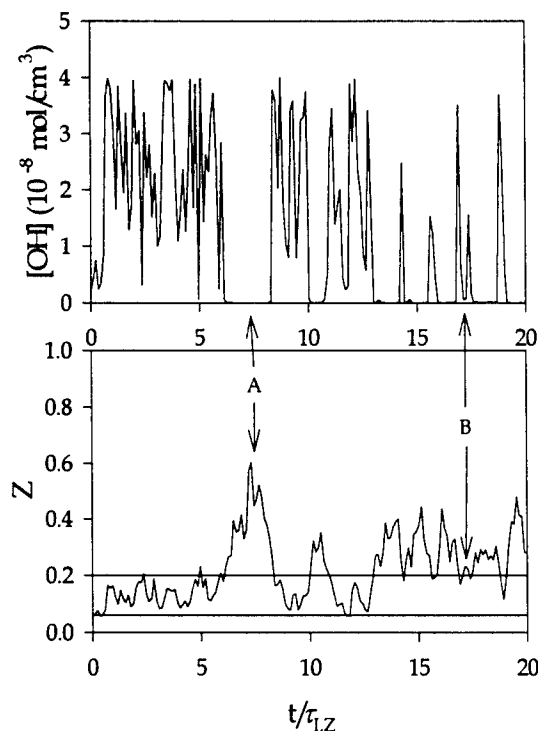


Figure 1. Sample simulated time series for OH and Z at $r/x=0.1$, $x/D=20$. Regions of scalar intermittency (A) and enhanced scalar fluctuations (B) are emphasized.

constructed using OPPDIF with GRI-2.11. The resulting scalar time series were then used to compute the mean, rms, PSD, PDF, and τ_1 for OH, CH, and number density (ND).

A sample time series for Z and OH is shown in Fig. 1, as simulated for $r/x=0.1$ at $x/D=20$. An exponential autocorrelation function and a Beta PDF are used for all of these simulations. Two reference lines on the Z time series show the limits ($Z=0.06-0.20$) beyond which negligible OH exists, based on the OH state relationship. This limited range causes several important differences between the Z and OH time series. First, the Z time series contains fluctuations outside the range $Z=0.06-0.20$ that are completely nonexistent in the scalar time series (position A). In contrast, position B shows a location where very small deviations in Z are amplified in the OH time series because they occur near the edge of the OH distribution. It is beneficial to define a scalar intermittency to aid in the interpretation of the above results. This intermittency represents the percentage of points in the time series for which the Z value falls outside the range 0.06-0.2 (for OH). This is not the same as the turbulence intermittency since reactive scalars such as OH will be zero in the presence of turbulent rich mixtures (as in region A).

The effect of increased scalar intermittency is clearly visible in the scalar PSDs. Figure 2 shows simulated Z, ND, OH, and CH PSDs for the same conditions as for Fig. 1. The ND and Z PSDs are essentially the same since the ND state relationship exists over all Z values (low scalar intermittency), but the OH and CH PSDs show an increasing change from the input Z PSD. The faster fluctuations visible in the OH and CH time series are represented in the PSDs by an extension to higher frequencies. The PSD shape is also modified at high frequencies.⁵

Figure 3 shows radial profiles of time scales for the four scalars at $x/D=20$. The ND time scales are nearly identical to the Z time scales for all radial locations except near the radial

where $Z(t_i)$ is the discrete time series, \bar{Z} is the mean, $\overline{Z^2}$ is the variance, $\tau_{1,Z}$ is the integral time scale, PSD_Z is the power spectral density shape, $\mathfrak{T}^{-1}\{f\}$ represents a complex inverse-Fourier transform, and $\Phi(f_i)$ is the phase spectrum. For the present simulations, the mean and rms are taken from curve fits to the data of Meier *et al.*³ in similar flames, and the PSD shape is computed from an exponential autocorrelation function (which is similar to the observed OH PSDs). The phase spectrum is computed randomly and $\tau_{1,Z}$ is computed from the local velocity divided by the jet momentum half-width (taken from the data of Schneider⁴). This simulated time series has a near Gaussian PDF; thus, the time series of Eq. (1) must be mapped to the chosen PDF_Z , which affects the PSD. An iterative procedure was developed to simultaneously specify both the PDF and PSD shapes for Z. For comparison to OH and CH data, the synthetic Z time series were again mapped using a one dimensional flamelet state relationship,

³ Meier, W., Barlow, R. S., Chen, Y.-L. and Chen, J.-Y., *Combust. Flame* 123:326-343 (2000).

⁴ Schneider, C., Personal Communication (2000).

⁵ Renfro, M. W., Sivathanu, Y. R., Gore, J. P., King, G. B., and Laurendeau, N. M., *Proc. Combust. Inst.* 27:1015-1022 (1998).

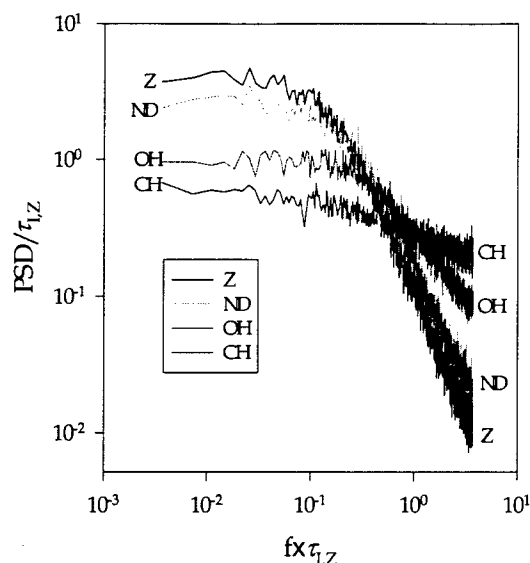


Figure 2. Predicted PSDs for ND, OH, and CH compared to the input Z PSD for the same conditions as Fig. 1.

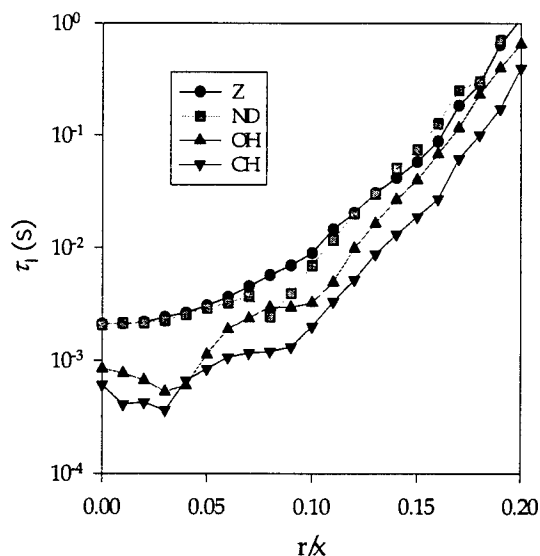


Figure 3. Predicted radial profile of scalar integral time scales compared to that for the input Z time scale using the same conditions as Fig. 1.

location of minimum average number density. For OH and CH, the scalar time scales are always lower than the input mixture fraction time scale because of the influence of scalar intermittency. Since CH has a narrower state relationship than OH, its time scale is lower than that of OH.

To assess potential errors in the prediction of the scalar time scales, each Z input was parametrically varied over a large range of conditions. The mixture fraction mean, rms, and PDF were found to significantly affect the same statistics for the predicted scalars, but the focus here is on the predicted scalar PSD and time scale. These two statistics are largely unaffected by the input mean and PDF shape for mixture fraction. In particular, the predicted radial profile for the OH time scale when using either a clipped Gaussian or Beta PDF shape are essentially the same. However, the PSD shape for each scalar is significantly affected by Z_{rms} .⁵ The PSD shape for Z does not affect the time scale profiles but is the primary factor in determining the scalar PSD shape. For a small scalar intermittency, the two are virtually identical and as the scalar intermittency increases, the scalar PSD departs from the input Z PSD (see Fig. 2 and Ref. 5).

The integral time scale for Z is not well documented in the literature for reacting jets; thus, the assumption of convective scaling may not be applicable. However, simulations of OH time scale profiles were compared for mixture fraction time scales spanning two orders-of-magnitude, and in each case, the ratio $\tau_{i,[OH]}/\tau_{i,Z}$ is unique and appears to be affected by only the scalar intermittency. The reduction in time scale caused by scalar intermittency is a convoluted function that depends on the shape of the state relationship as well as Z_{rms} .

Figure 4 shows a comparison of the OH measurements and simulations at each of the four axial heights investigated. For the simulations in the top graph, convective scaling was used for the mixture fraction time scale. Quantitative agreement between the simulations and measurements cannot be achieved because there is no basis for *a priori* selection of the proportionality constant in this scaling relationship. However, since the simulated scalar time scales depend linearly on the input time scales for mixture fraction (as demonstrated by the invariance of the scalar time scale ratios), the shapes of the profiles are a true test of the predictions. This feature is accentuated in the bottom graph of Fig. 4, where the profiles have been divided by a constant to improve the quantitative agreement with no effect on the profile shape. In general, the simulation does a good job of replicating the shape of the radial τ_i profiles. The nearly flat time-scale profile for $\Gamma < 0$ is surprising since the Z time scales decrease by a factor of two or more over this same range. Nevertheless, the laminar-flamelet approximation captures this

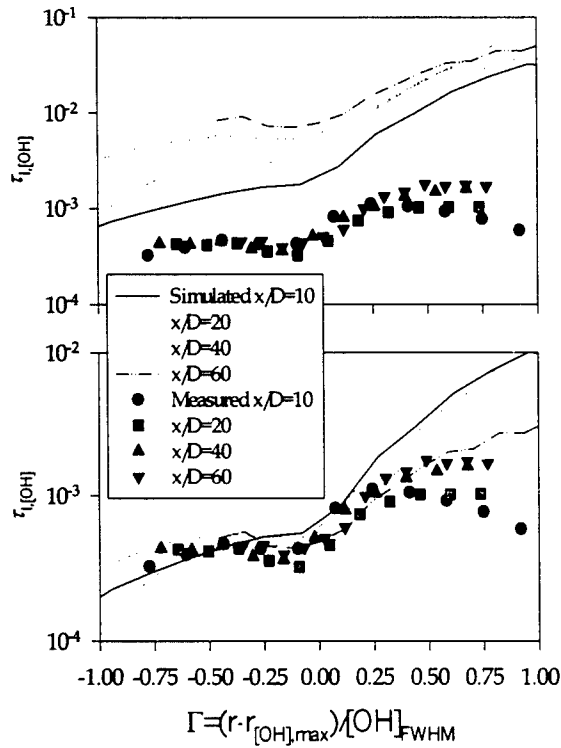


Figure 4. Comparison of predicted to measured OH integral time scale profiles. The predicted profiles in the bottom panel have been scaled but this does not alter the predicted profile shapes.

experimental trend with reasonable accuracy. However, the simulation does not capture the axial change in time scales. The measurements show that the time scale at the [OH] peak and on the fuel-side of the peak is invariant with axial height, whereas the simulation follows typical convective scaling.

Since the simulation does a good job of predicting the radial profile of the OH time scale in normalized coordinates, a reasonable extension of this technique is to extrapolate mixture fraction time statistics from the measured OH data. An estimate for the mixture fraction time scale was determined by dividing the measured OH, CH, and ND time scales by the predicted ratio $\tau_1/\tau_{1,Z}$. This was performed for each measured data point. The extrapolated mixture fraction time scales are shown in Fig. 5 for heights $x/D=20, 40$, and 60 . Included with the OH and CH data are recent number density measurements in the same flames.⁶

The number density and hydroxyl estimates for the Z time scales are independent estimates, and at each height the two calculations are nearly identical (with the exception of one point at $x/D=40$). A similar independent estimate taken from the CH data is shown for $x/D=20$, and this value is also close to the other calculations (CH data could not be collected at large x/D). A comparison of the three estimates of $\tau_{1,Z}$ cannot be made at all locations because of errors caused by entrainment of particles from the room air for the Rayleigh scattering technique⁶, and because the PSDs for CH at some locations are not represented by a single time scale¹.

For this flame, the number density should be well described by the laminar flamelet approximation, so the above simulation should yield the true Z time scale. Figure 5 also shows the convective time scales when using the measured velocity profile. Notice that the extrapolated mixture fraction profile is much shallower. Moreover, there is almost no discernable change of $\tau_{1,Z}$ with x/D for these conditions. These results suggest that for jets with heat release, the time scale cannot be simply computed as the jet width divided by local velocity.

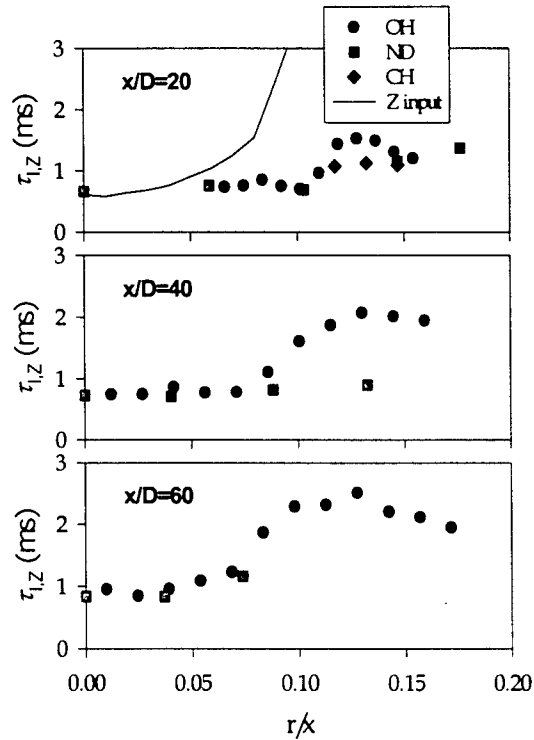


Figure 5. Extrapolated mixture fraction time scales. For each data set, the Z time scale has been computed by dividing the measured scalar time scale by the predicted time scale ratio.

⁶ Lakshmanarao, A., M. S. Thesis, Purdue University, West Lafayette, IN, 1999.

EXPERIMENTAL AND COMPUTATIONAL CHARACTERIZATION OF COMBUSTION PHENOMENA

AFOSR Task No. 93PR02COR

Principal Investigators: J. R. Gord and W. M. Roquemore

Air Force Research Laboratory
AFRL/PRTS Bldg 490
1790 Loop Rd N
Wright-Patterson AFB OH 45433-7103

SUMMARY/OVERVIEW:

Propulsions systems represent a substantial fraction of the cost, weight, and complexity of Air Force aircraft, spacecraft, and other weapon-system platforms. The vast majority of these propulsion systems are powered through combustion of fuel; therefore, the detailed study of combustion has emerged as a highly relevant and important field of endeavor. Much of the work performed by today's combustion scientists and engineers is devoted to the tasks of improving propulsion-system performance while simultaneously reducing pollutant emissions. Increasing the affordability, maintainability, and reliability of these critical propulsion systems is a major driver of activity as well. This research effort is designed to forward the scientific investigation of combustion phenomena through an integrated program of fundamental combustion studies, both experimental and computational, supported by parallel efforts to develop, demonstrate, and apply advanced techniques in laser-based/optical diagnostics and modeling and simulation. These technical approaches are applied to explore a host of fundamental combustion phenomena, including turbulent mixing, turbulence-chemistry interactions, combustion chemistry and kinetics (particularly as they apply to the formation of particulate emissions), ignition, and two-phase flow characteristics.

TECHNICAL DISCUSSION:

Providing enabling propulsion-system solutions for Air-Force applications is the primary motivator for this research effort. While improved performance can be described quantitatively in many terms (*e.g.*, specific fuel consumption, thrust-to-weight ratio, etc.), it often involves efforts to increase heat release during the combustion process. Improvements may be achieved as well by reducing the length and/or weight of the combustor through informed design decisions. Engine emissions that might adversely impact the environment and the military signature of Air-Force systems must be reduced while striving to improve performance. Judicious design and control of the combustor can significantly impact the affordability, maintainability, and reliability of the propulsion system by extending the useful life of engine components or by permitting the incorporation of less-expensive materials in combustor construction, for example. Pursuing these goals requires a thorough understanding of the fundamental physics and chemistry of combustion processes.

While this AFOSR-funded program involves numerous ongoing investigations designed to address these goals, just a few recent advances are described in this abstract. Specific activities cited include continuing development of terahertz-radiation ("T-ray") systems for combustion studies in the far infrared and exploration of vortex-flame interactions with emphasis on application to the design and development of vortex-based ignition schemes.

Far-Infrared Measurements with Terahertz Radiation. Terahertz radiation falls energetically between the far-infrared and microwave spectral regions. While some basic spectroscopy has been achieved at terahertz frequencies in the past using evacuated far-infrared instruments or microwave devices, this region remains a largely "undiscovered" spectral territory dominated by molecular rotational transitions; however, that territory is being rapidly developed as an explosion of new terahertz-radiation research is fueled by the availability of coherent sources and time-gated detection techniques.^{1,2}

There exist numerous potential advantages of T-ray technology over combustion measurements in the visible and ultraviolet regions of the spectrum. Many species of interest do not possess electronic transitions suitable for detection using techniques such as laser-induced fluorescence; however, many molecules of interest do possess suitable rotational transitions in the terahertz region. As compared to the ultraviolet and the visible, effects due to scattering, optical thickness, and beam steering are typically reduced in the far-infrared due to the wavelength dependence of scattering cross sections and the characteristics of the real and imaginary components of the wavelength-dependent refractive index. Indeed, combustor flowfields that are nearly opaque in the visible region of the spectrum may transmit sufficient terahertz radiation from a coherent source to permit detection and analysis. Our preliminary studies reveal that soot and liquid fuels (JP-8 and JP-8+100 aviation fuels, for example) are largely transparent in the terahertz spectral region. These observations suggest the possible utility of T-ray technology in real-world combustors that exhibit high pressures, significant optical depth, fuel droplets and sprays, and potentially substantial soot loadings.

T-rays may also represent a solution to many optical-access and geometric constraints imposed by real-world propulsion systems. Many production combustors are not easily modified for access to detection techniques based on visible or ultraviolet radiation. Even when such modifications are possible, complicated geometries can make analysis of visible signals difficult. Advantageous transmission characteristics driving other T-ray imaging applications may be of value when performing combustion measurements. Many solid materials that are opaque in the ultraviolet, visible, or near-infrared regions of the spectrum exhibit transparent bands at frequencies near one terahertz.³ This information suggests that it may be possible to study certain "windowless" combustors without installing glass, quartz, or sapphire windows when using terahertz radiation.

To explore the potential diagnostics utility of T-ray technology while building on Grischkowsky's pioneering combustion work,^{4,5} we recently teamed with Picometrix, Inc., and

¹ M. C. Nuss and J. Orenstein, "Terahertz Time-Domain Spectroscopy," in *Millimeter and Submillimeter Wave Spectroscopy of Solids*, G. Gruner, Editor, Springer (1998).

² An excellent terahertz-radiation tutorial is available at <http://elec-engr.okstate.edu/thzlab/>, and a long list of links is available at <http://www-ece.rice.edu/~daniel/groups.html>.

³ D. M. Mittleman, M. Gupta, R. Neelamani, R. G. Baraniuk, J. V. Rudd, and M. Koch, "Recent Advances in Terahertz Imaging," *Applied Physics B*, Vol. 68, p. 1085 (1999).

⁴ R.A. Cheville and D. Grischkowsky, "Observation of Pure Rotational Absorption Spectra in the ν_2 Band of Hot H₂O in Flames," *Optics Letters*, Vol. 23, pp. 531-533 (1998).

⁵ R.A. Cheville and D. Grischkowsky, "Far Infrared, THz Time Domain Spectroscopy of Flames," *Optics Letters*, Vol. 20, pp. 1646-1648 (1995).

Innovative Scientific Solutions, Inc., to construct and demonstrate T-ray systems based on traditional delay-line schemes and asynchronous optical sampling (ASOPS).^{6,7}

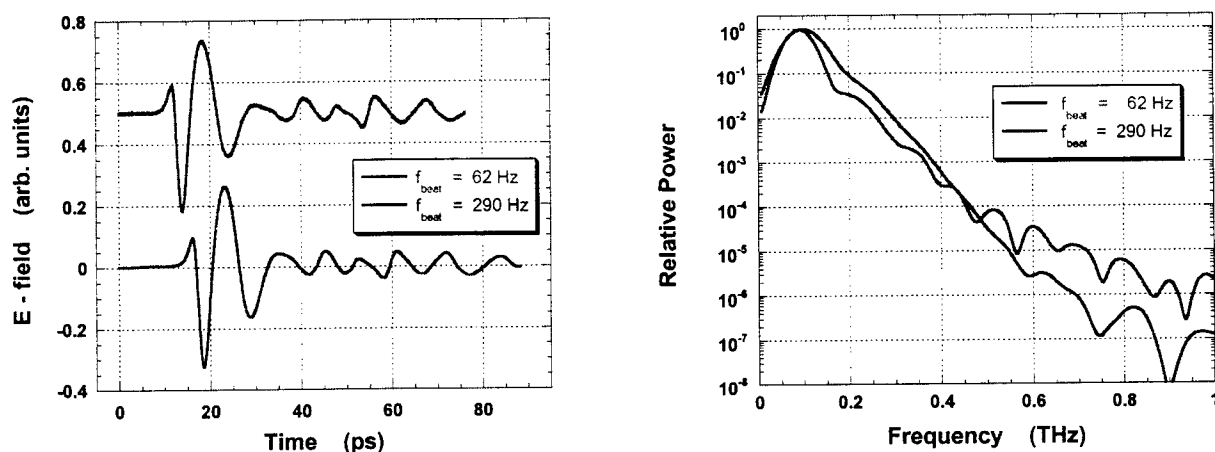


Figure 1. Time and frequency domain representations of the T-ray source spectrum.

Time-domain terahertz signals and the corresponding T-ray source spectra obtained by Fourier transformation are depicted in Fig. 1. These data were acquired at ASOPS beat frequencies of 62 and 290 Hz. (The ASOPS beat frequency describes the rate at which the optical delay is swept through the full free temporal range defined by the nominal laser repetition rate. In this case, the delay between the pulses is swept from zero to twelve nanoseconds at the rates identified above.) These signals were acquired for T-ray transmission through room air. Transmission and absorption spectra obtained in room air and a hydrogen-fueled Hencken flame are depicted in Fig. 2. These data reveal water's strong terahertz absorption features. Extensive signal averaging over the course of many seconds was required to achieve the signals depicted in these figures. Since this signal averaging impacts data-acquisition rates, ongoing efforts are devoted to improving sensitivity and system bandwidth. Continuing combustion experiments and efforts aimed at exploring transmission through various ceramics are underway as well.

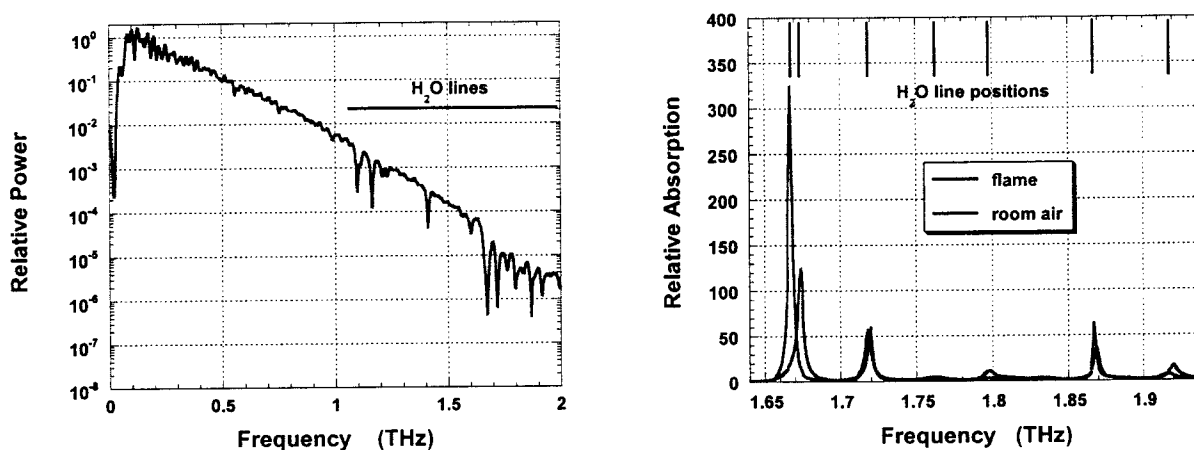


Figure 2. Terahertz spectra obtained in room air and in a hydrogen-fueled Hencken flame.

⁶ G. J. Fiechtner, G. B. King, and N. M. Laurendeau, "Quantitative Concentration Measurements of Atomic Sodium in an Atmospheric Hydrocarbon Flame with Asynchronous Optical Sampling," *Applied Optics*, Vol. 34, p. 1117, (1995).

Combustion in Impulsively Initiated Vortex Rings. Preliminary studies of reacting, premixed vortex rings have shown that flame propagation is highly sensitive to ignition timing, equivalence ratio, and vortex strength. During this investigation, a variety of divergent phenomena have been observed, including interior/exterior flame propagation, vortex-induced flame bridging across the jet column, annular extinction, flame-induced wrinkling, and the formation of unburned pockets. We have used planar laser-induced fluorescence of acetone, CH, and OH to study the non-reacting, reacting, and post-flame regions, respectively. Particle-image velocimetry has been used to measure the corresponding hydrodynamic conditions and establish input parameters required for direct numerical simulation. The flowfield includes well-characterized vortex rings of premixed methane and air generated at the exit of an axisymmetric nozzle using a solenoid-driven piston. Ignition is initiated at various phases of vortex development and propagation. PLIF data are being acquired for comparison with corresponding numerical simulations achieved with UNICORN, a time-dependent computational fluid dynamics code with chemistry. Time-resolved PLIF image sequences revealing the impact of post-actuation spark timing on vortex combustion are captured in Fig. 3. Similar parametric studies have been achieved to explore the impacts of equivalence ratio and vortex strength (as determined by piston stroke length) on combustion of the vortex.

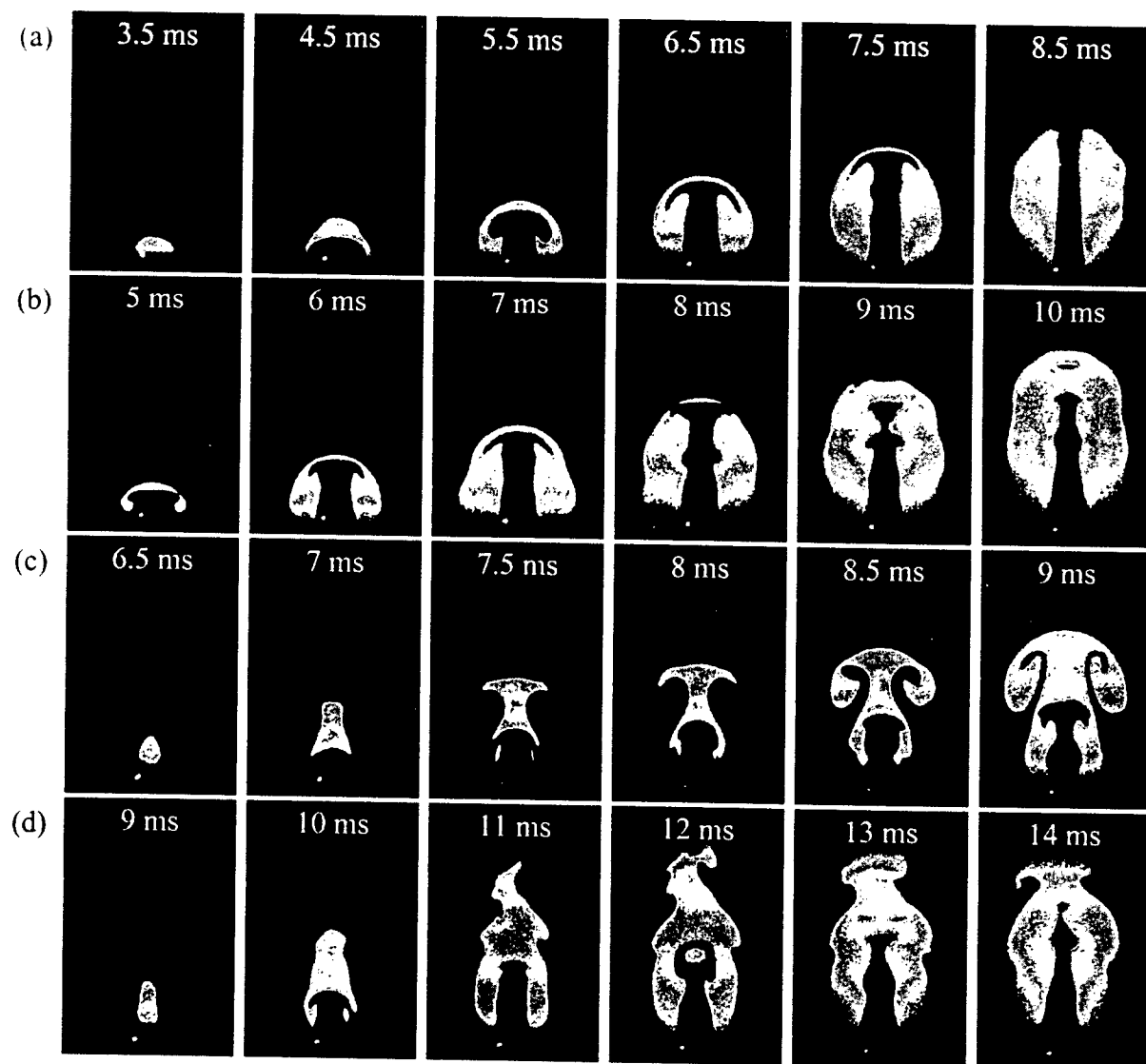


Figure 3. OH PLIF image sequence for spark timings of (a) 2.5 ms, (b) 4 ms, (c) 6 ms, and (d) 8 ms after piston actuation. Equivalence ratio is 1.0 and piston stroke is 3.3 mm.

CONCURRENT RESEARCH ON HIGH GRAVITY (G) COMBUSTION AND ENABLING MATERIALS

(LRIR: 99PR12ENT)

Principal Investigator(s): Dr. W. M. Roquemore (PR); Dr. R. J. Kerans (MLLN)

AFRL/PR, Bldg 490
1790 Loop Road North
WPAFB OH 45433-7103

SUMMARY/OVERVIEW:

This is a joint program between MLLN and PRTS. Fundamental combustion and materials science issues are being investigated that will lead to the development of a revolutionary propulsion system that operates on a highly efficient near-constant temperature (CT) cycle instead of the constant pressure cycle of today's engines. A key technology essential for the development of a propulsion system that operates on a CT cycle is an ultra-compact inter-turbine burner (ITB) that will efficiently add heat between the turbine stages and is constructed of advanced, lightweight ceramic-matrix composites (CMC) materials.

TECHNICAL DISCUSSION

Experiments have been conducted in an instrumented, small-scale, axi-symmetric, atmospheric pressure laboratory combustor with an outer circumferential cavity in which the flame is stabilized by a highly accelerated swirled flow. The swirl is generated by air jets around the outer wall of the cavity. Estimated g-loading in this cavity is $\sim 1000g$. Fuel is introduced into the cavity by pressure atomizing nozzles. Unswirled air flows down the center of the combustor with approximately 4x the mass flow rate of that introduced into the cavity. Observed flame lengths in this combustor are significantly shorter than those observed in a conventional swirl stabilized gas turbine combustor at similar equivalence ratios. These shorter flame lengths were achieved with no penalty to combustion efficiency; combustion efficiencies of +99% for both ethanol and JP-8 fuels were observed over a wide range of operating conditions and Longwell Parameters down to $O(10^7)$. High efficiencies have been observed for cavity equivalence ratios up to $\phi_{cav} > 2$ and overall equivalence ratio of $\phi_{cav} \approx 0.6$. Lean blowout occurs as low as $\phi_{cav} = 0.5$ in the cavity. These combustion results have been recently reported by R. A. Anthenien et al. in a paper entitled "Experimental Results for a Novel, High Swirl, Ultra Compact Combustor for Gas Turbine Engines" at the 2nd Joint Meeting of the U. S. Sections of the Combustion Institute, Oakland CA, 25-28 March 2001. Background information on this program will be presented in the Tuesday afternoon section on combustion and materials.

ABSTRACTS OF WORK UNITS NOT PRESENTED AT THE MEETING

IMPROVED MODELING OF DROP VAPORIZATION AND COMBUSTION IN DIESEL SPRAYS

(ARO Grant No. DAAG 55-98-1-0442)

Principal Investigator: John Abraham

Maurice J. Zucrow Laboratories
School of Mechanical Engineering
Purdue University
West Lafayette, IN 47907

SUMMARY/OVERVIEW

This program focuses on modeling the vaporization liquid drops and the penetration of the liquid phase in Diesel sprays under cold-start conditions. This work is carried out within the framework of multidimensional modeling of the physical processes in Diesel engines. In the prior reporting period, it was shown that though vaporization of the drops under warm operating conditions may be mixing controlled whereby the drop vaporization characteristic time is much shorter than the mixing time, the vaporization rate under cold-start conditions may not be assumed to be mixing controlled. Hence, drop size effects have to be considered under cold-start conditions. In this work, a drop vaporization model under high pressure conditions is included within the context of a locally homogeneous flow assumption.

TECHNICAL DISCUSSION

Under warm operating conditions in a Diesel engine, the chamber temperature would be about 1000 K or higher, and densities would be in the range of $15\text{--}30\text{ kg/m}^3$. During cold start, the temperature may be less than 800 K and the densities lower than 15 kg/m^3 . Under such conditions, the characteristic time of drop vaporization may be longer than the characteristic time associated with mixing in the spray. Hence, the accuracy of drop vaporization models that predict the vaporization characteristic times becomes an important factor in predicting spray penetration and fuel-air mixing when employing multidimensional models.

A summary of prior work on this topic as part of this research program will now be given. Several findings have been made. It has been shown that supercritical droplet vaporization is not likely to occur in Diesel engines under warm operating conditions and even less likely under cold-start conditions [1]. A phenomenological model for multicomponent droplet vaporization has been developed, implemented in the multidimensional code and computations carried out [2]. Under cold-start conditions the distribution of the different components of the fuel species may be different, and it may be important to include such effects in predictive models. But, this effect is not important under warm operating conditions. It has also been shown that the simplified models for droplet vaporization that are employed in multidimensional codes such as KIVA overpredict the droplet vaporization by about 30% under warm operating Diesel conditions [1]. This difference is not a factor that affects liquid vaporization in Diesel sprays under warm operating conditions when the vaporization characteristic times are much shorter than the mixing

characteristic times [3-5]. Under cold-start conditions, the vaporization times become of the same order or longer than the characteristic mixing times. Under such conditions, it is essential to model drop vaporization processes with adequate accuracy. It has also been shown that, from the point of employing droplet vaporization models in multidimensional models, a severe limitation is related to the inability to employ adequate grid resolution in the region close to the orifice [6-7]. This limitation arises as a result of employing the Lagrangian Drop Eulerian Fluid (LDEF) approach to modeling the liquid drops and makes it difficult to assess the accuracy of vaporization models by employing multidimensional models.

To overcome the limitation highlighted above, a locally homogeneous flow (LHF) approximation was employed to model the sprays and study the physics [4, 8]. In this case, adequate resolution can be employed. Figure 1 shows a typical grid employed for the computations whose results are presented below. The grid employed for the LDEF computations and the LHF computations are shown. It may be seen that with the LHF computations, grid sizes of an order of magnitude greater than for the LDEF computations may be employed. In the LHF approximation, it is assumed that the liquid and gas velocities are identical. This assumption is reasonable when injection velocities are over 300 m/s, the drop sizes are of the $O(10\ \mu\text{m})$ or less and the Stokes numbers are small. In prior work that has been discussed in the literature, a model for drop vaporization has not been included within the LHF formulation [4]. Vaporization has been assumed to be mixing controlled. In this work, we have developed an approach to include drop size effects and, hence, drop vaporization under high pressure conditions within the formulation of the LHF model. This may then be employed to study Diesel spray and vaporization characteristics under cold-start conditions [5].

Results are shown below when this vaporization model is employed for Diesel sprays. Figure 2 shows computed and measured overall spray penetration characteristics over a wide range of ambient densities. The measurements are those reported by Naber and Siebers [9]. It may be seen that the computed and measured penetrations show agreement within 5% for the range of conditions considered. Figure 3 shows computed and measured entrainment velocities in a spray at three axial locations as function of time after start of injection. The measurements are those reported by Cossali et al [10]. Again, the trends agree and there is quantitative agreement within 25%. Figure 4 shows computed and measured liquid penetrations in a Diesel spray when the injection pressure is changed. The Lagrangian-Drop-Eulerian-Fluid (LDEF) approach and the LHF approach with droplet vaporization effects are employed to compare the computed results with the measured ones. The measurements are those reported by Siebers [3]. Results for ambient densities of $30.2\ \text{kg/m}^3$ and $7.2\ \text{kg/m}^3$ are shown. The LDEF results are shown for the case with ambient density of $30.2\ \text{kg/m}^3$. It is seen that the computed results with the LDEF approach do not agree with the measured trends, but the results obtained with the approach developed here do give trends comparable to the measured trends. Figure 5 shows measured and computed liquid penetrations when the chamber density is changed. The figure shows two computed curves: One is obtained with the LHF model with the mixing controlled model for vaporization and the second one with the high pressure vaporization model developed here. It may be seen that the results with the vaporization model show trends that agree with the measured trends. Figure 6 shows computed and measured steady liquid penetrations as a function of ambient temperature for two different values of ambient density. Adequate agreement in trends is shown.

ACKNOWLEDGMENTS

Graduate students Venkatraman Iyer and Scott Post have contributed to the work described in this abstract.

REFERENCES

1. Abraham, J. and Givler, S.D., "Conditions in which Vaporizing Fuel Drops Reach a Critical State in a Diesel Engine," SAE Trans., 108, 601-612, 1999.
2. Abraham, J. and Magi, V., "A Model for Multicomponent Droplet Vaporization in Sprays," SAE Trans., 107, 603-613, 1998.
3. Siebers, D.L., "Liquid Phase Fuel Penetration in Diesel Sprays," SAE Paper 980809, 1998.
4. V. Iyer, S. Post, and J. Abraham, "Is the Liquid Penetration in Diesel Sprays Mixing-Controlled?" To appear in Proceedings of the Combustion Institute, Vol. 18, 2000.
5. Iyer, V., Magi, V. and Abraham, J., "Exploring Injected Droplet Size Effects on Steady Liquid Penetration in a Diesel Spray with an LHF Model," submitted to Intl. J. Heat and Mass Transfer, 2001.
6. Abraham, J., "What is Adequate Resolution in the Numerical Computations of Transient Jets?" SAE Trans., 106:141-155, 1997.
7. Aneja, R. and Abraham, J., "How Far does the Liquid Penetrate in a Diesel Engine: Computed Results vs. Measurements?" Combust Sci. Tech., 138:233-255, 1998.
8. Faeth, G.M., "Mixing, Transport and Combustion in Sprays," Prog. Energy Combust. Sci., 13:293-345, 1987.
9. Naber, J.D. and Siebers, D.L., "Effects of Gas Density and Vaporization of Penetration and Dispersion of Diesel Sprays," SAE Paper 960034.
10. Cossali, G.E., Berloano, A., Coghe, A. and Brunello, G., "Effect of Gas Density and Temperature on Air Entrainment in a Transient Diesel Spray," SAE Paper 96082, 1996.

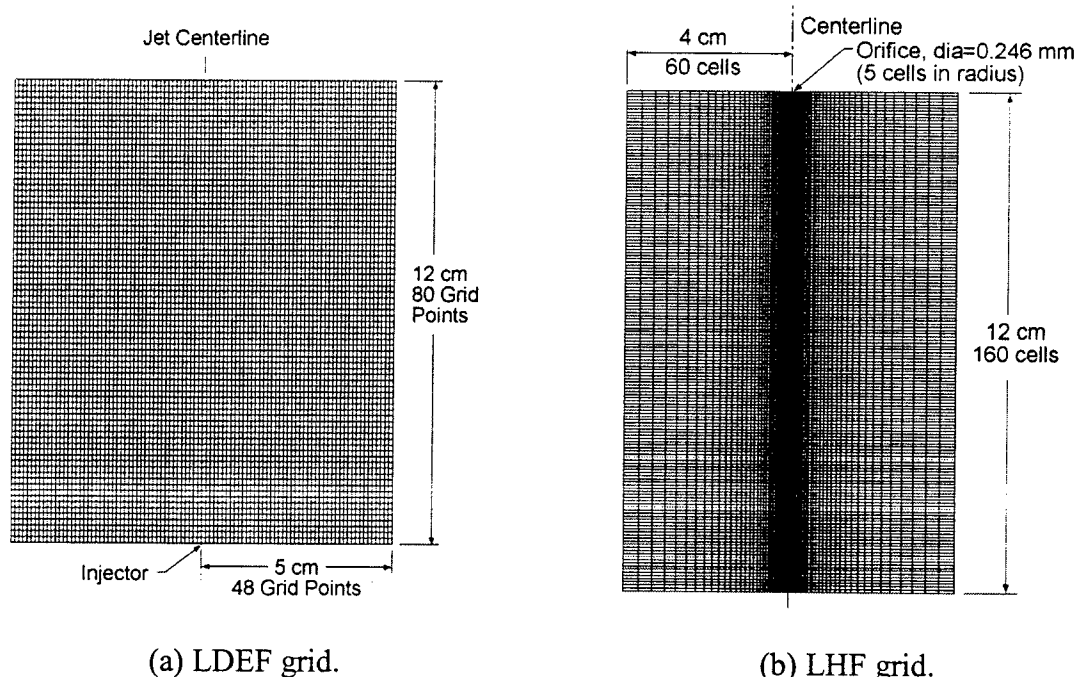


Figure 1. Computational grid.

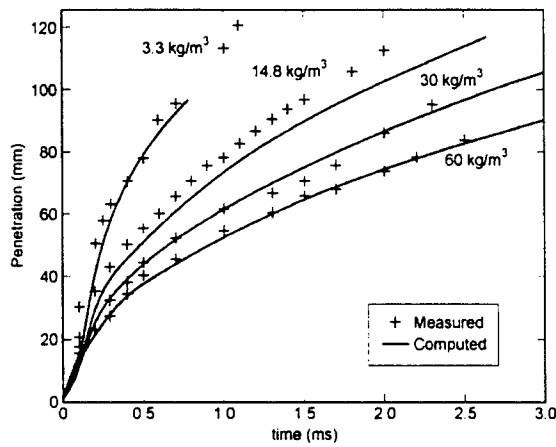


Figure 2. Spray penetration vs. time after start of injection.

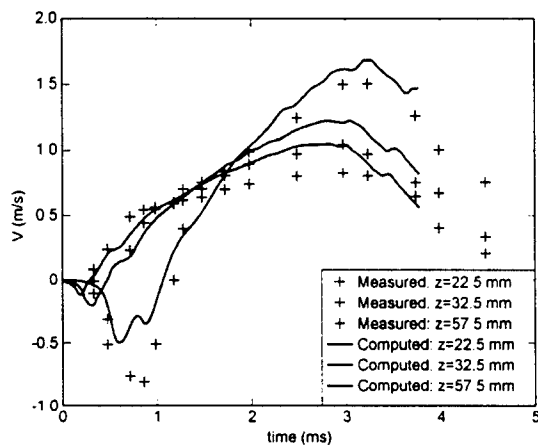


Figure 3. Computed and measured entrainment velocities as a function of time after start of injections. ($T=298$ K, $\rho=7.02$ kg/m³, $U_{inj}=230$ m/s)

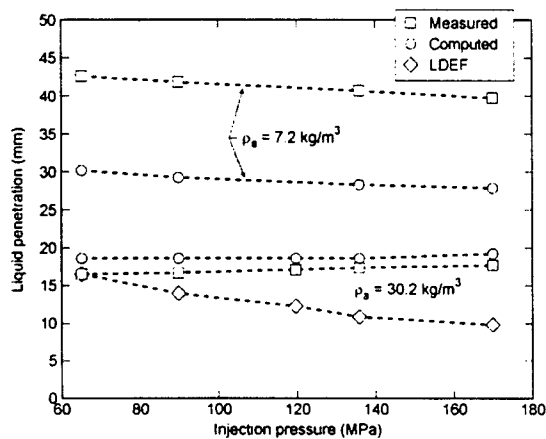


Figure 4. Liquid penetration vs. injection pressure. ($T_a=1000$ K, $d_{orif}=0.25$ mm)

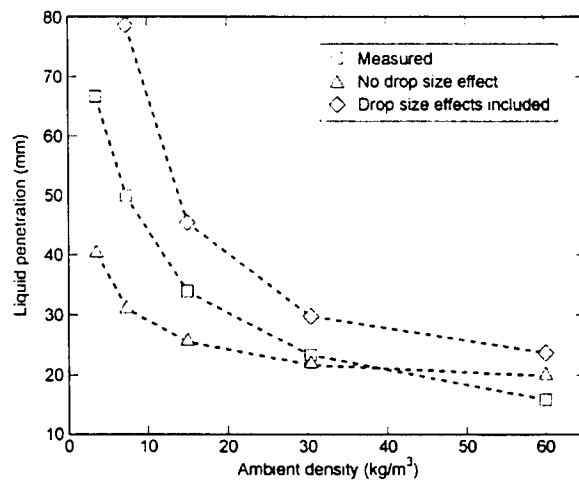


Figure 5. Liquid penetration vs. ambient density. ($T_a=850$ K, $P_{inj}=136$ MPa)

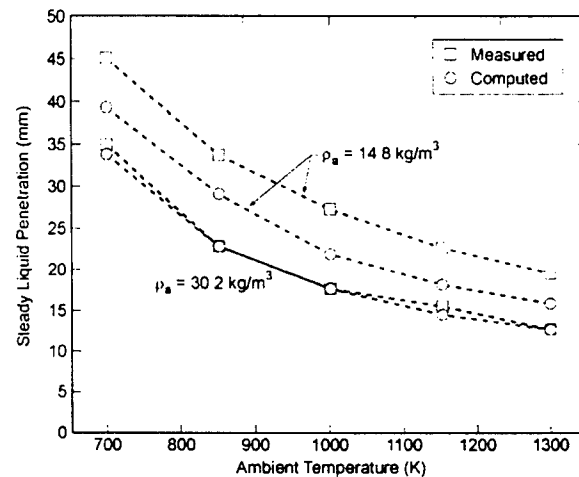


Figure 6. Liquid penetration vs. ambient temperature. ($\rho_a=30.2$ kg/m³, $P_{inj}=136$ MPa, $d_{orif}=0.25$ mm)

LARGE EDDY SIMULATIONS OF SUPERCRITICAL MULTICOMPONENT MIXING LAYERS

(Contract Number: AFOSR-ISSA-00-0012)

(ARO Proposal Number 41116-EG)

Principal Investigator: Dr. Josette Bellan

Jet Propulsion Laboratory
California Institute of Technology
4800 Oak Grove Drive
MS 125-109
Pasadena, Ca 91109-8099

SUMMARY/OVERVIEW:

The objective of this study is the fundamental understanding of fuel disintegration and mixing in a supercritical environment (relative to the fuel) in order to determine parameter regimes advantageous to mixing. The approach is based on developing a model of a supercritical, turbulent jet mixing with surrounding fluid. The method is one that combines the modeling of supercritical fluids with a systematic development based on the Large Eddy Simulation (LES) approach. This systematic development includes a consistent protocol based upon Direct Numerical Simulations (DNS) for developing a Subgrid Scale Model (SGS) appropriate to supercritical fluids, rather than choosing in an ad hoc manner an existing SGS model developed under assumptions inconsistent with supercritical fluid behavior. This SGS model will be used in the LES of a supercritical turbulent jet.

TECHNICAL DISCUSSION

The first step in this effort consisted in the development of a DNS and associated code for a supercritical shear layer. The shear layer is chosen as the simplest configuration from which one may obtain results that will establish, through DNS, a framework for understanding mixing of supercritical fluids at small scales. Because the turbulent behavior at the Kolmogorov scales is universal (i.e. geometric-configuration independent), once this behavior is determined (e.g. in a shear layer geometric configuration), it can be utilized to model a variety of geometric configurations (for the same fluids) having the same physics. Since the interest of AFOSR is in hydrocarbons, the chosen shear layer is that of heptane (lower stream) in nitrogen. Having conducted preliminary investigations in which the layer did not reach transition (Miller et al., 2001), and having analyzed the causes for the lack of transition (Okong'o and Bellan, 2000a), the activities were further focused on obtaining one or several transitional states and analyzing their behavior. To this end, there were several areas of emphasis:

(i) The real-gas boundary conditions of Okong'o and Bellan, 2000b (OB00jcp) were utilized in the DNS code and two simulations were conducted differing only by the value of the initial Reynolds number; the wavelength of the initial forcing was the typical one from the incompressible stability analysis. The results were documented in Okong'o and Bellan, 2000c (OB00jfm).

The transitional state was identified by global manifestations such as rapid and sustained momentum thickness growth, high rate of positive spanwise vorticity evolution, increased enstrophy, large product thickness, and large momentum thickness based Reynolds number. Analysis of the vorticity and vorticity magnitude budgets at transition highlighted the dominance of the stretching and tilting effect in the production of spanwise vorticity, and of the viscous contribution in the vorticity magnitude, although at some crosstream locations stretching and tilting exceeded viscous effects.

Visualizations of the spanwise vorticity at the transitional state revealed considerable local positive vorticity both in the braid and between the braid planes. Furthermore, visualizations of the magnitude of the density gradient displayed concentrated regions of high values exhibiting a convoluted and distorted appearance; these regions may be optically identifiable owing to the change in the index of refraction. Given the commonality of distinctive optical features between temporal and spatial shear layers, the observation of such regions in supercritical jet experiments provided encouragement that the essence of the situation has been captured. Analysis of the fluid composition in these regions of high density gradient magnitude revealed that the predominant species is that in the lower, entrained stream with small amounts of the entraining fluid transported and dissolved into it. Moreover, considerations based on the value of the mass diffusion factor identified these regions to contain a highly non-ideal mixture, implying mixing difficulties at the molecular level resulting from the thermodynamic properties of the mixture. Visualizations of the compression factor displayed large departures from perfect gas behavior in the lower heptane stream as well as in the layer.

The issue of the thermodynamic state of the mixture at transition was also explored through examination of departures from the critical locus both in the braid and between braid planes. The fluid was supercritical everywhere, as the temperature was always larger than that of the local critical point. However, the pressure was above the local critical point outside and below the local critical point inside the vortices, with the critical locus mapping the coherent vortices. The considerable reduction in the difference between the local values of the pressures and critical pressure inside the vortices was due to the change in fluid composition.

To investigate the primary mechanisms responsible for dissipation both during the evolution of the layer and at transition, the irreversible entropy production was calculated and analyzed. The three contributions to the dissipation arising from viscous stresses, species fluxes and heat fluxes were calculated and compared. Volume averages as well as RMS were computed at time stations after the second pairing, but prior to transition, and at transition. Moreover, by filtering the DNS solution and calculating the difference between the filtered and unfiltered variables, the contribution of the small scales (SGS) was evaluated. The overwhelming SGS contribution both to the average and the RMS is due to viscous effects, and the SGS activity is also dominated by viscous effects.

Since the transitional state was dominated by viscous effects, one could argue that the above conclusions are universal, i.e. independent of the species and only governed by the supercritical state. Such an argument may be in error since some of the important aspects of the transitional state, such as the fluid composition in the high magnitude density regions may be a result of the mixture thermodynamics. Ascertaining the species independent aspects of supercritical mixing layer behavior will constitute one of our future priorities.

Assumed PDF modeling, of particular interest for reacting flow representations, was shown to have only limited potential. Neither the beta-density nor the Gaussian PDF, both constructed using the DNS calculated moments, predicted reliably the mixing process or the transitional state, respectively. The same result was found at the subgrid scale. Moreover, the temperature and partial density PDFs were well (negatively) correlated, indicating that the

possible modeling of the reaction rate, which is a joint temperature-species PDF, by the product of the marginal PDFs holds poor prospects. This good correlation was obtained both for the DNS scale PDF and the SGS scale PDF (the filtered density function of Pope, 1991). Finally, it should be mentioned that the conclusions regarding the PDF representation are the result of studying only two realizations. It was realized that additional work is necessary to obtain more definitive conclusions.

(ii) The investigation described in (i) indicated the need for additional realizations of transitional states. However, each DNS simulation is very computationally intensive, and thus a good strategy was deemed necessary to minimize computational costs. Therefore, a linear inviscid stability analysis for real gas was conducted with the goal of finding other forcing wavelengths that perhaps promote quicker transition. The results of the stability analysis and the ensuing simulations were documented in Okong'o and Bellan, 2001. Two-dimensional (2D) stability results showed that the unstable growth rates for the compressible flow are smaller at all wavenumbers than the equivalent growth rates found from an incompressible analysis; also, the most unstable wavelengths occurred at smaller wavenumbers with increasing density stratification. 2D mixing layer simulations showed that at the same initial mean flow conditions the solution is virtually independent of the excitation wavelength. This observation raised the alluring prospect of finding the shortest streamwise compressible unstable wavelength at which rollup and pairing could be obtained in three-dimensional (3D) simulations; for such a wavelength, the size of the domain could be reduced (since it is four times the perturbation wavelength) leading to a reduced number of grid points for the same resolution. However, in contrast with the 2D problem where for each wavelength there is a single eigenvalue (i.e. propagation speed), in 3D it was found that additional to the wavelength of the perturbation, the angle of the wave direction in the streamwise-spanwise plane must be specified as well. To minimize the wavelength of the spanwise perturbation, it was shown that one must maximize the angle representing the direction of the perturbation. For the purpose of applications to 3D flow simulations, this implies that shorter wavelengths in the streamwise direction are counter balanced by the need to use a longer wavelength in the spanwise direction. Therefore, to avoid enlarging the spanwise domain size, the heuristic approach of using non-eigenfunction perturbations was adopted and simulations conducted for five shear layer were compared; for each of these simulations the streamwise domain size was four times the perturbation wavelength and the calculation was initiated with four vortices leading after two pairings to an ultimate vortex. Among these five simulations, two layers (differing by the value of the initial Reynolds number) were excited with the incompressible most unstable wavelength. The third and fourth layers (differing by the value of the initial Reynolds number) were excited with the shortest compressible unstable wavelength from the 2D stability analysis and the same amplitudes as the first two layers. The fifth layer was excited with the shortest compressible unstable wavelength from the two-dimensional stability analysis and a larger amplitude of the 3D excitation. Only three of these five layers achieved transition, and the expectation of reduced CPU time for the layer perturbed with the shortest compressible unstable wavelength did not materialize. Global evolution and contour plots showed that the inability of transition achievement by two of the layers perturbed with the shortest compressible unstable wavelength is due either to the inability of the formed small scales to produce substantial vorticity or to the early formation of small scales and vorticity production which destroy the coherence of the ultimate vortex preventing its growth and initiating its decay.

The results showed that transitional states with the same momentum thickness based Reynolds number can be achieved by perturbing with a variety of unstable wavelengths, and that they require similar CPU time. Simulations performed with a shorter wavelength perturbation

require larger initial Reynolds numbers to reach a transitional state. Transitional states obtained with different perturbation wavelengths had different global and detailed characteristics, and therefore such simulations were recommended for enlarging the database necessary to extract turbulence models utilizable in the mathematical description of turbulent spatial flows.

Further investigations are now devoted to enlarging the transitional states database by (1) considering other binary system species, particularly those for which contemporary experimental information is available (e.g. LOX/He), and (2) considering additional perturbation wavelengths to obtain transitional states with different characteristics.

1. Miller, R. S., Harstad, K. G. and Bellan, J., Direct Numerical Simulations of Supercritical Fluid Mixing Layers Applied to Heptane – Nitrogen, *J. Fluid Mech.*, 430, 1-39, 2001
2. Okong'o , N. and Bellan, J., Entropy production of emerging turbulent scales in a temporal supercritical n-heptane/nitrogen three-dimensional mixing layer, *Proceedings of the Combustion Institute*, Vol. 28, 497-504, 2000a
3. Okong'o , N., Bellan, J. and Harstad, K., Consistent boundary conditions for multicomponent real gas mixtures based on characteristic waves, submitted for publication to the *Journal of Computational Physics*, 2000b
4. Okong'o , N. and Bellan, J., Direct Numerical Simulation of a transitional supercritical mixing layer: heptane and nitrogen, submitted for publication to the *Journal of Fluid Mechanics*, 2000c
5. Pope, S. B., Computations of turbulent combustion: progress and challenges, *Proc. Combustion Institute*, 23, 591-612, 1991
6. Okong'o , N. and Bellan, J., Linear stability analysis of real gas two- and three-dimensional mixing layers, submitted for publication to *Physics of Fluids*, 2001

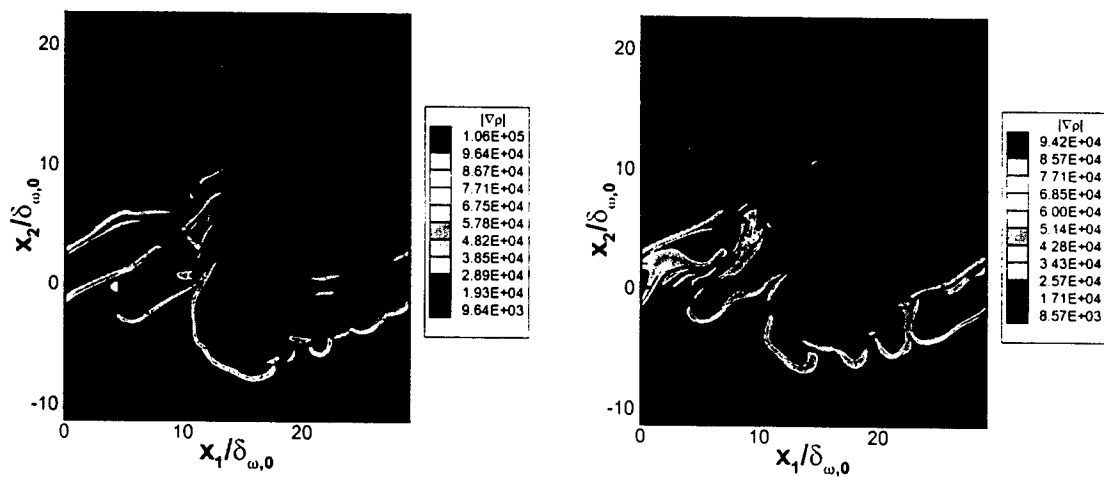


Figure 1 Density Gradient Magnitude at $t^*=135$ (corresponding to the attainment of a transitional state), in the braid plane (left) and in the between-the-braid plane (right). The initial Reynolds number is 600, the initial Mach number is 0.4, and the freestream temperatures are 1000 K for the upper, nitrogen, stream and 600 K for the lower, heptane, stream.

THE CHEMISTRY CONTROLLING IGNITION OF HYDROCARBONS AND THEIR MIXTURES AT HIGH PRESSURES

Contract No. DAAG55-98-1-0286; 37699-EG
AASERT Award DAAG55-97-1-0196; 36910-EG-AAS

David L. Miller and Nicholas P. Cernansky

Department of Mechanical Engineering and Mechanics
Drexel University, Philadelphia, PA 19104

SUMMARY/OVERVIEW:

This research program investigates the chemistry controlling ignition of hydrocarbons and their mixtures at elevated pressures. The objective of this program is the development of kinetic and mechanistic information in the low and intermediate temperature regime (600-1000 K) over a range of pressures (up to 20 atm). The methodology is to perform bench scale tests on single component pure fuels; on 2, 3, and 4 component mixtures of pure fuels; and on full boiling range fuels. The experiments are being carried out over a range of reaction conditions that are representative of actual engine conditions prior to and during the ignition process. Results from these studies will be used to provide kinetic and mechanistic information, to formulate hypotheses on autoignition mechanisms, to determine the relative effects of the various classes of components within multi-component fuel mixtures, and to provide combustion models that can be used in the design and evaluation of engine systems.

TECHNICAL DISCUSSION:

Efforts during this year focused on three specific research areas, the first was the oxidation of n-heptane and iso-octane in the Pressurized Flow Reactor (PFR) at Drexel. The second was the development of methods (GC and GC/MS) for the separation, identification, and quantification of large numbers of intermediate oxidation species. The third was part of a related AASERT program (DAAG55-97-1-0196) in which a technique for the spectral separation of radical from non-radical species using Magneto-Optic Rotation (MOR) coupled to Cavity Ringdown Laser Absorption Spectroscopy (CRLAS) has been developed and tested successfully. Efforts for next year will focus on the identification and quantification of intermediate species from 1-pentene, n-heptane, iso-octane, toluene, and their mixtures and the application of the diagnostic techniques. Furthermore, our efforts to develop a chemical surrogate for JP-8 will continue.

Hydrocarbon Mixtures -- Last year, we identified that JP-8 exhibited Negative Temperature Coefficient (NTC) behavior. This behavior occurs when the reactivity of a hydrocarbon species decreases with increasing temperature, something contrary to intuition. This behavior can be characterized utilizing a CO reactivity mapping technique. The resulting CO reactivity map for JP-8 had similar trends, namely temperature of maximum reactivity and peak shape, as other previously investigated Industry Standard Fuels (ISF) and simplified blends.

Therefore, this year's work focused on the detailed speciation of these simplified blends, specifically RON 92. RON 92 was developed at Drexel University two years ago by blending n-heptane, iso-octane, 1-pentene, and toluene. This blend exhibited NTC behavior similar to ISFs. n-Heptane and iso-octane were oxidized in our Pressurized Flow Reactor (PFR) to identify the existence of a Negative Temperature Coefficient (NTC) region and to indicate temperatures where detailed speciation experiments should be conducted. Utilizing the CO reactivity mapping technique, NTC behavior was observed for n-heptane and iso-octane. Initially plans were made to use the same operating conditions for the individual hydrocarbons and their mixtures to facilitate comparison. However, due to the differences in reactivity and heat release, this was not possible. The first experiments were with n-heptane at a pressure of 8 atm, equivalence ratio of 0.4, nitrogen dilution of 85%, and residence time of 100 ms. As the reactor cooled from 800 K to 625 K, a clear NTC behavior was observed [Figure 1]. The temperature at which the reactivity peaked, referred to as the start of NTC, occurred at 705 K. Next, iso-octane was oxidized at a pressure of 8 atm, equivalence ratio of 0.6, nitrogen dilution of 62%. Again, as the reactor cooled from 800 K to 625 K, NTC behavior was observed, the start of which occurred at 665 K [Figure 1]. Efforts are now under way to determine why iso-octane NTC behavior occurred at the lower temperatures. Furthermore, measurements of species formed during the oxidation of n-heptane are under way. Experiments with the RON 92 blend will be conducted shortly.

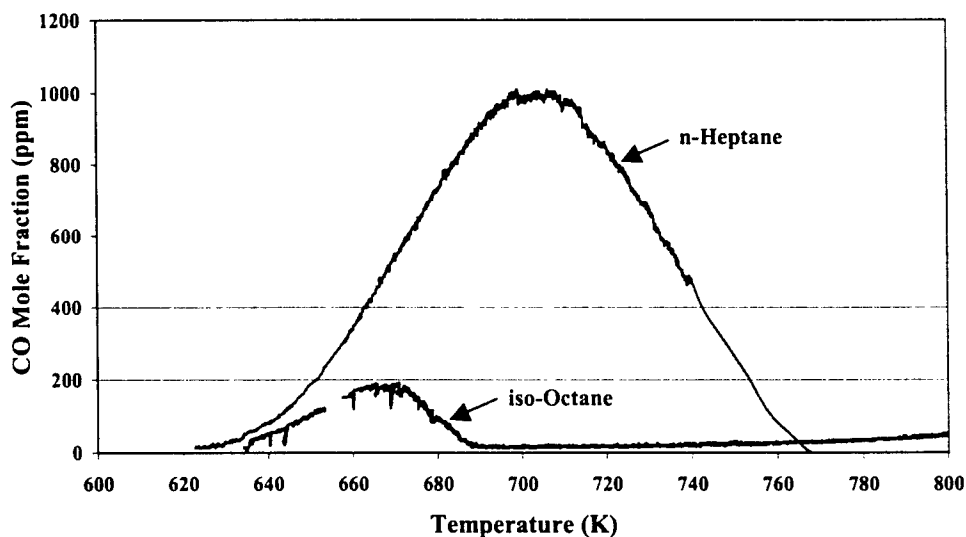


Figure 1: CO Reactivity mapping for n-heptane and iso-octane

Species Identification – The direction for this year was to obtain detailed speciation for each of the individual hydrocarbons and for their mixture as RON 92. In order to accomplish this task, a gas chromatographic technique capable of separating the large number of intermediate oxidation species expected from RON 92 had to be developed. The technique developed utilizes a single gas chromatograph (GC) column that is initially cooled to -20°C and slowly raised to higher temperatures. While this technique can separate large numbers of both large and small hydrocarbons, it requires a substantial amount of time (approximately 80 minutes per sample). Thus, development of techniques that can improve separation while minimizing the time required will continue. After separation, the compounds still need to be identified and quantified. Initially plans were to use a Fourier Transform Infrared (FT-IR) spectrometer for this purpose. However, upon coupling the GC to the FT-IR and using the desired separation technique, the FT-

IR did not have a sufficiently low detectability limit for the important species. As a result, the GC was then coupled with a shared use Mass Spectrometer (MS) in the Chemistry Department. Since this particular MS was used for identification of high molecular mass and high concentration samples, the instrument had to be tuned for low molecular weight and low concentration samples. The MS system has now been thoroughly tested with our GC method and it has the required sensitivity. It is also equipped with the NIST MS spectral library for identification of the oxidation species.

Laser Diagnostics -- In the related AASERT program, we have been developing advanced laser diagnostics techniques for measuring radical and stable species in combustion environments. Previously, we adapted the sensitive technique of Cavity Ringdown Laser Absorption Spectroscopy (CRLAS) and the selective technique of Magneto-Optic Rotation (MOR) to measuring highly reactive radicals in flame environments. This year, we continued to refine both the MOR and CRLAS techniques and began to couple CRLAS and MOR, developing a technique dubbed Cavity Enhanced Magneto-Optic Rotation (CEMOR). Refining MOR, we conducted experiments investigating concentration and experimental configuration effects on MOR with two weakly paramagnetic species, gallium and calcium, seeded into an air-acetylene flame. We observed absorption and MOR spectra of both calcium and gallium and determined sensitivity limits and optimal laser configuration. Lower detection limits were approximately 40 ppm and 50 ppb for gallium and calcium, respectively. Next, we investigated the absorption and MOR spectra of tellurium isotope 130, a non-paramagnetic species, and calcium in the blue region of the visible spectrum (420-425 nm). While detection of the Ca absorption line among the Te lines was very difficult using standard absorption techniques [Figure 2], MOR enabled selective observation of the weakly paramagnetic calcium [Figure 3]. The MOR technique will greatly expand our ability to identify and quantify radical species in regions of the electromagnetic spectrum congested by multiple stable species with multiple lines by virtually eliminating the signals from these species.

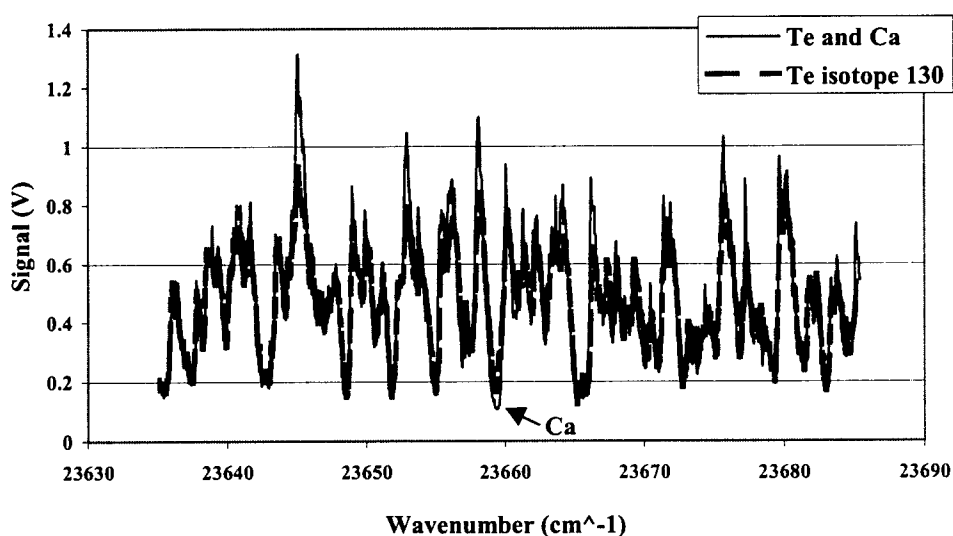


Figure 2. Absorption spectra of Te isotope 130 and Ca.

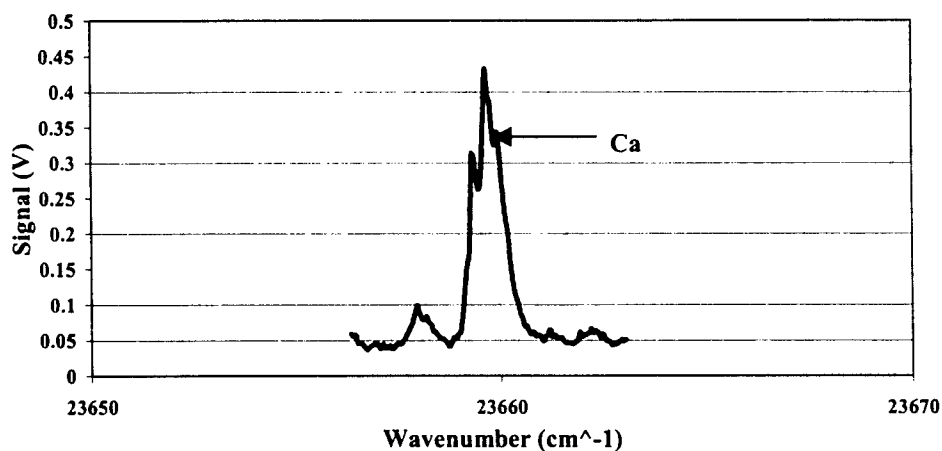


Figure 3. MOR spectra of Te isotope 130 and Ca.

Coupling the MOR technique within a CRLAS setup resulted in the developed of Cavity Enhanced Magneto-Optical Rotation (CEMOR). The resulting technique is capable of selectively detecting paramagnetic species even at extremely low concentrations. The polarized light enters the cavity where it interacts with the analyte, where a fraction of the light is absorbed and the remainder is rotated by a small amount. The rotation and adsorption of the light increases with each pass through the cavity, appearing as a maximum immediately before cavity losses overcome further rotation increases. The tail end of this signal appears similar to a ringdown absorption curve. Characterization of the CEMOR signal as a function of both cavity losses and rotation effects will enable us to use this technique for quantitative measurements. Initial efforts to characterize these effects have been accomplished utilizing gallium in an air-acetylene flame. In experiments spanning a range of gallium concentrations, we observed that the time to the maximum signal occurs earlier for higher concentrations [Figure 4]. These initial observations indicate that the time associated with this maximum could be used to determine concentration. Further investigation of this technique and modeling of the effect is required for a more precise quantification and identification of species. CEMOR is very promising for study of radical species, as it allows the detection of trace quantities using IR regions with multiple absorbers.

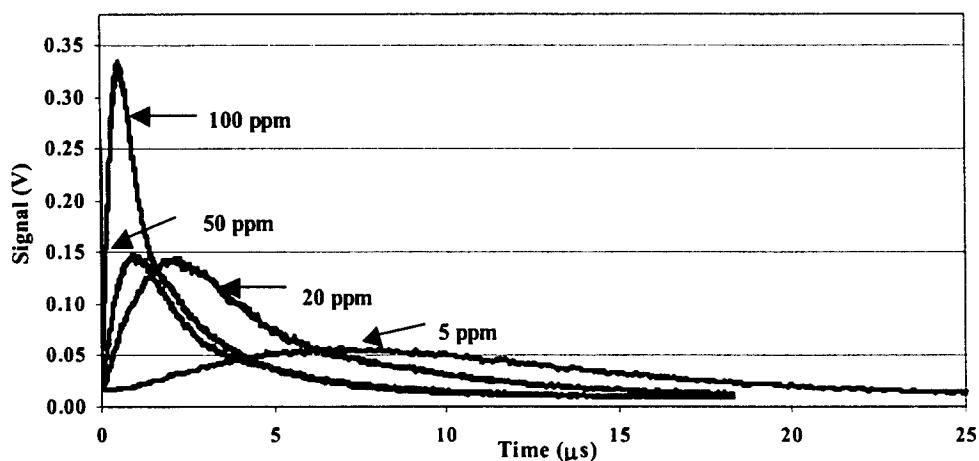


Figure 4. CEMOR signal of Gallium in air-acetylene flame, 417.204 nm.

ADVANCED SUPERCRITICAL FUELS

AFOSR Task # 93WL002

Principal Investigators: Tim Edwards, Jim Gord, Chris Bunker

Air Force Research Laboratory
AFRL/PRSF Bldg 490
1790 Loop Rd N
Wright Patterson AFB, OH 45433-7103

SUMMARY/OVERVIEW:

Increases in aircraft and engine performance are increasing the heat load being transferred into an aircraft's primary coolant--the fuel. This research is aimed at understanding the limitations of operation of fuel heated to 480 C (900 F) and beyond. Important issues are expected to be thermal stability, heat transfer/flow instabilities, and injection/combustion properties.

TECHNICAL DISCUSSION

Jet fuels are almost intractably complex, containing hundreds of hydrocarbons in an ever-shifting mix driven by source crude oil composition and processing. One approach for modeling and experimentation is the use of "surrogates"--simpler mixtures of hydrocarbons to represent the properties of interest. The complexity of the surrogate required varies with the fuel property being studied [1]. Another approach is to use multivariate analysis techniques on the principal fuel components (as determined by gas chromatography) to create eigenvalues and eigenvectors characteristic of each fuel. As shown in Figure 1, multiple analyses of single samples of JP-5, 7, and 8 show that the reproducibility from GC trace to GC trace is sufficient to identify differences between the various fuels. This time-intensive and tedious approach is being extended to multiple samples of each fuel. JP-8's (and Jet A's) can vary widely and it remains to be seen if the natural variation among samples will still allow the fuel types to be identified using this technique. The study of the properties of supercritical fuels continues, with the study of supercritical injection behavior [13] and with an analysis of the effect of hydrocarbon type on solvent-solute interactions. As shown in Figure 2, fluorescence of pyrene is being used to probe the effects of pressure (density) on solvent/solute interactions [9,15]. The differences between the hydrocarbons shown was the initial observation of such a structural effect and was unexpected.

Studies of thermal-oxidative and pyrolytic deposition continue [4,5,10,11,14,16]. A surprisingly strong interaction between deposition and the character of the fuel-wetted surface has been identified. As shown in Figure 3, several tests were performed with a silica-coated tube (Silcosteel®) of various lengths, joined to a stainless steel tube. In a series of tests, the silcosteel/stainless junction was moved to various locations along the heated zone, representing different portions of the fuel oxidation pathway. Early in the fuel oxidation process, the character of the heated surface appears to be relatively unimportant. But, as the junction is moved past the point of maximum deposition, a dramatic decrease in deposition is seen. This indicates the surface is active in the deposition process, as opposed to the early oxidation

processes that lead to deposition. In combination with the use of the dispersant additive in JP-8+100, the deposition is reduced by almost two orders of magnitude with the use of Silcosteel. It is expected that achievement of high thermal stability required by advanced applications [2,3,8,12] will require a combination of advanced additives, fuel deoxygenation, and an inert surface coating like Silcosteel. Pyrolytic deposition is important at 900 F (480 C) and above, and is also being studied [10,11,14]. The complexities of jet fuel pyrolysis are almost overwhelming, with the stability ranking of fuels changing as a function of fuel time-temperature-pressure history. In general, it appears that the formation of aromatics inside the fuel system is a precursor to pyrolytic deposit formation, analogous to PAH formation being a precursor to soot formation. An initial analysis has attempted to link both processes in a time-scale analysis [7].

New diagnostic approaches are being examined to probe the complex processes occurring as jet fuels are heated. The ultimate goal of this work is a field- or flight-portable instrument that can rapidly assess the state of the fuel, as opposed to the spectrum of time-consuming and costly tests used now to assure jet fuel quality and to study its reactions. One option being examined is the "chemical nose", which has the potential to identify fuels and reactions pathways with a group of 32 sensors sensitive to various hydrocarbons.

1. Edwards, T., and Maurice, L. Q., "Surrogate Mixtures to Represent Complex Aviation and Rocket Fuels," AIAA Journal of Propulsion and Power, Vol. 17(2), pp. 461-466, 2001
2. Maurice, L. Q., Edwards, T., Griffiths, J., "Liquid Hydrocarbon Fuels for Hypersonic Propulsion," pp. 757-822 in Scramjet Propulsion, Vol. 189, AIAA Progress in Astronautics and Aeronautics, Curran E. T. and Murthy, S. N. B. eds., 2001.
3. Lander, H. R., L.Q. Maurice, W.E. Harrison III, T. Edwards, "Advanced Aviation Fuels: a Look Ahead via a Historical Perspective," Fuel, Vol. 80, pp. 747-756, 2001.
4. J.S. Ervin, S. Zabarnick, and T.F. Williams, "One-Dimensional Simulations of Jet Fuel Thermal-Oxidative Degradation and Deposit Formation within Cylindrical Passages," Transactions of ASME, Journal of Energy Resource Technology, Vol. 122, pp. 229-238, 2001.
5. Jones, E. G., Balster, L. M., "Interaction of a Synthetic Hindered-Phenol with Natural Fuel Antioxidants in the Autoxidation of Paraffins," Energy & Fuels, Vol. 14, pp. 640-645, 2000.
6. Striebich, R. C., B. Grinstead, and S. Zabarnick, "Quantitation of Metal Deactivator Additive by Derivatization and Gas Chromatography-Mass Spectrometry," J. Chrom. Sci., Vol. 38, pp. 393-398, 2000.
7. Ballal, D. R., Harrison, W. E., "A Time Scale Approach to Understanding Jet Fuel Combustion and Particulate Formation and Growth," AIAA 2001-1085, Jan. 2001.
8. Edwards, T., Harrison, W. E., Maurice, L. Q., "Properties and Usage of Air Force Fuel: JP-8," AIAA 2001-0498, Jan. 2001.
9. Bunker, C. Gord, J. "Physical and Structural Properties of Jet Fuels Studies at High and Low Temperature Extremes using Laser-Based Diagnostics Methods," ACS Petroleum Chemistry Division Preprints, Volume 45(3), pp. 522-525, August 2000.
10. Corporan, E., Minus, D., "Pyrolytic Deposition Characteristics of JP-7 and JP-8 Fuels," ACS Petroleum Chemistry Division Preprints, Volume 45(3), pp. 474-477, August 2000.
11. Corporan, E., Minus, D., "Thermal Stability Assessment of High Naphthenic Fuels," 2000 JANNAF APS/CS Meeting, Monterey, CA, Nov 2000.
12. Edwards, T., "System Drivers for High Heat Sink Fuels," ACS Petroleum Chemistry Division Preprints, Volume 45(3), pp. 436-439, August 2000.
13. Ervin, J. S., Williams, T. F., Bento, J., Dounghip, T., "Studies of Jet Fuel Thermal Stability and Flow Characteristics within a Nozzle Under Supercritical Conditions," ACS Petroleum Chemistry Division Preprints, Volume 45(3), pp. 538-541, August 2000.

14. Minus, D., Corporan, E., "Aromatic Species formation in Thermally Stressed Jet Fuel," D. Minus and E. Corporan," ACS Petroleum Chemistry Division Preprints, Volume 45(3), pp. 436-439, August 2000.
15. Phelps, D., Bunker, C., Gord, J., "Solvatochromic Shifts in Supercritical Fuels," ACS Petroleum Chemistry Division Preprints, Volume 45(3), pp. 518-521, August 2000.
16. Zabarnick, S., "Investigation of Fuel Additives for a JP-8+225 Jet Fuel Using the Quartz Crystal Microbalance," ACS Petroleum Chemistry Division Preprints, Volume 45(3), pp. 440-443, August 2000.

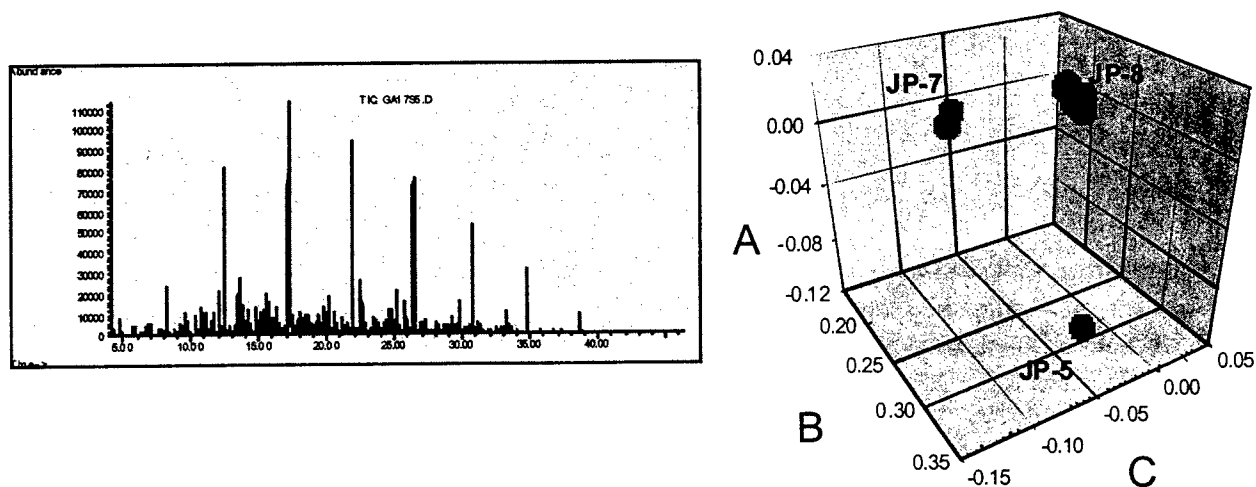


Figure 1 – Multivariate analysis of GC/MS data shows measurable differences between JP fuels.

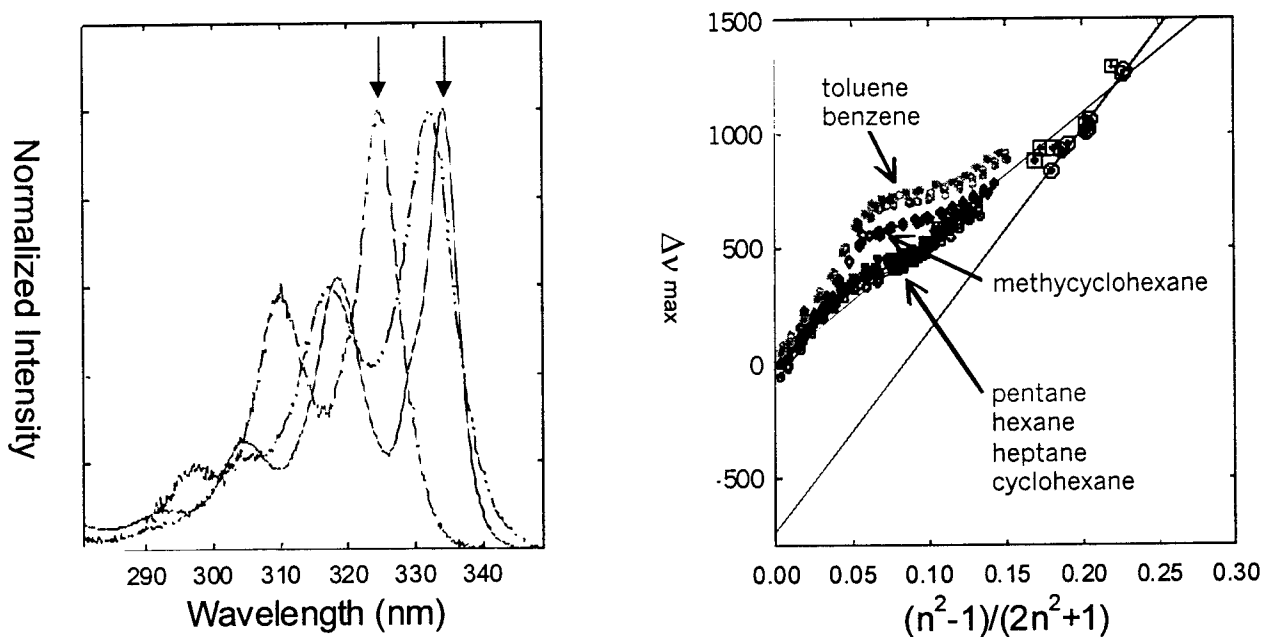


Figure 2 – (left) Pyrene fluorescence spectra in supercritical hexane at 245 C at various pressures; (right) shift in peak of fluorescence as a function of dispersion parameter (pressure).

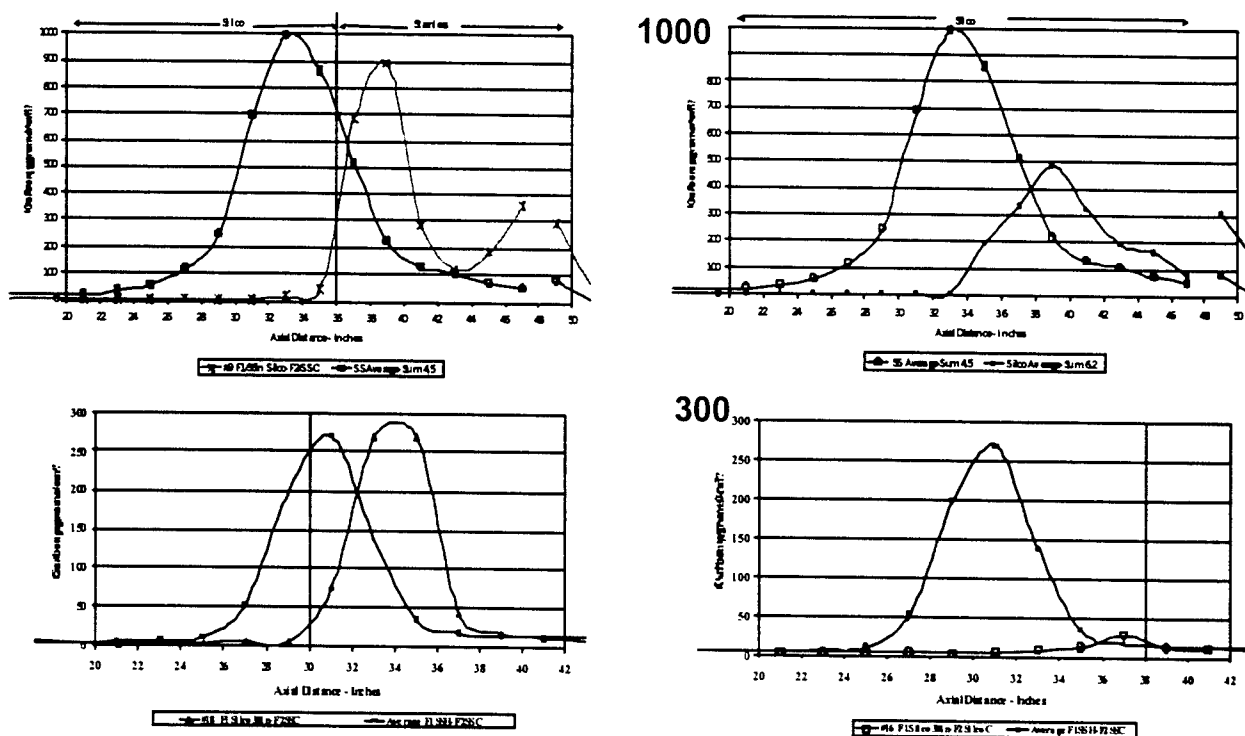


Figure 3 – (top left and right) Deposition profiles in tests with varying tube surfaces. (top left) deposition peak at roughly 1000 for stainless steel, deposition peak shifted to right and lowered by tube transitioning from stainless to Silcosteel at vertical line. (top right) Deposition profile for totally-Silcosteel-lined tube (lower profile), compared with stainless steel. (lower left) JP-8+100 deposition profile in stainless steel (left peak) compared with stainless steel/silcosteel tube[change at line]. (lower right) Deposition profile for primarily Silcosteel tube (low curve) as compared to original JP-8+100/stainless steel deposition curve.

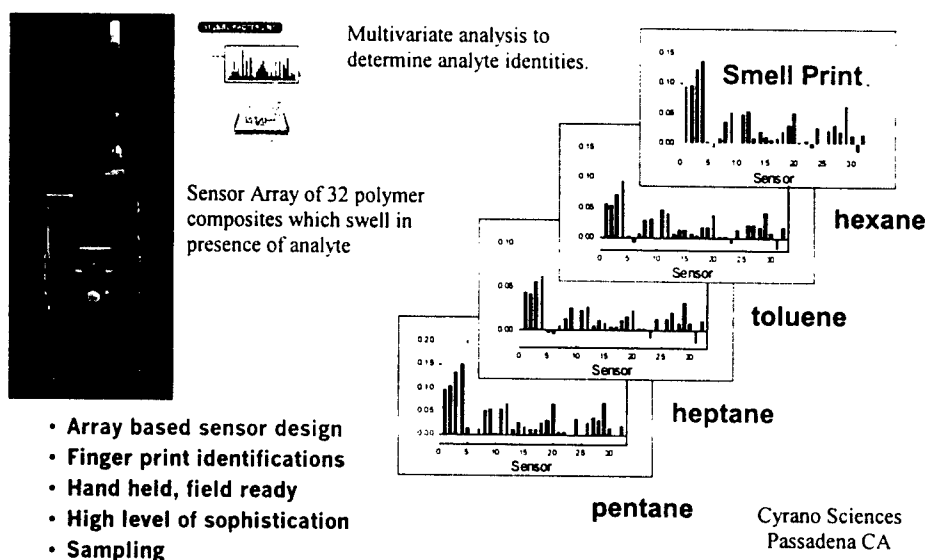


Figure 4 – Chemical nose concept.

DROP/GAS INTERACTIONS IN DENSE SPRAYS

(AFOSR Grant No. F49620-99-1-0083)

Principal Investigator: G.M. Faeth

Department of Aerospace Engineering
The University of Michigan
3000 François-Xavier Bagnoud Bldg.
Ann Arbor, Michigan 48109-2140, U.S.A.

SUMMARY/OVERVIEW:

Turbulence generation and liquid breakup are being studied due to their relevance to dense combusting sprays found in propulsion systems. Turbulence generation is the main source of turbulence in dense sprays; it consists of drop wake disturbances embedded in a turbulent interwake region. Both regions are unusual compared to conventional fluid flows: the drop wakes are laminar-like turbulent wakes typical of intermediate Reynolds number wakes in turbulent environments; the turbulent interwake region consists of isotropic turbulence in the little-studied final decay period. Work already completed has resolved the properties of the turbulent interwake region and overall flow properties for monodisperse particle (drop) flows; current work is addressing these properties for more practical polydisperse particles (drops).

Primary and secondary liquid breakup are important because they are the rate-controlling processes of dense sprays and fix initial conditions for dilute sprays. Past work has shown that liquid breakup should be treated as a rate process and has provided the temporal properties of secondary drop breakup at large liquid/gas density ratios based on experiments. Current work is considering drop deformation and breakup based on time-dependent numerical simulations, emphasizing conditions where liquid/gas density ratios are small and effects of liquid viscosity are large, which are important for practical applications but are difficult to consider using experiments.

TECHNICAL DISCUSSION:

TURBULENCE GENERATION. Early studies of turbulence generation (drop or particle-generated turbulence) showed that these flows were not typical of conventional turbulence (Parthasarathy and Faeth 1990; Mizukami et al. 1992). Subsequently, Wu and Faeth (1994, 1995) studied the properties of particle wakes for turbulence generation conditions and found that they scaled like laminar wakes but with enhanced mixing due to the presence of turbulence, and called them laminar-like turbulent wakes as a result. Work under the current grant then showed for monodisperse particles that the flow consisted of laminar-like turbulent wakes embedded in a turbulent interwake region, that the turbulent interwake region consisted of isotropic turbulence in the rarely observed final-decay period defined by Batchelor and Townsend (1948), that turbulence is sparse in the final-decay period yielding several unusual properties (unusually large rates of dissipation, unusually large ratios of macro-to-micro-scales in spite of small turbulence Reynolds numbers (less than unity), and decreasing ratios of macro-to-micro-scales with increasing Reynolds number rather than the opposite behavior observed for conventional turbulence), and that overall flow properties could be simulated accurately based on conditional averages of the newly resolved properties of laminar-like turbulent wakes and the turbulent interwake region (Chen and Faeth 2000, 2001; Chen et al. 2000).

Current work is considering the properties of flows caused by turbulence generation for more practical polydisperse particle flows (Lee et al. 2001). Measurements and predictions of streamwise relative turbulence intensities resulting from turbulence generation due to monodisperse and binary particle distributions in gases are illustrated in Fig. 1; the comparison between measurements and predictions is excellent with the polydisperse flows handled reasonably well using mixing rules based on the theory. Typical measurements of streamwise PDF's of streamwise velocities for binary particle flows are illustrated in Fig. 2; the unusual form of these PDF's is caused by effects of mean streamwise velocities in particle wakes because these disturbances are included with the turbulence because wake arrivals are random. Work in progress seeks to resolve the moments, PDF's, spectra and scales of the interwake region, the structure of the laminar-like turbulent wakes, and the properties of the overall flow for turbulence generation due to practical polydisperse particle flows.

SECONDARY BREAKUP. Past experimental studies have found secondary drop breakup regimes and outcomes (Hsiang and Faeth 1992, 1993, 1995), have shown that secondary breakup should be treated as a rate process (Faeth 1996), and have resolved the temporal properties of secondary breakup (Chou et al. 1997; Chou and Faeth 1998; Dai and Faeth 2001). These results were limited to breakup processes at normal pressures (where liquid/gas density ratios are large and effects of liquid viscosity are small). Current work is seeking to address liquid breakup properties at high pressure conditions typical of combusting sprays in propulsion systems, where liquid/gas density ratios and effects of liquid viscosity are large. These conditions are being addressed using time-dependent numerical simulations because they are difficult to reach with experiments.

Initial computations considered the problem of round liquid jet breakup in uniform crossflow which is the planar analog of axisymmetric drop breakup due to a shock wave disturbance. Recent measurements of deformation and breakup of such jets, due to Mazallon et al. (1999), are being used to evaluate the computations. An important finding of these measurements is that round liquid jet breakup in a uniform crossflow is qualitatively similar to secondary drop breakup. A typical prediction of the continuous phase properties of this flow is illustrated in Fig. 3 where effects of eddy shedding on flow properties are seen. Evaluation of the present computations using existing measurements yielded very satisfactory results, e.g., for wake sizes, onset of eddy shedding, eddy shedding frequencies, drag coefficients, etc.

Given successful evaluation of the predictions, they were used to find liquid jet breakup properties. The traditional secondary breakup regime map for drops due to Hinze (1975) was not effective for these results because regime boundaries were significantly affected by liquid gas viscosity ratios when effects of liquid viscosity were large. A better approach was to account for liquid viscous effects directly by plotting the ratio of drag forces to liquid viscous forces, $We^{1/2}/Oh$, as a function of the ratio of surface tension to liquid viscous forces, Oh^{-1} , where We and Oh are the Weber and Ohnesorge numbers of the flow. These results are illustrated in Fig. 4. The approach shown yields breakup regime boundaries that are relatively independent of liquid/gas density and viscosity ratios and are in excellent agreement with the measurements of Mazallon et al. (1999). The computations show that increasing liquid viscosity stabilizes the liquid jet to breakup by impeding the rate of deformation of the jet. Work in progress is considering numerical simulations of secondary drop breakup to both shock wave and gradual disturbances, but continues to emphasize small liquid/gas density ratio and large liquid viscosity conditions of particular interest for combusting sprays found in practical propulsion systems.

REFERENCES

- Aalburg, C.M. et al. (2001) *Int. J. Multiphase Flow*, in preparation.
 Batchelor, G.K. and Townsend, A.A. (1948) *Proc. Roy. Soc. (London)* 193A, 539.
 Chen, J.-H. and Faeth, G.M. (2000) *AIAA J.* 38, 995.

- Chen, J.-H. and Faeth, G.M. (2001) *AIAA J.* 39, 180.
 Chen, J.-H. et al. (2000) *AIAA J.* 38, 636.
 Chou, W.-H. and Faeth, G.M. (1997) *Int. J. Multiphase Flow* 24, 889.
 Chou, W.-H. et al. (1997) *Int. J. Multiphase Flow* 24, 651.
 Dai, Z. and Faeth, G.M. (2001) *Int. J. Multiphase Flow* 27, 217.
 Faeth, G.M. (1996) *Proc. Combust. Inst.* 26, 1593.
 Hinze, J.O. (1975) *Turbulence*, 2nd ed., McGraw-Hill, New York, 539.
 Hsiang, L.-P. and Faeth, G.M. (1992) *Int. J. Multiphase Flow* 18, 635.
 Hsiang, L.-P. and Faeth, G.M. (1993) *Int. J. Multiphase Flow* 19, 721.
 Hsiang, L.-P. and Faeth, G.M. (1995) *Int. J. Multiphase Flow* 21, 545.
 Lee, K. et al. (2001) *AIAA J.*, in preparation.
 Mazallon, J. et al. (1999) *Atom. Sprays* 9, 291.
 Mizukami et al. (1992) *Int. J. Multiphase Flow* 18, 397.
 Parthasarathy, R.M. and Faeth, G.M. (1990) *J. Fluid Mech.* 220, 485.
 Wu, J.-S. and Faeth, G.M. (1994) *AIAA J.* 32, 535.
 Wu, J.-S. and Faeth, G.M. (1995) *AIAA J.* 33, 171.

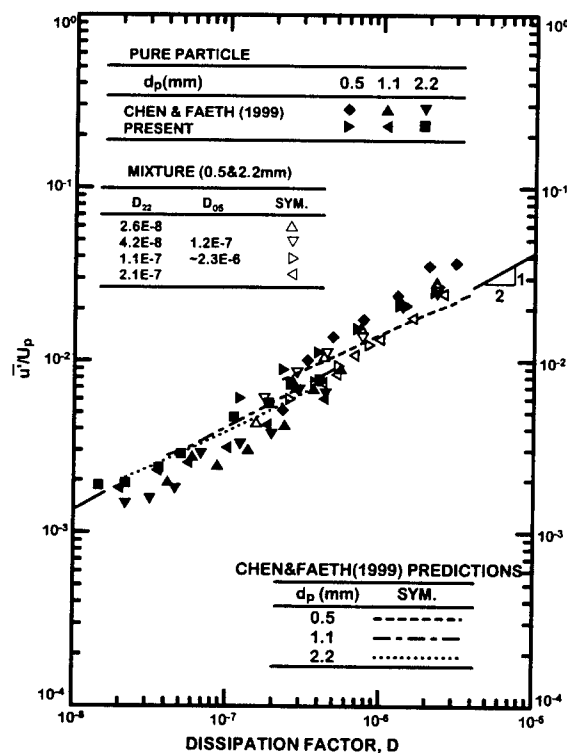


Fig. 1 Measurements and predictions of streamwise relative turbulence intensities of the overall flow as a function of dissipation factor for monodisperse and binary particle flows. From Lee et al. (2001).

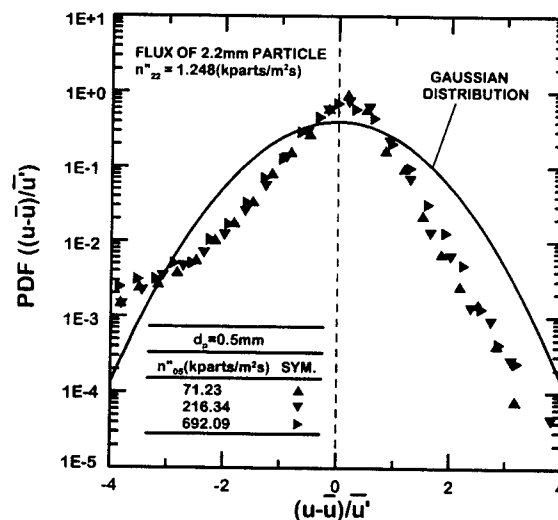


Fig. 2 Typical PDF's (logarithmic scales) of streamwise velocities of the continuous phase for bimodal mixtures of 0.5 and 2.2 mm nominal diameter particles. From Lee et al. (2001).

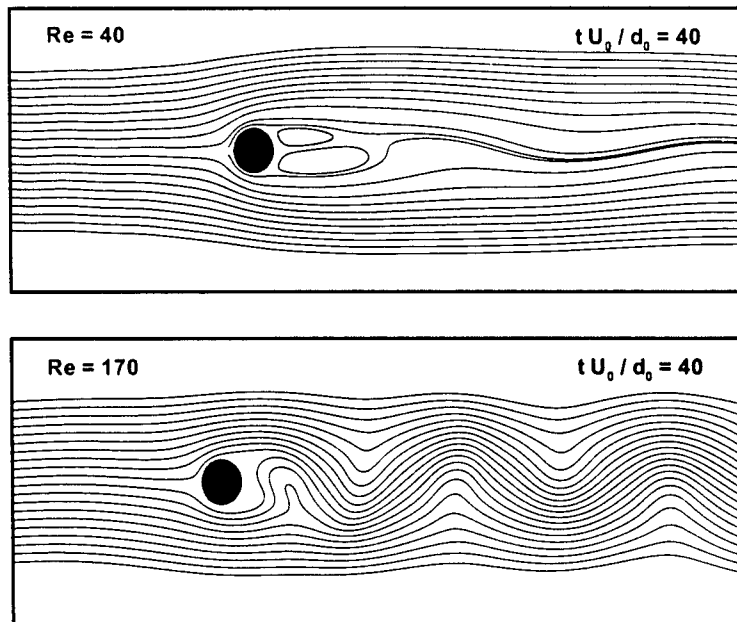


Fig. 3 Streamline patterns for eddy shedding behind a circular cylinder in crossflow for $Re = 40$ and $tU_0/d_0 = 40$. From Aalburg et al. (2001).

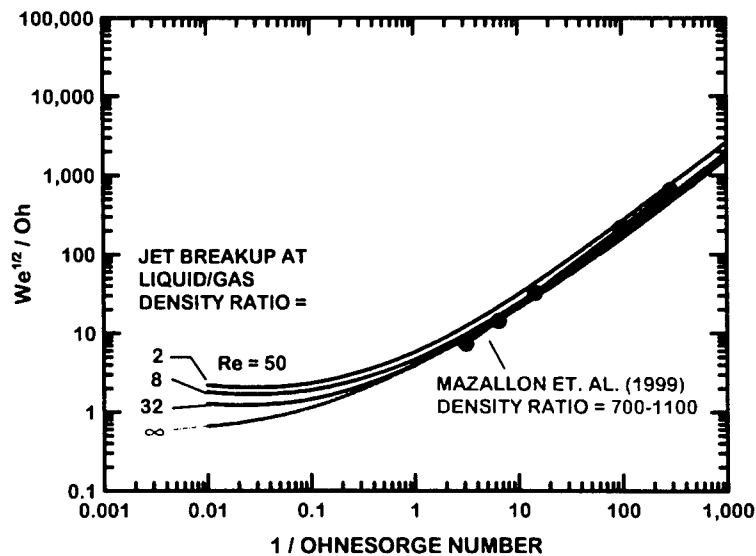


Fig. 4 Breakup regime map for nonturbulent round liquid jets in crossflow plotted according to the large Ohnesorge number limiting form. From Aalburg et al. (2001).

ADVANCED STIMULATED SCATTERING MEASUREMENTS IN SUPERCRITICAL FLUIDS

(AFOSR Contract F49620-01-C-0020)

Principal Investigator: Gregory W. Faris

SRI International
Menlo Park, California 94025

SUMMARY/OVERVIEW

We are using stimulated scattering (stimulated Rayleigh, Brillouin, and Raman scattering) to study supercritical fluids. New diagnostics are needed in the supercritical regime because low pressure diagnostics do not work well. From our measurements we can determine thermal, compressional, and compositional properties of supercritical fluids *in situ*. These techniques should improve our knowledge of fluid properties in the supercritical state.

TECHNICAL DISCUSSION

Objectives

The objectives of this research are to develop stimulated scattering as a diagnostic for supercritical fluids, and use this technique to improve our understanding of fluids in the supercritical state.

The study of supercritical fluids and flows requires new diagnostic techniques. Currently available techniques such as laser-induced fluorescence (LIF) and coherent anti-Stokes Raman scattering (CARS) are complicated by increased molecular interactions, leading to stronger quenching, larger absorption and refractive index, and incomplete understanding of the influence of local conditions on spectroscopic parameters such as linewidths, nonresonant background contributions, and quenching rates. We believe that stimulated scattering techniques hold great promise for studying supercritical fluids.

Stimulated Scattering

Rayleigh, Brillouin, and Raman scattering occur commonly as spontaneous scattering. These scattering processes arise from natural oscillation modes of materials and can be used to determine the physical parameters responsible for those oscillations. When these collective modes are excited with a powerful laser, the mode oscillations can be driven so hard that they grow exponentially. In this case, the oscillations cause stimulated scattering. The dominant advantage of stimulated scattering is that the scattered signal can be made arbitrarily large; otherwise, these processes produce extremely weak signals. By using a probe to measure the induced amplification, we can obtain very good quantitative results. This technique is distinct from the stimulated scattering that builds up from noise, in which case quantification is very difficult.

The large signals from stimulated scattering are particularly helpful for investigating Rayleigh and Brillouin scattering, where the weak signals available from spontaneous scattering are difficult to discriminate from background excitation light. Other advantages of stimulated scattering include excellent temporal resolution, and improved spectral resolution and signal-to-noise ratio. Furthermore, the use of two laser beams allows spatial registration and point measurement of local conditions.

With a single detection system, all three processes—Rayleigh, Brillouin, and Raman—can be measured. These processes together provide measurements of a wide range of material properties. Rayleigh scattering provides information on thermal properties, Brillouin scattering

on compressional or elastic properties, and Raman scattering on chemical and compositional properties, density, and temperature. While spontaneous Brillouin and Raman scattering have been applied to supercritical fluids, the use of stimulated scattering for supercritical fluids is new.

Experiment

Stimulated scattering allows measurements of the physical properties of fuels, including compressibility, speed of sound, thermal diffusivity, and chemical composition, density, and temperature while at supercritical conditions. This is significant, because much work on supercritical fuels has been performed after returning the fuels to ambient conditions, rather than in the supercritical state. Our work complements well work on optical diagnostics of supercritical fuels being performed at Wright-Patterson using spontaneous Raman and fluorescence measurements.

Stimulated scattering measurements are performed by producing strong scattering interactions using a pump laser and then probing the scattering using a second probe laser. As a pump laser for our stimulated scattering measurements we use an injection-seeded Nd:YAG laser. The probe laser is a tunable diode laser. The pump laser sets up an electric polarization oscillating at the characteristic frequency of a scattering mode of the material.¹ For strong laser driving, this polarization acts as a driving force, leading to amplification of both the material oscillation and the scattered optical wave. The optical amplification is detected as a gain or loss on the probe beam. Spatial resolution is determined by the overlap volume of the pump and probe beams.

We have previously reported the design and construction of a cell for capable of operation up to 600 K and 2000 psi. In design of that cell, we have drawn on information gained from conversations with Tim Edwards and Chris Bunker of AFRL-Wright-Patterson in their work on high pressure / high temperature systems. We have subsequently made a number of modifications to this cell. To avoid leaks at high temperatures, we substituted titanium bolts for the steel bolts, and glass windows for the fused silica windows. Titanium and glass have nearly the same thermal expansion coefficient. When operating the cell at high temperature, we found that convection near the windows caused beam wander, particularly in the region of the critical point. To minimize these effects, we have shortened the cell to an internal length of 2.5 cm.

We have used the modified cell to perform stimulated scattering measurements in the supercritical and near critical regimes. These are the first stimulated Rayleigh and stimulated Brillouin scattering at supercritical conditions to our knowledge. An example of measurements performed at 200 C and 630 psi is shown in Fig. 1. The abscissa is the difference in frequency between the pump and probe lasers determined by the wavemeter. The gain signal is divided by the pump and probe laser intensities to compensate for intensity fluctuations in each laser. The outer two peaks are Brillouin peaks; the central pair of peaks is due to stimulated Rayleigh scattering. The positive-going Brillouin peak to the left is a gain peak, corresponding to transfer of power from the Nd:YAG laser to the probe laser. The negative-going peak to the right is a loss peak, wherein power is transferred from the probe laser to the pump laser.

We performed fits to the measured lineshapes to determine linewidths, lineshifts, and peak heights. The electrostrictive Brillouin lineshape is described by the real part of the complex Lorentzian profile; the thermal Brillouin and Rayleigh lineshapes are described by the imaginary parts of a complex Lorentzian profile.² The measured lineshapes are given by the convolution of the Gaussian spectral lineshape of the Nd:YAG pump laser with these Lorentzian profiles. These convolved lineshape may be expressed as the real and imaginary parts of the complex error function for the Brillouin and Rayleigh peaks, respectively (the former is a Voigt profile). Complex error function fits to the data were performed using the algorithm of Humlicek,^{3,4} and the Igor graphics program (WaveMetrics, Inc.). We used the Fourier-transform limited linewidth calculated from pulsewidth as the spectral linewidth of the pump laser. To eliminate the contribution of the 10 Hz dither used to lock the Nd:YAG laser to the seed laser, measurements were performed at 5 Hz. The seed laser linewidth is specified to be less than 300 kHz in 50 ms.

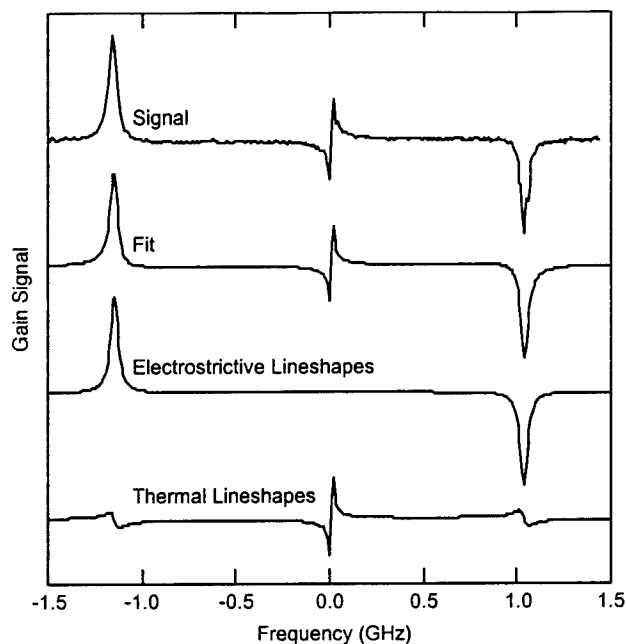


Fig. 1. Stimulated Rayleigh and Brillouin spectrum for hexane at 200 °C and 630 psi.

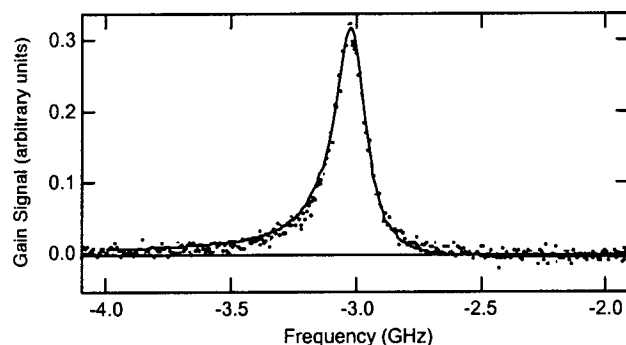


Fig. 2. Data (points) and fit (solid line) for stimulated Brillouin gain peak for n-hexane at 1064 nm. Stimulated thermal Brillouin scattering gives an asymmetry to the peak.

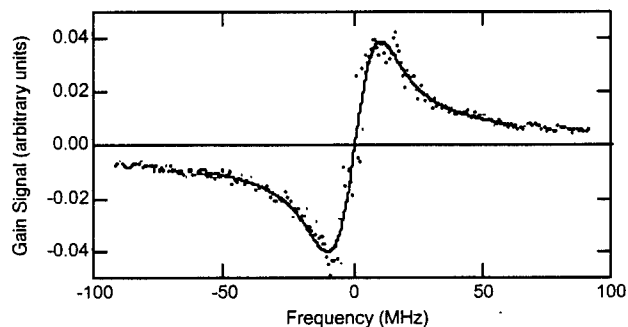


Fig. 3. Data (points) and fit (solid line) for stimulated thermal Rayleigh scattering in n-hexane at 1064 nm.

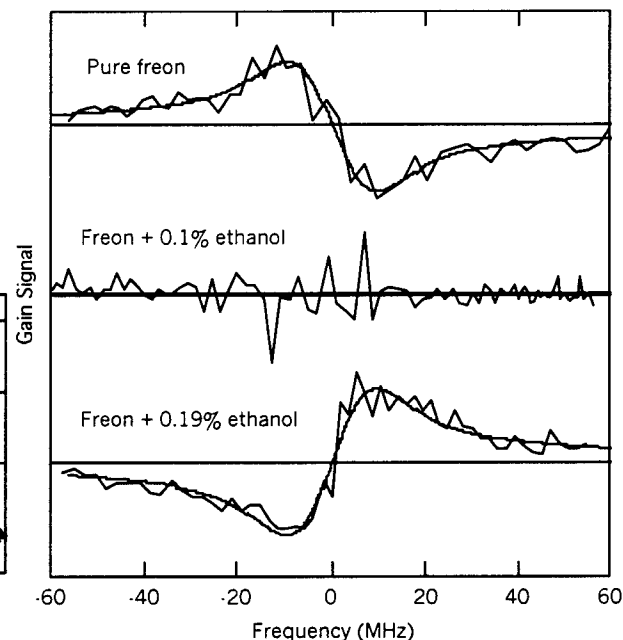


Fig. 4. Measured stimulated Rayleigh gain signal (solid curve) and fitted profile (dashed curve) in pure freon 113 (top), and freon with 0.1% ethanol (middle) and 0.19% ethanol (bottom).

Table 1.

Properties measured in hexane using stimulated Rayleigh /Brillouin scattering at 1064 nm.

Property	Our Results	Literature Values
Brillouin shift	2.91±0.06 GHz	
Brillouin width	151±8 MHz	
Rayleigh width	7.9±3.2 MHz	
Ratio of electric to absorptive coupling constants	8.8±0.6	
Acoustic damping time	1.06 ns	
Acoustic velocity	1.14 km/s	1.10 km/s
Acoustic attenuation coefficient	$8.3 \times 10^5 \text{ m}^{-1}$	$7.4 \times 10^5 \text{ m}^{-1}$
Effective mass diffusion coefficient	$7.4 \times 10^{-6} \text{ m}^2/\text{s}$	
Isentropic compressibility	$1.2 \times 10^{-9} \text{ m}^2/\text{N}$	
Thermal diffusivity	$9.6 \times 10^{-8} \text{ m}^2/\text{s}$	$9.2 \times 10^{-8} \text{ m}^2/\text{s}$

The full fit to the Rayleigh/Brillouin spectrum is shown as the curve labeled "fit" in Fig. 1. Very good agreement is found between the measured and fit lineshapes (see also Figs. 2 and 3). The electrostrictive and thermal contributions to the overall fit are shown separately at the bottom of Fig. 1. The thermal scattering is due to absorption by OH or CH overtone or combination bands. This absorption increases the size of the stimulated Rayleigh peak (it is otherwise difficult to observe) and causes an asymmetry in the stimulated Brillouin peak due to the imaginary Lorentzian shape of the thermal Brillouin scattering.

Expanded spectra for stimulated Brillouin and stimulated Rayleigh scattering in hexane at room temperature are shown in Figs. 2 and 3. Also shown are fits to these spectra. The frequency values for the stimulated Rayleigh peak in Fig. 3 were determined from the heterodyne signal between the seed and probe lasers. This peak is quite narrow. The average linewidth determined from multiple fits such as shown in Fig. 3 gives value of 7.9 ± 3.2 MHz, which is in good agreement with the value expected from the thermal diffusivity for n-hexane. These measurements were performed with a pulsewidth for the Nd:YAG laser of approximately 30 ns, which corresponds to a full width half maximum spectral linewidth of about 15 MHz. Thus the laser linewidth is about twice the measured linewidth of the Rayleigh peak. The good agreement with the expected linewidth confirms that the Nd:YAG laser has a transform-limited linewidth of 15 MHz. The spectroscopic and thermodynamic properties for n-hexane determined from numerous such fits are given in Table 1. The errors are standard deviations of values averaged from 14 or more measurements. These calculations use the refractive index for hexane (extrapolated to 1064 nm from a literature expression⁵) as appropriate.² Good agreement is obtained with values available in the literature.

We have observed electrostrictive stimulated Rayleigh scattering in a liquid and created a transition to stimulated thermal Rayleigh scattering with the addition of an absorbing liquid. With the proper amount of absorption, the electrostrictive and thermal contributions to the scattering exactly cancel, resulting in no stimulated Rayleigh scattering. This effect is shown in Fig. 4. The top curve shows a pure electrostrictive stimulated Rayleigh peak in pure freon 113. With an addition of 0.1% ethanol (an absorption coefficient of 0.00012 cm^{-1}) the stimulated thermal scattering cancels the stimulated electrostrictive scattering (center curve). With addition of more ethanol, the stimulated peak has flipped over (bottom curve)

We are currently investigating fluctuations near the critical point. These fluctuations can cause flow and pressure instabilities, which have been found to have destructive effects on tubing.^{6,7} Avoiding these fluctuations is very important for fuel systems that transition into the supercritical regime.

REFERENCES

1. G.W. Faris, L.E. Jusinski, and A.P. Hickman, "High-resolution stimulated Brillouin gain spectroscopy in glasses and crystals," *J. Opt. Soc. Am. B* **10**, 587-599 (1993).
2. W. Kaiser and M. Maier, "Stimulated Rayleigh, Brillouin, and Raman spectroscopy," in *Laser Handbook*, F. T. Arecchi and E. O. Schulz-Dubois, Eds. (North-Holland, Amsterdam, 1972), Vol. 2, pp. 1077-1150.
3. J. Humlicek, "Optimized computation of the Voigt and complex probability functions," *J. Quant. Spectrosc. Radiat. Transfer* **27**, 437-444 (1982).
4. F. Schreier, "The Voigt and complex error function: A comparison of computational methods," *J. Quant. Spectrosc. Radiat. Transfer* **48**, 743-762 (1992).
5. H. El-Kashef, "Molecular properties of hexane," *J. Modern Opt.* **46**, 1389-1399 (1999).
6. W.S. Hines and H. Wolf, "Pressure oscillations associated with heat transfer to hydrocarbon fluids at supercritical pressures and temperatures," *ARS Journal*, 361-366 (March 1962).
7. L.E. Faith, G.H. Ackerman, and H.T. Henderson, Heat sink capability of jet A fuel: Heat transfer and coking studies, NASA Report No. CR-72951 (1971).

SUB- AND SUPER-CRITICAL EVAPORATION AND COMBUSTION OF A MOVING DROPLET

DAAD19-99-1-0116

Principal Investigator: George Gogos

**University of Nebraska-Lincoln
303 Canfield Administration Bldg
Lincoln, NE 68588-2618**

SUMMARY: We are conducting a comprehensive computational study of fuel droplet evaporation and combustion in sub- and super-critical ambient conditions under forced convection. An experimentally validated model for a moving spherical droplet that undergoes evaporation has been developed. The model is used to predict droplet lifetimes and droplet penetration distances over a wide range of ambient pressures. In addition, a low pressure, experimentally validated model for a moving spherical droplet that undergoes combustion has been developed. This model employs a one-step overall reaction and is used to predict extinction velocities for different size droplets. Future work will allow for droplet deformation and semi-detailed chemical kinetics.

TECHNICAL DISCUSSION Two aspects of droplet evaporation/combustion have been studied and are discussed below.

I. Evaporation of a Spherical Moving Fuel Droplet over a Wide Range of Ambient Pressures within a Nitrogen Environment (with Dr. Hongtao Zhang). Modeling evaporation of moving fuel droplets within high pressure and high temperature environments is of critical importance in devices such as diesel engines, liquid-fueled rocket engines and high-output combustors for aircraft jet engines. Studies on droplet evaporation at elevated pressures have been mostly limited to stagnant surroundings.

In this study results have been obtained for evaporation of a n-heptane droplet translating within a high pressure and high temperature nitrogen environment. The axisymmetric numerical model that has been developed allows for inert species solubility in the liquid phase. Most studies on moving droplets assume a spherical shape. However, at a large Reynolds number, the Weber number may be large enough to cause deformation and even break-up of the droplet. The extensive numerical results of Dandy and Leal [1] show that the droplet remains nearly spherical for Weber numbers less than 1.0 even at Reynolds numbers as high as 400. We have employed the above criterion of droplet sphericity in our axisymmetric model to be consistent with our assumption that the droplet remains spherical. Future work at higher Weber numbers will allow for droplet deformation and possibly droplet break-up.

The gas and liquid phase solutions are obtained by solving the axisymmetric unsteady equations of mass, species, momentum, and energy conservation in spherical coordinates. These equations are coupled via the conservation equations at the interface and are solved iteratively. The effect of gravity is neglected. The finite-volume [2] and SIMPLEC [3] methods are used to discretize the governing equations in the computational domain. Staggered grids and the hybrid scheme are used in the discretization equations. Real gas effects are modeled using the Peng-Robinson equation of state with the appropriate binary interaction coefficient and transport and thermodynamic properties as recommended by Reid et al. [4]. Calculations are terminated when $(d/d_0)^2 \leq 0.2$, or when the critical state for the binary system is reached.

The current axisymmetric numerical model is validated by comparison to the experimental results of Gokalp et al. [5]. Fig. 1 presents the time histories of $(d/d_0)^2$ for n-heptane droplets with initial diameters of 1.43 mm ($U_\infty=2.53$ m/s) and 1.18 mm ($U_\infty=6.00$ m/s) evaporating in a nitrogen environment at an ambient temperature of 297 K and an ambient pressure of 0.101 MPa (1 atm) under micro-gravity conditions. The relative velocities between the droplet and the gas phase remain constant throughout the droplet lifetime. These conditions correspond to the experimental conditions in Gokalp et al. [5], with the exception that Gokalp et al. used air as the gas phase, whereas nitrogen is used in the current numerical model. The droplet lifetime can be obtained from Fig. 1. The droplet lifetimes from the experimental results of Gokalp et al. [5] and numerical results of Fig. 1 are listed in Table 1. Very good agreement is shown. The axisymmetric numerical model has been also validated using the n-heptane experimental data of Nomura et al. [6]. Extensive presentation can be found in Zhang [7].

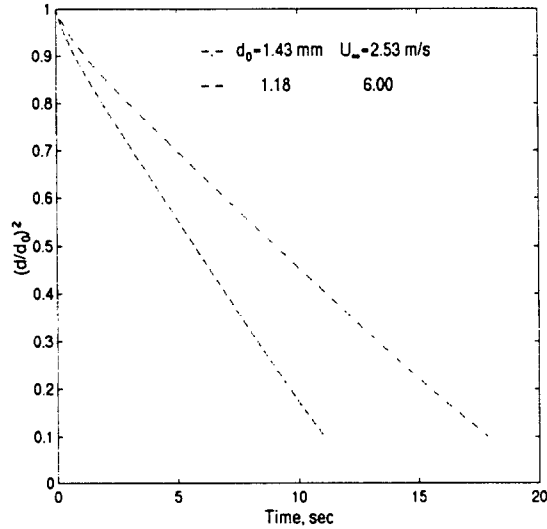


Table 1: Comparison of droplet lifetime

d_0 (mm)	U_∞ (m/s)	Lifetime (s)	
		Experimental [5]	Numerical
1.43	2.53	19.20	19.98
1.18	6.00	12.04	12.46

Fig. 1. Time histories of $(d/d_0)^2$ ($p_\infty=0.101$ MPa, $T_\infty=297$ K)

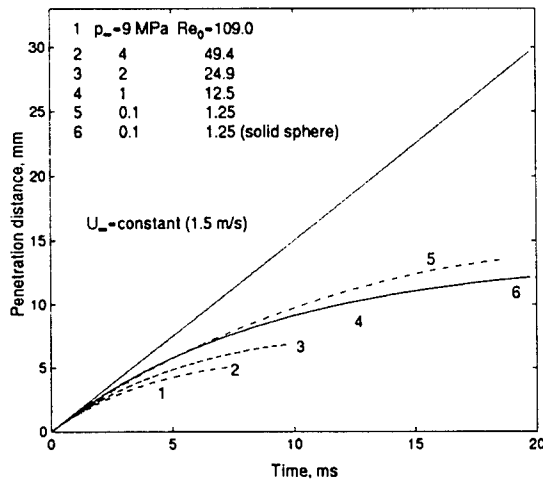


Fig. 2a. Droplet penetration distance with time for different ambient pressures ($U_{\infty 0}=1.5$ m/s).

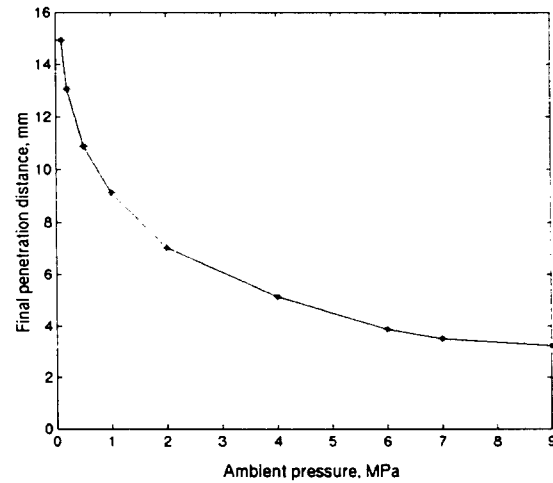


Fig. 2b. Final penetration distance with ambient pressures ($U_{\infty 0}=1.5$ m/s).

Results presented in Fig. 2 were calculated for a moving n-heptane droplet evaporating within a nitrogen environment. The initial diameter is 100 μ m and the initial temperature is 300 K. Fig. 2a shows the droplet penetration distance as a function of time for different ambient pressures at an initial droplet velocity of 1.5 m/s. Cases 1-5 are for n-heptane droplets. The moving droplets experience deceleration while undergoing vigorous evaporation. The lower the ambient pressure, the larger the droplet penetration distance. Actually, the final droplet penetration distance decreases exponentially with ambient pressure (see Fig. 2b). In case 6, a solid sphere with the same density as in case 5 is considered, which is moving under the same ambient conditions (temperature and pressure) as in case 5. The drag coefficient for a solid sphere recommended by Mills [8] is employed. The reduction

in the drag force experienced by the evaporating droplet, a result known for a long time in the literature [9], leads to a higher droplet penetration distance (case 5) compared to that for the solid sphere (case 6). The straight solid line in Fig. 2a corresponds to the penetration distance of a solid sphere moving with a constant velocity.

II. Numerical Simulation of Droplet Extinction Due to Forced Convection (with doctoral student Daniel N. Pope). The literature has shown that envelope flames surrounding droplets could extinguish in the presence of “adequately strong” convective flows. The present work numerically investigates the extinction of fuel droplets due to forced convection. A zero-gravity environment at atmospheric pressure is considered. The gas phase solution was obtained using the axisymmetric quasi-steady equations of mass, species, momentum, and energy conservation in spherical coordinates. Droplet internal circulation was accounted for by solving the quasi-steady momentum equations for the liquid phase. The gas and liquid phase were solved iteratively and coupled via the interfacial conservation equations. The governing equations were discretized using the finite volume [2] and SIMPLEC [3] methods. A staggered grid was adopted and relaxation was incorporated via an artificial time-step that was embedded in the discretization equations. Hyperbolic tangent stretching functions were used to concentrate grid points near the fore and aft lines of symmetry and at the droplet surface in both the gas and liquid phase. The discretization equations were solved using the ADI method with the TDMA used on each line of the two alternating directions.

A one-step overall reaction was used to describe combustion. Values for the activation energy, and oxygen and fuel concentration exponents in the finite-rate kinetics were adopted from Westbrook and Dryer [10]. The pre-exponential factor was determined by comparison of numerical results with experimental data [11] for extinction velocity. For n-heptane, a pre-exponential factor three times that of Westbrook and Dryer [10] was selected. An initial condition of a chemically frozen environment with a high temperature region near the droplet was used to cause ignition of the fuel/air mixture in the gas phase. The extinction velocity was obtained by selecting an initial freestream velocity that resulted in an envelope flame and then incrementing the freestream velocity by 1 cm/s between successive quasi-steady solutions until the evaporation constant exhibited a sharp decrease.

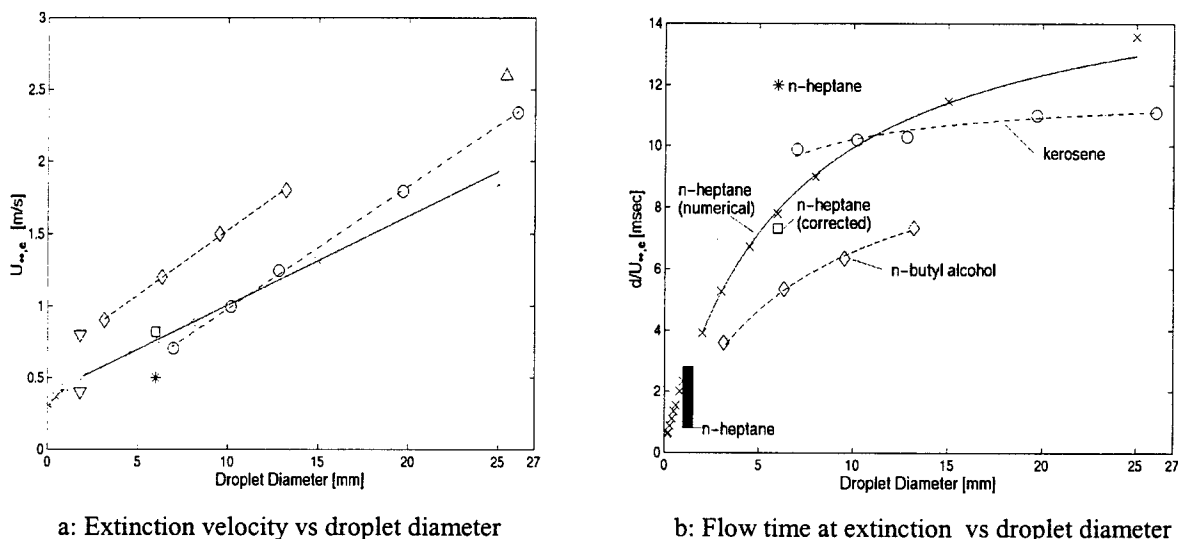


Fig. 3. Extinction velocity and flow time vs. droplet diameter: (x) - numerical predictions for n-heptane under zero-gravity ($T_{\infty} = 300$ K and $p_{\infty} = 1$ atm). Experimental data under normal-gravity for various fuels in air at “room” temperature and atmospheric pressure; (o) - kerosene (Spalding [12]), (◇) - n-butyl alcohol (Agoston et al. [13]), (*) - n-heptane (Gollahalli and Brzustowski [15]), (□) - previous point corrected for natural convection, (▽) - gasoline (Agafonova et al. [16], lower: aiding natural convection, upper: opposing natural convection), (Δ) - n-heptane (Gore et al. [17]), (shaded box) - n-heptane (Chauveau et al. [18]).

Results are presented for extinction velocities of n-heptane droplets burning in air at room temperature (300 K) and a pressure of 1 atm. Droplet diameter (d) is varied from 0.18 to 25.0 mm to determine its effect on extinction velocity ($U_{\infty,e}$). The fact that the available experimental data for extinction velocities under microgravity conditions are very limited complicates the process of model validation. However, experimental data for the extinction velocities of various fuels under normal-gravity exist in the literature. These data have been very useful for a qualitative validation of our code. Fig. 3a shows the predicted extinction velocity for n-heptane droplets in air as a

function of droplet diameter. The value of $U_{\infty,e} = 0.43$ m/s for $d=1$ mm corresponds to the results of Okajima and Kumagai [11]. This experimental study was used to determine the pre-exponential factor for our numerical model. The figure also includes experimental results from the literature for the extinction velocity of various fuels under normal-gravity. Spalding [12] and Agoston et al. [13] conducted porous sphere experiments employing kerosene and n-butyl alcohol, respectively. Both studies show that the extinction velocity varies linearly with diameter. Our numerical results (solid line) predict this linear dependence for approximately $d > 2$ mm. Large activation temperature asymptotics [14] also predict this linear dependence. The magnitudes of the measured extinction velocities in [12] and [13], however, differ from our predictions possibly because the fuels are different. Buoyancy effects are negligible for the size of porous spheres employed by Spalding [12] and Agoston et al. [13] due to the small Richardson number (~ 0.05). Gollahalli and Brzustowski [15] employed the same fuel (n-heptane) as we did in our simulations. The buoyancy-induced flow in their experiment aids the forced convection flow. Fig. 3a shows that the extinction velocity corrected for the presence of natural convection lies very close to the numerical prediction for the same fuel. In addition, Fig. 3a shows that for diameters in the range of $180\text{ }\mu\text{m} - 1000\text{ }\mu\text{m}$, our numerical model predicts that the extinction velocity exhibits a nonlinear dependence. Extrapolating the linear curve predicted for larger droplets may provide an erroneous value for extinction velocities of droplets of, say, $100\text{ }\mu\text{m}$, which are encountered in a typical spray.

The characteristic flow time at extinction ($d/U_{\infty,e}$) as a function of droplet diameter is shown in Fig. 3b. Spalding [12] observed a nearly constant flow time in his experiments using kerosene. This is to be expected since extinction velocity varies linearly with diameter, intercepts the vertical axis at a small velocity, and only extinction velocities for large diameters are reported. The numerically predicted flow time for n-heptane approaches a constant at much larger diameters and decreases rapidly with decreasing diameter. Additional experimental data for n-heptane from Chauveau et al. [18] for suspended droplets under normal-gravity conditions and diameters between 1.0 and 1.5 mm are shown in Fig. 3b (shaded box).

The numerical predictions are in good agreement with experimental results from the literature, despite the use of a one-step overall reaction. Extensive presentation of this study can be found in Pope [19]. Future modifications to the numerical code will include semi-detailed chemical kinetics.

References

1. D. S. Dandy, and L. G. Leal, *J. Fluid Mech.* 208:161 (1989).
2. S. V. Patankar, *Numerical Heat Transfer and Fluid Flow*, Hemisphere Publishing Corporation, New York, 1980.
3. J. P. Van Doormaal, and G. D. Raithby, *Numerical Heat Transfer* 7:147 (1984).
4. R. C. Reid, J. M. Prausnitz, and B. E. Poling, *The Properties of Gases and Liquids (4th ed)*, McGraw-Hill, Inc., New York, 1987.
5. I. Gokalp, C. Chauveau, J. R. Richard, M. Kramer, and W. Leuckel, *Proceedings of the Combustion Institute*, 22:2027 (1988).
6. H. Nomura, Y. Ujiie, H. J. Rath, J. Sato, and M. Kono, *Proceedings of the Combustion institute*, Vol. 26:1267 (1996).
7. H. Zhang, *Evaporation of a Spherical Moving Fuel Droplet over a Wide Range of Ambient Pressures within a Nitrogen Environment*, Ph.D Dissertation, University of Nebraska-Lincoln, Lincoln, Nebraska, 2000.
8. A. F. Mills, *Heat Transfer*, IRWIN, 1992.
9. C. H. Chiang, M. S. Raju, and W. A. Sirignano, *Int. J. Heat Transfer*, 35:1307 (1992).
10. C. K. Westbrook, and F. L. Dryer, *Comb. Sci. and Tech.*, 27:31 (1981).
11. S. Okajima and S. Kumagai, *Proc. Combust. Inst.*, 19:1021 (1982).
12. D. B. Spalding, *Fuel*, 32:169 (1953).
13. G. A. Agoston, H. Wise, and W. A. Rosser, *Proc. Combust. Inst.*, 6:708 (1957).
14. X. Wu, C. K. Law, and A. C. Fernandez-Pello, *Comb. Flame*, 44:113 (1982).
15. S. R. Gollahalli, and T. A. Brzustowski, *Proc. Combust. Inst.*, 15:409 (1975).
16. V. R. Kuznetsov, and V. A. Sabel'nikov, *Turbulence and Combustion*. Hemisphere, 1990.
17. J. P. Gore, W. Meng, and J. Jang, *Comb. Flame*, 82:126 (1990).
18. C. Chauveau, X. Cheneau, and I. Gokalp, *AIAA - 31st Aerospace Sciences Meeting and Exhibit*, AIAA-0824 (1993).
19. D. N. Pope, *Numerical Simulation of Convective Fuel Droplet Vaporization and Combustion in a Low Pressure Zero-Gravity Environment*, Ph.D Dissertation, University of Nebraska-Lincoln, Lincoln, Nebraska, 2001.

CROSSED-PLANE LASER IMAGING OF PREMIXED TURBULENT COMBUSTION PROCESSES

DAAD19-99-1-0324

F. C. Gouldin

Cornell University, Ithaca, NY 14853

Overview

The objective of our research is to measure, using crossed-plane imaging, normal vectors and the instantaneous thermal structure of flamelets in premixed turbulent flames. Data for surface normal vectors can be used to calculate important quantities such as Σ , the flamelet surface density. Σ is a measure of the wrinkling of the flamelet surface and is proportional to the rate of product formation per unit volume in the flame, $\langle w \rangle$, which appears as an unclosed term in premixed flame models and is related to the burning intensity. Flamelet thermal structure data can be used to estimate the constant of proportionality between $\langle w \rangle$ and Σ . Instantaneous flamelet normals have been measured in three dimensions using crossed-plane imaging via either laser tomography or planar laser induced acetone fluorescence. We are now exploiting crossed-plane imaging for flamelet normal measurements in different burners and over a range of conditions. In addition we are developing crossed-plane Rayleigh imaging in order to measure temperature gradients within flamelets and thereby to determine their thermal structure. Through measurements of flamelet normal and thermal structure we can estimate $\langle w \rangle$.

I. Introduction

Premixed turbulent combustion has a broad range of practical applications, from powering the vehicles we drive to proposed low emissions jet engine combustors. In many cases, conditions fall within what is called the flamelet regime in which reactions are confined to thin sheets, called flamelets, separating regions of reactants and regions of products. For these conditions, the burning intensity is related to the degree of wrinkling of the flame: the wrinkling serves to increase Σ and hence $\langle w \rangle$. Σ can be expressed as a function of the probability density function, PDF, of the flamelet surface normal vector, \underline{N} , and the flamelet crossing density, n_c . Thus it can be determined by crossed plane imaging measurements of \underline{N} and n_c . Furthermore, the constant of proportionality, the mean rate of production formation per unit of flamelet area, relating Σ and $\langle w \rangle$ can be estimated from data on the thermal structure of the flamelets.

Crossed-plane imaging was developed in 1997 [1] at Cornell with ARO support to provide, for the first time, data for \underline{N} in three dimensions. The first measurements were performed to validate the technique and measure \underline{N} in laboratory flames and to find \underline{N} in a research spark-ignition, SI, engine [1-3]. Repeated measurements of \underline{N} allowed its PDF to be determined. It was found that, for laboratory V and engine flames, the PDF of \underline{N} has a simple form depending on a single parameter, ζ . In turn crossing density data, n_c , were used with the PDF of \underline{N} to determine Σ and mass burning rate information in V and engine flames. More recently, the technique has been applied to examine the dependency of the PDF of \underline{N} on Markstein number, Ma [4]. It was found for the flames studied that the dependency is very weak.

In the past year, we have investigated the use of single-plane imaging to find the fit parameter, ζ , in flames where the \underline{N} PDF form is the one found in V-flames and engine flames. We have studied the effect of engine cycle-to-cycle variations, CCV, on our engine measurements and have worked on crossed-plane Rayleigh imaging.

II. Crossed-Plane Imaging

Crossed-plane imaging is an extension of imaging techniques such as laser tomography (LT), planar Rayleigh imaging (PRI) and planar laser induced fluorescence (PLIF). In LT, oil droplets are added to the reactants and are consumed within the flamelet. A pulsed laser sheet is propagated through the flame, and an image is recorded normal to the laser sheet. The image contains bright reactant regions, where light is scattered from the oil droplets, and dark product regions where there is no scattering. The flamelet is located by the interface of the bright and dark regions, and fitting this interface provides two dimensional information about \underline{N} . PRI and PLIF can be used in much the same way as LT in crossed-plane imaging, except that the laser frequency must be chosen such that either molecular fluoresce (PLIF) or molecular scattering (PRI) is excited. In either case, lines of constant fluorescence or constant scattering can be identified in the illumination plane. Crossed-plane imaging involves simultaneous imaging from two orthogonal, pulsed laser sheets that intersect along a line, the measurement line. In the case of crossed-plane tomography, at points where the measurement line intersects the flamelet curves identified in the recorded images, tangent vectors to these curves are tangents to the flamelet surface. Thus the cross product of two such tangents is parallel to \underline{N} in three dimensions. In crossed-plane PLIF and crossed-plane PRI contours of constant light intensity can be determined. Tangents to an iso-contour are also tangents to the corresponding iso-concentration surface in the case of PLIF or iso-thermal surface in the case of RRI. Thus along the line of intersection of the two illumination planes pairs of iso-surface tangents can be determined and their cross product used to find iso-surface normals. We are preparing now to use crossed-plane PRI to find iso-thermal surface normals and temperature gradients using the relationship between the temperature gradient and the directional derivative of the temperature.

III. Single Plane Measurements of the Fit Parameter.

The most significant discovery so far from our crossed-plane imaging measurements has been that the PDF of \underline{N} appears to have a universal form: the surface weighted PDF of \underline{N} is

$$P_s(\phi, \theta) \sin\phi d\phi d\theta = A \exp(-\phi^2/\zeta^2) \sin\phi d\phi d\theta \quad (1)$$

when written in spherical coordinates with the polar axis aligned with the mean of the \underline{N} , $\langle \underline{N} \rangle$, or equivalently with the normal to a mean progress variable constant ($\langle c \rangle$) surface, $\underline{N}_{\langle c \rangle}$ [2-4]. ϕ is the polar angle, θ is the azimuthal angle, and A is a normalization constant.

It is desirable when possible to extract three-dimensional \underline{N} data from single plane, two-dimensional image data because of the simplicity of such measurements. Single plane imaging allows measurements of flamelet orientation at any point along the flamelet curve, while in crossed-plane imaging, which involves simultaneous orthogonal, single plane measurements, orientation data can only be obtained along the line of intersection of the two illumination planes.

To evaluate the potential for single plane measurements we determined the relationship between the PDF of \underline{N}_{yz} , the projection of \underline{N} onto a plane perpendicular to the $\langle c \rangle$ constant surfaces and the PDF of \underline{N} given in Eq. (1) [5]. We found that because of the rotational symmetry about the polar axis three-dimensional information can be obtained from two dimensional image data if the imaging plane contains the polar axis, which it does if aligned

perpendicular to the $\langle c \rangle$ constant surfaces. The angle between \underline{N}_{yz} and the polar axis is defined as α . Computations were performed to generate the PDF of α , $P(\alpha)$, from the crossing-weighted PDF of \underline{N} . The resulting α PDF is found to depend on a single fit parameter γ that is a unique function of ζ , Figure 1 [5].

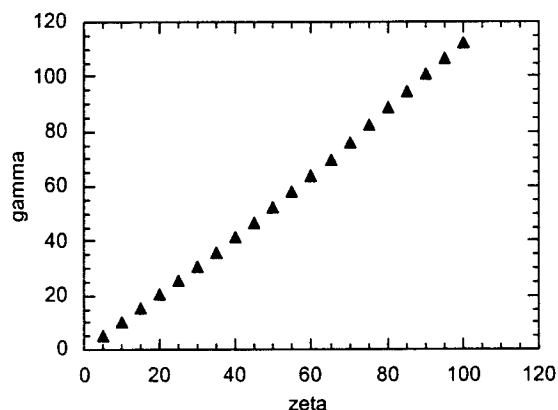


Figure 1. γ , the PDF fit parameter of α generated over a range of ζ , the PDF fit parameter of \underline{N} .

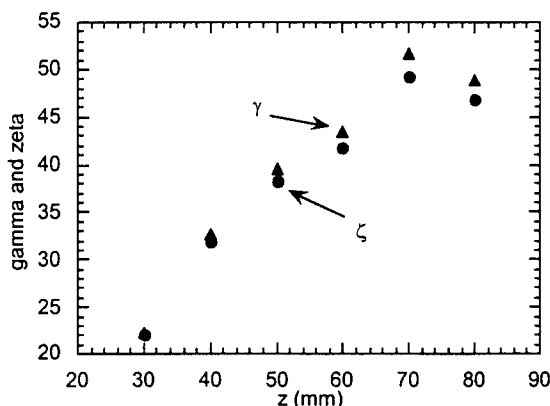


Figure 2. Variation of measured γ and calculated ζ with increasing downstream distance, z .

To demonstrate the utility of this relationship, the evolution of ζ , and γ with increasing downstream distance in a methane-air V-flame was studied. α was measured by imaging a single, vertical plane perpendicular to the V-flame stabilizing rod. $\langle c \rangle$ constant surfaces for a V-flame are planes containing the stabilizing rod; therefore the normal to a $\langle c \rangle$ constant surface, the polar axis, is within the imaging plane described above. The PDF of α and the two-dimensional fit parameter γ were estimated from repeated measurements. Using the relationship between γ and ζ determined computationally (Fig. 1), ζ was obtained from γ . Six positions were studied, beginning at 30 mm downstream from the stabilizing rod with measurements taken in 10 mm increments. These measurements [5] show that ζ initially increases linearly with z close to the stabilizing rod, while the relationship becomes nonlinear further downstream, Figure 2. This trend seems reasonable. While u' decreases with downstream distance, wrinkling is damped close to the flame stabilizing rod and is expected to grow downstream.

IV. SI Engine: Study of Cycle-to-Cycle Variation (CCV) Effects

In Reference 3 we reported SI engine, crossed-plane acetone PLIF measurements of \underline{N} and the use of these \underline{N} data to estimate mass burning rates. The mass burning rate estimates were compared to values obtained from pressure data and found to be quite high. In the last year we reanalyzed the image data for evidence of CCV and its possible influence on these estimates [6].

Evidence for the presence of CCV and its effects were found in the imaging data. Determination of an effective turbulent flame area was found to be affected by CCV, however these CCV effects did not result in an over-prediction of the area, and therefore burning rate, as expected. Other possible factors contributing to the discrepancy in burning rate values based on \underline{N} data include the choice of the surface that is used to define the turbulent flame area and underestimation of the perturbation of flamelet structures by turbulence.

V. Crossed-Plane Rayleigh Imaging

At low levels of turbulence the flamelet is wrinkled by turbulent flow fluctuations thereby increasing Σ , but its internal structure is not perturbed. As the turbulence intensity increases perturbation of the flamelet structure increases, first in the low temperature preheat zone and then, as the intensity continues to increase, all over. Finally at high turbulence the flamelet can be quenched locally. To help quantify the perturbing effect of turbulence and how it increases with turbulence intensity we will be making crossed-plane Rayleigh imaging measurements.

To perform these measurements we are using a frequency doubled Nd: YAG laser and two intensified CCD cameras. Rayleigh scattering is proportional to the molecular number density and in the case of lean methane-air mixtures the scattering cross section of the gases is a weak function of c . Thus by PRI we will be able to identify using the ideal gas law iso-thermal contours in the recorded Rayleigh scattering images. Then with crossed-plane imaging we will be able to find along the line of intersection of the laser illumination planes normal vectors to iso-thermal surfaces. Directional temperature derivatives along this line can also be determined, and the combination of surface normal and directional derivative used to find the temperature gradient.

Our plan is to make crossed-plane Rayleigh measurements in a variety of flames and find T and $\text{grad } T$ versus the progress variable. Then to assess the degree of flamelet structure perturbation we will compare measured values of T and $\text{grad } T$ to ones calculated for unperturbed flames based on GRIMech chemistry.

To date we have set up the Rayleigh imaging system and have made measurements on a laminar flame. Measured and calculated temperature profiles have been compared and good agreement found.

VI. Summary

Crossed-plane imaging was developed to measure flamelet normal distributions and has been used in V-flame and engine measurements. The PDF of the normal takes a simple form with a single parameter. We have shown how single plane measurements can be used to find this parameter and using this approach measured the spatial variation of this parameter in V-flames. Review of our engine data shows effects of CCV. Progress in developing crossed-plane Rayleigh scattering is reported. High quality single image data have been obtained. Crossed-plane measurements will begin soon. For the next year we will pursue flamelet normal and flamelet thermal structure measurements and thanks to a DURIP award add stereo-PIV to our measurement capabilities.

References

1. Bingham, D. C., M. S. Thesis, Cornell University, Ithaca, NY (1998).
2. Bingham, D. C., Gouldin, F. C., Gouldin, F. C., *Proc. Comb. Inst.* **27**: 77-84 (1998).
3. Knaus, D. A., Gouldin, F. C., Hinze, P. C., Miles, P. C., SAE Paper 1999-01-3543, 1999.
4. Knaus, D. A., Gouldin, F. C., to appear in *Proc. Comb. Inst.* **28** (2000).
5. S. S. Sattler, D. A. Knaus, and F. C. Gouldin, "Measurements of Three-Dimensional Flamelet Orientation Distributions of Turbulent V-Flames at Various Axial Heights From Two-Dimensional Data", Proceedings of the Second Jt. Meeting of the US Sections of the Combustion Institute, Combustion Institute, Pittsburgh, PA. (2001)
6. Knaus, D. A., Gouldin, F. C., "Cycle-to-Cycle Variations and Burning Rate Estimates of SI Engine Flames Based on Flamelet Orientation Measurements," Proceedings of the Second Jt. Meeting of the US Sections of the Combustion Institute, Combustion Institute, Pittsburgh, PA. (2001)

SIMULTANEOUS MEASUREMENT OF RELATIVE OH
CONCENTRATION, TEMPERATURE, AND FLOW VELOCITY IN
H₂/O₂ FLAME BY SATURATED PHOTOTHERMAL SPECTROSCOPY

ARO Grant No. DAAG55-98-1-0278

Principal Investigator: R. Gupta

Department of Physics
University of Arkansas
Fayetteville, Arkansas 72701

SUMMARY/OVERVIEW:

The object of our experiments is to develop photothermal deflection spectroscopy (PTDS) into a technique capable of measuring minority species concentration, temperature, and flow velocity, simultaneously in a flame. We have demonstrated the simultaneous measurement of *relative* OH concentration, temperature, and flow velocity in an H₂/O₂ flame using saturated PTDS. By working in the saturation regime, relatively large signal-to-noise ratio is obtained, and effect of pulse-to-pulse energy fluctuation is minimized. In the next period we will try to obtain *absolute* concentration measurements, along with the temperature and the flow velocity.

TECHNICAL DISCUSSION:

The goal of our experiments is to develop photothermal spectroscopy (PTDS) for a simultaneous measurement of the minority species concentration, temperature, and flow velocity in a flame. The basic idea is as follows: A laser beam (hereafter called the pump beam) passes through the flame. The laser is tuned to the absorption frequency of the molecules to be measured. The molecules absorb energy from the laser. Subsequently, most of the molecules decay by nonradiative means (i.e., they are collisionally de-excited). Thus, the optical energy eventually appears in the thermal modes of the flame gases. In other words, the optically irradiated region gets slightly heated. The heating is accompanied by a change in the index of refraction. This refractive index change is probed by another, weaker laser beam which we shall refer to as the probe beam. The change in the refractive index has a spatial profile that mimics the spatial profile of the pump beam. The pump beam is assumed to have a Gaussian spatial profile. Thus, the probe beam experiences an inhomogeneous refractive index, and gets deflected by a small amount. We measure this deflection and the amplitude of the deflection is proportional to the concentration of the absorbing species. We use a pulsed laser for the pump beam. Thus, the absorption of the pump beam produces a pulse of heat. In a flowing medium, the heat pulse travels downstream with the flow. We set our probe beam slightly downstream from the pump beam. We measure the transit time of the heat pulse and, from it, deduce the flow velocity of the medium. The heat pulse broadens due to thermal diffusion as it travels downstream. From a measurement of this broadening we determine the thermal diffusion

constant of the medium. Since the thermal diffusion constant is proportional to the temperature of the medium, we can measure the temperature of the medium. Thus, the measurements of the amplitude, transit time, and the broadening of the photothermal deflection signal can yield measurements of the species concentration, flow velocity, and temperature, respectively, all simultaneously in a single laser pulse.

We started our experiments in a well-characterized cold flow (a room-temperature jet of N_2 , seeded with 0.5% of NO_2). We chose NO_2 as the seed gas for experimental convenience. NO_2 is gaseous at room temperature, and has a quasi-continuous absorption throughout the visible range of the spectrum. Photothermal signals from laser absorption by NO_2 were observed. For laser energy necessary to obtain sufficient signal-to-noise ratio, the PTDS signals were observed to have significant optical saturation. The analysis of the signals in the presence of optical saturation is complicated. The effect of optical saturation on the PTDS signals, with the absorbing species modeled as a two-level system, was investigated.¹ The PTDS signals from NO_2 were analyzed for NO_2 concentration, temperature, and the flow velocity by a multiparameter fitting procedure and, after correction for the effects of optical saturation and flow velocity gradients, reliable values of the three parameters were obtained.²

Having learned about all the issues that can complicate the analysis of the PTDS signals and could possibly lead to erroneous results in a well-characterized cold flow, we have now started the flame experiments. PTDS signals generated by OH in a stoichiometric H_2/O_2 flame have been observed, and analyzed to yield relative OH concentration, temperature, and flow velocity by the multiparameter fitting procedure. Figure 1 shows the three measured parameters as a function of the position from the center of the flame. Panel (a) shows the relative OH concentration; Panel (b) shows the temperature; and, Panel (c) shows the flow velocity. In Panel (a), the solid circles represent the profile of the relative OH concentration determined from the PTDS signal amplitude with the probe beam 0.03mm upstream from the pump beam where the maximum PTDS amplitude occurs immediately after the laser excitation. The open circles represent profile of the relative OH concentration obtained from the PTDS signal with the probe beam 0.33m downstream from the pump beam. The general agreement between these two profiles gives us confidence that the relative OH concentration shown here is the true profile of the OH concentration. The measured temperature shown in Panel (b) is obtained from the measured thermal diffusivity via the temperature dependence of the thermal diffusivity of the H_2O steam. The dashed line in Panel (b) indicates the theoretical temperature of 3080K, for a 1:1 H_2/O_2 flame. It shows that the measured temperature is close to the literature value. The open circles in Fig. 1(c) show the measured values of the flow velocity. The solid line is a fit to the data, assuming that the velocity profile is given by an ideal laminar flow. The fitted value of maximum velocity is 45.0m/s, which is close to the value, 43.2m/s, derived from the measurement of the flow rate of the gases by a flowmeter and assuming the radius of the flame at the measurement height to be 4.4mm (which is the half-width of the solid curve in Fig.1(c)) and the flame temperature to be 3080K. These results have been submitted for publication to *Applied Optics*.³

In conclusion, we have demonstrated, for the first time, the measurement of the kinetic temperature of a flame by the PTDS technique, and also demonstrated that a simultaneous measurement of the relative concentration of minority species, temperature, and the flow velocity can be made from the analysis of a *single data trace*. To the best of our knowledge, no other technique has demonstrated the *simultaneous* measurement of these three parameters in a flame.

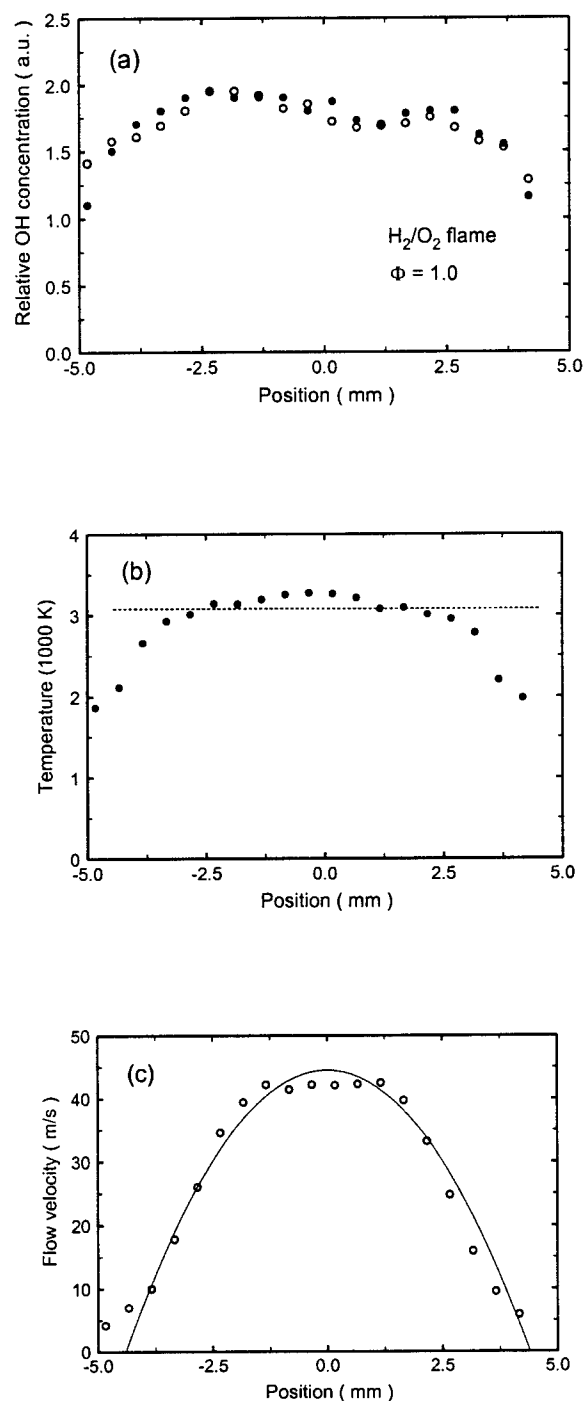


Figure 1. The radial distribution of the (a) relative OH concentration; (b) temperature; and, (c) flow velocity, simultaneously measured in a 1:1 H_2/O_2 flame. The open circles in (a) represent the relative OH concentration measured with the probe beam 0.33mm downstream from the pump beam whereas the solid circles represent that measured with the probe beam 0.03mm upstream. The dashed line in (b) shows the theoretical value of the temperature. The solid curve in (c) is the best fit to the data by the velocity distribution of an ideal laminar flow.

We have worked in the energy range where the PTDS signal is optically saturated, thus, an accurate measurement of the laser pulse energy is not important and pulse-to-pulse fluctuations in energy do not significantly degrade the reliability of the results.

OH concentration measurements we have made are the *relative* concentration measurements. It is the goal of our experiments to measure absolute concentrations without calibration against a flame with known concentration. In order to obtain absolute concentration without calibration, we need to have a quantitative understanding of the effects of optical saturation on a real molecule like OH, which cannot be modeled as a simple two-level system. Our goal in the next reporting period is to achieve such an understanding and to make absolute concentration measurements simultaneously with temperature and flow velocity.

References:

- B. C. Li and R. Gupta, *Journal of Applied Physics*, **88**, 5515-5526 (2000).
- B. C. Li and R. Gupta, *Journal of Applied Physics*, **89**, 859-868 (2001)
- B. C. Li and R. Gupta, *Applied Optics*, submitted, 2001.

SHOCK TUBE MEASUREMENTS OF IGNITION PROCESSES IN DIESEL-RELATED FUELS

ARO contract - to begin June 1, 2001

Principal Investigator: Ronald K. Hanson

High Temperature Gasdynamics Laboratory
Mechanical Engineering Department
Stanford University, Stanford, California 94305-3032

SUMMARY/OVERVIEW

We are beginning a three-year program of basic research concerned with chemical kinetics of diesel and diesel fuel surrogates. The work is intended to support efforts underway in other laboratories to develop improved diesel engine performance. The research will be carried out in the Stanford shock tube facilities and will focus on two areas: (1) measurement of shock tube ignition times and individual species concentration time-histories in gas-phase diesel surrogates, and (2) investigation of the reactive behavior of fuel spray droplets in shock-heated gases. Both high-pressure and low-pressure shock tubes will be used in the gas-phase investigations, and a new facility will be assembled (from an existing shock tube) for fundamental studies of fuel sprays in shock-heated gases. Modern optical diagnostic techniques will be employed to build data sets for these reactive flows.

TECHNICAL DISCUSSION

The research will involve (1) accurate measurements of ignition time and their use to create reliable correlations for a variety of diesel fuel surrogates, and blends of surrogates to simulate diesel, useful over wide ranges of temperature, pressure, fuel mole fraction, and stoichiometry, (2) measurements of individual species concentration time-histories behind shock waves to improve or validate detailed kinetic mechanisms and establish reduced mechanisms, (3) use of a new UV absorption kinetic spectrograph for the identification of transient fuel fragments, and (4) acquisition of data on fuel spray behavior that will aid development and validation of CFD models of spray break-up, evaporation and combustion.

Measurements of species concentration time-histories place stronger constraints on kinetic models than ignition times alone. Figure 1 shows a comparison of post-shock OH species time-histories for n-decane oxidation acquired using ring-dye laser absorption and modeled using the kinetic mechanism of Lindstedt and Maurice (1995). Though the modeled ignition times are within a factor of two of the experimental values, improvements in the model are clearly needed to bring the model results into agreement with the data.

The identification of elementary decomposition products of primary fuel components, and of transient intermediates in the combustion process, are also needed for development of correct kinetic mechanisms. Figure 2 shows two high temperature UV absorption spectra, that of 1,3-butadiene and cyclopentadiene, that were acquired using our recently acquired kinetic

spectrograph. This new diagnostic enables recording of broad absorption spectra (190-300 nm) at 10 μ s intervals, i.e. multiple spectra can be recorded in each shock tube kinetics experiment. The intermediates shown in Fig. 2 are expected to be present on the reaction pathway from diesel fuel decomposition and oxidation to aromatic and soot formation. By quantifying the absorption spectra of these and other intermediate fuel products, and recording time-resolved spectra using the kinetic spectrograph, we hope to identify the primary decomposition and oxidation pathways for diesel fuel surrogates and to build a data base for the time histories of these species in shock-heated mixtures.

The availability at Stanford of unique flow facilities (low and high-pressure shock tubes and a new shock tube spray combustion facility) and diagnostic capabilities (high-speed schlieren, PLIF, laser absorption, UV kinetic spectrograph, and other spectroscopic techniques) will enable acquisition of new and unique data on hydrocarbon fuel pyrolysis and oxidation, and lead eventually to improved, detailed kinetic models of combustion in engines.

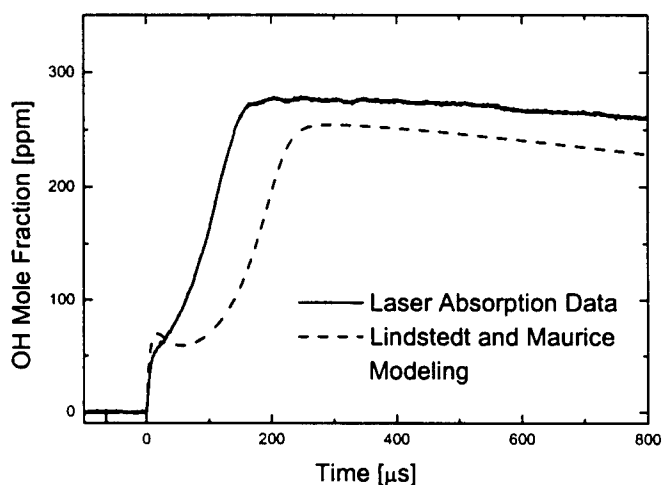


Fig. 1. n-Decane oxidation. A comparison of measured and calculated OH time-history in shock heated n-decane/oxygen/argon. Reflected shock conditions: 300 ppm n-decane, $\phi = 1.0$, $T = 1661$ K, $P = 2.08$ atm

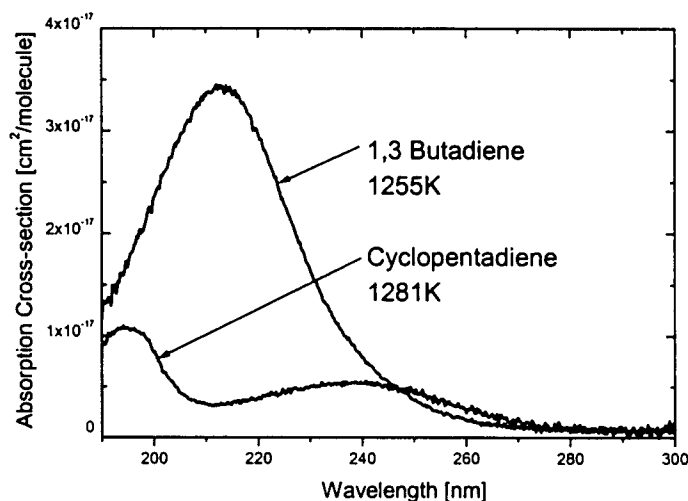


Fig. 2. UV absorption spectra of two dienes acquired behind reflected shock waves using the kinetic spectrograph. These and other high temperature spectra will be used to identify stable and transient decomposition products of diesel and diesel fuel surrogates

ADVANCED DIAGNOSTICS FOR REACTING FLOWS

AFOSR 01-1-0145

Principal Investigator: Ronald K. Hanson

**High Temperature Gasdynamics Laboratory
Mechanical Engineering Department
Stanford University, Stanford, California 94305-3032**

SUMMARY/OVERVIEW:

The goal of this research is to develop advanced laser-based techniques for non-intrusive measurements relevant to air-breathing combustion. In general, the program emphasizes spectrally-resolved absorption using tunable laser sources and planar laser-induced fluorescence (PLIF), conducted using either near-infrared or ultraviolet laser sources. Detailed below is progress on the exploration of IR PLIF as a diagnostic for imaging IR-active gases and on the suitability of pentanone as an alternative flow tracer to acetone for PLIF imaging. Furthermore, a novel absorption sensor for NO_2 at temperatures up to 1900 K has been developed, and continuing work is reported on the spectroscopy of high-pressure gases.

TECHNICAL DISCUSSION:

Infrared PLIF Imaging

Infrared Planar Laser-Induced Fluorescence (IR PLIF) has high potential for visualizing CO , CO_2 , and other IR-active species in reactive flows. Fig. 1 shows a basic IR PLIF set up, including an IR laser source. The slow characteristic times of vibrational relaxation and the large mole fractions for CO and CO_2 in typical flows lead to high IR PLIF signal levels, despite the low emission rates typical of vibrational transitions. Analyses of rotational energy transfer (RET) and vibrational energy transfer (VET) show that excitation schemes in either linear (weak) or saturated (strong) limits may be developed, with the fluorescence collected directly from the laser-excited species or indirectly from bath gases that are in vibrational resonance with the laser-excited species. An example of the latter scheme is shown in Fig. 2, where PLIF images are obtained of CO fuel and the CO/CO_2 interface of a laminar diffusion flame, by using an identical excitation of CO . Near-resonant vibrational energy transfer (VET) processes carry energy from the laser-pumped CO molecules into the CO_2 molecules such that CO_2 fluorescence is observed at the CO/CO_2 interface.

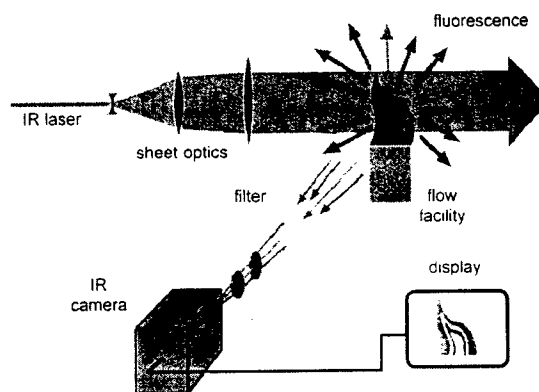


Fig. 1 Simplified Schematic of IR PLIF Imaging setup.

Linear excitation is appropriate for CO due to its slow vibrational relaxation. However, linear excitation is not well-suited for CO₂ imaging due to fast H₂O-enhanced VET and the attendant difficulty in interpreting the resulting signal. Saturated excitation using a CO₂ laser technique, however, has been found to be appropriate for CO₂, as it generates high signals and mitigates spatial variations in fluorescence quantum yield. Fig. 3 shows results from IR PLIF imaging of CO₂ in a lifted diffusion flame along with comparisons to benchmark CFD predictions and a composite of fifty, 5000-shot-averaged, 1-D, Raman measurements conducted at Yale by Smooke and Long.

Accomplishments in this work include the first IR PLIF diagnostics for CO and CO₂, the first detailed analysis of excitation schemes for these species, the first results using saturated laser excitation, and the first techniques that use combined laser / VET pumping schemes. These diagnostic developments enable single-shot images of these species in a manner not previously realized. Since IR PLIF is in principle applicable to all IR-active species, it has high potential for expanding the diagnostic possibilities available to combustion researchers, which might include visualization of the preflame (fuel) region of lifted flames, CO formation regions in flames, or mixing of hot exhaust gases with the atmosphere.

Ketone Photophysics for Quantitative PLIF Diagnostics

Our past research on acetone fluorescence included the following elements:

- 1) fundamental photophysical research to quantify the relative strength of fluorescence as a function of temperature, pressure, and bath gas environment, and
- 2) using the fundamental results, development and demonstration of PLIF techniques to measure relevant parameters in flowfields of practical interest (e.g. mixing regions of combustors).

To this end, we studied acetone fluorescence up to 1000 K and 16 atmospheres and developed a photophysical model that allows extrapolation beyond current experimental data. We also

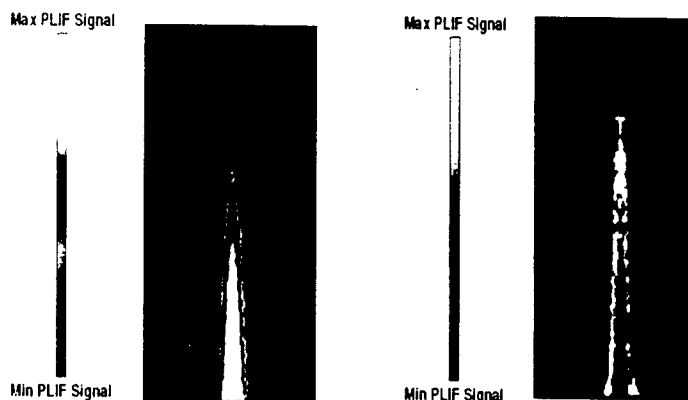


Fig. 2 The above two PLIF images of a steady CO/Ar/H₂ diffusion flame are realized by the excitation of the R(12) line of CO (2.35 μ m) followed by collection of CO fluorescence to visualize the fuel (left), and collection of CO₂ fluorescence to visualize the fuel/product interface (right).

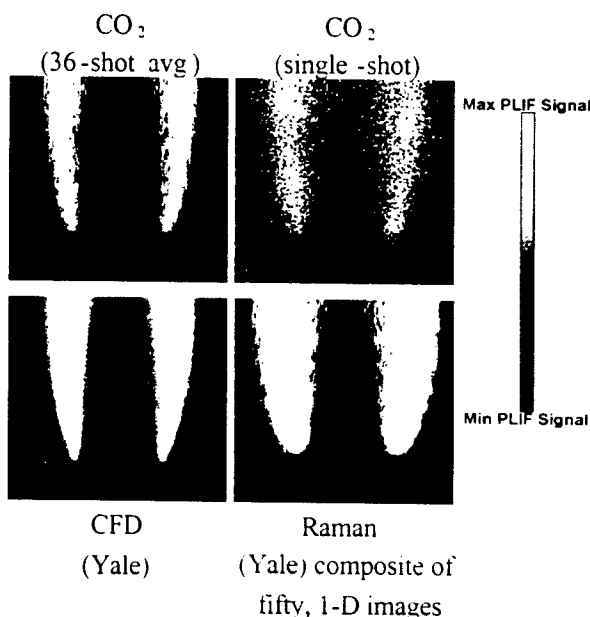


Fig. 3 Measurement and prediction of CO₂ distribution in a laminar lifted CH₄ diffusion flame. Clockwise from top left: 36-shot average IR PLIF image of CO₂; single-shot image of CO₂; overlay of fifty, 5000-shot-averaged, 1-D, Raman images (Yale); and computational prediction of CO₂ concentration (Yale). Yale results are courtesy of M. B. Long and M. D. Smooke.

demonstrated simultaneous, two-dimensional temperature and concentration measurements in unsteady flows.

Recently, we have begun to study attractive alternatives to acetone using the same fundamental approach. This was motivated by the need for a variety of tracers with physical properties (e.g. boiling points, diffusion coefficients) that match relevant fuels. Other ketones, because of their photophysical similarity to acetone (boiling point 56 °C) are primary candidates. We are thus investigating larger molecules like 3-pentanone (boiling point 100 °C), and we have discovered some key differences between pentanone and acetone. Most importantly, the ratio of fluorescence from two different excitation wavelengths as a function of temperature is not the same for acetone and 3-pentanone; rather, 3-pentanone tends to be more temperature-sensitive for similar excitation wavelengths (e.g., see Fig. 4, comparing the two 308/248 nm curves). The trade-off for this increased temperature sensitivity is a decrease in the signal at high temperatures. However, the temperature range of 3-pentanone PLIF can be extended by choosing a slightly less sensitive wavelength combination, e.g. 308/266 nm excitation. Through continued fundamental studies, a ketone database is being developed that will allow optimal selection of tracer and excitation strategy for a broad range of practical applications.

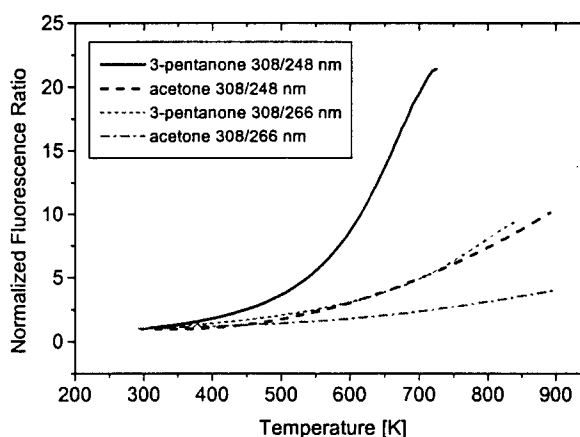


Fig. 4 Fluorescence ratio of acetone and pentanone as a function of temperature for two combinations of excitation wavelength.

Blue Diode Laser Absorption Sensor for NO₂

A highly sensitive and economical NO₂ diagnostic has been developed using a stable diode laser light source tuned to 390.130 nm. Single-pass absorption techniques were used to measure the absorption cross-section of NO₂ at 298 K in a flowing cell, and at elevated temperatures behind incident and reflected shocks in a shock tube. Optical absorption at this wavelength, in the dense NO₂ A-X spectrum, was found to have little variation with wavelength and pressure, thus simplifying analysis. The absorption cross-section, shown in Fig. 5, was found to vary approximately linearly with temperature. The utility of this diagnostic was demonstrated by studying NO₂ decomposition at temperatures ranging from 1500 K to 1900 K, and comparing the results with model predictions using established reaction rate constants.

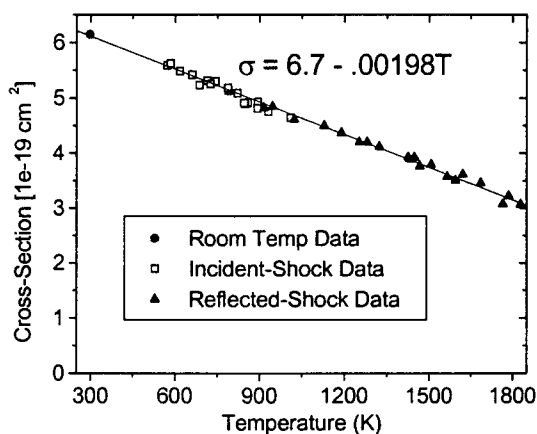


Fig. 5 NO₂ cross-section vs. temperature at 390.13 nm (at pressures of 0.2 to 1.7 atm).

Laser-Induced Fluorescence Diagnostics for NO in High-Pressure Combustion Gases

Laser-induced fluorescence (LIF) of NO in the A-X bands has become an important tool for monitoring pollutant production and for measuring properties such as gas temperature or velocity in flows seeded with trace quantities of NO. Earlier work at Stanford identified two difficulties which must be overcome for routine application of NO LIF at combustion temperatures and high

pressures. First, pressure broadening causes NO and hot vibrational O₂ transitions to overlap. As a result, LIF from O₂ obscures the NO signal, especially in fuel-lean, high-pressure environments found in advanced gas turbine combustors. Second, the spectroscopic database for NO and O₂ does not contain sufficient hot band positions, pressure-broadening information, or collisional energy transfer rates (rotational and vibrational) for quantitative LIF measurements.

NO (X²Π) has three vibrational levels with sufficient population at combustion temperatures for practical LIF: v=0, 1, and 2. We began a systematic investigation of high-pressure NO LIF, emphasizing the A-X (0,1) transitions where there is a paucity of data. In a new high-pressure, premixed burner, we excited nascent and 300 ppm seeded NO using wavelengths between 236.5 and 237.5 nm at pressures between 1 and 60 bar. The ensuing fluorescence was dispersed in an imaging monochromator, and the fluorescence spectrum was recorded with an intensified CCD array. We observed that the NO structure is discrete at 1 bar, becomes blended by pressure broadening at 10 bar, and is dominated by O₂ interference at 40 bar. The NO rotational structure is not discernable at 60 bar. Work is in progress to quantify and model these spectra and to evaluate the relative merits of measuring NO by LIF of the A-X (0,0), (0,1) or (0,2) bands.

The choices between NO LIF strategies are complicated by unexpected optical absorption of hot flame gases; e.g., in-cylinder absorption spectra indicate that light at 225 nm (NO A-X (0,0)) is significantly absorbed by unknown species and bands. We have used a newly-developed UV kinetic spectrograph to measure the optical absorption of shock-heated CO₂ between 190 and 300 nm and found surprisingly strong temperature dependence in this optical absorption. This recent observation may explain the unexpected UV absorption of hot combustion gases.

PUBLICATIONS:

E.R. Furlong, R.M. Mihalcea, M.E. Webber, D.S. Baer and R.K. Hanson, "Diode Laser Sensors for Real-Time Control of Pulsed Combustion Systems," *AIAA J.* **37**, 732-737 (1999).

M.C. Thurber and R.K. Hanson, "Simultaneous Imaging of Temperature and Mole Fraction using Acetone Laser-Induced Fluorescence," *Experiments in Fluids* **30**, 93-101 (2001).

M.C. Thurber and R.K. Hanson, "Pressure and Composition Dependence of Acetone Laser-Induced Fluorescence with Excitation at 248, 266 and 308 nm," *Appl. Physics B* **69**, 229-240 (1999).

D.F. Davidson and R.K. Hanson, "Spectroscopic Diagnostics," in *Handbook of Shock Waves*, Vol. 1, Chapter 5.2, Academic Press, eds., 2001.

G. Totschnig, D.S. Baer, J. Wang, F. Winter, H. Hofbauer and R.K. Hanson, "Multiplexed Continuous-Wave Diode-Laser Cavity Ringdown Measurements of Multiple Species," *Appl. Optics* **39**, 2009-2016 (2000).

J. Wang, M. Maiorov, D.S. Baer, D.Z. Garbuzov, J.C. Connolly and R.K. Hanson, "In Situ Measurements of CO using Diode Laser Absorption near 2.3 microns," *Applied Optics* **39**, 5579-5589 (2000).

A. Ben-Yakar and R.K. Hanson, "Characterization of Expansion Tube Flows for Hypervelocity Combustion Studies in the Flight Mach 8-13 Engine," *J. Prop. and Power*, submitted 5/2000.

J. Wang, S.T. Sanders, J.B. Jeffries and R.K. Hanson, "Oxygen Measurements at High Pressures using Vertical Cavity Surface-Emitting Lasers," *App. Phys. B* **72**, (2001).

S.T. Sanders, J. Wang, J.B. Jeffries and R.K. Hanson, "VCSEL Absorption Sensor for Line-of-sight Temperature Distributions," *App. Optics*, submitted 12/2000.

A. Ben-Yakar and R.K. Hanson, "Cavity Flame-Holders for Ignition and Flame Stabilization in Scramjets: An Overview," *J. Prop. and Power*, in press.

J.T.C. Liu, R.K. Hanson and J.B. Jeffries, "High-Sensitivity Absorption Diagnostic for NO₂ using a Blue Diode Laser," *J. Quant. Spectrosc. and Radiat. Transfer*, in press.

B.J. Kirby and R.K. Hanson, "CO₂ Imaging using Saturated Planar Laser-Induced Vibrational Fluorescence," *Applied Optics*, submitted 1/2001.

MODELING DIESEL ENGINE INJECTOR FLOWS

ARO Contract Number DAAG55-98-1-0318

Stephen D. Heister and Gregory A. Blaisdell

Purdue University, School of Aeronautics and Astronautics
1282 Grissom Hall, W. Lafayette, IN 47907-1282

SUMMARY/OVERVIEW:

This project is focused on the study of flows inside diesel injector flow passages with emphasis on resolution of time-dependent cavitation regions within the device. During the past year, the turbulent axisymmetric model has undergone substantial validation. In addition, an improved inflow boundary condition has been developed to increase accuracy in predicting discharge characteristics of these devices.

TECHNICAL DISCUSSION

A drilled orifice is widely used to provide a simple solution for atomizing liquids and the presence of cavitation inside such a nozzle has received much attention in the past due to its broad applications. Recent experiments have shown that the turbulence in the nozzle hole resulting from cavitation is a mechanism that promotes atomization. Gopalan and Katz^[1] observed that the unsteady cavity collapse involves substantial increases in turbulence intensity, and momentum and displacement thicknesses in the boundary layer. They also showed that the collapse of bubbles is the dominant source of vorticity downstream of a cavity. The present calculations add $k - \omega$ turbulence model to Chen and Heister's^[2] homogeneous fluid model to simulate the turbulent cavitating flow in a nozzle hole. We chose to use the $k - \omega$ model because it has better performance than other turbulence models in adverse pressure gradient flows which are common cases in cavitating flows.

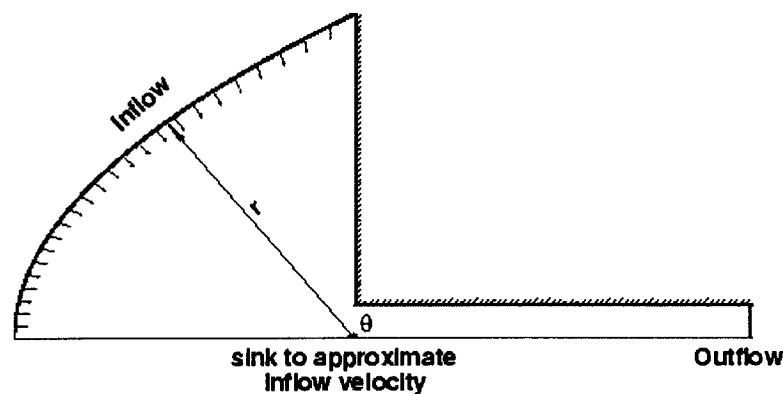


Figure 1 Schematic representation of a sink approximation of inflow velocity.

In flow velocity boundary conditions are obtained by placing an artificial sink at the origin as shown in Fig. 1. For a 2-D problem the velocity at the inflow boundary is calculated by $u_{in} = -(\Lambda / 2\pi r) \cos \theta$, $v_{in} = -(\Lambda / 2\pi r) \sin \theta$. The strength of the sink is updated during each time step by the conservation of mass flow rate through the nozzle passage. The only difference between an axisymmetric problem and a 2-D problem at this point is that a three-dimensional sink is utilized for the former. A few axisymmetric runs were made to compare with the discharge coefficient, C_D , measurements by Nurick^[3] on a circular orifice. Fig. 2 shows the

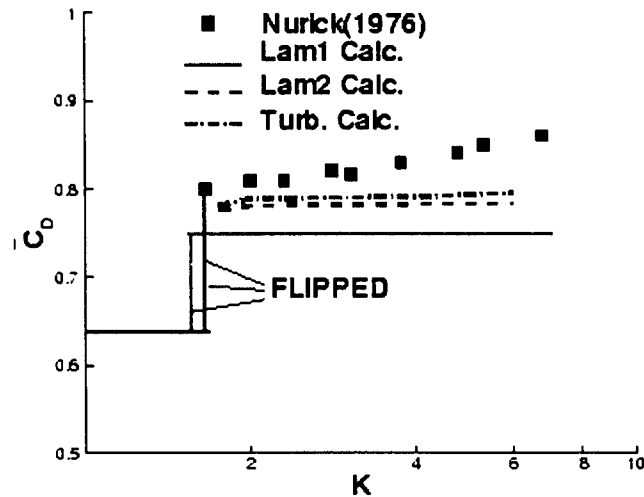


Figure 2 Discharge coefficient C_D comparison with experimental results; $L/D = 6$, $D = 3.18$ mm.

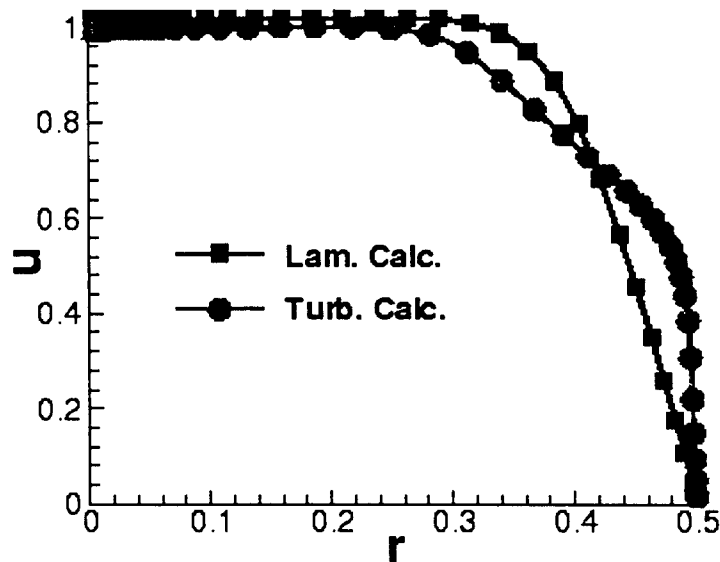


Figure 3 Comparison of velocity profiles at exit for laminar and turbulent solutions $L/D = 6$, $D = 3.18$ mm.

results of a comparison on an orifice of $L/D = 6$, $D = 3.18$ mm, under a back pressure of $P_2 = 13.8$ psi. As shown in Fig. 2, the sink inflow velocity treatment (Lam 2) greatly improves the prediction of discharge coefficient. The turbulence model shows a further improvement and gives results somewhat closer to the experimental data. The differences between the turbulence model and laminar predictions on C_D might be explained by Fig. 3 in which the exit velocity profiles are plotted for both laminar and turbulent calculations. The turbulent velocity profile is fuller than the laminar one. Due to this feature, the turbulence model yields a larger C_D by 1.6%.

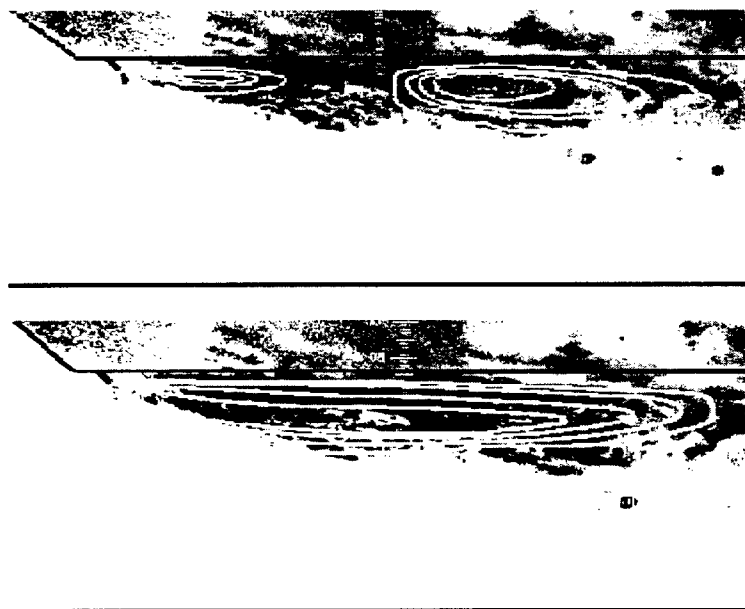


Figure 4 Side-View overlay of cavitation field and predicted pseudo-density contours. The upper image provides a comparison with a laminar flow calculation while the lower image depicts the improved results with a turbulent simulation.

Fig. 4 shows density contours, which denotes the cavity region, obtained from laminar (the upper one) and turbulent (the lower one) calculations, overlaying one photographic snapshot by Henry.^[4] Although the laminar simulation results in an overall cavitation extent consistent with experiment, it indicates two separate regions of cavitation. The turbulent model improves on this point by generating a single cavitation region which appears to be quite consistent with experimental results both in axial and cross-stream directions.

Fig. 5 shows velocity profiles inside the location of the cavity region for cavitating and non-cavitating conditions in a 2-D slot. The flow inside the cavitation region in general is slower under cavitating conditions than under non-cavitating conditions. Especially in the middle of the cavity ($x = 2$) a strong reverse flow occurs between the wall and cavity. At the end of the cavitation region ($x = 3$) the velocity profiles approach the same shape for both cavitating and non-cavitating conditions. Cavitation has a significant effect on the boundary layer development downstream. Although the turbulence model predicts the boundary layer thickness is almost identical for both cavitating and non-cavitating conditions, it produces increased displacement and momentum thicknesses for cavitating conditions. Other researchers^[1] have observed similar behavior experimentally.

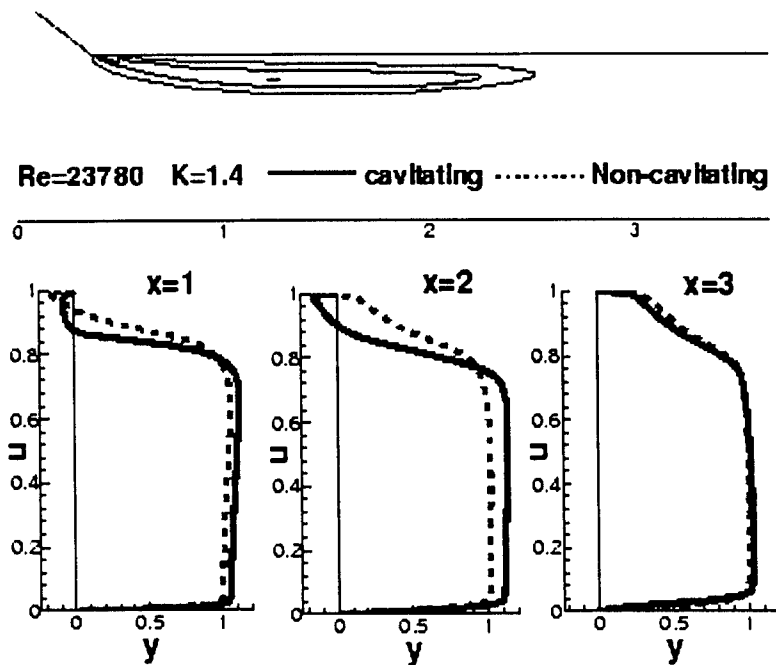


Figure 5 Velocity profiles under cavitating and non-cavitating conditions, $Re = 23780$, $K = 1.4$.

CURRENT EFFORTS

Most of the above results were published in.^[5] Current efforts are aimed at completing the work to be done under this grant. Turbulence model calculations are being done of the nozzle flow experiments of Katz.^[1] To date the comparison shows a discrepancy between the turbulence model computations and the experimental results. Much of the difficulty seems to lie with the turbulence model's ability to capture single phase separated flow. In addition work is progressing on examining three-dimensional effects due to a cross flow velocity at the inlet. The on-going work should be completed near the end of the summer.

REFERENCES

1. Gopalan, S. and Katz, J., "Flow Structure and Modeling Issues in the Closure Region of Attached Cavitation," *Physics Of Fluids*, Vol. 12, No. 4, April, 2000.
2. Chen, Y. and Heister, S.D., "Modeling Hydrodynamic Non-Equilibrium in Bubbly and Cavitating Flows," *J. Fluids Engineering*, V118, 172-178, 1995.
3. Nurick, W. H., "Orifice Cavitation and Its Effect on Spray Mixing," *Journal of Fluids Engineering*, Dec., pp. 681-687, 1976.
4. Henry, M. and Collicott, S.H., "Visualization of Cavitating Slot Flow," To Appear, *Atomization and Sprays*.
5. Xu, C., Blaisdell, R.A., and Heister, S.D., "Simulations of Turbulent, Cavitating Flows in an Injector Slot/Orifice," *Multiphase Flow 2001*, March 14-16, 2001, Orlando, FL.

ⁱAUTOIGNITION, COMBUSTION INSTABILITY AND WHITE SMOKE UNDER TRANSIENT CONDITIONS with JP-8 FUEL

Grant Number DAAG55-98-1-0285

Principal Investigator: Naeim A. Henein

Wayne State University
Center for Automotive Research
College of Engineering
5050 Anthony Wayne Drive
Detroit, MI 48202

SUMMARY

The goal of this project is to reduce the cold starting problems of military and commercial heavy-duty diesel engines, particularly the emission of white smoke. The failure of the autoignition process and/or combustion instability has been found to be the major causes of the cold starting problems. The approach is mainly experimental, supported by detailed analysis of the autoignition process. Models for the ignition delay period are developed considering the heterogeneity of the charge and the effect of piston motion during the ignition delay period. The maps developed for the stable combustion zone agreed fairly well with the experimental data. Also, the effect of diluents, such as exhaust gas recirculated into the fresh air (EGR) is experimentally investigated in two single-cylinder diesel engines. The effect of EGR on the global activation energy of the autoignition reactions is currently under investigation.

BACKGROUND

Cold starting problems in military and commercial diesel engines include the emission of large amounts of unburned fuel in the form of white smoke, hesitation, unreliable starting and complete failure of the engine to start. The current research showed that two factors contribute to such problems: a) failure of the autoignition process, and b) misfiring after starting due to combustion instability

EXPERIMENTAL WORK

Experiments were conducted in the cold room on a single-cylinder and a 4-cylinder heavy-duty diesel. The experiments covered two fuels: diesel fuel DF-2 used in the commercial sector and JP-8 fuel used in military vehicles. At normal room temperatures, combustion was unstable with JP-8, while it was stable with DF-2. At lower ambient temperatures, the engine failed to start on JP-8. With DF-2, combustion instability and white smoke increased with the drop in temperature.

The delayed start of combustion late in the expansion stroke has been found to cause the failure of the autoignition process. This indicated the low rates of the autoignition reactions resulting in fairly long ignition delays.

IGNITION DELAY

In order to develop strategies for successful autoignition, injection timing need to be advanced to account for the increase in the ID. A correlation is needed to account for the increase in ID due to the drop in temperature and piston motion during the expansion stroke. The commonly used correlation accounts for the change in temperature, and is only suitable for ignition in a constant volume environment.

$$\tau_{id} = Ap^{-n} \exp\left(\frac{E_A}{RT}\right)$$

Where p: pressure, E_A : global activation energy, R : universal gas constant and T: absolute temperature.

A NEW IGNITION DELAY FORMULATION

A new correlation is developed in this program for dF-2 to account for the change in the cylinder volume V during ID:

$$\frac{dX}{dt} = 0.876 p^{1.899} e^{-\frac{4665}{T}} - \frac{X}{V} \frac{dV}{dt}$$

X is the ratio of the chain carriers produced at any time t divided by the critical concentration of the chain carriers. In this model, autoignition is assumed to occur when the concentration of the chain carriers reaches a critical value.

PREDICTION OF MISFIRING ZONE BOUNDARIES

The ID, in crank angle degrees, is calculated for DF-2, at an ambient temperature of 20°C, at different injection timings as shown in the figure. The injection timing for minimum ID occurs earlier before TDC as the speed increases. Retarding the injection beyond a certain point results in complete misfiring. This is caused by the drop in the gas temperature during the expansion stroke and the resulting slowing down of the autoignition reaction rates. The analysis indicated that misfiring occurs at an earlier injection timing at higher speeds. Figure (1) shows the boundaries of the misfiring zone, predicted by the theoretical analysis.

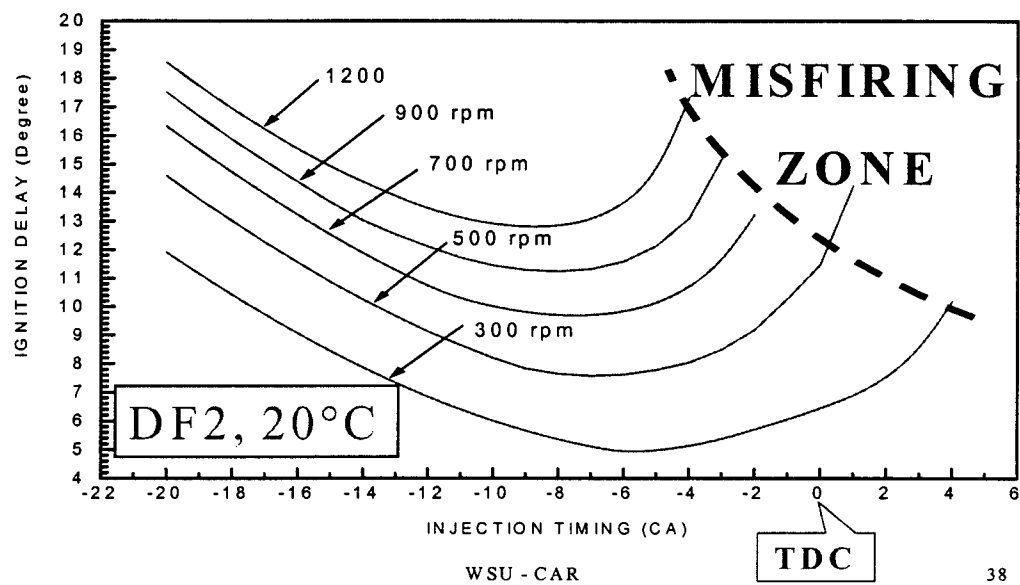


Figure 1. Effect of injection timing on ignition delay and misfiring zone

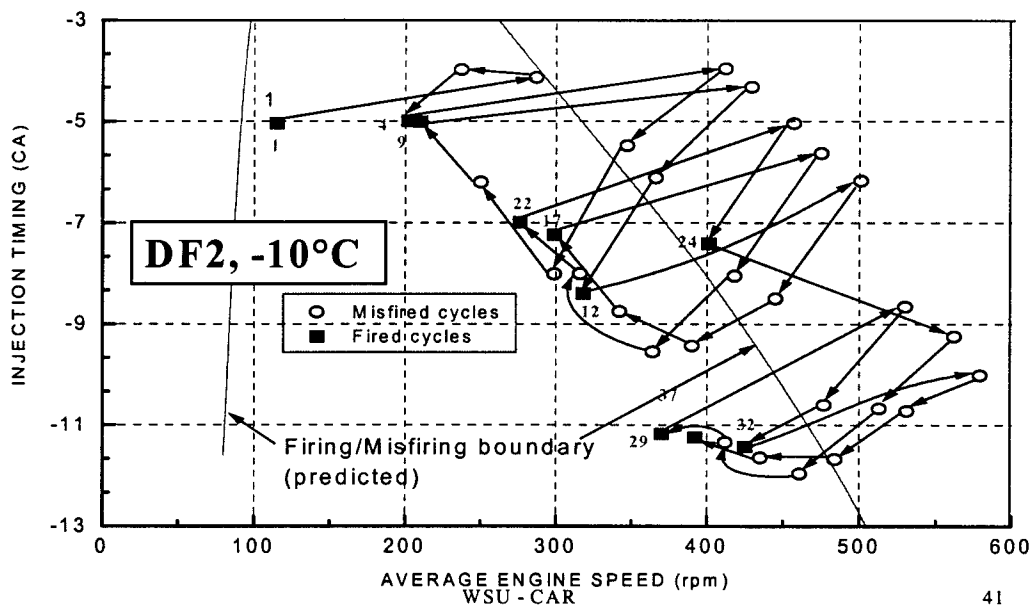


Figure 2. Comparison between the predicted and experimental misfiring cycles.

COMPARISON BETWEEN PREDICTED MISFIRING ZONE AND ACTUAL ENGINE DATA

Figure (2) shows the predicted misfiring boundary and the actual injection timing of the 4-cylinder engine during the first 37 cycles of the starting transient at -10°C . It can be noticed that the misfiring boundary lies at the center of a band of injection timings and engine speeds. The engine moved from the firing zone to the misfiring zone many times. The majority of the misfiring cycles lie in the predicted misfiring zone. The trend is misfiring occurs as the engine accelerates after firing. Because of misfiring, the engine decelerates to a lower speed in the firing zone and fires again. This explains the unstable combustion observed during cold starting of diesel engines.

PAPERS PUBLISHED FROM THIS RESEARCH PROJECT

1. "Diesel Ignition Model Considering Charge Heterogeneity and Global Reaction Rates," Yasuhiko Itoh, Naeim A. Henein and Walter Bryzik, The Fourth International Symposium COMODIA 98, pp129-133, (1998)
2. "A New Ignition Delay Formulation with Predictions of Diesel Engine Cold Start Misfiring," Zhiping Han, Naeim A. Henein and Walter Bryzik, SAE Paper No. 2000-01-1184, SP-1533, pp 175-184, 2000.
3. "Combustion and Emission Characteristics of a single-cylinder HSDI Diesel Engine," N. A. Henein, M-C. Lai, D-H Wang and Paul Miles, Central State Section/The Combustion Institute, Indianapolis, IN, April 16-18, 2000.
4. "Diesel Cold Start Combustion Instability and Control Strategy," Zhiping Han, Naeim Henein, Bogdan Nitu and Walter Bryzik, SAE Paper No. 2001-01-1237.
5. "Emissions Trade-Off and Combustion Characteristics of a High-Speed Direct Injection Diesel Engine," Naeim A. Henein, Ming-Chia Lai, Inderpal Singh, Dahai Wang and Liang Lui, SAE Paper No. 2001-01-0197.

PLANAR IMAGE PARTICLE ANALYZER FOR WHOLE FIELD SPRAY APPLICATIONS

Contract DAAD19-01-C-0011

Cecil Hess
MetroLaser, Inc.
Suite 100
18010 Skypark Circle
Irvine, CA 92614
(chess@metrolaserinc.com)

The purpose of this work is to develop a whole field measurement technique that is capable of simultaneously sizing multiple transparent droplets on a plane from scattered light features that are independent of laser beam intensity and obscuration. Light scattered by reflection and refraction from droplets immersed in a laser sheet is recorded holographically to yield the smallest possible probe volume and correspondingly largest number density. Last year we reported droplet size results obtained with conventional optical holography and some preliminary results of different objects obtained with digital holography. This year we report the first droplet size results obtained with digital holography.

DESIGN AND DEVELOPMENT OF A DIGITAL HOLOGRAPHIC PIPA-SYSTEM

The recording medium in the case of digital holography is a high resolution CCD-sensor. Holograms collected on this sensor are subsequently reconstructed mathematically yielding complete 3-D information of the object. Figure 1 shows a schematic of the system. The laser was a pulsed ruby laser. The remaining components are lenses (Li), mirrors (Mi), and beamsplitters (BSi)

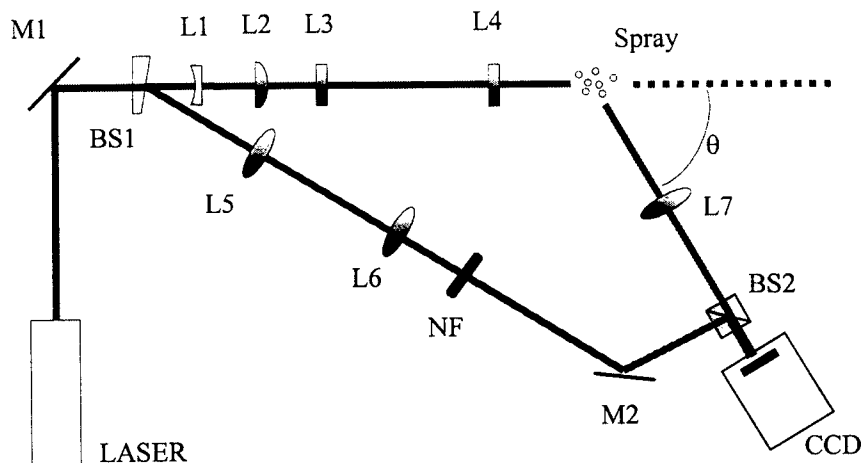


Fig. 1 Schematic of digital holographic PIPA system

A manual sprayer filled with water generated the spray. The droplets were aimed manually into the light sheet. The distance between the CCD-sensor and the image of the laser sheet was about

5 cm. In this configuration a defocused image was recorded and the focused image was subsequently calculated using the digital holography algorithm.

EVALUATION OF RESULTS

Figure 2 shows a typical hologram recorded with the system described above.

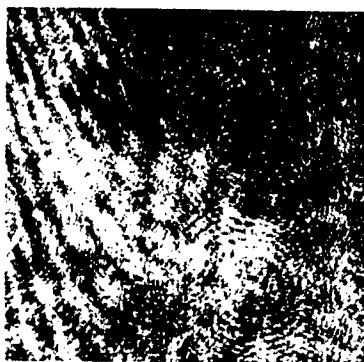


Fig.2 Digital hologram of water droplets

Although the contrast is poor, spherical interference fringes generated by the droplets can be observed. The holograms serve as input for the digital reconstruction procedure. In Fig.3 the reconstructed intensity is shown for different distances.

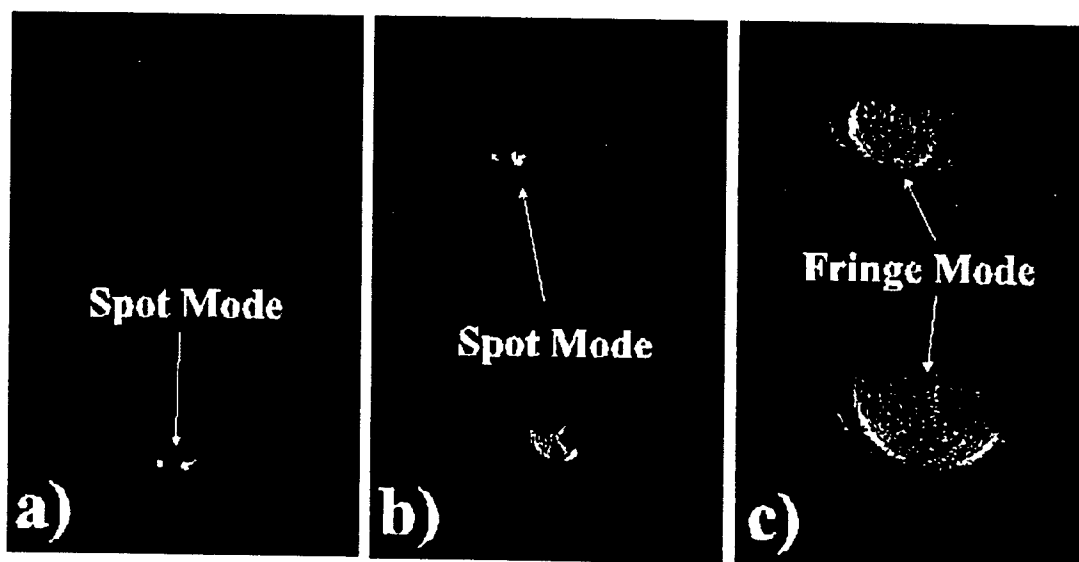


Fig.3 Reconstruction of droplets at a reconstruction distance of a) 4.6 cm, b) 5.1 cm and c) 5.8 cm

The results show that the spots of the refracted and reflected spherical waves can be reconstructed and evaluated. The diameter of the droplets were calculated from the spot separation in the reconstruction. In the case of the upper droplet the separation was determined to be 109 μm (Fig 3a) and in the case of the lower droplet 143 μm (Fig. 3b).

The spot separation can easily be determined from the numerical reconstruction. The fringes in Fig. 3c) have a poor contrast due to a high noise level and different intensities of the spots. Furthermore the intensity patterns in Fig. 3 c) are not spherical. This is because the imaging system and/or the CCD did not collect part of the reflected/refracted light. This problem can be

mitigated by optimizing the imaging system and by reducing the distance between image and CCD-target.

The experiments show that the undesired virtual image appears as background noise. It reduces the image quality but it does not overlap with the real image, which would make further evaluation impossible. The noise can be reduced using a filtering technique that also can be used to separate the information from different droplets. This filter is described in detail in the next section.

APPLICATION OF NUMERICAL FILTER

In order to avoid the overlapping of reflected/refracted wavefronts from different, adjacent droplets a filter can be applied in digital holography. This filter can also be used to reduce the noise in the reconstructed image. The principle of this filtering technique is shown in Fig.4.

In the presence of noise the fringes reconstructed with digital holography have a poor contrast. To apply the numerical filter the complex wavefront corresponding to each droplet is first reconstructed in the 'spot-mode'-plane where the wavefront of interest has its minimal extension and can be separated from noise and other spots. This is achieved by multiplying the complex image with a window function that takes a value of 1 in the region of interest and 0 elsewhere. Subsequently to applying the filter the numerical reconstruction is used to reconstruct the wavefront at a convenient 'fringe-mode'-plane. The result of the filtering is shown in Fig. 4b). In comparison with Fig. 4a) the fringes are less noisy and the second droplet does not exist.

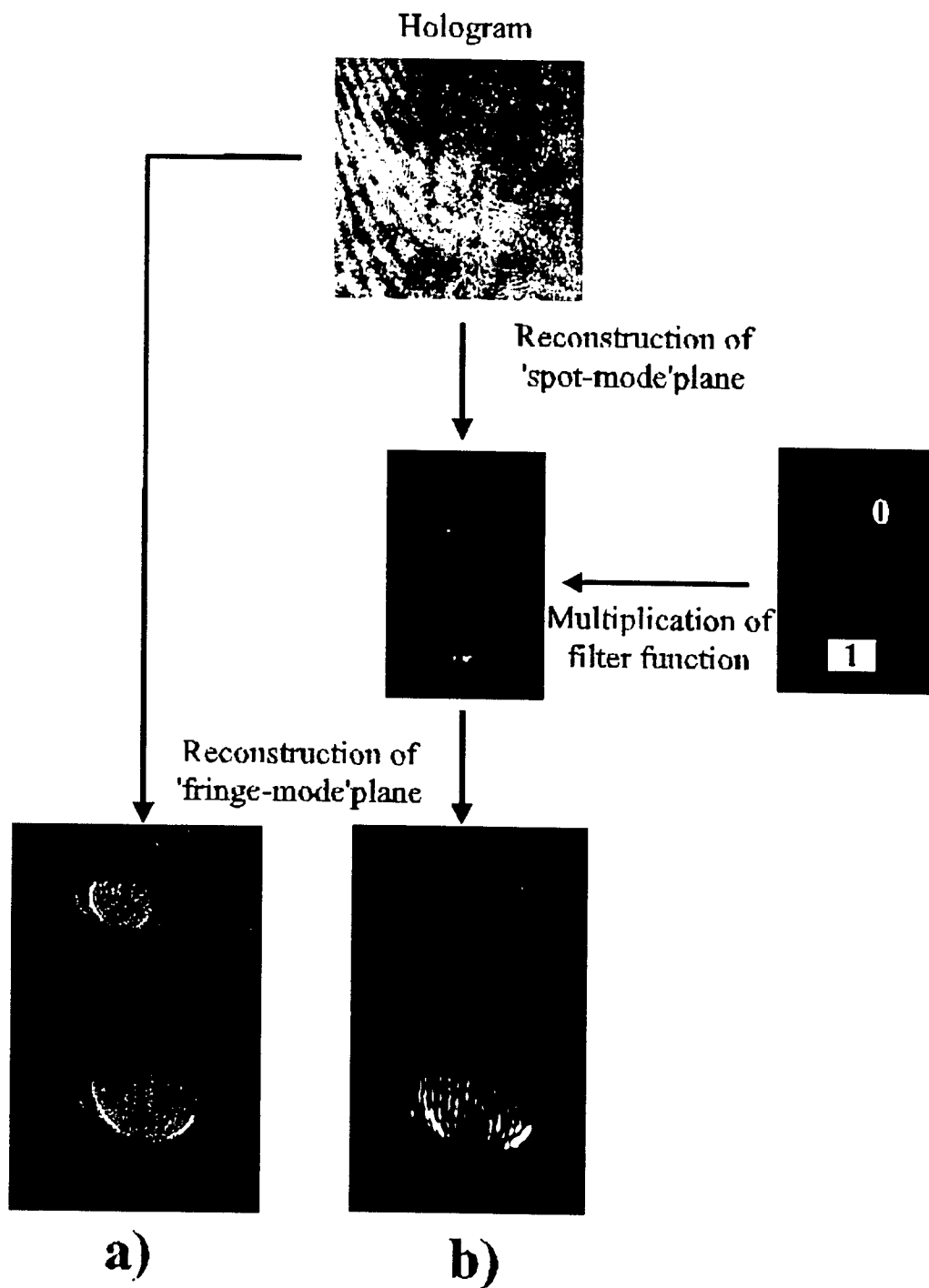


Fig.4 Reconstruction without (a) and with application of filter (b)

CONCLUSIONS

We have demonstrated the ability to record and numerically reconstruct wavefronts corresponding to single droplets both in the two-spot and the fringe mode regimes. A numerical filter applied to images reconstructed in the two-spot regime significantly improved the quality of the fringes.

FLAME SPREADING AND COMBUSTION BEHAVIOR OF GUN PROPELLANTS UNDER HIGH LOADING DENSITY CONDITIONS

(Grant/Contract Number: DAAD 19-01-1-0573)

Principal Investigator: Dr. Kenneth K. Kuo

The Pennsylvania State University
140 Research East Building
University Park, PA 16802

SUMMARY/OVERVIEW:

The ballistic performance of tank gun systems can be increased by using high loading density propellant charges. However, the exact dependency of the muzzle velocity on loading density is not known. Furthermore, there are some uncertainties associated with combustion behavior under extremely high loading density conditions. The burning rate of the propellant and the flame-spreading rate along the propellant charge could be affected by the close proximity of its neighboring propellant grains.

TECHNICAL DISCUSSION

In the experimental investigation, an extensive database will be developed for studying this gap width effect on the burning rate behavior by using an available doubled-ended windowed strand burner (DEWSB) with detailed diagnostics, including the electro-optical methods for gap distance measurement and close-up photographic recording of the burning surface and combustion event. The propellant regression rate and burning behavior will be characterized as a function of gap space, chamber pressure, and initial temperature. In the theoretical investigation, a comprehensive model will be formulated, numerically solved, and compared with experimental data for model validation. This model will simulate the combustion behavior of two opposing end-burning solid propellant strands with their burning surfaces controlled at a fixed separation distance.

For studying the effect of packing density on flame spreading rate of stick propellants, an existing high-pressure stick propellant bundle combustion test rig will be adopted for measuring the flame spreading rate with an array of fast-response photo-detectors, as well as pressure wave phenomena associated with the flame spreading process. A comprehensive flame-spreading model will also be developed for simulating the flame-spreading phenomenon in tightly packed propellant bundles. This model will be modified from an existing stick-propellant bundle combustion code, developed earlier by Kuo and his co-workers. Both the opposing burning strand model and the flame-spreading model will be compared with experimental data for detailed model validation.

The knowledge to be acquired, and the technique to be developed from this investigation, will be highly beneficial to Army's ballistic and propulsion program. The final output of this research project will be threefold: (1) a detailed characterization of the gap-distance effect on the combustion behavior of gun propellants so that the alteration of propellant regression rate under high loading density conditions can be incorporated into future charge design considerations; (2) the ignition and flame spreading processes over a tightly packed bed of stick propellants will be measured and analyzed for improved understanding of the high loading density effect in order to facilitate future artillery system design; and (3) any engineering correlations to be developed will be very useful for modular integration into the Army's ballistic predictive programs for simulating combustion processes. In addition, this research project will produce more trained engineers to pursue further research in the gun ballistics area.

PLANAR THERMOMETRY IN SOOTING TRANSIENT DIFFUSION FLAMES

(ARO Grant/Contractor No. DAAG55-98-1-0222)

Principal Investigator: William Roberts

Dept. of Mechanical and Aerospace Engineering
Box 7910
North Carolina State University
Raleigh, NC 27695-7910

SUMMARY/OVERVIEW:

Recent computational and experimental studies have shown that conditions exist where the assumption that flamelets respond quasi-steadily to the unsteady strain rates of the turbulent flow-field is invalid [1-4]. If the turbulent Reynolds number is sufficiently large, there exists a range of eddy sizes where the characteristic turnover times of the smallest eddies are comparable to the diffusion times of the laminar flamelets. This also leads to a wide range of characteristic frequencies. Therefore, it is necessary to investigate the frequency response of flamelets to extend the applicability of the flamelet model. The purpose of this investigation was to quantify the response of the reaction-zone temperature and thickness and the strain rate to a time varying flow field.

TECHNICAL DISCUSSION:

A counterflow diffusion burner was used to model a flamelet in the mixing zone of a turbulent reacting flow field. The temperature field in the reaction zone was experimentally determined using two-line OH planar laser-induced fluorescence (PLIF) thermometry [5-7]. Particle image velocimetry (PIV) was used to quantify the velocity and strain rate relationships between measured parameters as a function of flow rate oscillation frequency. Simultaneous with velocity, the OH-field width was measured using PLIF. Reaction-zone thickness was characterized by the full width at half maximum (FWHM) of the OH field [8].

An unsteady flow field was imposed on the counterflow diffusion flame by providing a sinusoidal voltage to the speakers capping plenums located at the entrance to both the fuel and air tubes [9]. Velocity, temperature, and relative [OH] measurements were made as a function of initial steady strain rate (SSR) and forcing frequency. In general, these measurements were made at four temporal locations within the sinusoidal voltage oscillation applied to the speakers: 1) zero amplitude with positive slope, designated $0+$; 2) maximum amplitude, designated Max ; 3) zero amplitude with negative slope, designated $0-$; and 4) minimum amplitude, designated Min . The forcing frequencies considered in this study were 30, 50, 100, 200 and 500 Hz. Results for three flow conditions are reported here and these flows are defined by their measured steady strain rate (SSR), which is defined as the gradient of the air-side axial velocity just prior to the heat release zone.

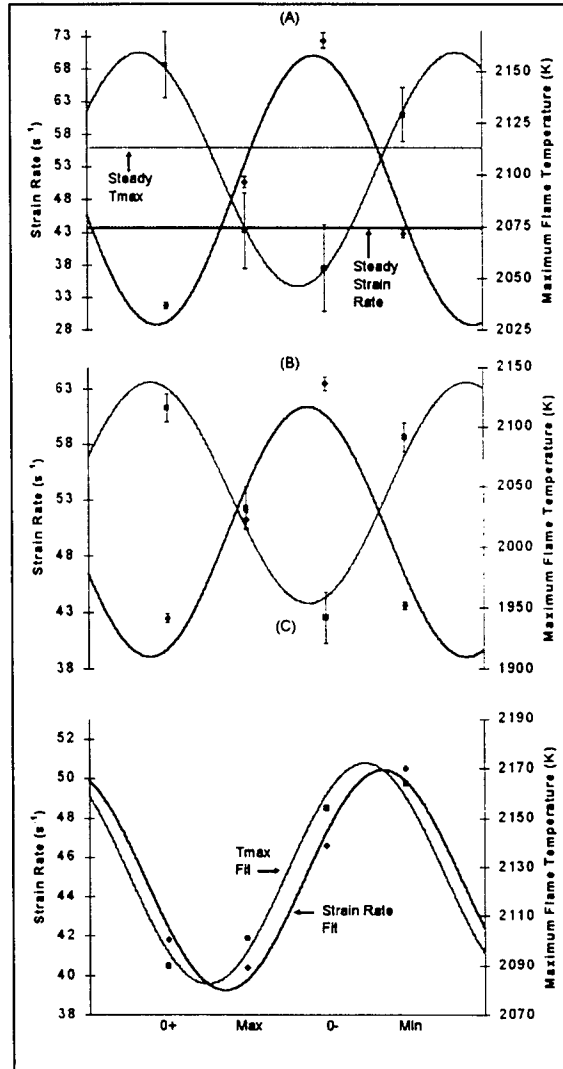


Figure 1: Maximum reaction-zone temperature, T_{\max} (Boxes), and instantaneous strain rate (Diamonds) at 30 Hz (A), 50 Hz (B), 200 Hz (C) at the four phases. The error bars represent twice the standard deviation of the mean.

The measured strain rates and the maximum reaction zone temperatures, T_{\max} , are plotted in Figure 1 for a SSR of 44 s^{-1} at various forcing frequencies. Note that the temperature and velocity measurements were not simultaneous; rather, the PIV measurements were coupled with a single OH PLIF measurement.

At a forcing frequency of 30 Hz (Figure 1 A), the measured strain rate increases between the temporal locations of $0+$ and $0-$ from 30 s^{-1} to 73 s^{-1} . During this period T_{\max} decreases from 2153 K to 2055 K. Then, between locations $0-$ and Min , the strain rate decreases to 41 s^{-1} and T_{\max} increases to 2129 K. At this forcing frequency, the flame appears to be responding in a quasi-steady manner, i.e., with increasing strain rate, T_{\max} decreases, and when the strain rate decreases, the T_{\max} increases. However, for steady strain rate, the T_{\max} continuously decreases with increasing strain rate (decreasing Damkohler number) due to increasing thermal and species concentration gradients.

As the forcing frequency is increased to 50 Hz (Figure 1 B), the measured strain rate is found to increase from 38 s^{-1} to 64 s^{-1} between the $0+$ and $0-$ locations, while T_{\max} decreases from 2116 K to 1942 K. Between the $0-$ and Min phases, the strain rate decreases to 41 s^{-1} and T_{\max}

increases to 2091 K. Thus, as evidenced by this phase relation between imposed strain and T_{\max} (i.e., $\sim 180^\circ$ out of phase), the flame is responding in a quasi-steady manner at both 30 and 50 Hz.

The flame behavior shows unsteadiness when the forcing frequency is increased to 200 Hz, as illustrated in Figure 1 (C). The strain rate and the maximum reaction zone temperature are approximately in phase at the 200 Hz oscillation frequency, which is a significant departure from quasi-steady behavior. This result illustrates the diffusion limited frequency response of the reaction zone. Essentially, the flame will respond to the reactants delivered to the flame front. Convective velocities away from the flame front and diffusive velocities near the reaction zone govern the transport of these reactants. Effectively, the diffusion zone is the bottleneck for reactant delivery. No matter what the rate of change of reactants delivered to the edge of the convective-diffusive zone, these reactants still must travel through the diffusive zone. Thus, as the time necessary to travel through the diffusive zone becomes larger relative to the convective velocities cycle time, a phase lag shows up equal to the diffusion time.

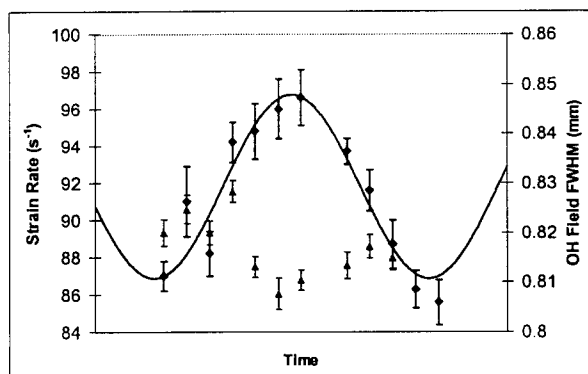


Figure 2: High-resolution strain rate (Diamonds) and OH-field width (Triangles) for a SSR 84 s^{-1} at 500 Hz.

Figure 2 shows the results of a SSR 84 s^{-1} case with a 500 Hz oscillation. The measured strain rate response is reasonably sinusoidal, but no discernable trends are seen in the OH-field response. This would suggest that at this oscillation amplitude and frequency, the changes are undetectable with the resolution used for these measurements. Given the strain rate and OH-field information, an attempt was made to determine if these measured parameters could be used to derive collapsed non-dimensional data plots.

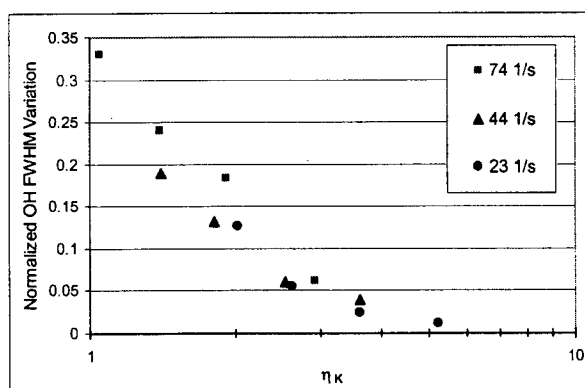


Figure 3: Normalized amplitude of the OH width oscillation as a function of the Stokes parameter.

In a recent numerical investigation, Egolfopoulos and Campbell [3] were able to correlate the variation in maximum flame temperature with a dimensionless frequency, a so-called Stokes parameter η_K , defined as,

$$\eta_K = \left(\frac{\pi f}{K} \right)^{1/2} \quad (1)$$

Where, f is the forcing frequency and K is the cycle mean strain rate. This comparison can also be made with the variation in reaction-zone width. In Figure 3, the variation in thickness of the OH zone through the oscillation (amplitude of the oscillation) normalized by the mean value is plotted against the logarithm of this Stokes parameter. All the data from the four forcing frequencies (30, 50, 100 and 200 Hz) and three different initial strain rates (23, 44, and 74 s⁻¹) collapse onto a single line with a fairly steep negative slope. At the largest η_K , however, the slope magnitude appears to decrease, perhaps due to the limited spatial resolution of the OH PLIF system. The Stokes parameter ranges from about 1 to 6 in these experiments, which is similar to the results reported in [3]. Fundamentally, this plot illustrates that the OH-field width oscillations are attenuated in a predictable fashion with increasing frequency for the conditions illustrated. This illustrates the tendency for diffusion processes to smear gradients, which is well illustrated by Stokes second problem. For the condition shown in Figure 2, the Stokes parameter is ~ 4.4 and based on the Stokes plot, the normalized OH FWHM variation would be ~ 0.018 . As a result of the dramatically reduce oscillation strength, which is a function of frequency, the fluctuations of the reaction zone thickness were not resolvable at the 500 Hz oscillation.

References:

1. Darabiha, N., *Combust. Sci. and Tech.* **86**, pp. 163-181 (1992).
2. Im, H. G., Law, C. K., Kim, J. S., Williams, F.A., *Combust. Flame* **100**, pp. 21-30 (1995).
3. Egolfopoulos, F. N., Campbell, C. S., *J. Fluid Mech.* **318**, pp. 1-29 (1996).
4. Brown, T. M., Pitz, R. W., Sung, C. J., *Proc. Combust. Inst.* **27**: 703-710 (1998).
5. Palmer, J. L., Hanson, R. K., *Applied Optics* **35**, pp. 485-498 (1996).
6. Seitzman, J. M., Hanson, R. K., DeBarber, P. A., Hess, C. F., *Applied Optics* **33**, pp. 4000-4012 (1994).
7. Seitzman, J. M., Hanson, R. K., *Appl. Phys. B* **57**, pp. 385-391 (1993).
8. Welle, E. J., Roberts, W. L., Donbar, J. M., Carter, C.D., DeCroix, M.E., *Proc. Combust. Inst.* **28**, (2000).
9. DeCroix, M. E., Roberts, W. L., *Comb. Sci. and Tech* **160**, pp. 165-190 (2000).

SOOT MORPHOLOGY IN UNSTEADY COUNTERFLOW DIFFUSION FLAMES

(ARO Grant/Contractor No. DAAD19-00-1-0429)

Principal Investigator: William Roberts

**Dept. of Mechanical and Aerospace Engineering
Box 7910
North Carolina State University
Raleigh, NC 27695-7910**

SUMMARY/OVERVIEW:

As Diesel engines consume the majority of the injected fuel in diffusion controlled combustion processes compared to the relatively short initial premixed phase, and diffusion flames have a greater propensity to form soot, particulate matter emission from Diesel engines can be considerable. These particles have a much stronger thermal signature compared to gas phase products, water and carbon dioxide, and render Diesel-powered vehicles susceptible to tracking and targeting via IR sensors. This IR signature will decay with time as the particles cool, and this temporal profile is a function of the morphology of the soot. Therefore, it is important to understand, and eventually control, not only the soot volume fraction of the particulate matter, but also its morphology.

TECHNICAL DISCUSSION:

In order to understand the very complicated coupling between the three dimensional, unsteady fluid dynamics in a turbulent flowfield and the chemical kinetics of combustion, it is necessary to simplify either the flowfield or the chemistry, or both. The turbulent flame has been successfully modeled as an ensemble of one-dimensional strained laminar flamelets under certain conditions [1]. A counterflow geometry has been used for many years as both a computational and experimental model of such a flamelet [2]. Until recently, the structure of these flamelets was assumed to be only a function of the strain rate, defined as the air side axial velocity gradient just prior to the heat release zone. However, it has become apparent that knowledge of the instantaneous strain rate is not sufficient, and the history must also be known for rapidly varying strain rates [3,4].

DeCroix and Roberts [5] have measured the soot volume fraction in an unsteady counterflow diffusion flame burner. Unsteadiness was imposed on the flame by oscillating the reactant flow rates, thereby imposing an oscillation in the strain rate. Measurements of f_{sv} were made as a function of initial strain rate, oscillation frequency and oscillation amplitude using a calibrated Laser Induced Incandescence (LII) technique. Table 1 shows results of these measurements, where A_1 and A_2 are two different forcing amplitudes, relative to the respective global quenching or flow reversal amplitude, whichever is less, at each initial strain rate. The

values in the table are normalized to the steady peak soot volume fraction measured at the corresponding initial strain rate. As seen in this table, at low frequencies, the unsteady flames have peak soot volume fractions that are as much as six times higher than their steady counterpart. The peak augmentation occurs for moderately low initial strain rates. Below this, the flame is already heavily sooting and the unsteadiness contributes relatively little. At higher oscillation frequencies, there can be a large difference in the behavior of the peak soot volume fraction, depending upon the initial strain rate. At low initial strain rates, the higher oscillation frequencies are seen to drastically reduce the peak f_{sv} , while at higher initial strain rates, the f_{sv} becomes relatively insensitive to the imposed oscillations.

Frequency (Hz)	SR 15 s ⁻¹ Steady max $f_{sv}=1.00$ ppm		SR 30 s ⁻¹ Steady max. $f_{sv}=0.20$ ppm		SR 60 s ⁻¹ Steady max. $f_{sv}=0.05$ ppm		SR 90 s ⁻¹ Steady max. $f_{sv}=0.03$ ppm	
	A ₁	A ₂	A ₁	A ₂	A ₁	A ₂	A ₁	A ₂
25	2.4	1.9	3.4	6.5	1.8	3.4	2.0	3.0
50	1.1	0.7	1.5	1.9	1.6	1.4	1.7	2.3
100	0.9	0.3	1.3	0.9	~1	~1	~1	~1
200	0.8	0.1	1.1	0.5	~1	~1	~1	~1

Table 1 Peak soot volume fraction in unsteady counterflow diffusion flame burner as a function of initial strain rate, oscillation frequency and amplitude, as measured with LII.

As stated above, the morphology of the soot is of importance in determining the radiation signature. LII has been very successful at measuring the f_{sv} , but there are difficulties in deriving particle size information from the incandescence signal. As the flow field is sensitive to physical obstructions, sampling probes are problematic. In-situ light scattering and extinction measurements, therefore, have usually been employed in order to obtain critical soot data in flames. Almost all of the early literature inferred soot particle size and number densities using Mie or Raleigh theories [6,7]. Typical soot primary particle size is 30 – 50 nm, much smaller than the wavelength of visible radiation, and fully within the Rayleigh regime. However, soot is composed of aggregates containing hundreds to thousands of primary particles. The effective diameter of these aggregates is considerably larger than the wavelength of visible radiation, fully within the Mie regime. Unfortunately, these primary particles do not cluster into a larger sphere, rendering both scattering models inaccurate, but not irrelevant [8,9].

By making a single extinction measurement along with angularly resolving the scattered light, looking at all four polarization options, the morphology of the soot may be determined. The main difficulty in the interpretation of these optical measurements was a scattering theory that relates optical cross section to aggregate morphology and size. This obstacle has been overcome by recent developments in fractal concepts. RDG/PFA theory [10] was found to be a reliable approximation to evaluate the measured optical cross sections of soot aggregates, based on extensive experimental [11,12] and computational [13] evaluations. RDG/PFA provides a general approach that yields N_g (geometric mean of number of primary particles per aggregate) and σ_g (for a log-normal distribution), and fractal prefactor k and mass fractal dimension, D_f .

This theory also allows determination of the probability density function of N as well as the primary particle diameter, which are the most crucial parameters in particle growth and aggregation studies.

This approach requires numerous angular measurements, and may not be practical in many environments. By making a few experimentally-justified assumptions, the number of angular measurements can be reduced significantly. It has been shown that the fractal prefactor and fractal dimension of the soot aggregate are fairly constant for a wide range of fuels and flame geometries [14,15]. Also, the number of spherules per aggregate does follow a log-normal distribution whose width is fairly constant. Thus, by assuming the k , D_f , and σ_g are known, the number of angular measurements can be reduced to three.

Thus, by making a few good assumptions, RDG/PFA theory may be used to obtain soot morphological parameters in the unsteady counterflow diffusion flame burner as a function of steady strain rate and oscillation frequency and amplitude. Currently, this technique has only been used at a point using a focused cw laser and photomultiplier tube. However, if the focused beam is replaced with a sheet and the pmt is replaced with an ICCD camera, planar measurements of soot morphology may be possible. Sufficient laser fluence is necessary to obtain measurable signals, especially normal to the laser beam. However, if the fluence is too high, then unwanted photons from laser induced incandescence and laser induced fluorescence processes become a significant problem. Therefore, an un-Q-switched Nd:YAG will be used, as shown in Figure 1 below.

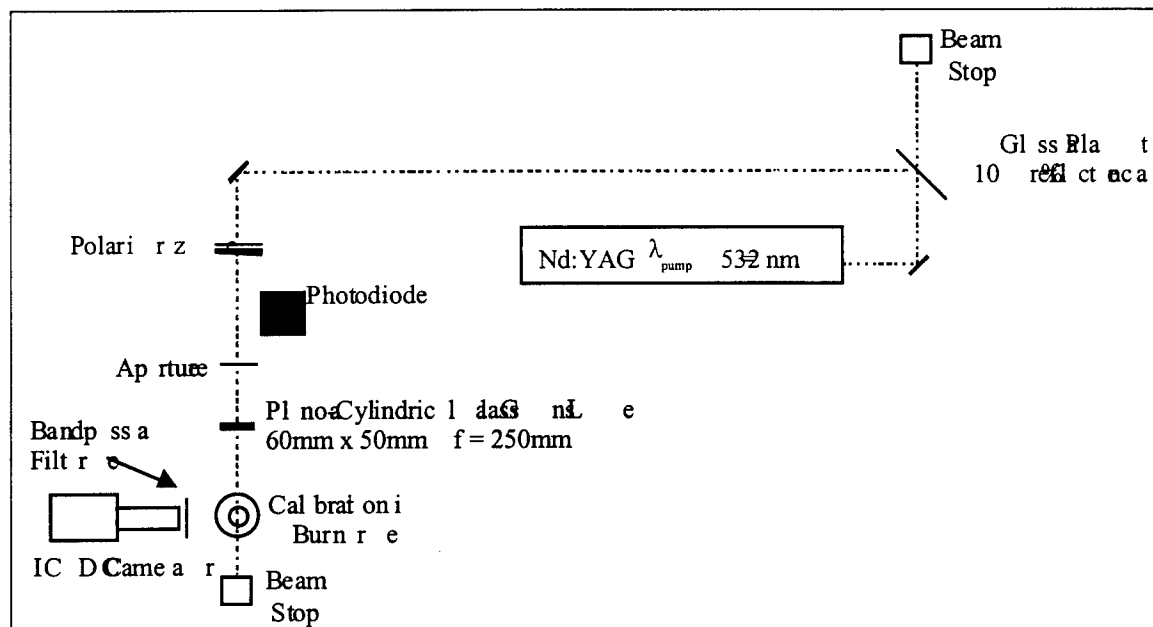


Figure 1. Planar RDG/PFA soot morphology measurement layout.

Currently, the PI is making point measurements in a laminar co-flow diffusion flame, identical to the "Santoro" burner, which is extensively characterized in the literature. Upon completion of these point measurements, planar measurements in this same flame will begin. By

developing this planar RDG/PFA technique in a well characterized, steady, axisymmetric flame, correction algorithms for extending the point technique to a planar technique can be devised and tested. When spatially resolved soot morphology measurements are completed in the co-flow flame, the "Santoro" burner will be replaced with the unsteady counterflow diffusion flame burner.

Soot morphology measurements will be made at the same conditions as listed in table 1. Concurrently, the temperature field is also being measured in this burner [16] at these same locations. Upon completion of these two studies, the effects of unsteady strain rate on the formation of soot and its morphology will be well quantified in these one dimensional flamelets.

References:

1. Peters, N. (1984). *Prog. Energy Comb. Sci.*, Vol. 10, pp. 319-339.
2. Tsuji, H. (1982). *Prog. Energy Comb. Sci.*, Vol. 8, pp. 93-119.
3. Im, H. G., Law, C. K., Kim, J. S., Williams, F.A., *Combust. Flame* **100**, pp. 21-30 (1995).
4. Egolfopoulos, F. N., Campbell, C. S., *J. Fluid Mech.* **318**, pp. 1-29 (1996).
5. DeCroix, M. E., Roberts, W. L., *Comb. Sci. and Tech* **160**, pp. 165-190 (2000).
6. Kent, J.H. and Wagner, H.Gg. (1982). *Comb. Flame*, **47**, 53-65.
7. Santoro, R. J., Semerjian, H.G., and Dobbins, R.A. (1983). *Comb. Flame*, **51**:203-218.
8. Köylü, Ü. Ö., and Faeth, G. M. (1993). *J. Heat Transfer*, **115**:409-417.
9. Köylü, Ü. Ö., and Faeth, G. M., (1996). *J. Heat Transfer*, **118**:415-421.
10. Moutain, R.D., and Mulholland, G.W., (1988). *Langmuir*-4:1321-1326.
11. Köylü, Ü. Ö., and Faeth, G. M., (1994a). *J. Heat Transfer*, **115**:971-979.
12. Köylü, Ü. Ö., and Faeth, G. M., (1994b). *J. Heat Transfer*, **116**:152-159.
13. Farias. T.L., Carvalho, M.G., Köylü, Ü. Ö., and Faeth, G. M., (1995). *J. Heat Transfer*, **117**:152-159.
14. De Iuliis, S., Cignoli, F., Benecchi, S., and Zizak, G., *Proc. Comb. Inst*, Vol. 27, pp. 1549-1555 (1998)
15. De Iuliis, S., Cignoli, F., Benecchi, S., and Zizak, G., *Applied Optics*, Vol. 37, No. 33 (1998)
16. Welle, E. J., Roberts, W. L., Donbar, J. M., Carter, C.D., DeCroix, M.E., *Proc. Combust. Inst.* **28**, (2000).

CHEMICAL-KINETIC CHARACTERIZATION OF AUTOIGNITION AND COMBUSTION OF DIESEL AND JP-8

(Grant/Contract Number DAAD19-99-1-0259)

Principal Investigator: Dr. Kalyanasundaram Seshadri

Department of Mechanical and Aerospace Engineering
University of California at San Diego
La Jolla, California 92093

SUMMARY/OVERVIEW:

The principal objective of the research is to obtain a fundamental understanding of the mechanisms of autoignition and combustion of diesel and JP-8. Chemical-kinetic mechanisms describing autoignition and combustion of these fuels are not available. This research will address this deficiency by first developing simulated diesel and simulated JP-8 each preferably made up of three hydrocarbon compounds. Chemical-kinetic mechanisms will be developed for these hydrocarbon fuels. Experimental and numerical studies are in progress.

TECHNICAL DISCUSSION:

Numerical and analytical studies were carried out to elucidate the ignition characteristics of premixed mixtures of *n*-heptane and air in homogeneous, nonflowing systems. In particular two-stage ignition characteristics of the reactive mixture was investigated. The results are described in Ref. 1. Chemical-kinetic mechanisms of combustion of propene (C_3H_6), and ethene (C_2H_4) are considered to be subsets of chemical-kinetic mechanism of combustion of *n*-heptane. To test the accuracy of these subsets, experimental and numerical studies were carried out to elucidate the fundamental mechanisms of extinction and autoignition of propane (C_3H_8), propene, ethane (C_2H_6), and ethene in nonpremixed systems. The results are reported in Ref. 2. Alkylated benzenes are an important class of hydrocarbons because they comprise a significant portion of diesel. Knowledge of the oxidation chemistry of alkylated benzenes is needed in developing predictive models that can treat autoignition, and premixed and nonpremixed burning of transportation fuels in internal combustion engines. Toluene ($C_6H_5CH_3$) has the simplest molecular structure of the alkylated benzenes and is a reasonable starting point for the development of detailed chemical-kinetic mechanisms for alkylated benzenes. An experimental and numerical study was performed to elucidate the chemical-kinetic mechanism of combustion of toluene. The results are described in Ref. 3.

Temperature Cross-Over and Non-Thermal Runway at the Two-Stage Ignition of n-Heptane

This research was carried out in collaboration with Professor N. Peters and Mr. G. Paczko at RWTH Aachen Germany. Numerous studies have addressed ignition of *n*-heptane in homogeneous, nonflow systems. A particular striking feature is two-stage ignition which is also related to cool flame phenomena and the negative temperature coefficient

(NTC) of the ignition delay time. The procedure used in this study is to first develop a skeletal mechanism made up of minimum number of reaction steps that is able to reproduce ignition delay times in the low and high temperature regime. The skeletal mechanism is obtained from a detailed chemical-kinetic mechanism. Reduced chemical-kinetic mechanisms are obtained from the skeletal mechanism. The reduced chemical-kinetic mechanisms are used to predict ignition delay times.

Two reduced mechanisms are derived for describing the low temperature regime as well as the intermediate temperature regime and the high temperature regime. In these formulations the OH radical is consumed by fast reactions with the fuel until the fuel is depleted. The steady state relations for OH shows the concentration of OH to become very large when the fuel is depleted. Therefore depletion of the fuel is used as a suitable criterion for ignition. In the intermediate temperature regime the first stage ignition is related to a change from chain-branching to chain-breaking as the temperature crosses a certain threshold. The chain branching reactions result in a build-up of ketohydroperoxides which dissociate to produce OH radicals. This is associated with a slight temperature rise which leads to a crossing of the threshold temperature with the consequence that the production of OH radicals by ketohydroperoxides suddenly ceases. The subsequent second stage is driven by the much slower production of OH radicals owing to the dissociation of hydrogen peroxide. In all three regimes analytical solutions for the ignition delay are obtained. It is found that dissociation of the ketohydroperoxide dominates the low temperature regime and the first stage ignition of the intermediate temperature regime, while dissociation of hydrogen peroxide dominates the second stage of the intermediate temperature regime and the high temperature regime.

Experimental and Numerical Studies of Extinction and Autoignition of C_3H_8 , C_3H_6 , C_2H_6 , and C_2H_4

This research was carried out in collaboration with Dr. W. J. Pitz at Lawrence Livermore National Laboratory, Livermore California. Experimental and numerical studies are conducted to clarify the physical and chemical mechanisms of extinction and autoignition of ethene, ethane, propene, and propane. The studies are performed in the counterflow configuration. Here the reactive layer stabilized near the stagnation plane of two counterflowing streams is considered. Nonpremixed and premixed systems are considered. In nonpremixed systems one stream, called the fuel stream, is made up of fuel and nitrogen, and the other stream, called the oxidizer stream, is made up of air mixed with nitrogen. In premixed systems one stream, called the premixed reactant stream, is made up of ethene, air and nitrogen, and the other stream, is made up of nitrogen.

Critical conditions of extinction of nonpremixed flames, giving the mass fraction of various reactants in the streams as functions of strain rates, are obtained. In the autoignition experiments on nonpremixed systems, at a fixed value of the strain rate, the temperature of the oxidizer stream was increased until spontaneous ignition took place. Autoignition temperatures are obtained for several values of the strain rate. Experimental results are shown in Fig. 1. Studies on premixed systems are carried out with ethene as the fuel. One series of experiments gives strain rates at extinction for different equivalence ratios

and dilutions of the premixed reactant stream. Here, the nitrogen stream is at ambient temperature. In the second series of experiments, strain rates at extinction are obtained as a function of the nitrogen stream temperature.

Numerical calculations are performed using detailed chemistry at several conditions corresponding to those in the experiments. Critical conditions of extinction and autoignition are calculated. The numerical results are compared with the experiments.

Chemical-Kinetic Characterization of Combustion of Toluene

This research was carried out in collaboration with Dr. W. J. Pitz and Dr. C. K. Westbrook at Lawrence Livermore National Laboratory, Livermore California, Prof. J. W. Bozzelli at New Jersey Institute of Technology, Newark, and Dr. I. Da Costa, Dr. R. Fournet, Dr. F. Billaud, and Dr. Battin-Leclerc at CNRS-ENSIC, BP. 451, 1, rue Grandville, 51001 Nancy, France. Here a study is performed to elucidate the chemical kinetic mechanism of combustion of toluene. A detailed chemical-kinetic mechanism for toluene was improved by adding more accurate description of the phenyl + O₂ reaction channels. Results obtained using the chemical-kinetic mechanism are compared with experimental data obtained from premixed and nonpremixed systems. Under premixed conditions, predicted ignition delay times are compared with new experimental data obtained in shock tube. Profiles of a number of chemical species were measured previously in the Princeton atmospheric-pressure flow reactor. These measured profiles are compared with numerical calculations using the chemical kinetic mechanism developed here. Ignition delay times are calculated and compared with previous data obtained in rapid compression machines and shock tubes. Critical conditions of extinction and ignition were measured in strained laminar flows under nonpremixed conditions. Numerical calculations were performed using the chemical kinetic mechanism at conditions corresponding to those in the experiments. Critical conditions of extinction and ignition were obtained and compared with the experimental data. Figure 2 compares experimental data on autoignition with results of numerical calculations. For both premixed and nonpremixed systems, sensitivity analysis was used to identify the reaction rate constants that control the overall rate of oxidation in each of the systems considered.

References

- [1] N. Peters, G. Paczko, R. Seiser, and K. Seshadri, "Temperature Cross-Over and Non-Thermal Runway at Two-Stage Ignition of *n*-Heptane," submitted for publication in *Combustion and Flame*, March 2001.
- [2] R. Seiser, K. Seshadri, and W. J. Pitz, "Experimental and Numerical Studies of Extinction and Autoignition of C₃H₈, C₃H₆, C₂H₆, and C₂H₄," Paper # 149, 2nd Joint Meeting of the U. S. Sections of the Combustion Institute, Oakland, CA, March 25-28, 2001.
- [3] W. J. Pitz, R. Seiser, J. W. Bozzelli, I. Da Costa, R. Fournet, F. Billaud, F. Battin-Leclerc, K. Seshadri, and C. K. Westbrook, "Chemical Kinetic Characterization of Combustion of Toluene," Paper # 252, 2nd Joint Meeting of the U. S. Sections of the Combustion Institute, Oakland, CA, March 25-28, 2001.

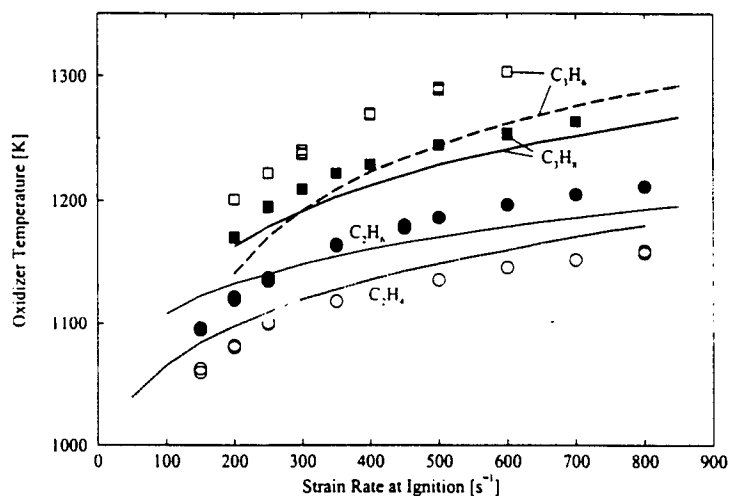


Figure 1: The oxidizer temperature as a function of the strain-rate at autoignition. The points represent measurements and the lines are results of numerical calculations.

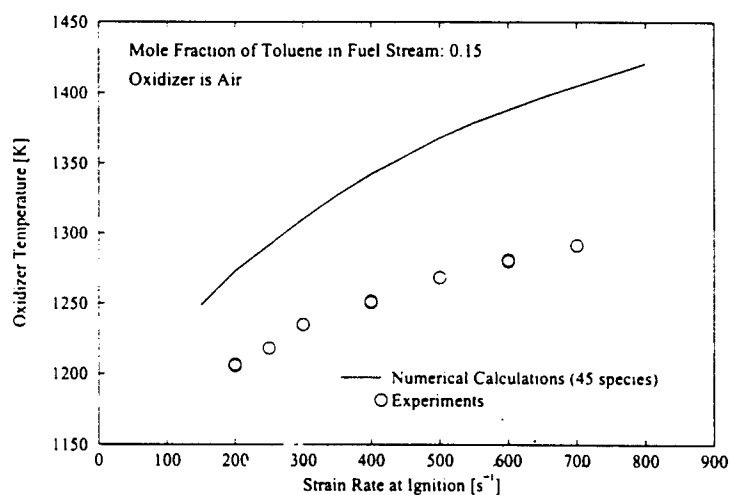


Figure 2: The oxidizer temperature as a function of the strain-rate at autoignition. The points represent measurements and the lines are results of numerical calculations.

CATALYTIC IGNITION AS A TOOL FOR CONVERTING SMALL ENGINES TO EFFICIENT JP-8 OPERATION

DAAD19-00-1-0134

Principal Investigator(s): Steciak, J., Beyerlein, S., McIlroy, D., and Blackketter, D.

University of Idaho
800 Park Boulevard
Boise, ID 83712-7742

University of Idaho
Moscow, ID 83844-0902

SUMMARY/OVERVIEW:

Catalytic ignition permits small engines to operate efficiently with heavy fuels. The technology advances the Army towards its goal of a 'one-fuel' military and can improve the performance of heavy fuel engines operating under part-load conditions. Findings discussed below include: 1) selection of a 1-kW genset for catalytic ignition conversion after consultation with Army CECOM; 2) conversion of a 5-kW genset from gasoline to jet fuel operation at rated power using Smart Plug® catalytic igniters; and 3) design changes to improve Smart Plug® durability.

TECHNICAL DISCUSSION

Work began on this project during the summer of 2000. Key issues that were addressed were selection of small engine test platforms, conversion of a 5 kW gasoline genset to catalytic ignition of aviation fuel, continued development of a reactor for detailed mechanism studies, changing catalytic igniter design features for JP 8 operation, expanding engine testing infrastructure, and development of local emissions testing infrastructure to compensate for laboratory facilities at Idaho National Engineering and Environmental Laboratory (INEEL) that are no longer available.

Portable Genset Platform

Personnel at CECOM in the Army's power generation branch explained the Army's problems with mobile power generation during our visit to Ft. Belvoir in October. These problems, and our approach to create solutions, are summarized below.

Although the Army's 2-kW gensets use L-40 or L-48 Yanmar diesel engines successfully with JP-8 or diesel, the gensets have problems with engine longevity at light loads. Carbon

buildup from wet stacking has killed lightly loaded gensets in the field. The current idea for control is to apply a 750 W heater to the engine, or to apply a dummy load. These gensets weigh ~140 lbs. and are expensive at \$5k each.

The radical pool generated by the catalyst may help obtain complete combustion to prevent C buildup, as well as permit easier cold start.

The Army's diesel 5-kW gensets (800 pounds) also exhibit performance degradation with extended operation at low loads.

While the Army has a work-around planned for the 2-kW genset (externally heating the engine or creating a dummy load), one reason for the light loading problems is the need for 500 W to 1 kW gensets. The Army currently has no gensets with this power output that operate on diesel or JP-8. Commercially available gensets in this size range – for example, Honda models 1800 and 2000 – meet the weight requirement (these gensets weigh less than 20 lbs) but run on gasoline.

Conversion of a small genset, like the Honda, to operation with heavy fuels (D1, D2, JP-5 and/or JP-8) would meet a need the military has today. The Army does not need a large number of gensets each year; finding a world market for small multi-fuel gensets is key for a manufacturer to make this product line successful – and even more promising if the genset could also operate on gasoline. The Army did not have problems with a contractor purchasing an existing system and modifying it to meet its needs, especially since this could keep the price per unit down.

In addition to cold start, maintaining rated power at altitude and high temperature, the Army wants a fast response system - one that will go from idle to full power without stall. Ergonomic considerations - convenience of use, lightweight, quiet operation - must be addressed. Efficiency, power output and durability are also important.

Consequently, in the scope of this project we intend to investigate:

- Conversion of a small genset to heavy fuel operation, followed by
- Optimizing operation of a 2 kW genset with heavy fuel.

After an igniter is designed and the electrical system modified for a small genset, a series of tests are needed. We plan to:

- Perform endurance testing following the Engine Manufacturer's Association (EMA) guidelines
- Devise a new test for prolonged operation at idle or 10% load
- Develop small engine cold start test capabilities (-30°F)
- Perform power rating tests either at simulated altitude testing and elevated temperature (140°F) (e.g. using an Army facility) or devise a self-contained trailer that we can pull to 8,000 feet in Idaho
- Conduct sound tests using a portable sound sensor

- Perform emissions measurements
- Monitor engine wear and catalyst erosion

Finally, other applications of the igniter technology are possible, for example, rotary engine genset/pumpsets, power units for the AAHV (Advanced Amphibian Assault Vehicle), or auxiliary power units for hybrid electric vehicles. Lessons learned in this project can be applied to other small engines throughout the military.

Conversion of a 5 kW Gasoline Genset to Jet Fuel Operation

An Army 5-kW gasoline-fueled genset with a Wisconsin engine was converted to jet fuel operation with catalytic ignition. The converted genset ran at rated power. The conversion require replacing the spark plugs with Smart Plug® catalytic igniters and removing the high-tension coil and distributor system.

Igniter Development

Two significant design improvements to the Smart Plug® catalytic igniters have been made.

One of the main issues of igniter failure has been with the electrical heater that supplies heat to the catalyst during startup. The igniter would run fine while the engine was running, but once cooled down, if the heater wire was broken [Figure 1], it was not possible to start the engine again. The heater wiring has been changed so that the grounding side of the heater exits out of the bottom of the pre-chamber instead of wrapping it back up to the top – where it usually fails. This uses less of the expensive wire, and has proven to be more robust providing a longer igniter life.

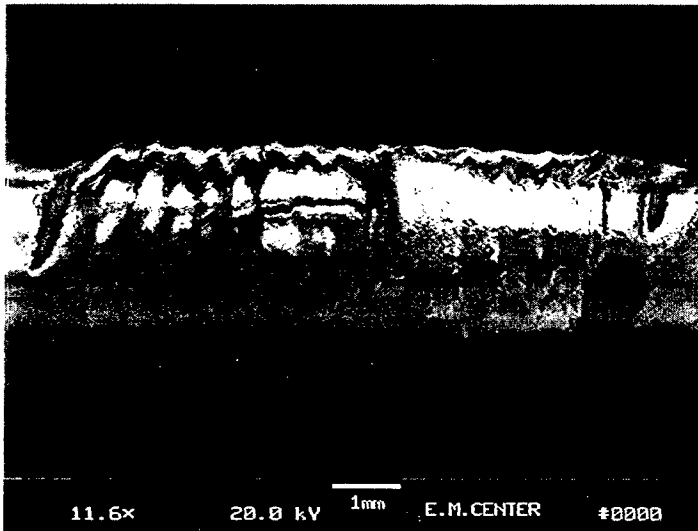


Figure 1. SEM photograph of catalytic igniter failure.

Another change was in the geometry of the igniter bodies. Previous Smart Plug® designs had used changes in the core length to produce changes in ignition timing. The new concept uses changes in pre-chamber diameter to vary the ignition timing. This provides an easier way to change timing that does not require making new cores, which are expensive. The cores can be manufactures more universally – thus dropping manufacturing costs. Only the igniter bodies need to be changed for each application.

EXPERIMENTAL STUDY OF PLASMA-PROPELLANT INTERACTIONS

ARO Contract Number DAAG55-98-1-0519

Principal Investigators: Stefan T. Thynell and Thomas A. Litzinger

Department of Mechanical and Nuclear Engineering
The Pennsylvania State University
University Park, PA 16802

SUMMARY/OVERVIEW:

The use of a plasma as an ignition source has revealed several attractive benefits over conventional igniter systems, such as a shorter ignition delay, reduced temperature sensitivity of the propellant, better controlled propellant mass generation rates, and reduced susceptibility to anomalous ignition transients. However, the causes of these attractive benefits at a fundamental level are not well understood. To address the issues in this experimental program, different diagnostic tools are used, including high-speed photography, fast-response heat flux gages, and species measurements using a micro-probe mass spectrometer. Tests with homogeneous and composite propellants, including JA-2 and an azido/AP propellant, were conducted to determine the conditions required for ignition.

TECHNICAL DISCUSSION:

The electrical circuit and plasma chamber were designed and constructed in this program. The overall experimental facility includes several major components: 1) a plasma generation chamber, 2) a sample holder interfaced to a triple-quadrupole mass spectrometer, 3) an electrical circuit for discharging up to 10 kJ of electrical energy in about 0.3 milliseconds, and 4) various diagnostic components such as pressure transducers, thermocouples, IR-detectors and high-speed film camera. The electrical circuit and plasma chamber are shown in Fig. 1. In this report, we show results obtained by using the triple quadrupole mass spectrometer (TQMS), and update the progress in the design and construction of a fast-response heat flux gage.

Triple-Quadrupole Mass Spectrometry

In order to overcome the short test duration, and to increase the likelihood that propellant samples would ignite, a series of tests in which the plasma was fired into a small chamber (see Fig. 2) was performed. Pressure in the chamber reaches a maximum of approximately 3.5 MPa at 0.38 milliseconds. The velocity at which the precursor shock front of the plasma traveled through the chamber was deduced from the two pressure traces, and found to be approximately 1300 m/s. The slow decrease of pressure evident in the data results from the loss of mass through the port for sampling and from heat transfer from the hot gases to the chamber walls.

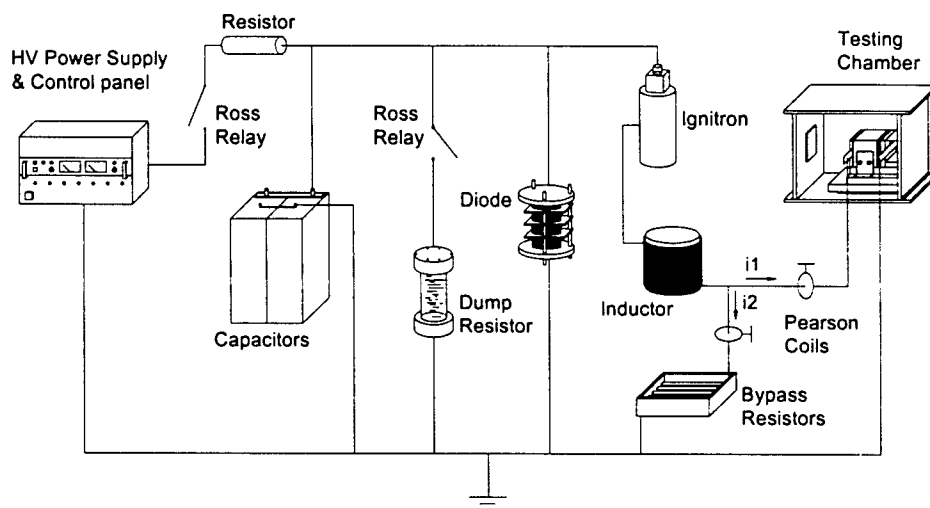


Figure 1. The electrical circuit for the Pulse Forming Network (PFN).

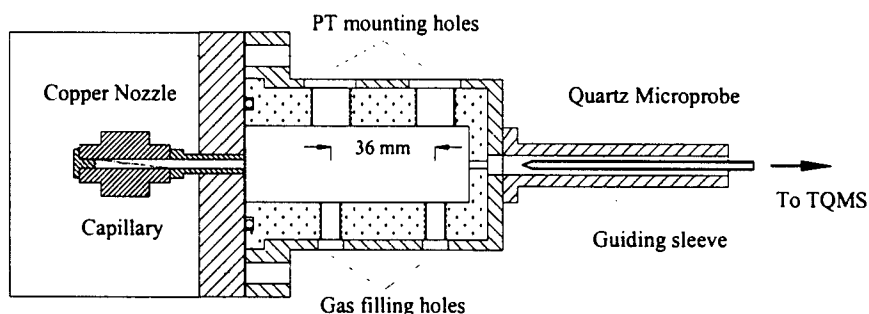


Figure 2. Setup for closed chamber testing (showing the closed chamber interfaced to TQMS and connected to the plasma chamber).

For this configuration, two significant mass signals at 26 and 28 amu were consistently measured during the micro-probe MS parent mode testing. A typical species result for a firing without a propellant sample is presented in Fig. 3. The signal at 26 amu corresponds to acetylene (C_2H_2), which is expected to be a major product from the plasma using a polyethylene capillary. The signal at 28 amu could be N_2 , CO or C_2H_4 , which cannot be differentiated due to the presence of air in the chamber.

This difficulty in separating the species at 28 amu led to modifications of the test chamber to allow it to be purged of air using oxygen or argon. Using oxygen was expected to sustain combustion, while eliminating the nitrogen, and argon was expected to allow pyrolysis and soot formation chemistry within the plasma to be studied, by eliminating oxygen. Results using oxygen as the ambient gas are shown in Fig. 4. Elimination of nitrogen in the ambient gas changes the trends in the signal at 28 amu. It was first detected at about 1.6 milliseconds with intensity of about 1700, reaches its peak of slightly higher than 8000 at 25 milliseconds, then decreases to 4400 at 200 milliseconds, and thereafter keeps around this level. Since the chamber was initially void of N_2 , the signal at 28 amu must be CO or C_2H_4 , or both.

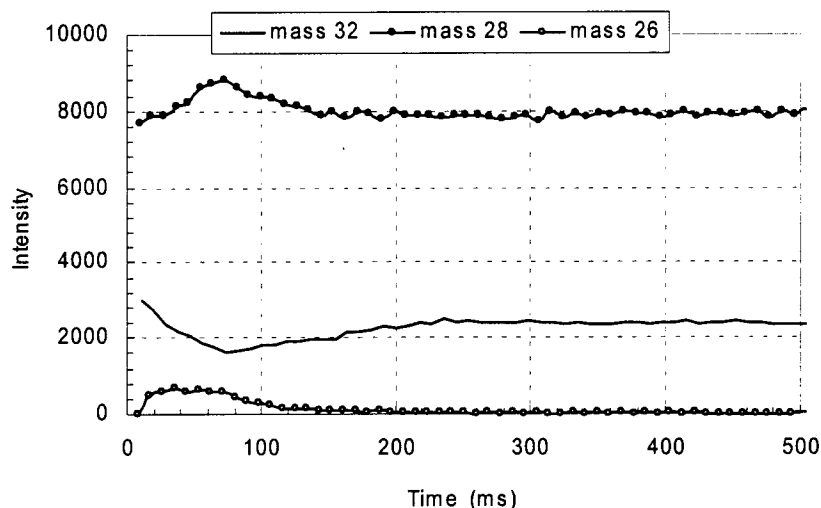


Figure 3. MPMS parent mode sampling from 4kV plasma jet generated from an 8.0mm bore PE capillary and injected into a closed chamber with air as ambient gas.

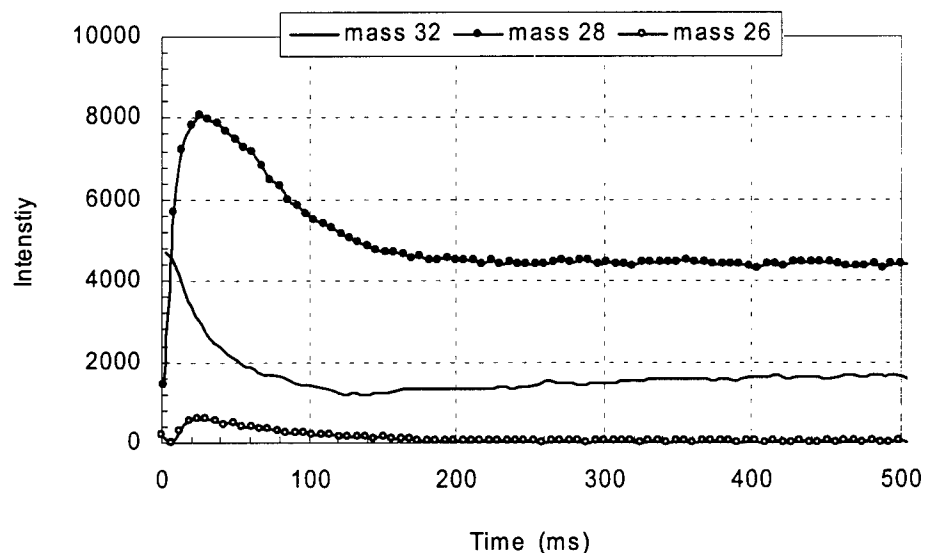


Figure 4. MPMS parent mode sampling from 4kV plasma jet generated from an 8.0mm bore PE capillary and injected into a closed chamber with O_2 as ambient gas.

Tests were then run with argon as the ambient gas, and the results are shown in Fig. 5. The results show a much larger signal for mass 26, C_2H_2 , when argon is the ambient gas and also lower maximum signal at mass 28, C_2H_4 or CO. These trends indicate that oxidation is occurring in the tests with oxygen as the ambient gas, but this conclusion must be verified with daughter mode testing. In cooperation with ARL, modeling studies will be conducted to investigate the mixing and reaction in the closed chamber. Also extension of the chemical mechanism of the model to include pyrolysis and soot formation chemistry is planned to track the formation of species such as acetylene and ethylene.

The triple quadrupole mass spectrometer has undergone a major equipment upgrade, to allow molecular beam sampling. Efforts are now in progress to utilize this instrument to obtain information about highly transient species, which are present in the high-temperature plasma.

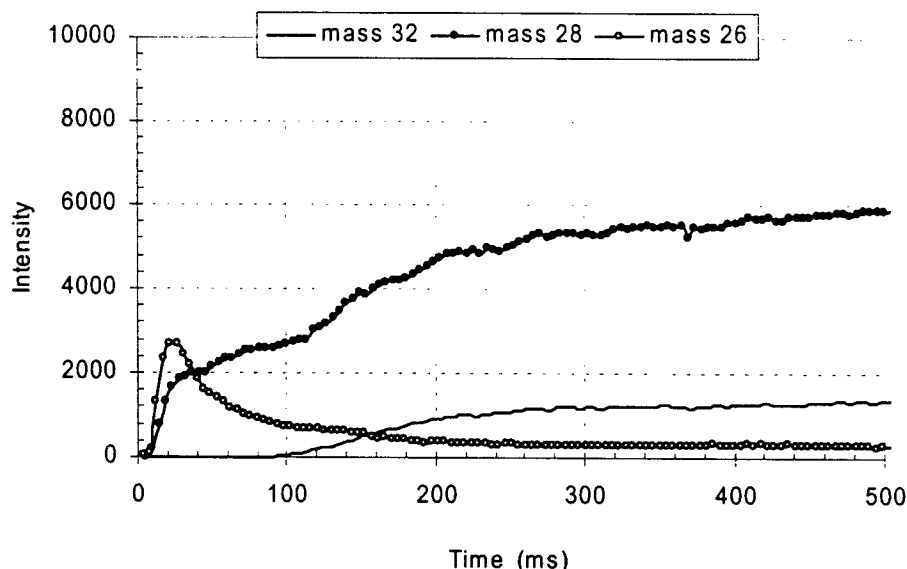


Figure 5. MPMS parent mode sampling from a 5kV plasma jet generated from a 3.2 mm bore PE capillary and injected into a closed chamber with Argon as ambient gas.

Fast-Response Heat Flux Gage

There is limited understanding of the importance of thermal radiation for achieving ignition, its in-depth heating effects, as well as the extent of in-depth chemical reactions from UV absorption. Furthermore, the overall rate of heat transfer (radiative and convective) from the plasma to the propellant's surface is also largely unknown. To ascertain the role of thermal radiation and convection, a fast-response heat flux gage is needed. This gage must also have low-noise characteristics, be readily replaceable, and be inexpensive. Such a gage has been designed and constructed. The gage itself is a thin titanium film sputtered onto a polyimide substrate. The 8 nm thick titanium film is inert and has relatively high electrical resistance. The resistance varies with temperature. By driving a constant current through the film and measuring the voltage drop, the resistance is determined. From calibration charts, the surface temperature can be deduced. An inverse heat conduction analysis is utilized to compute the heat flux variation, corresponding to the measured surface temperature variation. The gage and calibration facility have been designed and constructed. The electrical circuit that quickly must respond to resistance changes has a 500kHz frequency response, which is more than adequate. The film itself appears to very rugged and withstands a repeated, but gentle impact of a solid material. Current efforts are focused on completing the calibration of uncoated titanium films, which are highly reflective. To deduce thermal radiation, the titanium film must be coated with a flat black paint and its response assessed and calibrated. This will be followed by parametric surveys to assess the role of radiation and convection. In addition, the setup utilizes five heat flux and four pressure gages, in order to obtain a spatial variation of the heat flux.

EXPERIMENTAL INVESTIGATION OF THE INTERACTION OF ELECTROTHERMAL PLASMAS WITH SOLID PROPELLANTS

Grant/Contract Number: DAAD19-00-1-0420
Philip L. Varghese and Noel T. Clemens

Center for Aeromechanics Research
Department of Aerospace Engineering and Engineering Mechanics
The University of Texas at Austin
Austin, TX 78712

SUMMARY/OVERVIEW:

The primary focus of the proposed work is a detailed experimental study of the plasma and its interaction with representative solid propellants. The objective of the work is to develop an extensive experimental database of species concentrations both during the plasma-propellant interaction and immediately thereafter. Such a data base is vital to develop a correct thermochemical model of mechanisms that lead to rapid, repeatable ignition and which permit temperature compensation of the gun charge. This knowledge is essential if the Army is to field plasma initiators.

TECHNICAL DISCUSSION

ARL studies of propellant charges ignited by plasma discharges have shown that this technique has significant advantages over conventional (primer) ignition. Ignition delay and jitter were substantially reduced, and temperature compensation achieved with a plasma energy input that was substantially smaller than the energy required to heat the propellant bed to the reference condition. However, the mechanism of the interaction is unknown. The plasma could function merely as an improved thermal source since it has a very high temperature compared to conventional combustion products. It could function as a radiant source that distributes the energy into the propellant bed more uniformly and rapidly than simple flame spread. Additionally, the plasma could provide a source of highly reactive species, not present in flames, which promote rapid and reliable ignition. Plasma jets issuing into the propellant beds may penetrate more effectively than combustion products from a primer, and thus give a more distributed ignition. It is also possible that the blast wave accompanying the plasma discharge causes microfractures in the propellant grains that increases the burning surface area sufficiently to provide temperature compensation, though it seems hard to reconcile the observed repeatability of the process with known mechanisms of microfracture.

A combination of several of these mechanisms might also contribute to the observed performance improvement. An improved fundamental understanding of the interaction will help the Army design better initiators that tailor the plasma to the propellant thus reducing energy required or enhancing gun performance. For example, it may be possible to achieve the observed temperature compensation with a much smaller energy input than is currently needed, which would reduce the size of the power source required. A fundamental understanding is also needed

to reduce risk. Because of the current lack of understanding, one cannot rule out the possibility that the plasma is interacting with only a minor component of the propellant charge, and thus plasma igniters could fail because of minor changes in propellant composition.

Owing to the complexity of the physical processes involved in plasma-induced ignition, achieving an understanding of the fundamental physics will likely be achieved only through computational/theoretical approaches aided by experimental data. To date, however, there is insufficient experimental data on the plasma-propellant interaction to properly develop and validate chemical models. Therefore, the primary goal of this project is to use advanced laser diagnostic techniques to develop a unique database that can be used to aid in the modeling efforts being undertaken at ARL and elsewhere.

We concentrate on studying the interaction of the plasma with solid propellants at atmospheric pressure. These conditions are representative of the ignition and initial stages of combustion before the gun chamber pressure rises. The reason for limiting this study to atmospheric pressure conditions is because of the difficulty of making meaningful measurements at high pressures especially with the intense background luminosity of the plasma.

The primary objective of this work is to generate as complete a picture as possible of the plasma-propellant interaction and subsequent ignition, by measuring a range of species that provide information on the distribution of the plasma or are important combustion intermediates. As a general philosophy, we try to make time resolved, simultaneous multi-point measurements whenever possible so as to build up an extensive database. The multi-point measurements will be supplemented with line of sight averages and single-point measurements when necessary.

The plasma-propellant flow field is a very challenging environment in which to make measurements because of the high temperatures and densities, complex chemistry and the transient nature of the interaction. Transient reacting flows are best studied by non-intrusive optical techniques that do not perturb the system. The high plasma luminosity presents the biggest challenge for laser-based studies of propellant ignition when interacting with a plasma, but we believe that a number of optical diagnostic techniques can be used effectively to study the plasma ignition process. However, we recognize that any single technique may not work as well as anticipated in such a severe environment. Thus we plan to employ a number of different techniques for studying different aspects of the problem.

The capillary plasma source is driven by a pulse forming network (PFN), consisting of a 251 μF capacitor charged to a maximum of 5.0 kV (3.1 kJ) and a 26 μH inductor. The discharge is initiated by closing an Ignitron switch that connects the capacitor to the capillary electrodes. The capillary is 3 mm in diameter by 30 mm long and is open at one end only. The wall material is polycarbonate (Lexan, $C_{16}H_{14}O_3$). To help initiate the discharge a thin copper fuse wire (64 μm) – which explodes when the Ignitron is closed – is inserted inside the capillary between the electrodes. Ablation and ionization of material from the capillary surface then sustains the discharge. The resulting plasma expands rapidly from the open end of the capillary and issues into room air. In order to reduce erosion, the electrodes were constructed with inserts made of copper-tungsten alloy (30% Cu, 70% W). The peak current through the plasma is approximately 4.6 kA for a discharge energy of 5 kV (3.1 kJ), and the discharge duration is approximately 250 μs . Figure 1 is a close-up of the present experimental layout showing the camera systems being used to study the flowfield via emission.

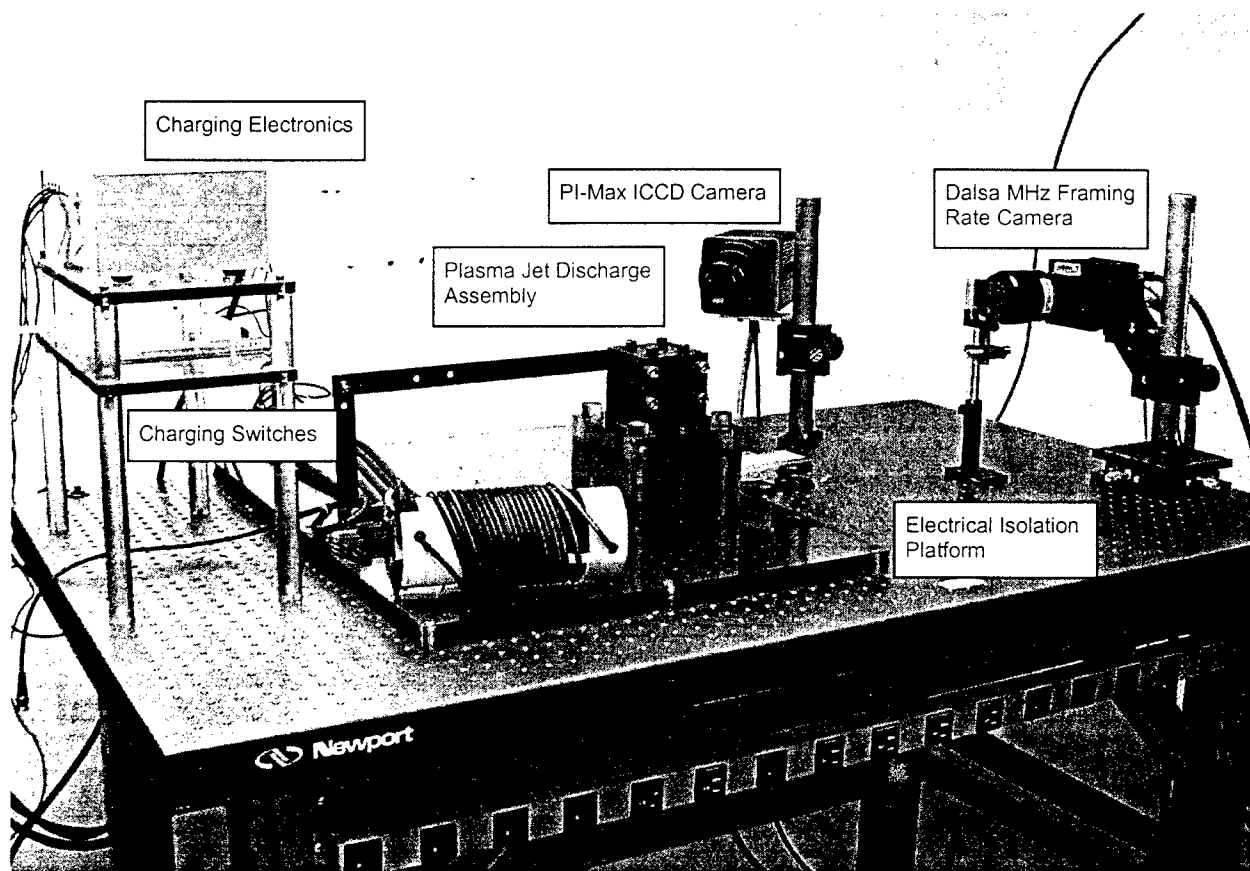


Figure 1. Close-up view of experimental set-up

The characterization of the pulsed plasma jet is accomplished using a variety of optical diagnostics. A gated-intensified CCD camera is used to capture images of visible emission and Schlieren images. Figure 2 shows a representative emission image in false color. This image was obtained for an initial charging voltage of 3 kV (1.1 kJ) and was captured 160 μ s after the initiation of the discharge. The gate-width (exposure time) used was 85 ns which was sufficiently small to freeze the flow. The barrel shock, Mach disk, contact surface and luminous bore-exit flow are clearly seen in the emission image. (Animations of the emission and Schlieren images showing the evolution of the plasma jet flow field can be found on the web page <http://www.ae.utexas.edu/research/FloImLab/plasma.html>.)

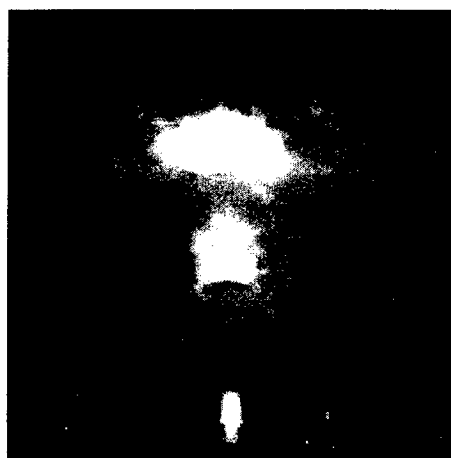


Figure 2. Image of the plasma emission 160 μ s after discharge initiation. Initial capacitor voltage 3kV, 85 ns gate width.

In addition to the imaging studies, we obtain instantaneous emission spectra at several axial positions within the jet and at different delay-times (measured from the initiation of the discharge). The emission spectra are used to investigate evolution of the excitation temperature and electron density fields. Using Boltzmann plots, the spectra are used to generate axial profiles of the excitation temperature in the plasma jet at different times. We define the nondimensional axial distance, $\zeta_l = x/x_m(t)$, where $x_m(t)$ is the axial distance from the bore exit to the Mach disk at time t . In experiments to date we observe that two temperatures (upstream and downstream of the Mach disk) can essentially characterize the entire axial profile, i.e. $T_{exc} = 14,000\text{ K}$ for $\zeta_l < 1$ and $T_{exc} = 25,000\text{ K}$ for $\zeta_l > 1$ for discharge energies of 3.1 kJ . Electron number density profiles are inferred from the linewidths of observed H_α lines. The profiles at different times are seen to be very similar when plotted vs ζ_l , with an abrupt increase in electron density near $\zeta_l = 1$. For a discharge energy of 3.1 kJ the measured electron number density ranges from $1.7 \times 10^{17}\text{ cm}^{-3}$ to $5.5 \times 10^{17}\text{ cm}^{-3}$ upstream of the Mach disk to 10^{18} cm^{-3} to $2.5 \times 10^{18}\text{ cm}^{-3}$ downstream of the Mach disk.

Figure 3 demonstrates the use of PLIF in this challenging flow-field. This preliminary PLIF image of atomic copper was obtained by pumping the $^2P_{3/2} \leftarrow ^2S_{1/2}$ line at 327 nm and detected the fluorescence from the $^2P_{3/2} \rightarrow ^2D_{5/2}$ line at 578 nm . The intense copper signal in the outer flow comes from the exploding wire used to initiate the discharge, whereas the smaller copper signal in the expanding jet comes from copper eroding from the Cu-W electrode during the discharge. The image was obtained by subtracting two 17 shot averages in order to remove the intense background emission from the plasma. We have purchased a second ICCD camera in order to obtain single-shot background corrected PLIF images. Over the next year we plan to use the system to obtain PLIF images of molecular species such as OH and NO when the plasma is impinging on a propellant sample.

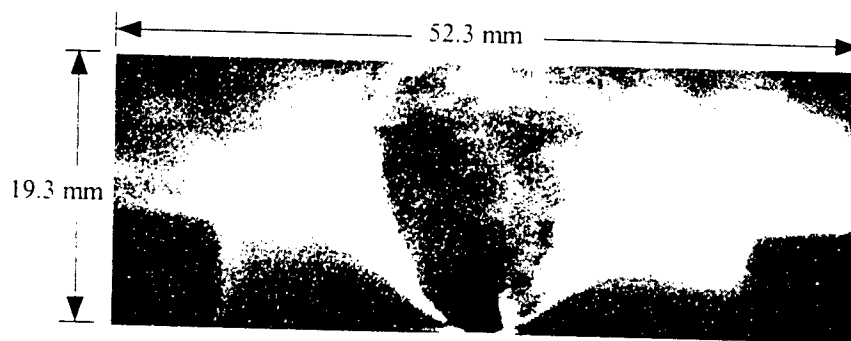


Figure 3. Grey scale image of Cu atoms detected by PLIF. 17 PLIF images were averaged, and background subtracted using a 17 shot average of plasma emission only. The excitation laser beam is passing from left to right and is retroreflected.

DEVELOPMENT AND OPTIMIZATION OF A COMPREHENSIVE KINETIC MODEL OF HYDROCARBON FUEL COMBUSTION

(Grant/Contract Number F49620-01-1-0144)

Principal Investigator:

Hai Wang

Department of Mechanical Engineering
University of Delaware, Newark, DE 19716

SUMMARY/OVERVIEW

The objective of the present research program is to develop a comprehensive, predictive, and detailed kinetic model of hydrocarbon combustion for aeropropulsion simulations. During the reporting period progress has been made in the following projects: (1) a comparative study of the influence of reaction rate constant and binary diffusion coefficient on laminar flame speed predictions and close coupled scattering calculations for the binary diffusion coefficients of H-He and H-Ar, (2) a study on the mechanisms for the initiation of radical chain reactions during homogeneous oxidation of unsaturated hydrocarbons, and (3) development of a comprehensive mechanism for C₁-C₄ fuel combustion. These three projects represent the two key ingredients that are necessary to the success of the overall research program. These are, (1) the formulation of physico-chemical properties that are relevant to kinetic model development and validation, and (2) further development of a unified and optimized kinetic model for higher hydrocarbon combustion.

TECHNICAL DISCUSSION

1. Influences of Binary Diffusion Coefficients on Laminar Flame Speed Predictions

Numerical simulation of complex combustion flows requires a valid chemical reaction model as well as a satisfactory transport model. Much of the research emphasis in the past has been placed on the chemical reaction model. This emphasis was completely valid, because thirty years ago the uncertainty in reaction kinetics was substantially larger than that of the transport model and parameters. While we had enjoyed a fruitful advance of knowledge in reaction kinetics, little to no advance was made in transport processes and notably in the theory of diffusion of gaseous free radical species.

The uncertainties of the transport parameters stem mainly from the difficulties to measure the viscosity, conductivity, and diffusivity of a free radical species. In general, the transport parameters of free radicals other than the H atom were approximated by those of their parent molecules. In the case of the H atom, the binary diffusion coefficients have only been measured at the room temperature and with inert gases such as He, Ar, and N₂. In addition, it is suspected on the basis of theoretical considerations that the Chapman-Enskog theory is inadequate when used for prediction of free radical diffusion. Our recent study [1] suggested that the diffusion coefficients of free radical species may be highly uncertain because of the formation of a transiently bound complex upon molecular collision. This type of collision applies to binary pairs H-N₂, H-CO, O-CO, H-CO₂, H-C₂H₂ etc, and may enhance the binary diffusion coefficient of a free radical species by as much as 50% at the temperature of 1500 K.

While transport uncertainties are apparent, it is not clear to what extent these uncertainties affect the predictions of laminar flame properties like the laminar flame speed. The objective of the present study is to determine the sensitivity of flame speed predictions with respect to binary diffusion coefficients for hydrogen-, methane-, acetylene-, and propane-air flames under fuel-lean, stoichiometric, and fuel-rich conditions, and near the lean flammability limits of these flames. The Sandia PREMIX program was modified to determine the sensitivity coefficient for binary diffusion coefficients. The sensitivity coefficient was obtained by solving the linear system of equations $(\partial F/\partial \phi)(\partial \phi/\partial D) + (\partial F/\partial D) = 0$, where F is the residual vector of the discretized governing equations, ϕ the solution vector (mass flux, temperature, and species mass fractions), and D is the binary diffusion coefficient. Here, $\partial F/\partial \phi$ is the Jacobian of the residue vector. The normalized sensitivity coefficient of laminar flame speed, s_u , is defined by $S_{ij} = \partial \ln s_u / \partial \ln D_{ij}$.

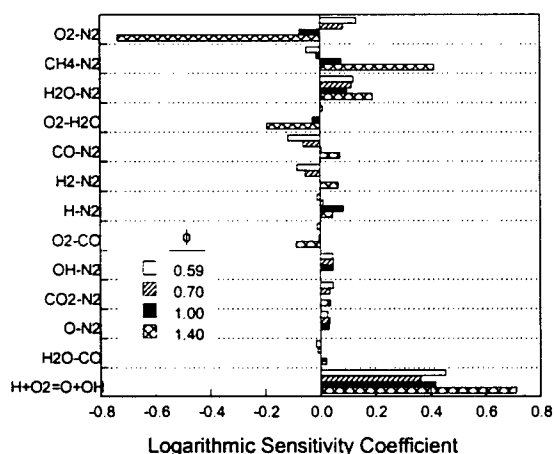


Figure 1. Ranked logarithmic sensitivity coefficients of the laminar flame speeds of methane-air mixtures with respect to binary diffusion coefficients, compared to that for the rate constant of chain-branching reaction $H + O_2 \rightarrow O + OH$.

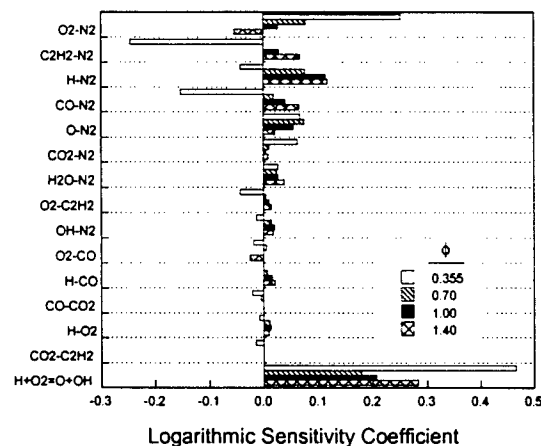


Figure 2. Ranked logarithmic sensitivity coefficients of the laminar flame speeds of acetylene-air mixtures with respect to binary diffusion coefficients, compared to that for the rate constant of chain-branching reaction $H + O_2 \rightarrow O + OH$.

Figures 1 and 2 present representative results of the logarithmic sensitivity coefficients computed for methane and acetylene flame speeds with respect to binary diffusion coefficients. For comparison, the respective sensitivity coefficients computed for the rate constant of $H + O_2 \rightarrow O + OH$ are also shown in the same figures. These and additional results obtained for the hydrogen and propane flames indicate that (a) the flame speed is markedly influenced by the diffusion coefficients of binary pairs involving the major combustion reactants and products and the major flame free radicals, e.g., H and O, with molecular nitrogen, and (b) depending on the nature of the fuel, these influences could be as significant as that of key elementary reactions, e.g., the $H + O_2$ chain branching reaction. Considering the uncertainties in these coefficients and comparing them to the uncertainties in reaction kinetics, we conclude that the transport model and coefficients deserve as much attention as the reaction kinetics in the development of predictable reaction models for hydrocarbon fuel combustion. At the present time, close coupled scattering and molecular dynamics calculations are underway to determine the binary diffusion coefficients, with the aim of reconciling the molecular beam scattering data with the binary diffusion coefficients of simple pairs like H-He and H-Ar. These computational methods will then be used to determine the diffusion coefficients of H-N₂, H-O₂, and H-CO in the next step of research.

The above results are reported in the Second Joint Meeting of the U.S. Sections of The Combustion Institute [2].

2. Initiation of Free-Radical Chain Reactions in Oxidation of Unsaturated Hydrocarbons

The initiation of free-radical chain reactions during homogeneous oxidation and ignition of hydrocarbon compounds is traditionally described by two types of reactions. The first is the C—H fission in the fuel molecule. The second is the hydrogen abstraction of fuel molecules by molecular oxygen. In most cases initiation reactions are overtaken by chain branching reactions at the very onset of reaction. For this reason they usually do not exhibit as large an influence as chain branching processes. On the other hand, an accurate prediction of the characteristics of fuel oxidation such as the shock-tube ignition delay cannot be made without adequately considering the nature and rates of initiation reactions.

A good example is the homogeneous oxidation of acetylene in shock tubes. It is well established that the initial radicals are produced from the reaction of acetylene and molecular oxygen, yet the nature of this reaction became known only until recently. Following the pioneering work of Kiefer and coworkers, we proposed that the initiation reactions during acetylene oxidation start with acetylene isomerization to vinylidene followed by the reaction of vinylidene with molecular oxygen. We showed that a detailed kinetic model of acetylene oxidation featuring this chain-initiation mechanism describes very well a variety of shock-tube ignition delay data reported for acetylene.

The conclusion of that study also opens up the possibility that there is a third type of initiation reactions for the oxidation of unsaturated fuels, namely, the isomerization or decomposition of the fuel molecule to a singlet carbene species followed by the reaction of carbene with molecular oxygen. In fact, many unsaturated hydrocarbons (e.g., acetylene, ethylene, propyne, and allene) can isomerize via 1,2-H shift to form singlet carbene species with threshold energy much smaller than that of C—H fission. If these carbene species are capable of reacting with molecular oxygen within their lifetime, they may provide a source of initial radicals to initiate chain reactions. In this work, we examine the viability of a chain initiation mechanism involving single carbene species in the homogeneous oxidation of representative unsaturated hydrocarbon compounds including ethylene, allene, propyne, and 1,3-butadiene. The work is of critical importance to a generalized understanding of the nature of radical-chain reactions during hydrocarbon combustion, and to the development of a comprehensive kinetic mechanism of hydrocarbon combustion.

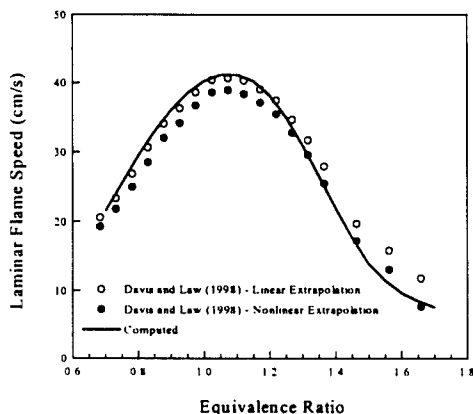
We propose that the initial radicals in the homogeneous oxidation of ethylene, propyne, allene, and 1,3-butadiene are produced from two types of singlet species, vinylidene ($\text{H}_2\text{CC:}$) and propenylidene ($\text{CH}_3\text{CHC:}$), as the intermediates of the initial decomposition or isomerization of the fuel molecules, i.e., $\text{C}_2\text{H}_4 \rightarrow \text{H}_2\text{CC:} + \text{H}_2$, $a\text{C}_3\text{H}_4$ and $p\text{C}_3\text{H}_4 \rightarrow \text{CH}_3\text{CHC:}$, and $1,3\text{-C}_4\text{H}_6 \rightarrow \text{H}_2\text{CC:} + \text{C}_2\text{H}_4$, followed by $\text{H}_2\text{CC:} + \text{O}_2 \rightarrow \text{free radicals}$ and $\text{CH}_3\text{CHC:} + \text{O}_2 \rightarrow \text{free radicals}$. Quantum chemistry calculations were carried out to estimate the thermochemistry of species that participate in these reactions and to explore the potential energy surfaces of selected reactions. The reaction steps were then included in a detailed kinetic model of $\text{C}_2\text{-C}_4$ fuel combustion [e.g., 3]. The validity of the initiation mechanism was verified by kinetic modeling of shock-tube ignition delay of ethylene, propyne, and allene, with and without the carbene chemistry. For every unsaturated fuels tested carbene reactions were found to produce initial free radicals at significantly faster rates than C—H fission and H-abstraction by molecular oxygen.

Thus we conclude that the initial radical pool during high-temperature, homogeneous oxidation of ethylene, propyne, allene, and 1,3-butadiene is produced by singlet carbene intermediates of initial fuel decomposition, followed by the rapid reaction of the carbene species with molecular oxygen. Combined with the findings of previous studies on the chain initiation mechanisms of acetylene, we conclude that the singlet carbene species plays a short-lived, yet significant role in the homogeneous oxidation of unsaturated hydrocarbons.

The above results are reported in the Second Joint Meeting of the U.S. Sections of The Combustion Institute [4].

3. Development of a Comprehensive Reaction Mechanism of C₁-C₄ Fuel Combustion

In this work we extended the previously developed and validated reaction model of 1,3-butadiene combustion [3] to *n*-butane, *i*-butane, 1-butene and 2-butene. In addition to mechanism development, there are two additional objectives in this study. First, we intend to address the question concerning the critical size of a well-optimized, small-hydrocarbon kinetic subset that can be used as secure foundations for extension to larger-hydrocarbon oxidation models. This question is motivated by our previous study which showed that a well-optimized C₁-C₂ kinetic subset cannot be used as a base set for the C₃ combustion model without reoptimizing the subset. Yet it is not clear whether there exists a critical kinetic subset larger than which a sequential optimization process can be conducted without having to re-optimize the critical subset when the combustion of a new hydrocarbon fuel is included in the comprehensive



reaction model. Second, in collaboration with Professors C. K. Law (Princeton) and C. J. Sung (Case Western Reserve), we have initiated a study of the laminar flame speed of fuel blends with a specific objective to examine the influence of kinetic coupling of fuel mixtures on laminar flame propagation [5]. The initial fuel blend used in the investigation was the *n*-butane and ethylene mixture, which is representative of an alkane-alkene fuel blend.

Figure 3. Experimental and computed flame speeds of *n*-butane-air mixtures at the atmospheric pressure.

A detailed reaction model was compiled, which consists of 81 species and 570 elementary reactions. Figure 3 presents the preliminary comparison between the experimental flame speeds and computational results of *n*-butane-air mixtures. The reaction model used in the computation was not optimized. Preliminary comparisons of the experimental data and modeling results for ethylene, 2-to-1, 1-to-1, and 1-to-2 mixtures of ethylene and butane, and butane flame speeds were also carried out. The results are found in the progress report of the Princeton group (Professor C. K. Law).

PUBLICATIONS AND CONFERENCE PRESENTATIONS (May 2000 – April 2001)

1. Wang, H. "Effect of transiently bound collision on binary diffusion coefficients of free-radical species," *Chemical Physics Letters* **325**, pp. 661-667 (2000).
2. Yang, Z., Yang, B., and Wang, H. "The influence of H-atom diffusion coefficient on laminar flame simulation." *Proceedings of the Second Joint Meeting of the U.S. Sections of The Combustion Institute*, March, 2001, Berkeley, CA, Paper 237.
3. Laskin, A., Wang, H. and Law, C. K. "Detailed kinetic modeling of 1,3-butadiene oxidation at high temperatures," *International Journal of Chemical Kinetics* **32**, pp. 589-614 (2000).
4. Wang, H. "Chain reaction initiation in homogeneous oxidation of ethylene, propyne, and 1,3-butadiene." *Proceedings of the Second Joint Meeting of the U.S. Sections of The Combustion Institute*, March, 2001, Berkeley, CA, Paper 151.
5. Hirasawa, T., Sung, C. J., Yang, Z., Wang, H., and Law, C. K. "Determination of laminar flame speeds using digital particle image velocimetry." *Proceedings of the Second Joint Meeting of the U.S. Sections of The Combustion Institute*, March, 2001, Berkeley, CA, Paper 138.

FUELS COMBUSTION RESEARCH: SUPERCRITICAL FUEL PYROLYSIS

AFOSR Grant No. F49620-00-1-0298

Principal Investigator: Mary Julia (Judy) Wornat

Princeton University
Department of Mechanical and Aerospace Engineering
Princeton, New Jersey 08544

SUMMARY/OVERVIEW:

The fuels used in the next generation of hypersonic aircraft [1] will have to operate under very high pressures (beyond the critical pressures of most hydrocarbons) and will have to sustain very high heat loads in order to meet aircraft cooling requirements. Potential candidates for meeting these stringent cooling requirements are "endothermic" fuels, fuels that can undergo a controlled heat-absorbing chemical reaction (*e.g.*, dehydrogenation) prior to combustion. Critical to the development of the fuel systems in these aircraft is an understanding of the fuel pyrolysis reaction mechanisms under the conditions that the fuels will be operating. Of particular interest are the reactions leading to polycyclic aromatic hydrocarbons (PAH), which can serve as precursors to fuel-line deposits, a problem of critical importance to avoid, for safe aircraft operation. In order to better elucidate the mechanisms and kinetics of the reactions of endothermic fuel pyrolysis and PAH formation under supercritical conditions, supercritical pyrolysis experiments are being conducted, under the present research program, with model fuels, over a range of supercritical pressures and temperatures. The model fuels include two endothermic fuels, methylcyclohexane and decalin, as well as toluene and heptane, hydrocarbons representative of the aromatic and aliphatic components of jet fuels. The reaction products are analyzed by high-pressure liquid chromatography with diode-array ultraviolet-visible absorbance detection (HPLC/UV), an isomer-specific technique ideally suited for the analysis of PAH [2]. It is anticipated that the results from this study will provide information of critical importance to the design and development of fuel systems for high-speed aircraft.

AUTHORS: M. J. Wornat, E. B. Ledesma, J. A. Sivo, and N. D. Marsh

TECHNICAL DISCUSSION

Pyrolysis experiments have been conducted with the model endothermic fuel methylcyclohexane (critical temperature 299 °C, critical pressure 34 atm) at a residence time of 30 sec; at temperatures of 330, 370, 430, 470, 530, and 570 °C; and at pressures of 20, 40, 60, 80, and 100 atm. Collection and analysis of the methylcyclohexane reaction products from these experiments reveals that for the 30-sec residence time employed and the entire range of pressures investigated, PAH are not produced at detectable levels at temperatures ≤ 430 °C. At the highest temperatures of 530 and 570 °C, PAH are produced at all pressures. At the intermediate temperature of 470 °C, PAH are detected at all pressures but in only minimally detectable amounts at the lowest pressure of 20 atm.

The methylcyclohexane pyrolysis experiments show that an increase in pyrolysis temperature brings about an increase in PAH production as well as an increase in the molecular sizes of the PAH formed. Figure 1 depicts an HPLC chromatogram of the products from methylcyclohexane pyrolysis at 570 °C and 100 atm, the highest temperature and pressure examined so far. Included in Figure 1 are the structures of the twenty-two PAH unequivocally identified by matching the chromatographic retention time and UV absorption spectrum of each sample component with those of authentic reference standards. The HPLC/UV technique is ideally suited for PAH analysis since each PAH exhibits a unique UV absorption spectrum. Compounds of similar chemical structure (e.g., benzo[*a*]pyrene and benzo[*e*]pyrene) are thus easily distinguished, one from another—a distinction very important in determining chemical reaction pathways. The UV spectral matches confirming the identities of two of the methylcyclohexane products of Figure 1, benzo[*a*]pyrene and anthanthrene, are displayed in Figure 2.

As illustrated in Figure 1, supercritical pyrolysis at 570 °C and 100 atm produces a variety of PAH, ranging in size from one to seven aromatic rings, and including several classes of compounds: 10 benzenoid PAH (those with only six-membered rings), 3 fluoranthene benzologues (those with an internal five-membered ring), 3 indene benzologues (those with a five-membered ring containing a methylene carbon), and 6 methylated PAH. The high abundance of methylated PAH distinguishes these methylcyclohexane products from products of purely aromatic fuels [3] and undoubtedly results from the abundance of methyl fragments readily produced from pyrolysis of a hydrogen-rich endothermic fuel such as methylcyclohexane. Additional methylated PAH are thought to be among the products not yet identified in Figure 1 due to the coelution of species and the consequent superposition of peaks in the product components' UV spectra.

Just as pyrolysis temperature has a large effect on PAH production from supercritical methylcyclohexane pyrolysis, so does pressure. Figures 3 and 4 illustrate the effect of pressure on the yields of 2-, 3-, and 4-ring PAH produced from methylcyclohexane pyrolysis at 530 °C and 30 sec. As these figures indicate, all PAH increase in yield as pressure is increased—the greatest jump occurring in the interval from 80 to 100 atm. Figures 3 and 4 also demonstrate that the 2-ring species naphthalene and indene are produced in greatest abundance, followed closely by the two methylnaphthalenes. Compared to these 2-ring species, the 3- and 4-ring species are roughly an order of magnitude lower in yield. The trend of decreasing yield with increasing molecular size is characteristic of pyrolytic molecular growth processes [2].

The increase of PAH production with increasing pressure can be tied to the findings of Stewart [4]. As proposed by Stewart [4] and demonstrated in Figure 5, methylcyclohexane pyrolysis produces an intermediate, the methylhexenyl radical, which either in the gas phase at atmospheric pressure or in the supercritical phase produces β -scission products such as ethene and propene. In the very dense environments characteristic of supercritical pressures, however, diffusion of β -scission products (away from one another) is impaired and collision processes are favored, enhancing carbon-carbon bond formation and facilitating the production of cyclic structures. Under supercritical conditions, therefore, the intermediate methylhexenyl radical produces dimethylcyclopentane [4], a hydrocarbon containing a methylated five-membered ring. Such five-membered-ring species have been shown [4 and references therein] to undergo facile conversion to structures containing six-membered aromatic rings. It thus makes sense that the higher pressures that enhance production of five-membered-ring species also enhance production of PAH, as demonstrated in the methylcyclohexane experiments (Figures 3 and 4).

Figure 6 illustrates the reaction [5] of two five-membered-ring species to give naphthalene, one of the most abundant PAH produced in the methylcyclohexane supercritical pyrolysis experiments. Figure 6 also shows how the 1-naphthyl radical, formed from hydrogen-abstraction of naphthalene, can combine [6] with benzene, also present in the supercritical methylcyclohexane pyrolysis products [4], to form the 4-ring product fluoranthene, another of the PAH observed in the methylcyclohexane experiments.

The results obtained so far highlight the importance of temperature and pressure on PAH formation from the pyrolysis of endothermic fuels under supercritical conditions. Future work will include: methylcyclohexane experiments at additional temperatures and residence times, supercritical pyrolysis experiments with other model fuels, and work on the reaction mechanisms of PAH formation in the supercritical context. Since PAH are precursors to carbon solids, determination of the reaction conditions and pathways responsible for PAH formation during the supercritical pyrolysis of endothermic fuels should provide information of critical value to the prevention of fuel-line fouling in high-speed aircraft.

REFERENCES

1. Edwards, T., "USAF Supercritical Hydrocarbon Fuels Interests," AIAA Paper 93-0807 (1993).
2. Wornat, M. J., Ledesma, E. B., and Marsh, N. D., *Fuel*, in press (2001).
3. Wornat, M. J., Sarofim, A. F., and Lafleur, A. L., *Proceedings of the Combustion Institute 24*: 955-963 (1992).
4. Stewart, J. F., Princeton University, Department of Mechanical and Aerospace Engineering, Ph.D. Thesis, 1999.
5. Melius, C. F., Colvin, M. E., Marinov, N. M., Pitz, W. J., and Senkan, S. M., *Proceedings of the Combustion Institute 26*: 685-692 (1996).
6. Badger, G. M., *Progress in Physical Organic Chemistry 3*: 1 (1965).

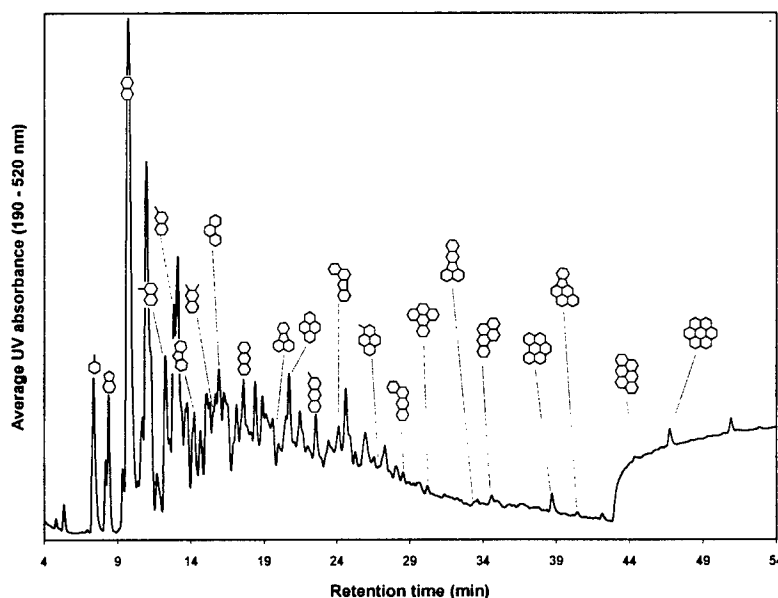


Figure 1. Reverse-phase HPLC chromatogram of products of methylcyclohexane supercritical pyrolysis at 570 °C and 100 atm. The rise in baseline at ~43 minutes corresponds to a change in mobile-phase composition to UV-absorbing dichloromethane. Identified components in order of elution from left to right, are: toluene, indene, naphthalene, 1-methylnaphthalene, 2-methylnaphthalene, fluorene, 2,3-dimethylnaphthalene, phenanthrene, anthracene, fluoranthene, pyrene, 2-methylantracene, benzo[*a*]fluorene, 1-methylpyrene, benz[*a*]anthracene, benzo[*e*]pyrene, benzo[*k*]fluoranthene, benzo[*a*]pyrene, benzo[*ghi*]perylene, indeno[1,2,3-*cd*]pyrene, anthanthrene, coronene.

Figure 2

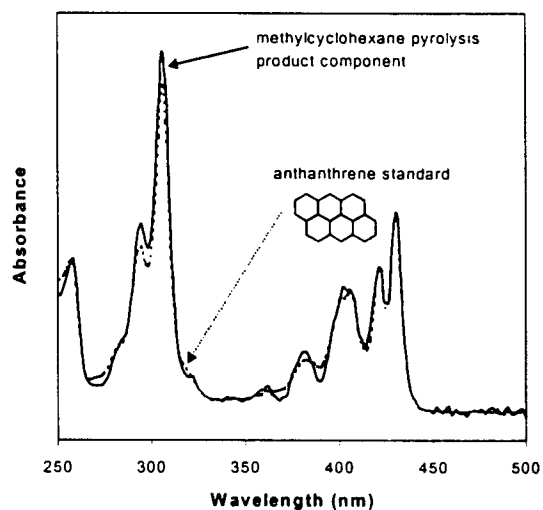
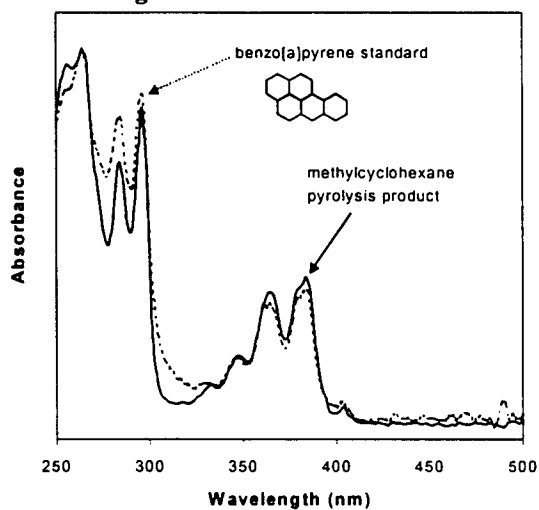


Figure 3

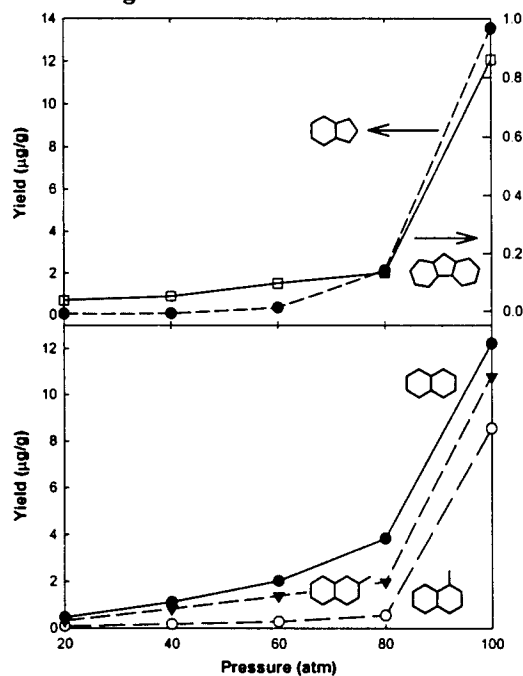


Figure 4

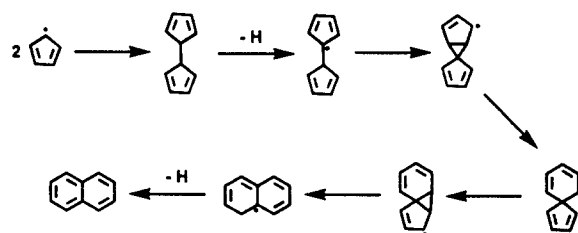
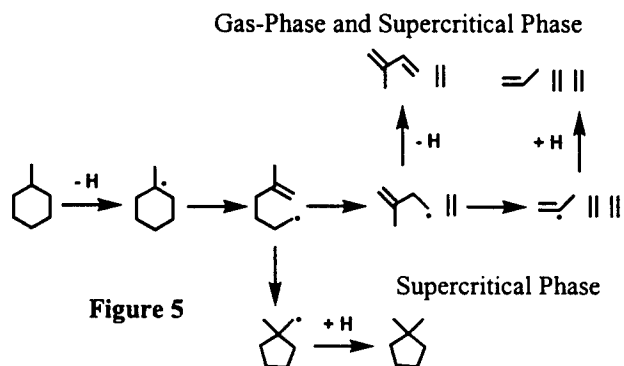
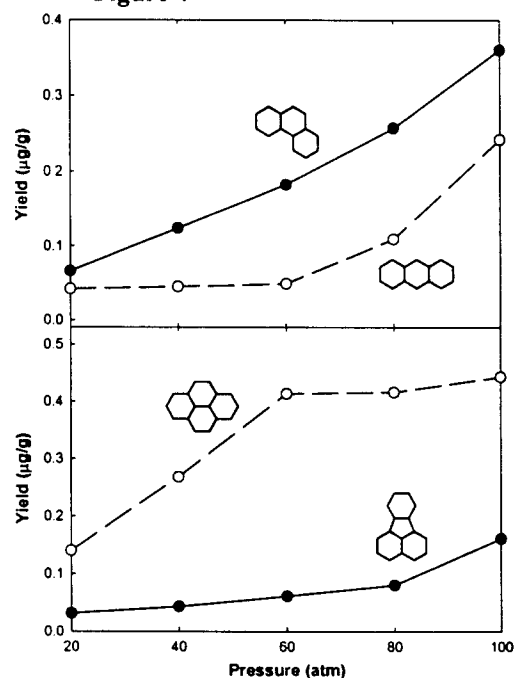
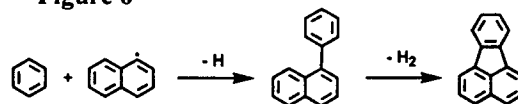


Figure 6



INVITEES

Dr. John Abraham
School of Mechanical Engineering
Purdue University
West Lafayette IN 47907
(765)494-1505
FAX:494-0530
jabraham@ecn.purdue.edu

Dr. Mukund Acharya
Allied Signal Engines, M/S 301-125
111 South 34th Street
PO Box 52181
Phoenix AZ 85072-2181
(602)231-2808
Mukund.Acharya@alliedsignal.com

Dr. M. S. Anand
Rolls-Royce Corporation,
P.O. Box 420
Speed Code T14
Indianapolis IN 46206-0420
(317)230-2828
FAX:230-3691
m.s.anand@rolls-royce.com

Dr. William Anderson
AMSRL-WM-BD
US Army Research Laboratory
Aberdeen Proving Ground MD 21005-5066
(410)278-9992
FAX: 278-7333
willie@arl.army.mil

Dr Kurt Annen
Aerodyne Research, Inc.
45 Manning Road
Manning Park Research Center
Billerica MA 01821-3976
(978)663-9500
FAX:663-4918
kannen@aerodyne.com

Dr Chris Atkinson
Dept of Mech. & Aerospace Eng.
West Virginia University
PO Box 6106
Morgantown WV 26506-6106
(304)293-4111
FAX:293-2582

Dr William Bachalo
Artium Technologies, Inc.
14660 Saltamontes Way
Los Altos Hills CA 94022-2036
(650)941-4233
wbachalo@aol.com

Dr S L Baughcum
Boeing Company
P O Box 3707, MS 67-MK
Seattle WA 98124
(425)965-0426
FAX:237-5247
slb0347@o3.ca.boeing.com

Dr Howard Baum
National Institute of
Standards and Technology
Center for Fire Research
Gaithersburg MD 20899
(301)975-6668

Dr John Bdzil
Los Alamos National Laboratory
Los Alamos NM 87545

Mr. Steve Beckel
Pratt and Whitney
M/S 715-83
P.O. Box 109600
West Palm Beach FL 33410-9600

Dr Josette Bellan
Jet Propulsion Laboratory
MS 125-109
4800 Oak Grove Drive
Pasadena CA 91109
(818)354-6959
FAX:393-5011
josette.bellan@jpl.nasa.gov

Dr Michael Berman
AFOSR/NL
801 North Randolph Street, Room 732
Arlington VA 22203-1977
(703)696-7781
FAX:696-8449
michael.berman@afosr.af.mil

Dr William Berry
Director for Research
Defense Research & Engineering
3040 Defense Pentagon
Washington DC 20301-3040

Dr Thomas Beutner
AFOSR/NA
801 North Randolph Street, Room 732
Arlington VA 22203-1977
(703)696-6961
FAX:696-8451
thomas.beutner@afosr.af.mil

Dr. Robert Bill
Propulsion Dir, Army Res. Lab.
NASA Glenn Res. Ctr., MS 77-12
21000 Brookpark Road
Cleveland OH 44135-3191
(216)433-3703
FAX:433-3000
Robert.C.Bill@lerc.nasa.gov

Dr Mitat Birkan
AFOSR/NA
801 North Randolph Street, Room 732
Arlington VA 22203-1977
(703)696-7234
FAX:696-8451
mitat.birkan@afosr.af.mil

Dr Kevin Bowcutt
North American Aircraft Div.
Rockwell International Corp.
P.O. Box 3644
Seal Beach CA 90740-7644

Mr. Andreja Brankovic
Flow Parametrics, LLC
15 Debra Drive
Bear DE 19701
(302)838-7368
FAX:838-7369
brankov@flowparametrics.com

Dr Kenneth Brezinsky
Department of Chemical Engrg
University of Illinois-Chicago
810 S. Clinton St, Room 204
Chicago IL 60607-7000
(312)996-9430
FAX:996-0808
kenbrez@uic.edu

Dr Garry Brown
Department of Mechanical and
Aerospace Engineering
Princeton University
Princeton NJ 08544-5263
(609)258-6083
GLB@pucc.princeton.edu

Dr R C Brown
Aerodyne Research, Inc.
45 Manning Road
Manning Park Research Center
Billerica MA 01821-3976
(978)663-9500
FAX:663-4918

Dr. Adam Bruckner
Aerospace and Engineering Research Prog.
University of Washington
120 Aero & Eng Rsch Bldg, FL-10
Seattle WA 98195
(206)543-6321
FAX:543-4719
bruckner@aa.washington.edu

Dr. Walter Bryzik
Propulsion Systems Division
ATTN: AMSTA-TR-R, MS 121
USA Tank-Automotive Command
Warren MI 48397-5000
(810)574-6461
FAX: 574-5054
bryzik@cc.tacom.army.mil

Dr John D Buckmaster
Department of Aerospace
Engineering
University of Illinois
Urbana IL 61801

Dr Dennis Bushnell
NASA Langley Research Center
Mail Stop 110
Hampton VA 23681
(804)864-4546
d.m.bushnell@larc.nasa.gov

Dr T D Butler
MS B-210 T-DO: THEORETICAL DIVISION
Los Alamos National Laboratory
Los Alamos NM 87545
(505)667-4401
FAX: 665-4055
tdbutler@lanl.gov

Dr H F Calcote
ChemIon Inc.
159 Philip Drive
Princeton NJ 08540
(609)921-6891
FAX:921-6891
calcote@alumni.princeton.edu

Dr George Caledonia
Physical Sciences, Inc
20 New England Business Center
Andover MA 01810
(508)689-0003
FAX:689-3232

Mr. Donald Campbell
NASA Glenn Research Center
21000 Brookpark Road
Mail Stop 3-2
Cleveland OH 44135
(216)433-2929
(216)433-5266

Dr Graham V Candler
Department of Aerospace
Engineering & Mechanics
University of Minnesota
Minneapolis MN 55455

Dr. Herb Carlson
AFOSR/CA
801 North Randolph Street, Room 732
Arlington VA 22203-1977
(703)696-7550
FAX:696-9556
herb.carlson@afosr.af.mil

Dr. Len Caveny
13715 Piscataway Drive
Ft Washington MD 20744
(301)292-5319
FAX:292-3724
Lcaveny@compuserve.com

Dr. Ismail Celik
Department of Mechanical and
Aerospace Engineering
West Virginia University
Morgantown WV 26506

Dr. Nicholas Cernansky
Mechanical Engineering Dept.
Drexel University
32nd and Chestnut Streets
Philadelphia PA 19104-2884
(215)895-2284
FAX:895-1478
ccernansk@coe.drexel.edu

Dr. Chine I Chang
Director
US Army Research Office
PO Box 12211
Research Triangle Park NC 27709-2211
(919)549-4203
FAX:549-4348
jchang@aro-emh1.army.mil

Dr. Harsha Chelliah
Department of Mechanical, Aero
and Nuclear Engineering
University of Virginia
Charlottesville VA 22903-2442
(804)924-6037
FAX:982-2037
harsha@virginia.edu

Dr. Jacqueline Chen
MS 9051
Sandia National Laboratories
P.O. Box 969
Livermore CA 94551-0969
(510)294-2586
FAX:294-1012
jhchen@sandia.gov

Dr S Y Cho
Department of Mechanical and
Aerospace Engineering
Princeton University
Princeton NJ 08544-5263

Mr. John M. Clarke
Caterpillar Inc.
Technical Center
P.O. Box 1875
Peoria IL 61656-1875
(309)578-3913
FAX:578-4232
john.clarke@cat.com

Mr R.W. Claus
NASA Glenn Research Center
21000 Brookpark Road
Cleveland OH 44135-3127
(216)433-5869

Dr M B Colket
United Technologies Research
Center
411 Silver Lane, MS 129-29
East Hartford CT 06108
(860)610-7481
FAX:610-7593
colketmb@utrc.utc.com

Dr S M Correa
GE Corp. Research & Development
PO Box 8, K1ES112
Schenectady NY 12301
(518)387-5853
FAX:387-7258
correa@crd.ge.com

Dr David Crosley
Molecular Physics Department
SRI International
333 Ravenswood Avenue
Menlo Park CA 94025-3696
(415)326-6200

Dr Eli Dabora
Mechanical Engineering Dept
University of Connecticut
Box U-139 ME
Storrs CT 06268
(203)486-2415

Dr Werner Dahm
Department of Aerospace Engineering
3056 FXB 2140
The University of Michigan
Ann Arbor MI 48109-2140
(734)764-4318
FAX:763-0578
wdahm@umich.edu

Mr. Eugene Danielson
Propulsion Systems Division
ATTN: AMSTA-TR-R, MS 121
USA Tank Automotive Command
Warren MI 48397-5000

Dr Ron Davis
Chemical Science and Techn Lab
Building 221, Room B312
National Inst of Stds & Tech
Gaithersburg MD 20899

Dr. Peter A. DeBarber
MetroLaser, Inc.
18006 Skypark Circle #108
Irvine CA 92714-6428

Dr George Deiwert
NASA Ames Research Center
MS 230-2
Moffett Field CA 94035
(415)604-6198

Dr Paul Dimotakis
California Institute of Tech
1201 East California Blvd.
MC 301-46
Pasadena CA 91125
(626)395-4456
(626)395-4447
dimotakis@caltech.edu

Dr. Glenn Diskin
NASA Langley Research Center
MS 197
Hypersonic Airbreathing Prop. Branch
Hampton VA 23681-2199
(757)864-6268
FAX:864-7923
g.s.diskin@larc.nasa.gov

Dr Richard Dobbins
Department of Engineering
Brown University
164 Angel Street
Providence RI 02912-9104
(401)863-2653
FAX:863-1157
richard_dobbins@brown.edu

Dr Gregory Dobbs
United Technologies Research
Center - Mail Stop 90
Silver Lane
East Hartford CT 06108
(860)610-7145

Mr. Lee Dodge
Southwest Research Institute
P.O. Drawer 28510
San Antonio TX 78284
(512)684-5111

Dr. James F. Driscoll
Department of Aerospace Engrg
3004 FXB Building
University of Michigan
Ann Arbor MI 49109-2118
(734)936-0101
FAX:763-0578
jamesfd@umich.edu

Dr. J. Philip Drummond
NASA Langley Research Center
Mail Stop 197
Hampton VA 23681-0001
(757)864-2298
FAX:864-7923
j.p.drummond@larc.nasa.gov

Dr C Dutton
Department of Mechanical and
Industrial Engineering
University of Illinois
Urbana IL 61801

Dr J T Edwards
AFRL/PRTG
Building 490
1790 Loop Road, N
Wright-Patterson AFB OH 45433-7103
(937)255-3524
FAX:255-1125
james.edwards@wpafb.af.mil

Dr. Fokion N. Egofoopoulos
Department of Mechanical Engrg
University of Southern Calif
Olin Hall 400B
Los Angeles CA 90089-1453
(213)740-0480
FAX:740-8071
egolfopo@almaak.usc.edu

Dr Phillip Emmerman
Harry Diamond Laboratories
Attn. SLCHD-ST-RD
2800 Powder Mill Road
Adelphi MD 20783-1197
(301)394-3000

Dr K C Ernst
Pratt and Whitney Aircraft
Group
Government Products Division
West Palm Beach FL 33402

Dr G M Faeth
Department of Aerospace Engineering
3000 FXB Building
University of Michigan
Ann Arbor MI 48109-2140
(734)764-7202
FAX:936-0106
gmfaeth@umich.edu

Dr. Daniel Fant
South Carolina Energy Research
and Development Center
386-2 College Avenue
Clemson SC 29634-5180
(864)656-2267
FAX:656-1429

Dr Gregory W Faris
Molecular Physics Laboratory
SRI International
333 Ravenswood Avenue
Menlo Park CA 94025-3493
(650)859-4131
FAX:859-6196
faris@mplvax.sri.com

Dr. Patrick Farrell
Engineering Research Center
University of Wisconsin-Madison
1500 Engineering Drive
Madison WI 53706
(608)263-1686
FAX:263-9870
farrell@enr.wisc.edu

Dr Richard Field
U. S. Army Armament R&D Center
DRSMC-LCA-G(D)
Building 382-S
Dover NJ 07801
(201)724-5844

Dr Farley Fisher
National Science Foundation
CTS/Room 525
4201 Wilson Boulevard
Arlington VA 22230
(703)306-1371
FAX:306-0319
ffisher@nsf.gov

Dr. David E. Foster
Engine Research Center
University of Wisconsin
Madison WI 53706
(608)263-1617
FAX:263-9870
foster@enr.wisc.edu

Dr Michael Frenklach
Department of Mechanical
Engineering
University of California
Berkeley CA 94720-1740
(510)643-1676
FAX:642-6163
myf@me.berkeley.edu

Dr Bish Ganguly
AFRL/PRPE
2645 Fifth Street, Suite 13
Wright-Patterson AFB OH 45433-7919
(937)255-2923
FAX:656-4095
biswa.ganguly@pr.wpafb.af.mil

Dr. Richard G. Gann
Building and Fire Research Laboratory
National Inst. Of Stds. & Technology
100 Bureau Drive, Stop 8650
Gaithersburg MD 20899-8650
(301)975-6866
FAX:975-4052
rggann@nist.gov

Dr Alan Garscadden
AFRL/PR
1950 Fifth Street, Building 18A
Wright-Patterson AFB OH 45433-7251
(937)255-2246
FAX:986-4657
alan.garscadden@pr.wpafb.af.mil

Dr. Kresimir Gebert
BKM, Inc.
5141 Santa Fe Street
San Diego CA 92109
(858)270-6760
bkm-inc@worldnet.att.net

Mr R Giffen
General Electric Company
Aircraft Engine Group
Neumann Way
Cincinnati OH 45215

Dr. Sharath Girimaji
Department of Aerospace Engineering
Texas A&M University
College Station TX 77843-3141
(979)845-1674
FAX:845-6051
girimaji@aero.tamu.edu

Dr Peyman Givi
Department of Mechanical and
Aerospace Engineering
State University of New York
Buffalo NY 14260-4400
(716)645-2593
FAX:645-3875
givi@eng.buffalo.edu

Dr Irvin Glassman
Department of Mechanical and
Aerospace Engineering
Princeton University
Princeton NJ 08544-5263
(609)258-5199
FAX:258-5963
glassman@princeton.edu

Dr. George Gogos
Mechanical Engineering Department
University of Nebraska
N104 Walter Scott Engrg Center
Lincoln NE 68516
(402)472-3006
FAX:472-1465
ggogos1@unl.edu

Dr Judah Goldwasser
Office of Naval Research
Mechanics Division, Code 333
800 North Quincy Street
Arlington VA 22217-5660
(703)696-2164
FAX:696-2558
goldwaj@onr.navy.mil

Dr. James Gord
AFRL/PRTS
Building 490
1790 Loop Road N
Wright-Patterson AFB OH 45433-7103
(937)255-7431
FAX:656-4570
james.gord@pr.wpafb.af.mil

Dr. Jay P. Gore
School of Mechanical Engrg
Purdue University
1003 Chaffee Hall
West Lafayette IN 47907-1003
(317)494-1500
FAX:494-0530

Dr. Sol Gorland
NASA Glenn Research Center
21000 Brookpark Road
Mail Stop 60-4
Cleveland OH 44135
(216)977-7561
FAX:977-7500
sol.h.gorland@lerc.nasa.gov

Dr Larry Goss
Research Applications Division
Systems Research Labs, Inc.
2800 Indian Ripple Road
Dayton OH 45440-3696
(513)252-2706

Dr Richard Gould
Department of Mechanical and Aerospace Engineering
Box 7910
North Carolina State University
Raleigh NC 27695-7910
(919)515-5236
FAX:515-7968
gould@eos.ncsu.edu

Dr Frederick Gouldin
Department of Mechanical and
Aerospace Engineering
Cornell University
Ithaca NY 14853-5692
(607)255-5280
fcg2@cornell.edu

Dr. Mark Gruber
AFRL/PRA
1790 Loop Road North
Wright-Patterson AFB OH 45433-7251
(937)255-2175
FAX:656-4659
Mark.Gruber@afrl.af.mil

Dr. Brian K. Gullett
U.S. Environmental Protection Agency
National Risk Management Research Laboratory
Air Pollution Technology Branch (MD-65)
Research Triangle Park NC 27711
(919)541-1534
FAX:541-0290
gullett.brian@epa.gov

Dr. Rajendra Gupta
Department of Physics
University of Arkansas
120 Ozark Hall
Fayetteville AR 72701-1201
(501)575-5933
FAX:575-4580
rgupta@comp.uark.edu

Dr. Mark A. Hagenmaier
AFRL/PRA
Building 18
1950 Fifth Street, Suite 10
Wright-Patterson AFB OH 45433-7251
(937)255-5210
FAX:476-4659
hagenma@possum.appl.wpafb.af.mil

Dr. Nabil S. Hakim
Director, Advanced Engineering
Detroit Diesel Corporation
13400 W. Outer Drive, R03-B
Detroit MI 48239-4001
(313)592-7455
FAX:592-5906

Dr Robert D. Hancock
AFRL/PRTS
Building 490
1790 Loop Road, N
Wright-Patterson AFB OH 45433-7103
(937)255-6814
FAX:255-1125
hancockr@ward.appl.wpafb.af.mil

Dr Ronald Hanson
Mechanical Engineering Department
Stanford University
Building 530, Room 112
Stanford CA 94305-3030
(650)723-4023
FAX:725-4862
hanson@me.stanford.edu

Dr D L Hartley
Sandia National Laboratories
MS0735
Albuquerque NM 87185-5800

Dr. Stephen D. Heister
Department of Aeronautics
and Astronautics
Purdue University
West Lafayette IN 47907-1282
(765)494-5126
FAX:494-0307
heister@ecn.purdue.edu

Dr. Naeim Henein
Department of Mechanical Engrg
Wayne State University
2121 Engineering Building
Detroit MI 48201
(313)577-3887
FAX:577-8789
henein@me1.eng.wayne.edu

Dr Cecil F. Hess
MetroLaser, Inc.
18006 Skypark Circle
Suite 108
Irvine CA 92714-6428
(714)553-0688
FAX:553-0495
chess@metrolaserinc.com

Dr David Hofeldt
125 Mechanical Engineering
111 Church Street, S E
University of Minnesota
Minneapolis MN 55455
(612)625-2045

Mr Robert Holland
United Technologies Chemical
Systems Division
P O Box 49028
San Jose CA 95161-9028
(408)224-7656

Dr Lawrence Hunter
Applied Physics Laboratory
Johns Hopkins University
Johns Hopkins Road
Laurel MD 20707-6099
(301)953-5000

Dr. Frank Hurley
US Army Research Office
PO Box 12211
Research Triangle Park NC 27709-2211
(919)549-4432
FAX:549-4310
hurley@aro-emh1.army.mil

Dr. Farhad Jaber
Department of Mechanical and
Nuclear Engineering
Kansas State University
Manhattan KS 66506
(785)532-5619
FAX:532-7057
jaberi@mne.ksu.edu

Dr. Thomas Jackson
AFRL/PRSC
Building 18
1950 Fifth Street
Wright-Patterson AFB OH 45433-7251
(937)255-2175
FAX:656-4659
thomas.jackson@afrl.af.mil

Dr Jay Jeffries
Mechanical Engineering Department
Thermophysics Division, Building 520
Stanford University
Stanford CA 94305-3032
(650)736-0007
FAX:723-1748
Jeffries@Navier.Stanford.edu

Mr Gordon Jensen
United Technologies Chemical
Systems Division
P O Box 49028
San Jose CA 95161-9028
(408)365-5552

Mr. Jeff Jensen
Kaiser-Marquardt
16555 Staycoy Street
Van Nuys CA 91406

Dr. William Johnson
BKM, Inc.
5141 Santa Fe Street
San Diego CA 92109
(619)270-6760

Mr. Craig Johnston
Lockheed Advanced Dev. Company
Lockheed-Martin Corporation
1011 Lockheed Way
Palmdale CA 93599-7212

Dr John Kelly
Altex Technologies Corporation
650 Nuttman Road
Suite 114
Santa Clara CA 95054
(408)980-8610

Dr G B King
Department of Mechanical
Engineering
Purdue University
West Lafayette IN 47907-1288
(765)494-6518
kinggb@ecn.purdue.edu

Dr Merrill K King
NASA Headquarters
Code UG
300 E Street, SW
Washington DC 20546
(202)358-0817
FAX:358-3091
mking1@mail.hq.nasa.gov

Dr William H Kirchhoff
Office of Energy Research
U.S. Department of Energy
19901 Germantown Road
Germantown MD 20874
(301)903-5820
william.kirchhoff@oer.doe.gov

Dr. David E. Klett
Mechanical Engineering Dept
North Carolina Agricultural
and Technical State Univ
Greensboro NC 27401-3209

Dr Charles Kolb
Aerodyne Research, Inc.
45 Manning Road
Manning Park Research Center
Billerica MA 01821-3976
(978)663-9500
FAX:663-4918

Dr George Kosaly
Mechanical Engineering Dept
University of Washington
Box 352600
Seattle WA 98195-2600
(206)543-6933
FAX:685-8047
kosaly@u.washington.edu

Mr David Kruczynski
Attn SLCBR-IBA
Interior Ballistics Division
Army Research Laboratory
Aberdeen Proving Gnd MD 21005-5066
(410)278-6202

Dr. Kenneth Kuo
Department of Mechanical
Engineering
Pennsylvania State University
University Park PA 16802
(814)865-6741
FAX:863-3203

Dr. Ming-Chia Lai
Department of Mechanical Engrg
Wayne State University
Detroit MI 48202

Dr John Larue
Department of Mechanical
Engineering
University of California
Irvine CA 92717

Dr Allan Laufer
Office of Energy Research
U. S. Department of Energy
19901 Germantown Road
Germantown MD 20874
(202)903-5820
Allan.Laufer@oer.doe.gov

Dr Normand Laurendeau
School of Mechanical
Engineering
Purdue University
West Lafayette IN 47907-1288
(765)494-2713
FAX:494-0539
Laurende@ecn.purdue.edu

Dr C K Law
Department of Mechanical and
Aerospace Engineering
Princeton University
Princeton NJ 08544-5263
(609)258-5271
FAX:258-6233
cklaw@princeton.edu

Dr C C Lee
Environmental Protection
Agency
Cincinnati OH 45268
(513)569-7520

Dr Anthony Leonard
Graduate Aeronautical Labs
California Institute of
Technology
Pasadena CA 91125
(626)395-4465

Dr Deborah Levin
Department of Chemistry
George Washington University
725 21st Street, NW
Washington DC 20013
(202)994-5637
FAX:994-5873
dalevin@gwu.edu

Dr. Arthur Lewis
University of Dayton Research Inst.
Aerospace Mechanics Division
300 College Park
Dayton OH 45469-0110
(937)229-4235
FAX:229-4251

Dr Goang Liaw
Department of Civil Engineering
Alabama A&M University
PO Box 367
Normal AL 35762
(205)851-5565

Dr. Charles L. Liotta
Department of Chemical Engrg
Georgia Institute of
Technology
Atlanta GA 30332-0100
(404)853-9344
FAX:894-6956

Dr Lyle N Long
Department of Aerospace Engrg
233 Hammond Building
Pennsylvania State University
University Park PA 16802
(814)865-1172
FAX:865-7092
lnl@psu.edu

Dr Marshall Long
Mechanical Engineering Department
Yale University
PO Box 208284
New Haven CT 06520
(203)432-4229
FAX:432-6775
long-marshall@yale.edu

Dr. Kevin Lyons
Department of Mechanical and Aerospace Engineering
Box 7910
North Carolina State University
Raleigh NC 27695
(919)515-7698
FAX:515-7968
lyons@eos.ncsu.edu

Dr Bruce MacDonald
Research Applications Division
Systems Research Labs, Inc.
2800 Indian Ripple Road
Dayton OH 45440-3696
(513)252-2706

Dr. John Magill
Physical Sciences, Inc.
20 New England Business Center
Andover MA 01810
(508)689-0003
FAX:689-3232

Mr Nick Makris
SA-ALC/SFT
Kelly AFB TX 78241-5000
AV945-8212
FAX:945-9964

Dr David Mann
U. S. Army Research Office
P. O. Box 12211
4300 South Miami Boulevard
Research Triangle Pk NC 27709-2211
(919)549-4249
FAX:549-4310
dmann@aro-emh1.army.mil

Dr Nagi Mansour
Computational Fluid Mechanics
Branch, RFT 202A-1
NASA Ames Research Center
Moffett Field CA 94035
(415)604-6420

Dr John Marek
NASA Glenn Research Center
Mail Stop 5-11
21000 Brookpark Road
Cleveland OH 44135-3127
(216)433-3584
FAX:433-3000
cecil.j.marek@lerc.nasa.gov

Dr. Jay Martin
University of Wisconsin-Madison
Engine Research Center
1500 Engineering Drive
Madison WI 53706
(608)263-9460
FAX:262-6707
martin@engr.wisc.edu

Dr James McDonald
Code 6110
Naval Research Laboratory
Chemistry Division
Washington DC 20375-5342
(202)767-3340

Dr Keith McManus
Physical Sciences, Inc
20 New England Business Center
Andover MA 01810
(508)689-0003
FAX:689-3232

Dr. Mehran Mehregany
Department of Electrical Engineering
Case Western Reserve University
10900 Euclid Avenue
Cleveland OH 44106-7221

Dr A M Mellor
Mech & Matls Engrg Dept
512 Kirkland Hall, Box 1592
Vanderbilt University
Nashville TN 37240
(615)343-6214
FAX:343-6687

Dr Lynn Melton
Programs in Chemistry
University of Texas, Dallas
P. O. Box 830688
Richardson TX 75083-0688
(972)883-2913
FAX:883-2925
melton@utdallas.edu

Dr. Suresh Menon
School of Aerospace Engineering
Georgia Institute of Technology
270 Ferst Drive
Atlanta GA 30332-0150
(404)894-9126
FAX:894-2760
suresh.menon@aerospace.gatech.edu

Dr. Hameed Metghalchi
Northeastern University
360 Huntington Avenue
Boston MA 02115
(617)373-2973
FAX:373-2921
metghal@coe.neu.edu

Dr Michael M Micci
Department of Aerospace Engrg
233 Hammond Building
Pennsylvania State University
University Park PA 16802
(814)863-0043
FAX:865-7092
micci@henry2.aero.psu.edu

Dr Andrzej Miziolek
AMSR-WM-BD
US Army Research Laboratory
Aberdeen Proving Gnd MD 21005-5066
(410)278-6157
FAX:278-6094
miziolek@arl.army.mil

Dr. H. C. Mongia
Manager, Combustion Technology
GE Aircraft Engines
One Neumann Way, M/D A404
Cincinnati OH 45215-6301
(513)243-2552
FAX:243-2538
Hukam.Mongia@ae.ge.com

Dr Edward Mularz
Attn: AMSRL-VP-C
NASA Glenn Res. Ctr., MS 77-12
21000 Brookpark Road
Cleveland OH 44135-3191
(216)433-5850
FAX:433-3720
Edward.Mularz@lerc.nasa.gov

Dr Arje Nachman
AFOSR/NM
801 North Randolph Street, Room 732
Arlington VA 22203-1977
(703)696-8427
FAX:696-8450
arje.nachman@afosr.af.mil

Dr Herbert Nelson
Code 6110, Chemistry Division
Naval Research Laboratory
4555 Overlook Avenue, SW
Washington DC 20375-5342
(202)767-3686

Dr G B Northam
NASA Langley Research Center
MS 188B
Hampton VA 23681
(804)864-6248
g.b.northam@larc.nasa.gov

Dr. Michael Nusca
AMSRL-WT-PC
US Army Research Laboratory
Aberdeen Proving Ground MD 21005-5066
(410)278-6108
FAX: 278-7333
nusca@arl.army.mil

Dr Elaine Oran
LCP&FD, Code 6404
US Naval Research Laboratory
4555 Overlook Avenue, SW
Washington DC 20375-5344
(202)767-2960
FAX: 767-4798
ORAN@lcp.nrl.navy.mil

Dr T E Parker
Engineering Division
Colorado School of Mines
Golden CO 80401-1887
(303)273-3657
FAX: 273-3602
tparker@mines.colorado.edu

Dr. Phillip H. Paul
MS 9051
Sandia National Laboratories
P. O. Box 969
Livermore CA 94551-9051
(510)294-1465
FAX: 294-1012
phpaul@sandia.gov

Dr Lisa Pfefferle
Department of Chemical
Engineering
Yale University
New Haven CT 06520-8286
(203)432-2222
FAX: 432-7232
pfefferle@htcre.eng.yale.edu

Dr Emil Pfender
Department of Mechanical Engrg
125 Mechanical Engineering
The University of Minnesota
Minneapolis MN 55455

Dr Robert Pitz
Department of Mechanical and
Materials Engineering
Vanderbilt University
Nashville TN 37235
(615)322-0209
FAX: 343-8730
pitzrw@ctrvan.vanderbilt.edu

Dr S B Pope
Department of Mechanical and
Aerospace Engineering
Cornell University
Ithaca NY 14853-7501
(607)255-4314
FAX: 255-1222
pope@mae.cornell.edu

Dr. David Pratt
AFRL/VAS
Building 45 Annex
2130 Eighth Street, Suite 1
Wright-Patterson AFB OH 45433-7542
(937)255-5042
FAX:656-7915
David.Pratt@va.af.mil

Dr. Martin J. Rabinowitz
Mail Stop 5/10
NASA Glenn Research Center
21000 Brookpark Road
Cleveland OH 44135-3191
(216)433-5847
FAX:433-5588
marty@lerc.nasa.gov

Dr. Larry Rahn
Sandia National Laboratories
7011 East Avenue
Mail Stop 9056
Livermore CA 94551-0969
(510)294-2091
FAX: 294-2276
rahn@sandia.gov

Dr. Mohan K. Razdan
Rolls-Royce Company
P.O. Box 420
Speed Code T10B
Indianapolis IN 46206-0420
(317)230-6404
FAX:230-3691
mohan.razdan@rolls-royce.com

Mr. Robert Reed
Sverdrup Technology, Inc.
AEDC
1099 Avenue C
Arnold AFB TN 37389-9013
(615)454-4648
(615)454-6317

Dr Rolf D Reitz
Mechanical Engineering Dept
University of Wisconsin
1500 Johnson Drive
Madison WI 53706
(608)262-0145
FAX:262-6717

Col. Steven Reznick
AFOSR/CD
801 North Randolph Street, Room 732
Arlington VA 22203-1977
(703)696-7555
FAX:696-9556
steven.reznick@afosr.af.mil

Dr. Kyung T. Rhee
Department of Mechanical and
Aerospace Engineering
Rutgers, The State Univ of NJ
Piscataway NJ 08854-0909
(732)445-3651
FAX:445-5313
ktrhee@jove.rutgers.edu

Dr James Riley
Mechanical Engineering Dept
University of Washington
Seattle WA 98195
(206)543-5347
73671.737@Compuserve.com

Dr William Roberts
Department of Mechanical and Aerospace Engineering
Box 7910
North Carolina State University
Raleigh NC 27695-7910
(919)515-5294
FAX:515-7968
wlrobert@eos.ncsu.edu

Mr. Gerald A. Roffe
GASL
77 Raynor Avenue
Ronkonkoma NY 11779

Dr W M Roquemore
AFRL/PRTS
Building 490
1790 Loop Road, N
Wright-Patterson AFB OH 45433-7103
(937)255-6813
FAX:656-4570
melr@ward.appl.wpafb.af.mil

Dr Daniel Rosner
Department of Chemical
Engineering
Yale University
New Haven CT 06520-8286
(203)432-4391
FAX:432-7232
daniel.rosner@yale.edu

Dr John Ross
Department of Chemistry
Stanford University
Stanford CA 94305-3032
(650)723-9203

Dr Gabriel Roy
Office of Naval Research
Mechanics Division, Code 1132
800 North Quincy Street
Arlington VA 22217-5660
(703)696-4406
FAX:696-0934
roy@ocnr-hq.navy.mil

Dr. Robert C. Ryder
Flow Parametrics, LLC
15 Debra Drive
Bear DE 19701
(302)838-7368
FAX:838-7369
rryder@flowparametrics.com

Mr Kurt Sacksteder
NASA Glenn Research Center
MS 500-217
21000 Brookpark Road
Cleveland OH 44135
(216)433-2857

Dr Michael Salkind
President
Ohio Aerospace Institute
22800 Cedar Point Road
Cleveland OH 44142
(440)962-3001
FAX:962-3120
MichaelSalkind@oai.org

Dr Mohammad Samimy
Ohio State University
Mechanical Engineering Dept
206 West 18th Street
Columbus OH 43210-1107
(614)422-6988
FAX:292-3163
msamimy@magnus.acs.ohio-state.edu

Dr G S Samuelsen
Department of Mechanical and
Aerospace Engineering
University of California
Irvine CA 92697-3975
(949)824-5468

Dr Lakshmi Sankar
School of Aerospace Engrg
Georgia Institute of
Technology
Atlanta GA 30332
(404)894-3014

Dr Domenic Santavicca
Propulsion Engineering Research Center
Pennsylvania State University
106 Research Building East - Bigler Road
University Park PA 16802-2320
(814)863-1863

Dr R J Santoro
Department of Mechanical
Engineering
Pennsylvania State University
University Park PA 16802-2320
(814)863-1285
FAX: 865-3389
rjs2@email.psu.edu

Dr Sutanu Sarkar
Department of Applied Mech
and Engr Science, MC 0411
University of California
La Jolla CA 92093-0411
(858)534-8243
FAX: 534-7599
ssarkar@ucsd.edu

Dr Klaus Schadow
Naval Air Warfare Center
Code 3892
China Lake CA 93555-6001
(760)939-6532
FAX: 939-6569
klaus_schadow@imdgw.chinalake.navy.mil

Dr John Schaefer
Energy and Environmental Div.
Acurex Corporation
555 Clyde Ave., P. O. Box 7555
Mountain View CA 94039

Dr. Frederick Schauer
AFRL/PRTS
Building 490, Room 104
1790 Loop Road, N
Wright-Patterson AFB OH 45433-7103
(937)255-6462
FAX: 255-1125
frederick.schauer@wpafb.af.mil

Dr. Peter Schihl
Propulsion Systems Division
ATTN: AMSTA-TR-R, MS 121
USA Tank Automotive Command
Warren MI 48397-5000
FAX: 574-5054
schihlp@tacom.army.mil

Dr. Lyle Schwartz
AFOSR/CC
801 North Randolph Street, Room 732
Arlington VA 22203-1977
(703)696-8457
lyle.schwartz@afosr.af.mil

Dr. Ernest Schwarz
Propulsion Systems Division
ATTN: DRSTA-RGD
USA Tank-Automotive Command
Warren MI 48397-5000
(810)574-5656
FAX: 574-5054
schwarze@cc.tacom.army.mil

Mr. Lee Scuderi
McDonnell Douglas Aerospace
P.O. Box 516
St. Louis MO 63166-0516

Dr. Corin Segal
AeMES Department
University of Florida
P.O. Box 116250
Gainesville FL 32611-6250
(352)392-6132
FAX:392-7303
cor@aero.ufl.edu

Dr Jerry Seitzman
School of Aerospace Engineering
Georgia Institute of Technology
Atlanta GA 30332-0150
(404)894-0013
FAX:894-2760
jerry.seitzman@ae.gatech.edu

Dr Hratch Semerjian
National Institute of
Standards and Technology
Chem Sci & Tech Laboratory
Gaithersburg MD 20899
(301)975-3145
FAX:975-3845
HRATCH@micf.nist.gov

Dr Kalyanasundaram Seshadri
Center for Energy and
Combustion Research, 0407
University of California at San Diego
La Jolla CA 92093-0407
(858)534-4876
FAX:534-5354
seshadri@ames.ucsd.edu

Dr Robert Shaw
Division of Chemical and
Biological Sciences
U S Army Research Office
Research Triangle Park NC 27709-2211
(919)549-0641

Dr. Adam Siebenhaar
Aerojet Propulsion Division
P.O. Box 13222
Sacramento CA 95813-6000

Dr. Gupreet Singh
U.S. Department of Energy
1000 Independence Avenue, S.W.
Washington DC 20585
(202)586-2333
FAX:586-4166
GUPREET.SINGH@hq.doe.gov

Dr William Sirignano
Department of Mechanical and
Aerospace Engineering
University of California
Irvine CA 92697-3975
(949)824-3700
FAX:824-3773
sirignan@uci.edu

Mr. Davey Smith
Northrop Grumman Corporation
B-2 Division Dayton Office
2850 Presidential Dr., Ste 100
Fairborn OH 45324

Dr. Jefferson W. Tester
M.I.T. Energy Laboratory
Room E40-455
Massachusetts Inst. Of Technology
Cambridge MA 02139
(617)253-3401
FAX:253-8013
testerel@mit.edu

Dr Julian Tishkoff
AFOSR/NA
801 North Randolph Street, Room 732
Arlington VA 22203-1977
(703)696-8478
FAX:696-8451
julian.tishkoff@afosr.af.mil

Dr Michael Trenary
Department of Chemistry
The University of Illinois
Chicago IL 60680

Dr James Trolinger
MetroLaser
18006 Skypark Circle
Suite 108
Irvine CA 92714-6428
(714)553-0688
FAX:553-0495
jtrolinger@vmsa.oac.uci.edu

Dr Timothy Troutt
Department of Mechanical
Engineering
Washington State University
Pullman WA 99164-2920

Dr. Gretar Tryggvason
Dept of Mech Engrg & Appl Mech
2350 Hayward, Room 2250
The University of Michigan
Ann Arbor MI 48109-2125
(734)763-1049
FAX:764-4256
gretar@umich.edu

Dr A D Vakili
University of Tennessee
Space Institute
Tullahoma TN 37388

Dr. Mark Valco
Propulsion Directorate
Army Research Laboratory, MS 49-1
NASA Glenn Research Center
Cleveland OH 44135-3127
(216)433-3717
FAX:433-2182
aamark@lims01.lerc.nasa.gov

Dr. David Van Wie
The Johns Hopkins University
Applied Physics Laboratory
11100 Johns Hopkins Road
Laurel MD 20723-6099
(240)228-5194
FAX:228-5850
David.VanWie@jhuapl.edu

Dr John Vanderhoff
Ballistic Research Laboratory
DRSMC-BLI(A)
Aberdeen Proving Ground MD 21005
(410)278-6642

Dr Gregory Smith
Department of Chem Kinetics
SRI International
333 Ravenswood Avenue
Menlo Park CA 94025-3493
(415)859-3496

Dr. Kenneth A. Smith
Department of Chemical Engrg.
Room 66-540
Massachusetts Inst. Of Technology
Cambridge MA 02139
(617)253-1973
FAX:253-2701
kas@mit.edu

Dr. Judi Steciak
University of Idaho-Boise
800 Park Boulevard
Boise ID 83712-7742
(208)364-4080
FAX:387-1246
jsteciak@uidaho.edu

Dr David Stewart
Department of Theoretical and
Applied Mechanics
University of Illinois
Urbana IL 61801

Dr Anthony Strawa
NASA Ames Research Center
MS 230-2
Moffett Field CA 94035
(415)604-3437

Dr Geoffrey J Sturgess
Innovative Scientific Solutions, Inc.
2786 Indian Ripple Road
Dayton OH 45440-3638
(937)252-2706
FAX:656-4652
gsturgess@aol.com

Dr B Sturtevant
Engrg and Appl Sci Dept
California Institute of
Technology
Pasadena CA 91125

Dr G Sullins
Applied Physics Laboratory
Johns Hopkins University
Johns Hopkins Road
Laurel MD 20707-6099
(301)953-5000

Dr. Rodney Tabaczynski
Director, Power Train Research Lab
Ford Motor Research Laboratory
3623 Scientific Research Lab, PO Box 2053
Dearborn MI 48121-2053
(313)322-8930

Dr. Douglas Talley
AFRL/PRSA
10 East Saturn Boulevard
Edwards AFB CA 93524-7660
(661)275-6174
FAX:275-6245
Douglas.Talley@ple.af.mil

Dr James Verdieck
Rockwell International
Rocketdyne Div, M/S FA26
6633 Canoga Avenue
Canoga Park CA 91303
(818)700-4709

Dr. Paul Waltrup
The Johns Hopkins University
Applied Physics Laboratory
11100 Johns Hopkins Road
Laurel MD 20723-6099
(240)228-5626
Paul.Waltrup@jhuapl.edu

Dr Joe Wander
AFRL/MLQL
139 Barnes Drive
Suite 2
Tyndall AFB FL 32403-5323
(904)283-6240
FAX:283-6064
Jwander@mlq.afri.af.mil

Dr. Hai Wang
Department of Mechanical Engineering
University of Delaware
Newark DE 19716
(302)831-2421
FAX:831-3619
hwang@me.udel.edu

Dr. Zhicheng Wang
Clark Atlanta University
223 James P. Brawley Drive SW
Atlanta GA 30314
(404)880-6125
FAX:880-6615
zhicheng_wang@hotmail.com

Dr Charles Westbrook
Lawrence Livermore National
Laboratories
P. O. Box 808
Livermore CA 94551
(925)422-4108
FAX:422-2644
westbrook1@llnl.gov

Dr. Phillip R. Westmoreland
Department of Chemical
Engineering
University of Massachusetts
Amherst MA 01003
(413)545-1750
(413)545-1647
westm@ecs.umass.edu

Dr James Whitelaw
Department of Mechanical Engrg
Imperial College of Science
and Technology
London SW7 2BX UK

Dr Forman Williams
Center for Energy and
Combustion Research, 0310
University of California
La Jolla CA 92093-0310
(858)534-5492
FAX: 534-7720
fwilliams@ucsd.edu

Dr. Skip Williams
AFRL/VSBXT
29 Randolph Street
Hanscom AFB MA 01731
(781)377-2076
FAX: 377-7091
skipw@plh.af.mil

Dr Bernard T Wolfson
Wolfson Associates
International
4797 Lake Valencia Blvd West
Palm Harbor FL 33563
(813)786-3007

Dr. Mary J. Wornat
Department of Mechanical and
Aerospace Engineering
D238 Engineering Quadrangle
Princeton NJ 08544-5263
(609)258-5278
FAX: 258-6109
mjwornat@princeton.edu

Dr J M Wu
University of Tennessee
Space Institute
Tullahoma TN 37388

Dr. Vigor Yang
Propulsion Engrg Rsrch Ctr
The Pennsylvania State Univ
111 Research Building East
University Park PA 16802-2320
(814)863-1502
FAX: 865-4784
vigor@arthur.psu.edu

Dr. Yaw Yeboah
Engineering Department
Clark Atlanta University
223 James P Brawley Drive, SW
Atlanta GA 30314
(404)880-6619
FAX: 880-6615
yyeboah@cau.edu

Dr Richard Yetter
Department of Mechanical and
Nuclear Engineering
Pennsylvania State University
State College PA 16802
(814)863-6375
rayetter@psu.edu

Dr Shaye Yungster
Institute for Computational
Mechanics in Propulsion
NASA Glenn Research Ctr
Cleveland OH 44135
(216)433-6680

Dr. Michael Zacharia
Department of Mechanical Engineering
University of Minnesota
111 Church Street, SE
Minneapolis MN 55455
(612)626-9081
zacha008@umn.edu

Mr Fred Zarlingo
Code 3246
Naval Air Warfare Center
China Lake CA 93555-6001
(760)939-7395

Dr Ben Zinn
School of Aerospace Engineering
Georgia Institute of Technology
Atlanta GA 30332-0150
(404)894-3033
FAX: 894-2760
ben.zinn@aerospace.gatech.edu